Fabrication of dye-sensitized solar cells using heteroatom-doped reduced graphene oxide, and metal oxide-based nanocomposites as a counter electrode or photoanode

by

Nonjabulo Philile Dominica Ngidi

Submitted in fulfilment of the academic requirement for the degree of Doctor of Philosophy in the School of Chemistry and Physics, University of KwaZulu-Natal, Durban, Westville campus

December 2021

ABSTRACT

Recent advancements in technology have led to an exponential increase in global energy demand. Non-renewable energy sources have been widely used to meet this demand; however, they are prone to depletion and have side-effects such as the emission of greenhouse gases that lead to environmental pollution and climate change. Thus, there is a need to develop and advance inexhaustible and clean energy sources that maximize the electrical power generated. This will be beneficial for reducing greenhouse gas emissions, excess power fluctuations and electricity bills. Therefore, renewable energy has been a centre of attention in the past few years. The improvement in renewable energy sources, particularly in terms of quality, efficiency, and accessibility to all, is a significant step towards addressing the challenge of failing to meet the ever-increasing energy demand. Thus, renewable energy sources, particularly solar energy, have evolved as a suitable alternative.

Among the photovoltaic devices that convert solar into electrical energy, dye-sensitized solar cells (DSSCs) offer a cost-effective route towards a reliable energy supply. However, the performance of DSSCs is limited by factors, such as poor optical absorption, inefficient electron transport and severe instability. Thus, the innovation and development of novel materials are required to improve the power conversion efficiency (PCE) and sustainability of DSSCs. Graphene has been recently investigated as a suitable material to replace metal-based electrodes and to enhance the properties of electronic materials in different fields, such as photovoltaics and sensors. However, a defect-free graphene sheet is not suitable as a counter electrode (CE) or photoanode in DSSCs because of its neutral polarity, which often restricts efficient charge transfer at the graphene/liquid interface, irrespective of the high in-plane charge mobility. Thus, the focus on graphene has been based on its alteration by chemical doping with various heteroatoms, such as nitrogen, oxygen, boron, sulfur, and phosphorus.

Chemical doping assists in improving the electronic properties of graphene to unlock potential characteristics that are advantageous in DSSCs. Thus, heteroatom-doped reduced graphene oxide (heteroatom-doped rGO) serves as a good material to replace conventional electrodes and enhance the PCE in DSSCs. Heteroatom-doped rGO-based CEs and heteroatom-doped rGO-metal oxide-based photoanodes are being developed to enhance the reduction activity of the redox couple, and to increase the electrical conductivity for efficient charge transfer, respectively. Hence, the focus is to reduce the cost, and to improve the performance and stability of DSSCs.

This study involved the synthesis of GO, rGO, nitrogen-doped reduced graphene oxide (N-rGO), boron-doped reduced graphene oxide (B-rGO), boron and nitrogen co-doped reduced graphene oxide (BN-rGO), and heteroatom-doped rGO-metal oxide-based nanocomposites: reduced graphene oxide-titanium oxide (rGO-TiO$_2$), N-rGO-TiO$_2$, B-rGO-TiO$_2$, reduced graphene oxide-bismuth oxide (rGO-Bi$_2$O$_3$), N-rGO-Bi$_2$O$_3$, B-rGO-Bi$_2$O$_3$, and their application in DSSCs as a CE or photoanode. The synthesized nanomaterials were further characterized by standard instrumental techniques to elucidate their structural, morphological, optical, physicochemical, electrical conductivity, and electrochemical properties.

The effect of doping temperatures (600, 700 and 800 °C), and various nitrogen precursors (4-nitroaniline, 4-aminophenol, and 4-nitro-o-phenylenediamine), on the physicochemical, optical, and conductivity properties of N-rGO were investigated. The lowest doping temperature (600 °C) resulted in less thermally stable N-rGO, yet with higher porosity, while the highest doping temperature (800 °C) produced the opposite results. The choice of nitrogen precursor significantly impacted the atomic percentage of nitrogen in N-rGO. The nitrogen-rich precursor, 4-nitro-o-phenylenediamine, provided N-rGO with favourable physicochemical properties (larger surface area of 154.02 m^2 g^{-1}) and an enhanced electrical conductivity (0.133 S cm^{-1}). Pyrrolic-N doping was achieved as the main constituent of nitrogen moieties in N-rGO.

In the study of B-rGO, where the boron concentration was varied, the elemental analysis revealed that the highest boron content incorporated into the rGO framework was 7.12%. An electronic band structure with a low charge resistance of 20.23 Ω and an enhanced electrical conductivity of 5.920 S cm^{-1} was observed and noted to be dependent on the concentration of boron incorporated. All the B-rGO samples demonstrated a p-type conductivity behaviour, which is attributed to an increase in the density of states near the Fermi level. Thus, the studies of N-rGO and B-rGO revealed that by adjusting the doping temperatures, dopant precursors, and dopant concentration, one could tailor various properties of heteroatom-doped rGO.

This study also determined the effect of the metal oxide (TiO$_2$ and Bi$_2$O$_3$) on the heteroatom-doped rGO-metal oxide-based nanocomposites. The integration of TiO$_2$ with heteroatom-doped rGO significantly enhanced the photon absorption, exciton generation and charge carrier separation, as well as reducing the recombination effect, resulting in the efficient transfer of photogenerated electrons from the photoanode to the collecting electrode. The low content of TiO$_2$ in N-rGO-TiO$_2$ rendered the DSSCs with excellent optoelectronic properties, leading to the fabrication of DSSCs with a relatively higher PCE of 3.94% compared with 1.78 and 2.55%

for devices based on rGO-TiO$_2$ and B-rGO-TiO$_2$, respectively. Similar to the TiO$_2$-based nanocomposites, Bi$_2$O$_3$-based nanocomposites also exhibited a higher PCE due to good electrochemical properties. Thus, the synergistic effect between the high electrical conductivity of TiO$_2$- and Bi$_2$O$_3$-based nanocomposites and the formation of a good ohmic contact at the anode/cathode layer interface facilitated charge carrier transport, while suppressing their recombination, to yield high PCEs.

It was also discovered that dual heteroatom-doped rGO is a promising material that can enhance the electrical conductivity compared with other materials, such as GO, rGO, and single heteroatom-doped rGO. When investigating the effect of single or dual heteroatom-doped rGO as CEs for DSSCs, a precursor-dependent electrical conductivity behaviour is demonstrated in BN-rGO samples. The BN-rGO-3 with polyaniline (PANi) polymer as a CE exhibited the best electrical conductivity, yielding a PCE of 4.13%. Several traits that linked the physicochemical properties and the PCE were successfully elucidated.

This affirms the hypothesized potential of heteroatom-doped rGO nanomaterials in DSSCs through understanding and controlling both (i) nano-structural parameters and (ii) physicochemical, optical, and electrical properties.

PREFACE

The study presented herein was carried out in the School of Chemistry and Physics, University of KwaZulu-Natal, Durban, Westville campus, from January 2017 to December 2020. The research work was conducted under the supervision of Prof Vincent O. Nyamori.

This research work represents the author's original work and has not been submitted in any form for any degree or diploma to any tertiary institution. Other people's work made use of herein has been duly acknowledged in the text.

Signed: Nonjabulo P.D. Ngidi

DECLARATION 1 – PLAGIARISM

I, **Nonjabulo Philile Dominica Ngidi** declare that:

1. The research reported in this thesis, except where otherwise indicated, is my original research.

2. This thesis has not been submitted for any degree or examination at any other University.

3. This thesis does not contain other person's data, pictures, graphs, or other information, unless specifically acknowledged as being sourced from the person.

4. This thesis does not contain other person's writing, unless specifically acknowledged as being sourced from other researchers. Where other written sources have been quoted, then:

    a. Their words have been re-written but, the general information attributed to them has been referenced.

    b. Where their exact words have been used, then their writing has been placed in italics and inside quotation marks and referenced.

5. This thesis does not contain text, graphics or tables copied and pasted from the internet, unless specifically acknowledged, and the source being detailed in the thesis and in the reference's sections.

Signed: Nonjabulo P.D. Ngidi

DECLARATION 2 – PUBLICATION AND CONFERENCE CONTRIBUTION

Details of contribution to publications that form part and/or include research presented in this thesis (publications in preparation, submitted, in press and published and give details of the contributions of each author to the experimental work and writing of each publication).

Publication 1

Nonjabulo P.D. Ngidi, Moses A. Ollengo and Vincent O. Nyamori. Heteroatom-doped graphene and its application as a counter electrode in dye-sensitized solar cells. International Journal of Energy Research. **2018**. 43. 1702-1734. https://doi.org/10.1002/er.4326

Contributions: I planned and wrote the review paper. Prof Nyamori, and Dr Ollengo provided general guidance and proofread the manuscript.

Publication 2

Nonjabulo P.D. Ngidi , Moses A. Ollengo and Vincent O. Nyamori. Effect of doping temperatures and nitrogen precursors on the physicochemical, optical, and electrical conductivity properties of nitrogen-doped reduced graphene oxide. Materials. **2019**, 12, 3376; https://doi.org/10.3390/ma12203376

Special issue information: Carbon-based Materials;

https://www.mdpi.com/journal/materials/special_issues/carbon_Mater

Contributions: I designed the experiments, synthesized the nitrogen-doped reduced graphene oxide, characterised, analysed the data and wrote the manuscript. Prof Nyamori who provided guidance and Dr Ollengo proofread the manuscript.

Publication 3

Nonjabulo P.D. Ngidi, Moses A. Ollengo and Vincent O. Nyamori. Tuning the properties of boron-doped reduced graphene oxide by altering the boron content. New Journal of Chemistry. **2020**. 44, 16864-16876; https://doi.org/10.1039/D0NJ03909H

Contributions: I designed the experiments, collected, and analysed the data, and wrote the manuscript. Prof Nyamori who provided guidance and proofread the manuscript. Dr Ollengo proofread the manuscript.

Publication 4

Nonjabulo P.D. Ngidi, Edigar Muchuweni and Vincent O. Nyamori. Enhanced performance by heteroatom-doped reduced graphene oxide/TiO_2-based nanocomposites as a photoanode in dye-sensitized solar cells. Submitted to International Journal of Energy Research. **2022**.

Contributions: I designed the experiments, synthesized the nanocomposites, characterised, analysed the data, and wrote the manuscript. Prof Nyamori provided guidance and proofread the manuscript. Dr Muchuweni assisted with reviewing the manuscript and provided guidance to the manuscript structure.

Publication 5

Nonjabulo P.D. Ngidi, Edigar Muchuweni and Vincent O. Nyamori. Synthesis and characterisation of heteroatom-doped reduced graphene oxide/bismuth oxide nanocomposites and their application as photoanodes in DSSCs. RSC Advances. **2022**. 12. 2462-2472; https://doi.org/10.1039/d1ra08888b

Contributions: I designed the experiments, analysed the data, and wrote the manuscript. Prof Nyamori provided guidance and Dr Muchuweni assisted with reviewing the manuscript and provided guidance to the manuscript structure.

Publication 6

Nonjabulo P.D. Ngidi, Edigar Muchuweni and Vincent O. Nyamori. Dual heteroatom-doped reduced graphene oxide and its application in dye-sensitized solar cells. Optical Materials. **2021**. 122. 111689. https://doi.org/10.1016/j.optmat.2021.111689

Contributions: I designed the experiments, synthesized, and characterised the single and dual heteroatom-doped reduced graphene oxide, performed electrical properties characterisation, data collection, and wrote the manuscript. Prof Nyamori gave guidance and proofread the manuscript. Dr Muchuweni assisted with reviewing the manuscript and proofreading the manuscript.

From all the above publications, my role included carrying out all the experimental work, and contributing to the writing of the manuscripts along with the guidance of my supervisor. My supervisors' roles were to check scientific content and my correct interpretation of data. Based on his expertise, he has added some parts to these manuscripts.

Signed: Nonjabulo P.D. Ngidi

CONFERENCE CONTRIBUTIONS

Presentations

1. Nonjabulo P. D. Ngidi and Vincent O. Nyamori. Effect of doping temperatures and nitrogen sources in graphene oxide during thermal treatment. UKZN, College of Agriculture, Engineering and Science. Postgraduate Research and Innovation Symposium 2018, Westville Campus, South Africa, 26th October 2017.

2. Nonjabulo P. D. Ngidi and Vincent O. Nyamori. Effect of doping temperatures and nitrogen sources in graphene oxide during thermal treatment. Nanotechnology Platform Workshop 2017, UKZN, Westville, South Africa, 17th November 2017.

3. Nonjabulo P. D. Ngidi and Vincent O. Nyamori. Effect of doping temperatures and nitrogen sources in graphene oxide during thermal treatment. 2018 SACI Postgraduate Colloquium, Hotel school DUT, Durban, South Africa, 2nd February 2018.

4. Nonjabulo P. D. Ngidi and Vincent O. Nyamori. Effect of doping temperatures and nitrogen sources in graphene oxide during thermal treatment. 7th international conference on nanoscience and nanotechnology in Africa (Nano Africa), Salt Rock Hotel, Durban, South Africa, 22-25th April 2018.

5. Nonjabulo P. D. Ngidi and Vincent O. Nyamori. Effect of boron concentration on the physicochemical properties of boron-doped reduced graphene oxide. UKZN, College of Agriculture, Engineering and Science. Postgraduate Research and Innovation Symposium 2018, Westville, South Africa, 25th October 2018.

6. Nonjabulo P. D. Ngidi and Vincent O. Nyamori. Boron and nitrogen co-doped reduced graphene oxide and its enhanced properties. UKZN, College of Agriculture, Engineering and Science. Postgraduate Research and Innovation Symposium 2019, Westville Campus, South Africa, 17th October 2019.

7. Nonjabulo P. D. Ngidi and Vincent O. Nyamori. Tuning the properties of boron-doped reduced graphene oxide by altering the boron content. School of Chemistry and Physics Seminar, UKZN, Virtual via Microsoft team, 21st May 2021.

8. Nonjabulo P. D. Ngidi and Vincent O. Nyamori. Dual heteroatom-doped reduced graphene oxide and its application in dye-sensitized solar cells. South African Chemical Institute-KwaZulu Natal, 2021, Postgraduate research colloquium. Virtual via Zoom and Twitter, 7th July 2021.

9. Nonjabulo P. D. Ngidi and Vincent O. Nyamori. Dual heteroatom-doped reduced graphene oxide and its application in dye-sensitized solar cells. International Solar Fuel Conference 2021, Virtual via Zoom. 26-29th July 2021.

Signed: Nonjabulo P.D. Ngidi

ACKNOWLEDGMENTS

DEDICATION

"I can do all things through Christ who gives me strength"

– Philippians 4: 13

Every challenging work requires self-effort as well as guidance of elders especially those who are close to our heart

My humble effort, I dedicate to my sweet and loving:

Father and Mother

Whose affection, love, encouragement and prays of day and night made me achieve such success and honour

I do hope my family, friends, and aspiring researchers can draw some

inspiration from this thesis

"For with God, nothing shall be impossible"

– Luke 1: 37

LIST OF ABBREVIATION

Abbreviation and symbol	Full meaning
Å	Angstroms
NH_3	Ammonia
AC	Amorphous carbon
Ar	Argon
ATR	Attenuated total reflection accessory
Ave.	Average
B_2O_3	Boric anhydride
B-doped graphene	Boron-doped graphene
B-GO	Boron-doped graphene oxide
B-rGO	Boron-doped reduced graphene oxide
$B-rGO-Bi_2O_3$	Boron-doped reduced graphene oxide-bismuth oxide-based nanocomposite
$B-rGO-TiO_2$	Boron-doped reduced graphene oxide-titanium oxide-based nanocomposite
B,N-rGO	Boron and nitrogen doped reduced graphene oxide
BC_4	Boron silane
BET	Brunauer-Emmet-Teller
CdTe	Cadmium telluride
CNTs	Carbon nanotubes
CO	Carbon monoxide
CO_2	Carbon dioxide
R_{ct}	Charge transfer resistance
CVD	Chemical vapour deposition
E_{CB}	Conduction band potential
CIGS	Copper indium gallium selenide
CE	Counter electrode
L_a	Crystallite size
J_{sc}	Current density
CV	Cyclic voltammetry
I_D	Disorder band
°C	Degree Celsius
°C min^{-1}	Degree Celsius per minute

DFT	Density functional theory
DBD plasma	Dielectric barrier discharge plasma
DSSCs	Dye-sensitized solar cells
EDLC	Electrochemical double-layer capacitance
e^-	Electron
EDX	Electron dispersive X-ray spectroscopy
EIS	Electron impedance spectroscopy
e^-/h^+	Electron-hole recombination
E_g	Energy bandgap
C_2H_4	Ethylene
R_{ct}	Faradaic charge transfer resistance
E_F	Fermi level
FE-SEM	Field emission-scanning electron microscopy
FF	Fill factor
FTIR	Fourier transform infrared spectrophotometer
FWHW	Full width at half maximum
FTO	Fluorine-doped tin oxide
G	Gram
GNRs	Graphene nanoribbons
GNSs	Graphene nanosheets
GO	Graphene oxide
GQDs	Graphene quantum dots
I_G	Graphitic band
BC_3	Graphitic boron
HWHM	Half-width at a half maximum
h-BN	Hexagonal boron nitride
HOMO	Highest occupied molecular orbital
HRTEM	High resolution transmission electron microscopy
Hr	Hour
N_2H_4	Hydrazine
H_2	Hydrogen gas
H_2S	Hydrogen sulfide
IPCE	Incident photon to current efficiency
ITO glass	Indium tin oxide glass

ICP-OES	Inductively coupled plasma-optical emission spectroscopy
d_{002}	Interlayer spacing
I^-/I_3^-	Iodide/triodide
LUMO	Lowest unoccupied molecular orbital
w.t %	Mass by mass percentage
CH_4	Methane
MPCVD	Microwave-plasma CVD
mg	Milligram
mL	Millilitre
mL min^{-1}	Millilitre per minute
Min	Minute
mol	moles
nm	Nanometre
HNO_3	Nitric acid
N-doped graphene	Nitrogen-doped graphene
N-rGO	Nitrogen-doped reduced oxide
N-rGO-Bi$_2$O$_3$	Nitrogen-doped reduced oxide-bismuth oxide-based nanocomposite
N-rGO-TiO$_2$	Nitrogen-doped reduced oxide-titanium oxide-based nanocomposite
N-GNRs	Nitrogen-graphene nanoribbon
ORR	Oxygen reduction reaction
P-doped graphene	Phosphorus-doped graphene
Pt	Platinum
PEDOT-GO	Poly-(3,4-ethylenedioxythiophene)-graphene oxide
KClO	Potassium hypochlorite
$KMnO_4$	Potassium permanganate oxide
P-XRD	Powder-X-ray diffraction
I_D/I_G	Ratio of D-band intensity to G-band intensity in Raman spectroscopy
rGO	Reduced graphene oxide
rGO-Bi$_2$O$_3$	Reduced graphene oxide-bismuth oxide-based nanocomposite
rGO-TiO$_2$	Reduced graphene oxide-titanium oxide-based nanocomposite

R_s	Resistance
SAED	Selected area electron diffraction
Si	Silicon
NaOH	Sodium hydroxide
S-doped graphene	Sulfur-doped graphene
SPG	Sulfur-doped porous graphene
SRGO	Sulfur-reduced graphene oxide
H_2SO_4	Sulfuric acid
TGA	Thermogravimetric analysis
TiO_2	Titanium oxide
TMCs	Transition metal compounds
TEM	Transmission electron microscopy
v/v	Volume-by-volume concentration
$Wm^{-1}K^{-1}$	Watt per meter per Kelvin
XPS	X-ray photoelectron spectroscopy

LIST OF FIGURES

LIST OF TABLES

LIST OF SCHEMES

TABLE OF CONTENTS

CHAPTER 2: Heteroatom-doped graphene and its application as a counter electrode in dye-sensitized solar cells

CHAPTER 5: Performance of heteroatom-doped reduced graphene oxide-TiO$_2$-based nanocomposites as photoanodes in dye-sensitized solar cells

CHAPTER 6: Synthesis and characterisation of heteroatom-doped reduced graphene oxide/bismuth oxide nanocomposites and their application as photoanodes in DSSCs

CHAPTER 7: Dual heteroatom-doped reduced graphene oxide and its application in dye-sensitized solar cells

CHAPTER 8: Conclusions and Future work

CHAPTER 1

1.   Preamble

This chapter presents the background information on solar cells and describes their characteristics. In addition, it contains the problem statement, motivation, aim, objectives, research questions, and thesis outline.

1.1   Introduction

There is a growing trend in finding alternative sources of energy to support the socioeconomic development of humankind [1]. This is because the global energy demands are on the rising trend due to technological advancement. The major current energy sources are fossil fuels and nuclear energy [2]. Fossil fuels are currently the biggest source of energy, and they include oil shales, coal, tar sands, natural gas, and crude oil. The major advantage of these fossil fuels, especially coal in South Africa, is that it is cheap and readily available. However, these fossil fuels are non-renewable, and current deposits have been estimated to last only up to a few coming years [3]. Also, fossil fuels are associated with environmental pollution, which increases health risks and causes climate change due to global warming [4,5]. Therefore, eco-friendly energy sources are being sought as alternatives to fossil fuels to overcome environmental issues. Hence, an extensive search to discover new renewable energy and conversion techniques for harnessing the generated energy into functional forms is underway worldwide.

Renewable sustainable energy sources include solar [6], geothermal [7,8], biomass [9], wind energy [6], biofuels [10], and hydroelectricity [11,12]. The facilities for renewable energy generally need less maintenance as compared with those for the traditional generation of energy from fossil fuels. Renewable energy obtained from natural resources tends to reduce the cost of operation [13-16]. Also, they are advantageous because they emit little or no pollution; hence, they have minimal or zero negative impact on the environment. The development of renewable energy sources can also raise the standard of living in diverse ways; for instance, it can lower the cost of irrigation in agricultural activities. A properly installed windmill can harness energy to pump water for irrigation, and generate electrical energy for scattered rural communities [17]. Moreover, developing and installing renewable energy projects in rural areas often create job opportunities for local communities, with poverty reduction benefits [18]. The initial installation and acquisition of solar cells, for example, is out of reach to many rural

poor people and those who can afford, the question of efficiency in energy generation lingers. Thus, nanoscience and technology can provide them with a platform to deal with many of the multi-dimensional problems related to the cost and efficiency of these renewable energy technologies.

1.2   Background information

The primary source of energy on our planet is the sun. The sun provides enough energy to the earth each year, which can substitute fossil fuel energy's yearly demand. The amount of solar radiation that strikes the earth for three days is estimated to be equivalent to the amount of energy stored in all non-renewable energy sources, including fossil fuels. However, solar radiation depends on many factors, such as weather, location, time of the day, and proximity of the sun to the earth's surface [19]. These factors affect the efficiency of radiation harvesters, i.e., solar cells.

Solar cells are electronic devices that can convert light energy into electricity using the photovoltaic effect [20-22]. The photovoltaic effect was first demonstrated in 1839 by Alexandre-Edmond Becquerel [23], and it relies upon the interaction of photons of light with electrons in a photovoltaic material. A photon must have sufficient energy to promote an electron from the valance band across the bandgap into the conduction band to produce a light-induced voltaic effect. Consequently, photovoltaic modules produce electricity directly from sunlight without emissions or vibrations.

The economic attractiveness of solar cells can be enhanced by reducing the cost of producing cells, including the associated equipment, increasing efficiencies, and creating new system designs with lower total cost per unit power output [24]. As a result, balancing these factors in the solar power production of electricity has been the uttermost challenge. Whilst the methods of using solar energy are quite simple, they require an efficient and long-lasting solar material [25].

Solar cells are widely used in terrestrial applications and are economically competitive as an alternative energy source for domestic appliances such as refrigerators [26,27]. Morden life requires energy for various reasons such as lighting, cooking, entertainment, communication, and transport. Thus, this has caused an increase in energy consumption per household. Farmer *et al.* [28] forecasted that electricity consumption will increase to 20% by 2030, whereas international energy predicts 16% by 2050. Despite the increasing energy demand, in 2016, Farmer *et al.* [28] demonstrated that from 1980, the price/kWh of electricity has been dropping

by 10% annually. The price drop has been facilitated by reducing the cost of production of electricity and its generation from alternative sources such as solar cells.

Solar cells are grouped into three generations based on the nature of the material and the power conversion efficiency (PCE) [29]. The first-generation solar cells consist of silicon-based solar cells fabricated on silica wafers [30]. There are two types of first-generation solar cells, i.e., single or monocrystalline silicon solar cells, and multicrystalline solar cells. These solar cells differ in their PCE. A single/monocrystalline silicon solar cell has a PCE of 20.6% [31], whereas a multicrystalline solar cell has a PCE of ~12-14% [29]. Though single crystalline solar cells have a higher PCE as compared with multicrystalline solar cells, the production of multicrystalline solar cells is still much cheaper and easier [32]. Manufacturing these cells requires high purity materials and a low concentration of structural defects [33]. The disadvantage of using these solar cells is that the light energy is not entirely converted into electricity since the incoming photon's energy is larger than the energy gap; therefore, the excess energy is often converted into heat or lost as heat.

The second-generation solar cells consist of thin light-absorbing layers of 1 µm thickness, for instance, amorphous silicon thin-film (a-Si) solar cells, copper indium gallium di-selenide (CIGS) solar cells, and cadmium telluride (CdTe) thin-film solar cell [29,34-36]. These films are made up of layers of semiconductor materials. During the synthesis of thin-film solar cells, low-cost processes and fewer materials are used when compared with the first-generation solar cells [37]. However, amorphous silicon thin-film solar cells are photodegradable and perform poorly when exposed to light [38]. It has been reported that thermal annealing reverses this effect [38]. The attractive feature of thin-films solar cells is their ease of large-area fabrication (from over 0 to 6 m^2), whereas silicon-based solar cells can only be grown on wafer dimensions [34]. Thin-film solar cells make use of low-cost copper tape as a substrate. Consequently, they are less expensive when compared with conventional silicon cells. However, they have a PCE of ~10.1% [35], which is lower than the first-generation solar cells. In addition, there are several other drawbacks that bedevil thin-film solar cells; firstly, they are environmentally unfriendly because of the substances released during the fabrication process [39]. Secondly, synthetic materials used in this generation are scarce, and the toxicity of heavy metals, such as cadmium, indium, and telluride, is of great concern.

In the quest to address challenges second-generation solar cells face, a third-generation has been developed. The third-generation includes concentrated solar cells, polymer-based solar cells, nanocrystal-based solar cells, perovskite solar cells, and dye-sensitized solar cells

(DSSCs). Most of these solar cells are still in the research phase, and they present promising novel technologies, which are yet to be commercially proven. Most importantly, these devices do not have a p-n junction and have improved PCE [40,41].

The concentrated solar cells have been reported to have a PCE of greater than 40% [42]. The fabrication processes of these cells are scalable and require no cost for thermal mass [43]. The major weakness of concentrated solar cells is their dependence on a large amount of direct solar radiation; as a result, energy output rapidly drops with cloud cover, unlike photovoltaics, which can produce electricity even from diffuse radiation [44]. Polymer solar cells are also called organic or plastic solar cells. They are flexible because of the presence of a polymer substrate [45-48]. They are simple due to their ease of fabrication, and they are also cost-effective. However, they tend to exhibit low PCE for hard materials and are prone to photochemical degradation. In recent years, the PCE of polymer solar cells has improved from 3 to 15% [49-51].

Nanocrystal-based solar cells use quantum dots as the absorbing photovoltaic material or semiconducting materials [52-56]. Quantum dots have bandgaps that are easily tunable across a large range of energy levels by altering the size of the dots [57]. The technologies that are associated with nanocrystal quantum dots as semiconductors for solar cells can theoretically convert 60% of the solar spectrum into electric power [58]. Nanocrystal-based solar cells are the replacement of bulk materials like CdTe, CIGS, and silicon [59]. In recent years, perovskite solar cells have demonstrated a remarkable advancement in PCE [60]. However, there are challenges that limit perovskite solar cells from becoming a competitive commercial technology, such as using absorber materials based on methylammonium lead halide, which results in an inefficient and unstable cell.

DSSCs are used as an alternative to the first- and second-generation solar cells [29,61,62]. This is because they can function at low light intensities and are environmentally friendly. DSSCs have attracted a lot of attention because of their simple fabrication process, low production cost, high efficiency, and feasibility of printing on a flexible substrate. Thus, cost-effectiveness is a major parameter for the production of DSSCs. DSSCs differ from conventional semiconductor devices in that they separate the function of light absorption from charge carrier transport. They absorb the incident sunlight and exploit the light energy capability to induce a vectorial electron transfer reaction. In general, DSSCs can be depicted as a simple photovoltaic device made from a working electrode, sensitizer (dye), redox-mediator (electrolyte), and the counter electrode (cathode) (Figure 1.1). The working principle of DSSCs entails three

4

fundamental steps: absorption of light, electron injection, and electron transportation. These steps are associated with the change of photons into the current.

The dye absorbs the light from the sun, and it excites a molecule (from the highest occupied molecular orbital (HOMO) to the lowest unoccupied molecular orbital (LUMO)) in the dye (equation 1 and Figure 1.1). The excited dye molecule then produces electrons (equation 2) and injects them from the LUMO of the dye to the conduction band of the semiconductor. These electrons can flow through the external circuit to the cathode and then to the electrolyte. Then, the electrolyte transports the electrons back to the dye molecule (equation 4) [63]. This charge collection flow delivers electric current to the electric load. The chemical reactions taking place in the DSSCs are shown below.

Photoelectrode:

- Absorption light: $$2S^o + 2h\nu \rightarrow 2S^* \qquad (1)$$

- Electron injection: $$2S^* \rightarrow 2S^+ + 2e^- \ (TiO_2) \qquad (2)$$

- Dye reduction and iodide oxidation: $$2S^+ + 3I^- \rightarrow 2S^o + I_3^- \qquad (3)$$

- Overall: $$3I^- + 2h\nu \rightarrow 2I_3^- + 2e^- \ (TiO_2) \qquad (4)$$

Counter electrode:

- Triiodide reduction: $$I_3^- + 2e^- \rightarrow 3I^- \qquad (5)$$
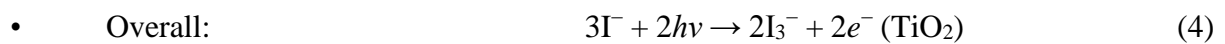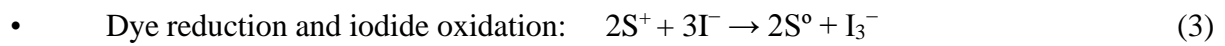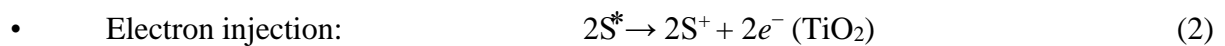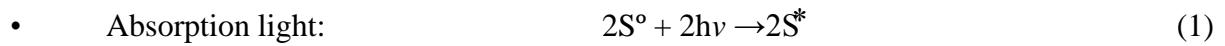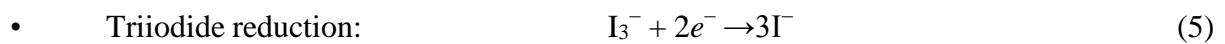
(S^o = ground state of the dye; S* = excited state; S^+ = the oxidized state)
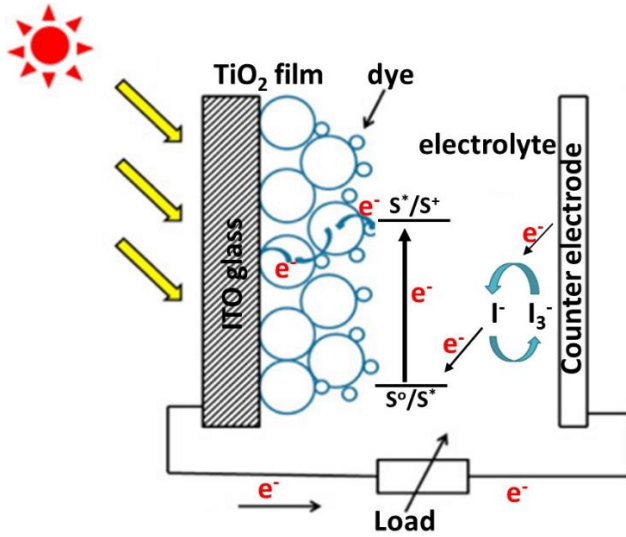
Figure 1.1: Mechanism involved in the DSSCs during light-harnessing.

1.2.1 Evaluation of DSSCs performance

The DSSCs performance can be investigated by utilizing the open-circuit (V_{oc}), short-circuit current density (J_{sc}), maximum power output (P_{max}), incident photon to current conversion efficiency (IPCE), fill factor (FF), and the overall efficiency (η), as shown in Figure 1.2:
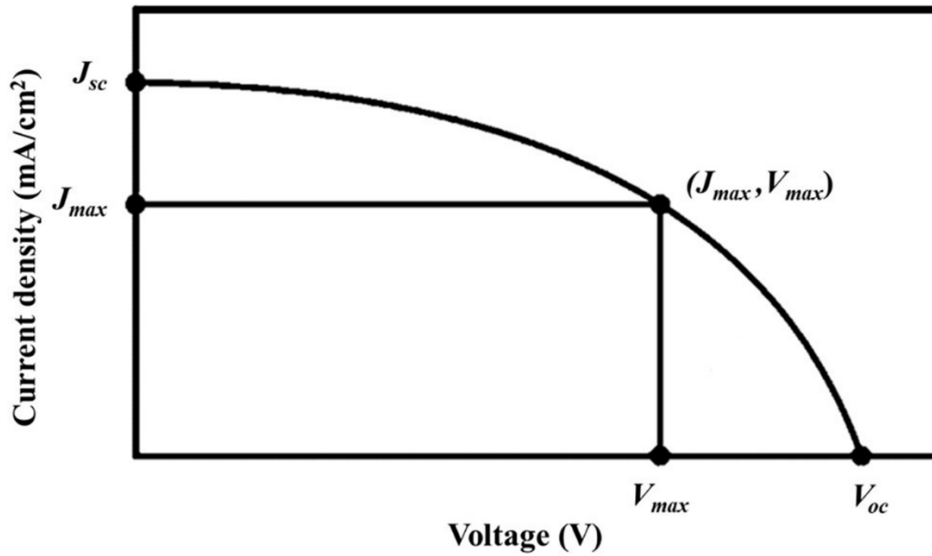
Figure 1.2: J-V curve to evaluate the performance of DSSCs [64].

where J_{sc} refers to the current produced when the positive and negative electrodes are short-circuited, i.e., at a zero voltage. Whereas, at zero current, under open-circuit conditions, the voltage across positive and negative electrodes is represented by V_{oc}. The P_{in} is the power of the incident solar radiation. FF represents the ratio of the maximum power output of the DSSC to its theoretical power output, and is defined by Equation 6:

$$FF = \frac{J_{max} \times V_{max}}{J_{sc} \times V_{oc}} \qquad (6)$$

Additionally, the percentage of solar energy that is converted into electrical energy is represented by the overall efficiency (η) (Equation 7), where η increases with the increase in the J_{sc}, molar coefficient of dye, $V_{oc,}$ and FF.

$$\eta = \frac{J_{sc} \times V_{oc} \times FF}{P_{in}} \qquad (7)$$

IPCE represents the ratio of the number of electrons moving through the external circuit to the number of photons incident on the surface of the cell at any wavelength (λ) [65]. It is determined by using Equation 8:

$$IPCE = 1240 \times \frac{J_{sc}}{P_{in} \times \lambda} \qquad (8)$$

1.2.2 Development challenges in DSSCs

A challenging but realizable goal for the current DSSCs is to achieve PCEs of above 15% and, in addition, to improve their environmental stability. The environmental stability of DSSCs refers to the performance of the entire cell at any time. Generally, high stability leads to longer lifetimes. The electrolyte and dye are susceptible to photodegradation which lowers the stability of DSSCs. Thus, solid-state electrolytes are required to prevent leakage, and the dye molecule must be stable to carry out a 10^8 turnover in order to achieve DSSCs with a lifetime of more than 20 years. The main cause of low PCE are low red and near-infrared absorption, and the low extinction coefficient of the photoanode (metal oxide) due to their smaller surface area; thus, a large surface area in nanomaterials is required to optimally adsorb dye molecules and increase the photo-exciton electrons, which can further improve the DSSCs. In addition, the poor contact between the electrodes, slow recombination kinetics of the I^-/I_3^- redox couple, and degradation of electrolyte and dye due to ultraviolet (UV) absorption of light [62] do lower the PCE values.

1.2.3 Various ways to augment the stability and efficiency

To enhance the environmental stability and PCE of DSSCs, researchers have reported various ways of fabricating the cells, modification of materials, such as the dye, counter electrode, electrolyte, and photoanode. Modifying these materials enables better light-harvesting, increases the electron injection efficiency, and prevents charge recombination. The electron injection efficiency can be improved by preventing the occurrence of molecular aggregation,

and thus the LUMO of the dye or sensitizer should overlap with that of the photoanode. After electron injection, the oxidized dye requires to be solidly reduced to its ground state. For instance, the regeneration process ought to be fast when contrasted with the process of oxidation of the dye. The development of numerous inorganic, organic, natural, and metal-free dyes has been explored to modify DSSCs [66-68]. Another form of enhancing electron injection efficiency is co-sensitization, which involves two or more sensitizing dyes that consist of various absorption spectrum ranges. The dyes are mixed to expand the spectrum response range [69]. The addition of energy relay dyes has been reported to enhance the performance of DSSCs [70]. The redox mediator potential (I^- ion) strongly affects the maximum photovoltage. Therefore, the potential of the redox couple needs to be close to the ground state of the dye [71]. Various electrolytes, such as quasi-solid-state [72], gel [73], and ionic liquid [74] electrolytes, have been investigated as mediators in DSSCs.

In order to improve the PCE, it is important to enhance the V_{oc}. This is done by using certain electrolyte solution additives, such as alkylpyridines (e.g., 4-*tert*-butylpyridine (TBP)), that can improve DSSC efficiency by increasing the V_{oc} without affecting the short-circuit current [75]. The addition of 4-*tert*-butylpyridine to the redox electrolyte used in dye-sensitized titanium oxide (TiO_2) solar cells tends to reduce the recombination of electrons in TiO_2 with triiodide in the electrolyte by preventing triiodide access to the TiO_2 surface. The V_{oc} is also improve by reducing charge recombination: (i) between the redox couple and injected electrons in the photoanode and (ii) between the oxidized sensitizer and injected electrons in the photoanode. The photoanode of DSSCs can be modified by coating a luminescent layer [76] or luminescent chromophores, like applying rare-earth-doped oxides [76]. The use of various nanomaterials in the fabrication of counter electrodes, such as nanowires of carbon, carbon nanotubes, and graphene, can tremendously improve the PCE of DSSCs [77]. The PCE of DSSCs may also be enhanced by synthesizing nanocomposites that are efficient for solar-harvesting and tailoring their physical dimensions, composition, morphology, and electrochemical properties. An investigation on the behavior of graphene-based nanomaterials at higher *wt.%* loading, optimization of the heteroatom in *wt.%* in such graphene-based nanomaterials, comparison of the synthetic methods are potential and promising frontiers in solar energy harnessing techniques. These various approaches mentioned above have by far improved the PCE of DSSCs, yet there is still some improvement needed to be done.

1.3   Thesis aim and objectives

1.3.1   Aim

The purpose of this study was to synthesize efficient solar-harvesting materials of single and dual heteroatom-doped (nitrogen- and boron-doped) reduced graphene oxide and further coat the single heteroatom-doped reduced graphene oxide (rGO) with a metal oxide (titanium dioxide (TiO_2) or bismuth oxide (Bi_2O_3)) and utilize these nanomaterials as a counter electrode or photoanode in DSSCs.

1.3.2   Objectives

The goal of this research was achieved by:

- Investigating the effect of varying the doping temperatures and nitrogen precursors on the physicochemical, optical, and electrical conductivity properties of the synthesized nitrogen-doped reduced graphene oxide (N-rGO).

- Tuning the electrical transport mechanism, electrochemical, and conductivity properties of boron-doped reduced graphene oxide (B-rGO) by varying the boron concentration.

- Synthesis of the nanocomposite by coating heteroatom-doped rGO with different metal oxides (TiO_2 and Bi_2O_3).

- Designing an efficient DSSC containing the heteroatom-doped rGO and their nanocomposites as a photoanode.

- Investigating the photovoltaic (PV) efficiency at different *wt.%* ratio of titania in heteroatom-doped rGO/TiO_2 nanocomposites constituents.

- Evaluating the performance of DSSCs when the single or dual heteroatom-doped rGO was applied as counter electrodes.

1.4   Research questions

- Which are the better doping temperature and nitrogen precursors for the synthesis of N-rGO?

- Can the synthesized N-rGO or B-rGO be coated with TiO_2 or Bi_2O_3, thus, attenuating their physical and chemical properties?

- Do the synthesis method and *wt.%* ratios in the single or dual heteroatom-doped rGO influence the light-harvesting capabilities?

- What are the physicochemical, electrochemical, and electrical conductivity properties ideal for light harnessing?

1.5   Structure of the thesis

Chapter 1 (Introduction)

This chapter presents the overall scientific concepts or background information on DSSCs and graphene-based nanomaterials; thus, it provides a general foundation for this research. Also, it includes the research motivation, thesis feasibility study, research aim and objectives, and the dissertation outline.

Chapter 2 (Paper 1)

This chapter entails the literature review on using heteroatom-doped graphene as a counter electrode in DSSCs. It provides an overview of the current advances, knowledge on graphene-based materials (including surface functionalization and doping), discussion on the fundamentals of DSSC operation, and various factors that influence the performance of DSSCs. Also, a comparative discussion of a graphene-based nanomaterial as counter electrodes against other counter electrodes, such as platinum-based counter electrodes and carbon black nanoparticle counter electrodes, are presented.

Chapter 3 (Paper 2)

This chapter shows a detailed synthesis and characterization of N-rGO. It further describes the effects of doping temperatures and the use of various nitrogen precursors on the physicochemical (structural), optical and electrical conductivity properties. It also explains the potential outcome of tailoring the nitrogen doping species (pyrrolic-N, pyridinic-N, and quaternary-N) of N-rGO by varying the doping temperatures. From this, we had the option to present the first report on the effect of varying the doping temperatures and nitrogen precursors on N-rGO.

Chapter 4 (Paper 3)

In this chapter, we evaluate the effect of doping with boron on the physicochemical properties of B-rGO. The effect of the *wt.%* of the boron-containing precursor on the amount of B-rGO was also determined. The specific objectives in this chapter include investigating the influence

of boron concentration on the electronic band structure, electrical transport mechanism, and electrochemical properties in B-rGO. Additionally, the chapter links the physicochemical properties to the electrochemical capabilities.

Chapter 5 (Paper 4)

This chapter entails the synthesis and characterization of N-rGO or B-rGO coated with TiO_2 *via* a hydrothermal reaction. The effect of TiO_2 concentration on the physicochemical, electrical conductivity properties, and photovoltaic performance of DSSCs fabricated using N-rGO, B-rGO, and their nanocomposite as a photoanode was investigated. In this chapter, we also explored the effects on the performance of DSSCs induced by variation of the dye.

Chapter 6 (Paper 5)

This chapter reports the physicochemical properties of nitrogen- or boron-doped reduced graphene oxide-Bi_2O_3-based (N-rGO/Bi_2O_3 or B-rGO/Bi_2O_3) nanocomposites. It also presents the influence of boron and nitrogen on the electrochemical properties and photovoltaic performance of the N-rGO/Bi_2O_3 and B-rGO/Bi_2O_3 nanocomposites.

Chapter 7 (Paper 6)

This chapter presents a comparison between single and dual heteroatom-doped rGO and their application in DSSCs as a counter electrode. This chapter also shows a link between the properties of heteroatom-doped rGO with the performance of DSSCs. The influence of the heteroatom-doped rGO on the device photovoltaic parameters, such as J_{sc} and FF, is discussed. The resulting PCE values from the single versus the dual heteroatom-doped rGO were evaluated.

Chapter 8 (Conclusion and future work)

This section is a comprehensive summary of the entire thesis. It features the major findings of this research work and provides suggestions and recommendations for future work. In general, this chapter highlights the new knowledge that this research contributes to the field of material science and solar energy conversion. Also, due to the nature of the research scope and findings herein, it offers an opportunity for future work as we strive for the continual advancement of solar cells.

References

1.   H. Khatib, *Energy policy*, **2012**, 48, 737-743.

2.   A. Demirbas, *Prog. Energy Combust. Sci.*, **2005**, 31, 171-192.

3.   I. Capellán-Pérez, M. Mediavilla, C. de Castro, Ó. Carpintero and L. J. Miguel, *Energy*, **2014**, 77, 641-666.

4.   C. M. Hsu, C. Battaglia, C. Pahud, Z. Ruan, F. J. Haug, S. Fan, C. Ballif and Y. Cui, *Adv. Energy Mater.*, **2012**, 2, 628-633.

5.   A. A. Farhat and V. I. Ugursal, *Int. J. Energy Res.*, **2010**, 34, 1309-1327.

6.   K. Solangi, M. Islam, R. Saidur, N. Rahim and H. Fayaz, *Renew. Sust. Energy Rev.*, **2011**, 15, 2149-2163.

7.   S. Haehnlein, P. Bayer and P. Blum, *Renew. Sust. Energy Rev.*, **2010**, 14, 2611-2625.

8.   J. W. Lund, D. H. Freeston and T. L. Boyd, *Geothermics*, **2011**, 40, 159-180.

9.   C. Posten and G. Schaub, *J. Biotechnol.*, **2009**, 142, 64-69.

10.   A. Azarpour, S. Suhaimi, G. Zahedi and A. Bahadori, *Arab. J. Sci. Eng.*, **2013**, 38, 317-328.

11.   A. Raheem, S. A. Abbasi, A. Memon, S. R. Samo, Y. Taufiq-Yap, M. K. Danquah and R. Harun, *Energy Sustain. Soc.*, **2016**, 6, 16-29.

12.   C. Gokcol, B. Dursun, B. Alboyaci and E. Sunan, *Energy Policy*, **2009**, 37, 424-431.

13.   R. Spalding-Fecher, H. Winkler and S. Mwakasonda, *Energy Policy*, **2005**, 33, 99-112.

14.   J. J. Klemeš, P. S. Varbanov, T. G. Walmsley and A. Foley, *Renew. Sust. Energy Rev.*, **2019**, 116, 109435-109442.

15.   K. Moustakas, M. Loizidou, M. Rehan and A. S. Nizami, *Renew. Sust. Energy Rev.*, **2020**, 119, 109418-109424.

16.   P. Y. Liew, P. S. Varbanov, A. Foley and J. J. Klemeš, *Renew. Sust. Energy Rev.*, **2021**, 135, 110385-110390.

17.   A. Pegels, *Energy policy*, **2010**, 38, 4945-4954.

18.   N. Asim, K. Sopian, S. Ahmadi, K. Saeedfar, M. Alghoul, O. Saadatian and S. H. Zaidi, *Renew. Sust. Energy Rev.*, **2012**, 16, 5834-5847.

19.   M. Iqbal, *An introduction to solar radiation*, Academic Press United States, 1st edn., **2012**, 1, 107-168.

20.   Y. Chu and P. Meisen, *Global Energy Network Institute*, **2011**, 1, 34-53.

21.   P. Choubey, A. Oudhia and R. Dewangan, *Recent Res. Sci. Technol.*, **2012**, 4, 203-212.

22. B. Anand, R. Shankar, S. Murugavelh, W. Rivera, K. Midhun Prasad and R. Nagarajan, *Renew. Sust. Energy Rev.*, **2021**, 141, 110787-110814.

23. M. Becquerel, *Comptes Rendus Acad. Sci.*, **1839**, 9, 561-567.

24. M. Bernardi, N. Ferralis, J. H. Wan, R. Villalon and J. C. Grossman, *Energy Environ. Sci.*, **2012**, 5, 6880-6884.

25. A. Fahrenbruch and R. Bube, *Fundamentals of solar cells: Photovoltaic solar energy conversion*, Academic Press, New York, 1st edn., **1983**, 1, 209-315.

26. N. Komerath and P. Komerath, *Phys. Procedia*, **2011**, 20, 255-269.

27. O. Okoro and T. Madueme, *Int. J. Sustain. Energy*, **2006**, 25, 23-31.

28. J. D. Farmer and F. Lafond, *Res. Policy*, **2016**, 45, 647-665.

29. S. Sharma, K. K. Jain and A. Sharma, *Mater. Sci. Appl.*, **2015**, 6, 1145-1155.

30. A. M. Bagher, M. M. A. Vahid and M. Mohsen, *Am. J. Opt. Photonics*, **2015**, 3, 94-113.

31. S. Zhang, X. Pan, H. Jiao, W. Deng, J. Xu, Y. Chen, P. P. Altermatt, Z. Feng and P. J. Verlinden, *IEEE J. Photovolt.*, **2016**, 6, 145-152.

32. V. Yerokhov, R. Hezel, M. Lipinski, R. Ciach, H. Nagel, A. Mylyanych and P. Panek, *Sol. Energy Mater. Sol. Cells*, **2002**, 72, 291-298.

33. M. Green, *Solar Energy*, **2004**, 76, 3-8.

34. A. Shah, H. Schade, M. Vanecek, J. Meier, E. Vallat-Sauvain, N. Wyrsch, U. Kroll, C. Droz and J. Bailat, *Prog. Photovolt.: Res. Appl.*, **2004**, 12, 113-142.

35. K. Chopra, P. Paulson and V. Dutta, *Prog. Photovolt.: Res. Appl.*, **2004**, 12, 69-92.

36. J. Major, R. Treharne, L. Phillips and K. Durose, *Nature*, **2014**, 511, 334-337.

37. D. Y. Goswami and F. Kreith, *Handbook of energy efficiency and renewable energy*, Crc Press, United State, 1st edn., **2007**, 1, 152-189.

38. D. E. Carlson and C. R. Wronski, *Appl. Phys. Lett.*, **1976**, 28, 671-673.

39. V. Sethi, M. Pandey and M. P. Shukla, *Int. J. Chem. Eng. Appl.*, **2011**, 2, 77-80.

40. M. A. Green, *Prog. Photovolt.: Res. Appl.*, **2001**, 9, 123-135.

41. M. Grätzel, *J. Photoch. Photobio. C*, **2003**, 4, 145-153.

42. D. Barlev, R. Vidu and P. Stroeve, *Sol. Energy Mater. Sol. Cells*, **2011**, 95, 2703-2725.

43. G. Paternoster, M. Zanuccoli, P. Bellutti, L. Ferrario, F. Ficorella, C. Fiegna, P. Magnone, F. Mattedi and E. Sangiorgi, *Sol. Energy Mater. Sol. Cells*, **2015**, 134, 407-416.

44. G. K. Singh, *Energy*, **2013**, 53, 1-13.

45. L. Lu, T. Zheng, Q. Wu, A. M. Schneider, D. Zhao and L. Yu, *Chem. Rev.*, **2015**, 115, 12666-12731.

46. C. Lee, S. Lee, G.-U. Kim, W. Lee and B. J. Kim, *Chem. Rev.*, **2019**, 119, 8028-8086.

47. M. Zhang, J. Wang, X. Ma, J. Gao, C. Xu, Z. Hu, L. Niu and F. Zhang, *APL Mater.*, **2020**, 8, 090703-090724.

48. M. A. Alkhalayfeh, A. A. Aziz and M. Z. Pakhuruddin, *Renew. Sust. Energy Rev.*, **2021**, 141, 110726-110734.

49. Z. Li, X. Xu, W. Zhang, X. Meng, Z. Genene, W. Ma, W. Mammo, A. Yartsev, M. R. Andersson, R. A. J. Janssen and E. Wang, *Energy Environ. Sci.*, **2017**, 10, 2212-2221.

50. R. Zhao, N. Wang, Y. Yu and J. Liu, *Chem. Mater.*, **2020**, 32, 1308-1314.

51. L. Zhang, T. Jia, L. Pan, B. Wu, Z. Wang, K. Gao, F. Liu, C. Duan, F. Huang and Y. Cao, *Sci. China Chem.*, **2021**, 64, 408-412.

52. K. P. Fritz, S. Guenes, J. Luther, S. Kumar, N. S. Sariciftci and G. D. Scholes, *J. Photoch. Photobiol. A: Chem.*, **2008**, 195, 39-46.

53. P. V. Kamat, *J. Phys. Chem. C*, **2008**, 112, 18737-18753.

54. S. Aina, B. Villacampa and M. Bernechea, *Mater. Adv.*, **2021**, 2, 4140-4151.

55. C. Liu, Q. Zeng, H. Wei, Y. Yu, Y. Zhao, T. Feng and B. Yang, *Small Methods*, **2020**, 4, 2000419-2000439.

56. A. a. O. El-Ballouli, O. M. Bakr and O. F. Mohammed, *Chem. Mater.*, **2019**, 31, 6387-6411.

57. A. P. Alivisatos, *Science*, **1996**, 271, 933-937.

58. W. A. Badawy, *J. Adv. Res.*, **2015**, 6, 123-132.

59. J. Ramanujam, D. M. Bishop, T. K. Todorov, O. Gunawan, J. Rath, R. Nekovei, E. Artegiani and A. Romeo, *Prog. Mater. Sci.*, **2020**, 110, 100619-100678.

60. J. Y. Kim, J.-W. Lee, H. S. Jung, H. Shin and N.-G. Park, *Chem. Rev.*, **2020**, 120, 7867-7918.

61. L. Zhang and J. M. Cole, *J. Mater. Chem. A*, **2017**, 5, 19541-19559.

62. A. Andualem and S. Demiss, *J. Heterocyclics*, **2018**, 1, 29-34.

63. K. Sharma, V. Sharma and S. S. Sharma, *Nanoscale Res. Lett.*, **2018**, 13, 381-426.

64. T. N. Murakami and M. Grätzel, *Inorganica Chim. Acta*, **2008**, 361, 572-580.

65. G. Palma, L. Cozzarini, E. Capria and A. Fraleoni-Morgera, *Rev. Sci. Instrum.*, **2015**, 86, 013112-013109.

66. A. Tomkeviciene, G. Puckyte, J. V. Grazulevicius, M. Degbia, F. Tran-Van, B. Schmaltz, V. Jankauskas and J. Bouclé, *Synth. Met.*, **2012**, 162, 1997-2004.

67. Z. Xie, A. Midya, K. P. Loh, S. Adams, D. J. Blackwood, J. Wang, X. Zhang and Z. Chen, *Prog. Photovolt.: Res. Appl.*, **2010**, 18, 573-581.

68. I.-P. Liu, Y.-C. Hou, C.-W. Li and Y.-L. Lee, *J. Mater. Chem. A*, **2017**, 5, 240-249.

69. B. E. Hardin, E. T. Hoke, P. B. Armstrong, J.-H. Yum, P. Comte, T. Torres, J. M. Fréchet, M. K. Nazeeruddin, M. Grätzel and M. D. McGehee, *Nat. Photonics*, **2009**, 3, 406-411.

70. M. M. Rahman, M. J. Ko and J.-J. Lee, *Nanoscale*, **2015**, 7, 3526-3531.

71. C. Bauer, G. Boschloo, E. Mukhtar and A. Hagfeldt, *J. Phys. Chem. B*, **2002**, 106, 12693-12704.

72. A. Mahmood, *J. Energy Chem.*, **2015**, 24, 686-692.

73. N. M. Saidi, F. S. Omar, A. Numan, D. C. Apperley, M. M. Algaradah, R. Kasi, A.-J. Avestro and R. T. Subramaniam, *ACS Appl. Mater. Interfaces*, **2019**, 11, 30185-30196.

74. N. I. Mohd Faridz Hilmy, W. Z. N. Yahya and K. A. Kurnia, *J. Mol. Liq.*, **2020**, 320, 114381-114392.

75. J. Wu, Z. Lan, J. Lin, M. Huang, Y. Huang, L. Fan and G. Luo, *Chem. Rev.*, **2015**, 115, 2136-2173.

76. N. Chander, A. F. Khan and V. K. Komarala, *RSC Adv.*, **2015**, 5, 66057-66066.

77. J. Wu, Z. Lan, J. Lin, M. Huang, Y. Huang, L. Fan, G. Luo, Y. Lin, Y. Xie and Y. Wei, *Chem. Soc. Rev.*, **2017**, 46, 5975-6023.

CHAPTER 2

REVIEW PAPER

WILEY ENERGY RESEARCH

Heteroatom-doped graphene and its application as a counter electrode in dye-sensitized solar cells

Nonjabulo P.D. Ngidi | Moses A. Ollengo | Vincent O. Nyamori

School of Chemistry and Physics, University of KwaZulu-Natal, Durban 4000, South Africa

Correspondence
Vincent O. Nyamori, School of Chemistry and Physics, University of KwaZulu-Natal, Westville Campus, Private Bag X54001, Durban 4000, South Africa.
Email: nyamori@ukzn.ac.za

Summary

The most frequently used counter electrode (CE) in dye-sensitized solar cells (DSSCs) is platinum on fluorine-doped tin oxide glass. This electrode has excellent electrical conductivity, chemical stability, and high electrocatalytic affinity for the reduction of triiodide. However, the high cost of metallic platinum and the poor electrochemical stability pose a major drawback in the commercial production. This has necessitated a search for a non-precious metal and metal-free electrocatalyst that demonstrates better catalytic activity and longer electrochemical stability for practical use in DSSCs. Graphene has been at the centre of attention due to its excellent optoelectronic properties. However, a defect-free graphene sheet is not suitable as a CE in DSSCs, because of its neutral polarity which often restricts efficient charge transfer at the graphene/liquid interface, irrespective of the high in-plane charge mobility. Hence, heteroatom-doped graphene-based CEs are being developed with the aim to balance electrical conductivity for efficient charge transfer and charge polarization for enhanced reduction activity of redox couples simultaneously. The elements commonly used in chemical doping of graphene are nitrogen, oxygen, boron, sulfur, and phosphorus. Halogens have also recently shown great promise. It has been demonstrated that edge-selective heteroatom-doping of graphene imparts both efficient in-plane charge transfers and polarity, thereby enhancing electrocatalytic activity. Thus, heteroatom-doped graphene serves as a good material to replace conventional electrodes and enhance power conversion efficiency in DSSCs. The focus is to reduce the cost of DSSCs. This review explores the performance of DSSCs, factors that influence the power conversion efficiency, and various physicochemical properties of graphene. It further outlines current progress on the synthetic approaches for chemical doping (substitutional and surface transfer doping) of graphene and graphene oxide with different heteroatoms in order to fine-tune the electronic properties. The use of heteroatom-doped graphene as a CE in DSSCs and how it improves the photovoltaic performance of cells is discussed.

KEYWORDS
counter electrode, dye-sensitized solar cells, graphene, heteroatom doped, renewable energytransparent conducting electrode

16

Heteroatom-doped graphene and its application as a counter electrode in dye-sensitized solar cells

Nonjabulo P. D. Ngidi, Moses A. Ollengo, Vincent O. Nyamori

School of Chemistry and Physics, University of KwaZulu-Natal, Westville Campus, Private Bag X54001, Durban 4000, South Africa

Graphical abstract
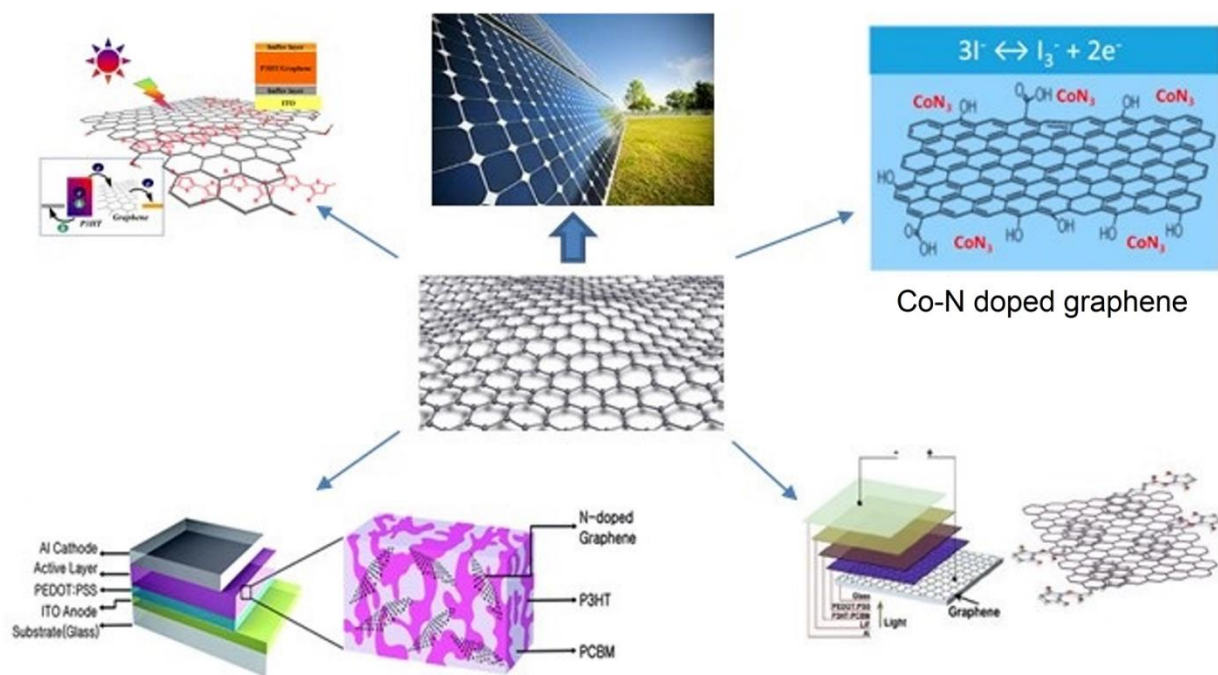
Summary

The most frequently used counter electrode (CE) in dye-sensitized solar cells (DSSCs) is platinum on fluorine-doped tin oxide (FTO) glass. This electrode has excellent electrical conductivity, chemical stability, and high electrocatalytic affinity for the reduction of triiodide. However, the high cost of metallic platinum and the poor electrochemical stability poses a major drawback in commercial production. This has necessitated a search for a non-precious metal, and metal-free electrocatalyst that demonstrates better catalytic activity and longer electrochemical stability for practical use in DSSCs. Graphene has been at the centre of attention due to its excellent optoelectronic properties. However, a defect-free graphene sheet is not suitable as a CE in DSSCs, because of its neutral polarity which often restricts efficient charge transfer at the graphene/liquid interface, irrespective of the high in-plane charge mobility. Hence, heteroatom-doped graphene-based CEs are being developed with the aim to balance electrical conductivity for efficient charge transfer and charge polarization for enhanced reduction activity of redox couples simultaneously. The elements commonly used in the chemical doping of graphene are nitrogen, oxygen, boron, sulfur, and phosphorus. Halogens have also recently shown great promise. It has been demonstrated that edge-selective heteroatom-doping of graphene imparts both efficient in-plane charge transfers and polarity, thereby enhancing electrocatalytic activity. Thus, heteroatom-doped graphene serves as a good material to replace conventional electrodes and enhance power conversion efficiency in DSSCs. The focus is to reduce the cost of DSSCs. This review explores the performance of DSSCs, factors that influence the power conversion efficiency, and various physicochemical properties of graphene. It further outlines current progress on the synthetic approaches for chemical doping (substitutional and surface transfer doping) of graphene and graphene oxide with different heteroatoms to fine-tune the electronic properties. The use of heteroatom-doped graphene as a CE in DSSCs, and how it improves the photovoltaic performance of cells is discussed.

Keywords

18

2.1 Introduction

The United Nations sustainable development goal, number 7, advocates for clean and affordable energy for all. To attain this goal, the global focus has been on renewable energy sources. Sustainable renewable energy sources include; solar [1], geothermal [2,3], biomass [4], wind [1], biofuels [5], ocean waves, and hydroelectricity [6,7]. Solar energy has proven to be highly sustainable posing negligible release pollutants if any, thus having, minimal or zero negative impact on the environment.

2.2 Solar cells

Solar cells are widely used for terrestrial applications and are economically competitive as alternative energy sources for domestic appliances, such as refrigerators [8,9]. Further, solar cells are used in various devices from handheld calculators to rooftop solar panels [10,11]. Solar cells are grouped based on the nature of materials used and the conversion efficiency [12]. Table 2.1 compares the efficiencies of various solar cells with first-generation solar cells.

Table 2.1: Energy conversion efficiency of different types of solar cells.

Types of solar cells	Efficiency/%	Ref.
Single/monocrystalline Si	20.6	[13]
Polycrystalline Si	~12-14	[12]
Amorphous Si	10.1	[14]
Cadmium telluride (CdTe) thin film	13	[15,16]
Copper indium gallium selenide (CIGS) thin film	21.9	[17]
Nanocrystal	7.2	[18]
Polymer	3-9 & 10.8	[19-21]
Concentrated	~40	[22]
Organic	9.5	[23]
Dye-sensitized	7.8	[24,25]

In the quest of addressing the challenges faced by current solar cells, newer efficient solar cells are under intensive investigation. These include concentrated solar cells, polymer-based solar cells, nanocrystal-based solar cells (quantum dot solar cells), and dye-sensitized solar cells (DSSCs). These novel technologies, although promising, are yet to be commercially proven. The most favourable technology is the use of DSSCs as an alternative to silicon-based solar

cells [12], firstly, because they can function at low light intensities and are environmentally friendly, secondly, have a simple fabrication process, low production cost, high efficiency, and feasibility to be printed on a flexible substrate. DSSCs differ from conventional semiconductor devices in that they separate the function of light absorption from charge carrier transport. They absorb the incident sunlight and exploit the capability of light energy to induce a vectorial electron transfer reaction.

The novelty of these solar cells emerges from the photosensitization of nano fine-grained titanium oxide (TiO_2) coated with active dyes, consequently improving the efficiencies of the cells[26]. DSSCs enjoy the flexibility of expanding the range of applications where conventional solar cells are unsuitable. However, DSSCs suffers from several challenges, such as photodegradation of the dye molecule [27]. The dye photodegradation generally occurs when the dye is exposed to infrared and ultraviolet radiation leading to a recombination lifetime and poor stability of the DSSCs. The major cause is poor optical absorption of the dye-sensitizer, and the resultant effect is lower conversion efficiency.

DSSCs are made up of four components, namely, a dye sensitizer, a semiconductor electrode (photoanode), the electrolyte, and a counter electrode (CE) (Figure 2.1). The photoanode contains a mesoporous oxide layer (generally, TiO_2) which is deposited on a transparent conductive glass substrate [28]. The dye-sensitizer is covalently bonded to the TiO_2 layer to harvest light and produce photo-excited electrons. The performance of DSSCs is mostly dependent on the molecular structure of the dye-sensitizer. Three different classes of dye sensitizers have been reported to be used in DSSCs, such as metal-free organic sensitizers, complex sensitizers, and natural sensitizers [29]. The electrolyte is made up of a redox couple (generally, iodide/triiodide (I^-/I_3^-) and $Co(2,2\text{-bipyridine})_3^{2+/3+}$) [30] in an organic solvent to accumulate electrons and cause dye-regeneration. The electrolyte also functions as a charge transport medium for the transmission of positive charge to the CE [31]. The electrolyte is expected to have low viscosity for faster ion diffusion to occur; high electrical conductivity, excellent contact between the CE and the nanocrystalline semiconductor, lack of absorption of light in the visible region, and no degradation of dye. The CE consists of a conductive glass substrate that is coated with platinum. It is mostly used to transport the electrons which come from the external circuit and go back to the electrolyte [32,33]. Accordingly, for effective charge transfer, the CE is required to display a high electrical conductivity and catalytic activity. Therefore, the catalyst is required to increase the rate of the reduction reaction.
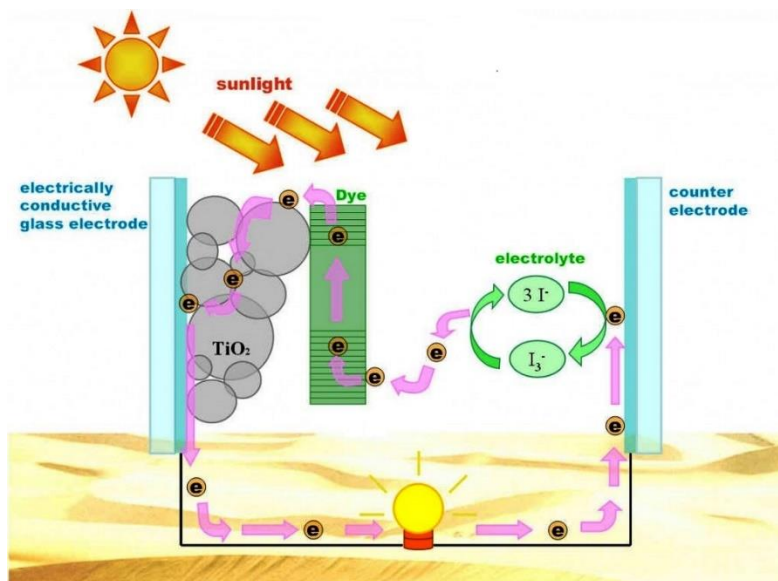
Figure 2.1: A schematic diagram of a DSSC [34].

2.3   Mechanistic issues in DSSCs

In DSSCs, the optical excitation of the dye causes electron promotion into the conduction band of the metal oxide. The promoted electrons are transported to the external circuit through the metal oxide film. A redox electrolyte is traditionally inserted into the film pores, which serves as a hole transporting material, and also serves to re-reduce the photo-oxidized dye and transfer the resultant positive charge to the CE [35,36]. The net effect of the structural design is an optimized electronic coupling that is sufficiently large for charge separation to compete effectively with excited state decay, and small enough to minimize charge recombination. An optimum DSSC performance is attained when the recombination dynamics are as slow as possible but allow fast electron injection to compete effectively with excited state decay, thus, minimizing kinetic redundancy in the system. Another approach to minimize system kinetic redundancy is the addition of a secondary electron donor or acceptor species, this increases the spatial separation of the electron and hole and slows charge recombination without necessarily retarding charge separation. The physical separation of the injected electrons and the oxidized dye retards the recombination reactions and modulates surface dipoles and pacifies surface states. The reduced recombination improves photovoltaic device performance [35].

Considering the solid-liquid interface at the CE, the interfacial charge-transfer mechanism requires an efficient electron transfer that is attributed to the strong overlap of wave functions between the excited states. In this case, an electron transfers adiabatically by occupying the bridging state in the lowest excited state once the exciton diffuses to the interface region [37]. Thus, to induce the charge separation process the closely lying single-particle states just above

21

(energetically) this electron-transferring bridge state, facilitate the exciton dissociation (complete transfer) to form the bound ion pairs. However, large vibronic couplings are expected among them because of the near degeneracy of these single-particle states and significant spatial overlap with the bridge state [37]. The near-degenerate single particle states enable efficient exciton dissociation and reduce the probability of the electron recombining with the hole through the bridge state. Another possible mechanism for exciton dissociation is the single-phase rearrangement of the near-degenerate single-particle states as a result of geometrical distortions. The geometrical distortions induce strong coupling of electronic structure and, particularly, the t_{1u} state is split into a combination of singly and doubly degenerate states [38]. It should be noted that a covalent activation of the graphene-surface, for instance, can change the relevant energetics by inducing a splitting of the degenerate lowest unoccupied molecular orbital (LUMO) states. Further, the energy alignment of electronic single-particle states at the interface is significantly altered in the excited state because of the transferring charge at the nanoscale heterojunction.

It has been recently suggested that a near degeneracy enables an asymmetric exciplex state that acts as an effective intermediate state for transferring charge thereby facilitating exciton dissociation. It can, therefore, be expected that the disruption of degenerate LUMO states in general accounts for less efficient exciton dissociation. Thus, the covalent functionalization of graphene induces disruption of the LUMO degeneracy [37]. It can be argued that a larger wave function overlap in the excited state partly satisfies this important criterion and allows for a fast adiabatic electron transfer. However, the existence of such an adiabatic transfer channel alone, may not solely lead to an efficient charge separation process unless there exists in the energetic vicinity other states that can facilitate the exciton dissociation efficiently. By functionalization of molecular chemistry at the surface, one can tailor the electronic structure such that the bridging state for the transferring electron forms near the conduction band minimum [37]. A conventional nonadiabatic electron-transfer mechanism can also serve to explain the observed ultrafast charge transfer assuming the semi-infinite acceptor states are in the conduction band of the metal oxide, and that the photoexcited electron within the dye has a very high total transition probability to the metal oxide [35].

A judious asymmetric activation of the graphene surface with different chemical moieties can lead to guided self-assembly of heteroatom-doped graphene sheets into hierarchically structured materials. The graphene edge and/or basal plane chemical activation may be *via* covalent or noncovalent interaction. These impart solubility, film-forming capability, and

enhanced chemical reactivity that modulate the properties for multifunctional applications [39,40]. For instance, Ju *et al.* [41] recently reported edge-selective doping as a way of preserving the pristine graphene basal plane and further showed that edge-selenated graphene nanoplatelets are robust metal-free catalysts for the iodine redox reaction in the CE of DSSCs. The value of the charge transfer resistance, R_{ct}, at the CE-electrolyte interface indicates the effectiveness of the CE in regenerating the iodine species in the electrolyte. A lower R_{ct} value shows an enhanced reduction of triiodide ions on the CE-electrolyte interface, thereby increasing the availability of I^- ions on the dye-electrolyte interface. The resultant effect is the suppression of charge recombination in the photoanode and an increase in the open-circuit voltage of the DSSCs. The iodine reduction reaction occurring at the CE/electrolyte interface is the major rate-determining step in DSSCs [42] and the energy of the I atom can serve as a good descriptor for the iodine reduction reaction.

2.4 Counter electrodes in DSSCs

The CE plays a big role in DSSC. It is responsible for catalyzing the reduction of I_2 to I^- after electron injection [43]. The CE is expected to be highly conductive and highly catalytic. Different methods have been reported for the preparation of CEs, such as chemical vapour deposition [44,45], chemical reduction [46,47], hydrothermal reaction [46,48], electrochemical deposition [49,50], thermal decomposition [51,52], in situ polymerization [53,54] and sputter deposition [55-57]. The preparation approach influences the morphology, surface area, small particle size, electro-chemical and catalytic properties of the electrode [58]. The large surface area and small particle size generate more catalytically active sites and enhance the improvement of the electrocatalytic activity of CE [58]. The preparation methods of CEs are different based on the material from which they are made.

Different CEs have been employed such as conductive substrates (conductive glass substrate, conductive polymer substrate and metal substrate) [59], transparent CEs [60,61], flexible CEs [62], polymer CEs [63,64], transition metal compound CEs (carbides and nitrides, chalcogenides, oxides) [65], hybrid CEs (platinum-loaded hybrids, transition metal compounds (TMCs)/carbon hydride, carbon/polymer hybrids, polymer/TMC hybrids) [66], metal and alloy CEs (platinum CE) [67] and carbon CEs (carbon black nanoparticles, carbon nanofibers, carbon nanotubes, graphene) [68].

In most cases, platinum-loaded conducting glass has been used as the CE because of its good conductivity and high catalytic activity [69]. However, platinum-loaded conducting glass tends to

result in high corrosion when used with I^-/I_3^- electrolyte in DSSCs [69,70]. Consequently, different platinum-based CEs have been intensively used, such as platinum nanoparticles and platinum composite materials [71-73]. Platinum nanoparticles are the best transparent and stable CEs because of their high density of catalytic sites and high surface area [71]. Platinum nanoparticles have been employed in DSSCs to produce a power efficiency of 9.75% whilst planar platinum produced an efficiency of 7.87%. Similar studies have been conducted to exhibit the photovoltaic and catalytic behaviour of various platinum facets.

Zhang *et al.* [74] demonstrated that different Pt facets, e.g. Pt(100), Pt(111), and Pt(411), exhibit different photovoltaic performance. Pt (111) was found to have a lower charge transfer resistance than other facets. The electrocatalytic activity was also improved by using a platinum composite containing a polymer and carbon. Yen *et al.* [72] reported the use of a Pt composite composed of Pt nanoparticles supported on fluorine-doped tin oxide (FTO) and platinum nanoparticle/graphene composite (Pt NP/GR) in DSSCs. Its photovoltaic performance and physical properties were compared with those of Pt films and graphene. It was revealed that Pt NP/GR have a higher surface area, hydrophilicity, and electron transfer rate because of the presence of oxygen in graphene. Pt NP/GR showed a photovoltaic performance of 6.35%, which was much higher than that of graphene and Pt film as a CE [72].

The problem with using platinum-based CEs is that Pt is very expensive due to its wider range of applications (especially in the vehicle industry) [75]. Therefore, platinum-free materials are employed in DSSCs as a replacement for platinum-based materials. Various materials, such as carbides [76], nitrides [77], transition metal sulfides [78], and carbon [79], are employed as CEs. The use of carbon materials in DSSCs is quite appealing because they are cheap, commonly available in large quantities, exhibit excellent catalytic activity, are environmentally friendly, and are corrosion resistant [43].

However, the photovoltaic performance of carbon in DSSCs has been reported to be poor compared with that of platinum-based materials [80]. Energy conversion efficiencies of 3.9%, 4.5%, and 5.75% in DSSCs have been obtained when carbon nanotubes [81], activated carbon [43] and graphite [82], respectively, are used as CEs. The disadvantage of using carbon-based CEs is that they require a large amount of carbon to produce a comparable efficiency to platinum-based CEs [83]. This makes the device opaquer and bulkier. However, different modifications of carbon have been performed in order to enhance the photovoltaic performance [83].

Carbon is an extremely light and versatile material. There are two common forms of carbon, diamond, and graphite (Figure 2.2). Diamond is hard and transparent whereas graphite is very soft and opaque. They differ in the structure or the hybridization of the carbon atoms, for example, graphite is sp^2-hybridized while the hybridization in diamond is sp^3. Graphite is a good thermal and electrical conductor within the layers; however, it is a poor thermal and electrical conductor between the layers. Due to its electrical conductivity, graphite is employed as an electro-chemical electrode [84]. Graphene is considered as the fewest layer of graphite [85] (one atom thick sheets). Graphene and its derivatives have been applied in solar cells since 2004 [86]. Graphene has been recommended as a substitute material for the CE. This is because it possesses a large surface area, excellent electrocatalytic properties, and high optical transmittance. It is frequently chemically doped with different heteroatoms to optimize its structure and tune its conductivity and catalytic activity to further improve the power conversion efficiency in solar cells [72,87]. The current work offers an in-depth review of the chemical doping of graphene, explores the creation of a bandgap in graphene, and revisits the heteroatom-doping of graphene and its effect on electrical conductivity. It further demonstrates the potential of heteroatom-doped graphene as a CE for DSSCs.

(a)   **(b)**
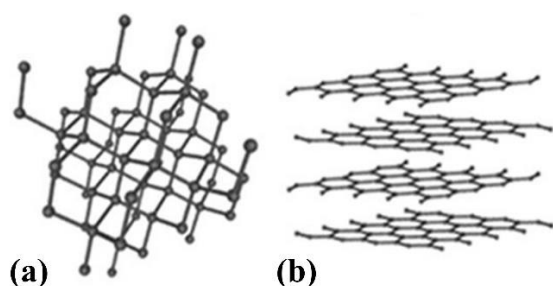
Figure 2.2: The common allotropes of carbon (a) diamond and (b) graphite [88].

2.5   Graphene as a counter electrode material

Graphene is a single, thin layer of carbon, the latest member of carbon-based nanomaterials. It is the fundamental structural component of other allotropes, such as diamond, fullerenes, and carbon nanotubes [89]. In graphene, the carbon atoms are bonded together in a hexagonal honeycomb lattice. It is a two-dimensional nanostructured carbon-based material [90]. The name graphene was introduced in 1994 by Boehm, Setton, and Stump [91].

The lateral dimensions of graphene may vary from several nanometres to microscale, e.g., monolayer, bilayer, and tri-layer [92]. Monolayer graphene is also called single-layer graphene and is preferred for use in high-frequency electronic applications [92]. It possesses high mobility, high optical transparency, and high surface area [92]. These properties allow

monolayer graphene to be a good material for improving the efficiency in DSSCs [92,93]. Bilayer or tri-layer graphene consists of two or three layers, respectively. As the number of layers increases, they display different electrical properties [86]. Monolayer graphene has a zero-bandgap while bilayer graphene has a parabolic band structure (effective mass m = 6.6 x 10^{-38} kg) [94] and its bandgap can be varied by using an external perpendicular electrical field [89,95,96]. Similarly, tri-layer graphene also has a parabolic band; however, the effective mass (m = 9.3 x 10^{-38} kg) is larger than that of bilayer graphene [94].

There are different types of graphene-based nanostructures with various morphologies that have been reported. These are zero-dimension (0-D) graphene quantum dots (GQDs), one-dimension (1-D) graphene nanoribbons (GNRs) and two-dimension (2-D) graphene nanosheets (GNSs) [97]. GQDs have nanometre-scaled graphene particles that contain an sp^2-sp^2 carbon bond [98]. They have a high surface area and high transparency which allows them to be applied in energy and display applications. GNSs are metal-like conductors with zero-bandgap while GNRs can be either semiconducting or metallic [99]. These new graphene materials have unique electrochemical properties in comparison with pristine graphene. The properties of GNRs and GQDs can be tailored by modulation of the respective edges and sizes [100]. For example, GNRs having a width that is narrower than 10 nm have good semiconducting characteristics while GNRs that have a width larger than 10 nm have weak semiconducting characteristics [97]. The mainly zigzag-edged GNRs (2.3 nm wide) show a smaller bandgap of 0.14 eV, while the armchair GNRs (2.9 nm wide) has a bandgap of 0.38 eV, which indicates that the higher concentration of zigzag edges causes the energy gap to decrease because of the staggered sub-lattice potential through the zigzag terminated edges [101,102].

Normally, the carbon atom contains a total of six electrons; two electrons are situated in the inner shell while the other four electrons are in the outermost shell and are available for chemical bonding. However, the carbon atom in graphene is bonded to three other atoms because of sp^2-hybridization. The other electron in the dimension remains unbonded so that it can be used during electronic conduction [103]. From a molecular orbital perspective, the stability of graphene is caused by the tightly packed carbon atom and sp^2 orbital hybridization with p_x, p_y, and s as atomic bonding orbitals on each constrained carbon atom creating three strong σ bonds along with three other surroundings atoms [104,105]. Each neighbouring atom has an overlapping p_z orbital which forms a valence band (filled band of π orbitals) and the conduction band (empty band π^* orbital). These bands are the essence of the electron properties of graphene by a means of a half-filled band that allows free-moving electrons [106]. Figure

2.3 shows the band structures of graphene and the zoomed energy bands of the Dirac point (showing the junction of the conduction band and valence band at the K and K′ points in the reciprocal space).
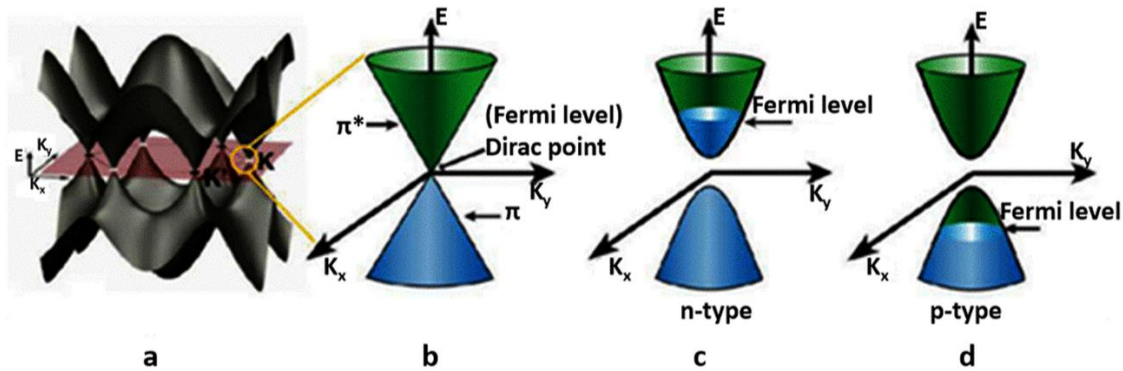
Figure 2.3: (a) The 3D band structure of graphene, [104] (b) the lower energy band structure of graphene with the two cones which intersect at the Dirac point and the bandgap of the energy band structure of (c) n-type graphene and (d) p-type graphene [105].

Graphene possesses high electrical conductivity and zero-gap as illustrated in Figure 2.3. Thus, it functions as a semimetal. This is because its conduction band can make contact with the valence band at the Dirac point [107]. Consequently, a device that is fabricated from zero-bandgap graphene tends to lose the advantage of the low static power consumption and is difficult to switch off due to the very low on/off ratio. Hence, creating a well-tuned and sizeable bandgap is a great challenge in graphene-based electron devices.

The absence of a bandgap is ascribed to the similar environment of the two sublattices of the carbon atoms in the unit cell of the graphene [107]. The Fermi level in an unperturbed graphene sheet coincides with the Dirac point where minimum conductivity occurs [108]. Figure 2.3 (b) shows pristine graphene exhibiting a strong ambipolar field-effect which further demonstrates the possibilities of doping. N- and p-type graphene (Figure 2.3 (c) and (d)) occurs when there is a shift in the Dirac point in relation to the Fermi level caused by chemical modification [109].

Many techniques have been proposed to create a bandgap in graphene; among them are bilayer graphene (GNRs and GQDs) with an induced bandgap or a substrate-induced bandgap. The chemical functionalization of graphene causes modifications of the carbon sp^2 lattice [110]. This changes the surface, chemical, and electronic properties of graphene and helps in enhancing free charge-carrier densities and electrical conductivity [110].

Chemical modification can be achieved by covalent and non-covalent interactions [109] for instance, atom doping of graphene [111,112], a phenomenon made possible by functionalizing

graphene, making use of the unsaturated structure of graphene. Non-covalent modification makes use of hydrogen bonding [113,114], coordination bonds [115,116], electrostatic interactions [117,118], π-π stacking interactions [119,120] and van der Waals forces [121-123]. The interactions that occur through non-covalent bonding are relatively weak compared with those from covalent modification [109]. Covalent modification of graphene forms stronger bonds between the modifier and graphene. The problem with covalent modification is that the bonds are unrecognizable because they lack functional groups that can be conjugated with carbon in graphene [124].

Chemical modification, such as hydrogenation [125], oxidation of graphene [126], chemical doping (heteroatom-doped graphene) [127,128] reduction of graphene oxide (GO) [129,130] and fluorination, [131] are alternative ways to create a bandgap in graphene. Balog *et al.* [132] investigated the bandgap opening process onto the Moire superlattice locality of graphene by using mosaic adsorption of atomic hydrogen. In this approach graphene that had been synthesized on an Ir(111) substrate was exposed to atomic hydrogen. This resulted in partially or fully hydrogenated graphene which displayed different thermopower, magneto-electronic and structural properties. Consequently, several working groups have reported the chemical doping (heteroatom doping) of graphene to improve the performance of graphene-based devices, thus opening up a wider range for the application of graphene [87,133,134].

This review focuses on heteroatom-doped graphene as a suitable material for the construction of CEs in DSSCs. In particular, the following aspects are discussed:

- The potential of heteroatom-doped graphene as a CE for DSSCs.

- The ability of chemical doping of graphene to create an energy bandgap and form catalytic sites.

- The enhanced electrical conductivity of heteroatom-doped graphene.

- The dependency of the heteroatom-doping level on the dopant and the different doping techniques.

- The synergistic effect between the co-dopants and graphene provides well-defined properties.

Hence, the review should offer in-depth comments on the chemical doping of graphene, explore the creation of a bandgap in graphene, revisit heteroatom-doping of graphene and its effect on

electrical conductivity, and demonstrate the potential of heteroatom-doped graphene as a CE for DSSCs.

2.6   Heteroatom-doped graphene

Chemical doping not only creates the bandgap but also controls the concentration and type of charge being injected into graphene [72,135,136]. It aids in modifying the electronic properties of graphene [72]. There are two types of chemical doping of graphene, namely, surface-transfer doping and substitutional doping. Surface-transfer doping occurs when a functional group is added to the graphene sheet [137]. It is attained by electron exchange between a semiconductor and a dopant that accumulates the electrons on the surface of a semiconductor. Thus, it is also called adsorbate-induced doping. During surface transfer doping, the structure of graphene is not disrupted [138,139]. Therefore, this doping process is reversible [140]. The charge transfer depends on the density of states of the dopant at the Fermi level of graphene [141]. The dopant acts as a donor when the charge transfer is found above the Fermi level of graphene, whereas when it is below the Fermi level, the dopant acts as an acceptor [138].

Substitutional doping is attained through the replacement of a carbon atom in the graphene lattice by another atom that has a different number of valence electrons [72,142]. The introduction of heteroatoms gives graphene more active sites [72,143]. Deng *et al.* [76] reported that the addition of a heteroatom with a different electronegativity from carbon reduces the electroneutrality of graphene and forms an active site. The active site causes graphene to exhibit unique physicochemical properties [76] and the characteristic of the nature of the heteroatom is in question. The heteroatom can be an electron acceptor or electron donor. Substitution with an atom with more valence electrons than carbon brings about n-type conductivity, whereas an atom with fewer valence electrons results in p-type conductivity [144] as described earlier. The synthetic methods for producing substitutional doped graphene are classified into two categories: post-treatment and *in situ* approaches.

The *in situ* approaches can be achieved by using different methods, namely ball milling [145,146], chemical vapour deposition (CVD) [146], and bottom-up synthesis [147,148]. Similarly, there are different types of post-treatment methods, such as thermal annealing [119,133], wet chemical methods [149,150], plasma treatment [151], and arc discharge [152] approaches. Different kinds of dopants have been incorporated in graphene; these include oxygen, nitrogen, boron, sulfur, and phosphorus [72]. However, nitrogen and boron have caught the attention of most scientists. This is because they both have atomic radii which are

similar to that of carbon. They also have a similar size, and hence, their incorporation into graphene is effortless.

2.6.1 Morphology of heteroatom-doped graphene

The adsorbed heteroatoms on graphene through doping distort the carbon atoms vertically, with almost no modification of the in-plane structures. Generally, heteroatoms distort the local geometry of graphene by locally rehybridizing the bonding from $pz + sp^2$ to sp^3 which causes a gap to open. This spin is quenched by the presence of a rotated C-C bond (a Stone-Wales defect) adjacent to or distant from the heteroatom [153,154]. The net effect is that the ground state shows a ferromagnetic order, with a total energy of a few tens meV lower than the nonmagnetic ground state. The heteroatom adsorption opens a gap that depends on the guest atom and the optical conductivities indicating fine structures at the band edge. However, the spin-orbit coupling and the nonzero off-diagonal components of the conductivity predict Kerr and Faraday effects without an external magnetic field [154] on doped graphene sheets. GO which is an oxidized derivative of graphene, with an oxygen-rich surface, has an improved dispersion in aqueous mixed matrices. Co-doping of heteroatoms synergistically enhances the asymmetric spin and charge densities of carbon atoms that are responsible for superior electro-catalytic activity [155]. Co-doping of N and S atoms on graphene nanosheets substantially enhances the asymmetric spin density as well as the charge density, which are responsible for the electrocatalytic activities.

2.6.2 Oxygen-doped graphene

Oxygen is one of the elements with higher electronegativity. It cannot be substitutionally doped into the graphene lattice because of its larger size and strong electronegativity. However, graphene can be covalently functionalized with a plethora of oxygen moieties [156]. These oxygen functionalities on the graphene sheet exhibit a surface-transfer doping effect. GO is widely studied and is oxidatively synthesized from graphite powder [129]. The introduction of oxygen functionalities in the graphite structure occurs during the oxidation of graphite with the use of a strong oxidizing agent [156]. This not only changes the structure but also expands the layer separation and causes the material to become hydrophilic. When graphite is exfoliated in water *via* sonication, a final product, usually consisting of a single or a few layers of graphene, called GO is obtained. The GO and graphite oxide differ in the number of layers. Graphite oxide consists of a multilayer system while GO has a few layers or consists of monolayer flakes [156].

This oxidation of graphite can be regarded as oxygen-doped graphene. The GO lattice contains a hydroxyl (-OH) and epoxy groups (-C-O-C) on the basal planes, while at the edges, it has carboxyl (-COOH) groups. The carbon atoms on which the oxygen groups are attached are transformed from the sp^2 to the sp^3 hybridization state with local distortions of the graphene planar structure. This disruption of the sp^2 hybridization state creates a bandgap in graphene and causes GO to be non-conductive [157]. It has been reported that GO consists of a heterogeneous electronic structure because of the assorted hybridizations (sp^2 and sp^3) [158].

The addition of oxygen to graphene can be performed by using either a top-down or bottom-up wet chemical oxidation [159]. The top-down wet chemical oxidation method is widely used because it generates a high yield of GO [160]. It involves the oxidation of graphite *via* different chemical routes such as Brodie's oxidation method (fuming nitric acid and potassium chlorate) [161], Staudenmaier method (fuming HNO_3, concentrated H_2SO_4 and $KClO_4$) [162], Hofmann method (concentrated HNO_3, concentrated H_2SO_4 and $KClO_4$) [163] and Hummers method (concentrated H_2SO_4 in the presence of $KMnO_4$) [164]. Hummer's method has been reported to be the best and simplest method to yield good quality GO [165-167].

Graphene oxide acts as an electrically insulating material because of the structural disorder applied by the C-O bonds (sp^3) which disrupts its conductive π-network [168]. The disruption in electrical conductivity can be restored by the reduction of GO. The oxygen functional groups in GO can be removed by using different methods such as chemical treatment or thermal annealing to form reduced GO (rGO). rGO can be synthesized by using different chemical techniques such as chemical reduction [169-171], thermal reduction [172], microwave and photo-reduction [173,174], photocatalyst reduction [175], and solvothermal/hydrothermal reduction [176-179]. However, the most frequently used technique for reduction is chemical reduction. rGO has similar properties to those of GO. Mathkar *et al.* [180] reported that reduction of GO also modifies the bandgap. The structural altering of GO to rGO causes gradual changes in thermal stability [181], electrical conductivity [182], carrier mobility [183], and optical bandgap [184].

The chemical reduction method uses different reducing agents, such as amino acid [185], sodium borohydride [130], urea [186], hydrazine hydrate [187], ascorbic acid [188], strong alkaline solution [189], and glucose [190], and this may involve ultrasonication of the chemicals with GO in water [191]. Chemical reduction of GO produces rGO and large quantities of graphene [192]. The rGO formed after ultrasonication bears resemblance to graphene, yet it contains residual oxygen and structural defects. After the reduction process,

some of the oxygen-containing groups are removed and the π-electron conjugation is partially reinstated in the graphene aromatic system.

The main challenge of the chemical reduction method is the use of hazardous chemicals as reducing agents, e.g., sodium borohydride, and thermal treatment consume a lot of energy. Therefore, green reduction methods are now sought as alternative approaches, e.g., the photothermal reduction method [192]. The photothermal reduction does not require the use of chemicals and high-temperature annealing. Cote *et al.* [193] demonstrated that GO can be reduced by using a flash-reduction approach whereby GO is exposed to a pulsed Xe flashlight under ambient conditions. Recently, Chien *et al.* [194] reported that the photoluminescence properties of rGO can be controlled by using a photothermal reduction method at different exposure times.

2.6.3 Nitrogen-doped graphene

Nitrogen, with an electronic configuration of $1s^2 2s^2 2p^3$, is a natural choice as a dopant. In the periodic table, it is situated next to carbon ($1s^2 2s^2 2p^2$). It possesses one more valence electron than carbon. It has a higher electronegativity ($\chi = 3.04$) than carbon ($\chi = 2.55$) [195]. Nitrogen atoms tend to donate electrons into graphene when incorporated into the basal plane of graphene occasioning n-type (negative) charge carrier characteristics. The n-type graphene occurs when a group 15 element is used as a dopant. Group 15 elements have five valence electrons, and thus, can donate an electron to the four-valent host material. Doping with nitrogen creates polarization in the *sp²* carbon network which influences the chemical and physical properties of graphene [196]. It has been reported that nitrogen doping can tune the characteristics of graphene materials, by creating a bandgap and inducing charge-carrier characteristics. The bandgap creation occurs near the Dirac point by suppressing the nearby density of states and granting graphene semiconducting properties [105]. Zhang *et al.* [197] reported a bandgap of 0.16 eV which demonstrated that doping with nitrogen tunes the electrical properties of graphene. Shao *et al.* [198] also demonstrated that the presence of nitrogen atoms in graphene improves their ability to donate electrons to the adjoining carbon atoms.

Nitrogen-doped graphene (N-doped graphene) usually has three common bonding configurations within the carbon lattice. These include graphitic-N (or quaternary-N), pyridinic-N, and pyrrolic-N atoms (Figure 2.4) [199]. Pyrrolic- and pyridinic-N occur at the defects sites, and these defects impose the p-doping effect through the withdrawing of electrons

from the graphene sheet [199]. Pyridinic-N refers to nitrogen bonded to two carbon atoms at the edges which donates one p-electron to the π system, while the pyrrolic-N refers to nitrogen atoms that donate two p-electrons to the π system [200]. In the graphitic-N, the nitrogen atom sits in-plane, replacing the carbon atoms in the hexagonal ring. These bonding configurations have different hybridization states of the nitrogen atom, which in turn has some effects on the electrical properties of N-doped graphene [199]. Quaternary-N and pyridinic-N are *sp²* hybridized since the nitrogen atom is coordinated to two atoms, while pyrrolic-N is *sp³* hybridized [199]. Besides these three-bonding configurations, nitrogen oxides of pyridinic-N have been discovered in both nitrogen-doped carbon nanotubes and N-doped graphene [198,201]. This configuration occurs when the nitrogen atom bonds with one oxygen and two carbon atoms. N-doped graphene and pristine graphene have different properties. For example, the charge distribution and spin density of carbon atoms in N-doped graphene will be affected by the neighbour nitrogen dopants [76,202]. This creates an "activation region" on the surface of graphene. This activation region can participate in catalytic reactions known as oxygen reduction reactions (ORR).
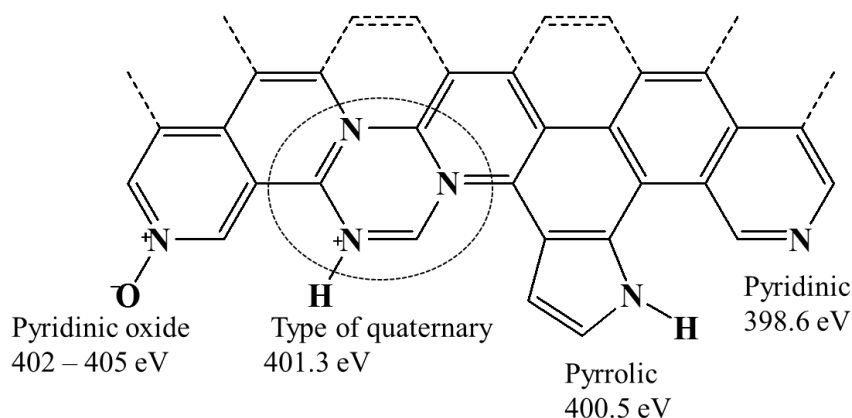
Figure 2.4: Schematic diagram of the bonding configurations of nitrogen atoms in N-doped graphene [199].

When monolayer graphene has been successfully doped with nitrogen, the Fermi level moves over the Dirac point [203,204] and the density of states near the Fermi level is suppressed [205]. This results in a band opening between the valence band and conduction band. This bandgap enables N-doped graphene to be further applied in semiconducting devices [205].

2.6.3.1 Preparation of N-doped graphene

N-doped graphene can be synthesized in two different ways, either by post-synthesis treatment or by direct synthesis. The post-treatment method mostly results in surface doping only, while

the direct synthesis method leads to homogeneous doping [206]. Specifically, post-synthesis treatment can be performed by using different techniques such as plasma treatment, hydrazine (N_2H_4) treatment, and thermal treatment [207]. However, the direct synthesis involves solvothermal, arc-discharge, and CVD [208].

Post-synthesis treatment

The thermal treatment strategy is an extensively used approach to introduce nitrogen into graphene frameworks. This approach enables the use of various dopant precursors in the synthetic method (Table 2.2). Doping of graphene or GO with nitrogen-containing compounds is performed through high temperature and hydrothermal treatment. Compounds containing nitrogen such as urea, melamine, cyanamide, polyaniline, ammonia, and hydrazine have been used as nitrogen sources [179]. It has been reported that when graphene is heated with ammonia at temperatures of 800 °C or above, N-doped graphene is obtained [209,210]. High-temperature annealing of graphene has resulted in N-GNRs [211].

Gou *et al.* [209] reported that the yield of N-doped graphene synthesized from the thermal treatment is relatively low, specifically having a doping level of 1.1% at a temperature of 1100 °C. However, Geng *et al.* [210] discovered that at temperatures of 800 °C and 900 °C, there was the highest nitrogen doping level of 2.8%. The low nitrogen content may be ascribed to high temperature which breaks the graphene C-N bonds lowering defect numbers in graphene [210]. They argued that nitrogen doping in graphene more likely happens at the edge and defect sites [210]. They also proposed that more dominant bonding configurations which occur during high temperatures are pyrrolic-N and pyridinic-N [210]. However, Wang *et al.* [211] concluded that the nitrogen atom insertion in GNRs favours edge functionalization. All these reports showed that temperature has a crucial impact on an increasing level of N-doped graphene.

Apart from graphene, GO has also been employed in the synthesis of N-doped graphene using thermal treatment with different nitrogen precursors [212]. Sheng *et al.* [213] investigated the effect of high temperatures between 700 °C and 1000 °C during the process of annealing GO with melamine. They reported that at these higher temperatures, the GO was not only doped with nitrogen but also the oxygen functional groups were reduced. The higher the temperature, the higher the reduction of oxygen functional groups. Similar findings were reported by Li *et al.* [119] where they reported that the high temperature does not only reduce oxygen functional groups but also lowers the nitrogen content. However, Sliwak *et al.* [214] reported the

nitrogen-doped reduced GO obtained from the hydrothermal route gave a very high nitrogen content of 10.9% to 13.4%. Hence, no single conclusion can be drawn as the results are contradictory.

N-doped graphene tends to have different layer distribution, which is highly dependent on the synthesis parameters, especially temperature. Many researchers have reported that doping of GO at higher temperatures results in few-layer N-doped graphene [215-217]. However, Ying *et al.* [215] reported few-layer N-doped graphene synthesized at a lower temperature of 180 °C. N-doped graphene is not only highly dependent on growth temperature but also on the synthetic mass ratio of nitrogen source and GO. The highest nitrogen doping (10.1%) is attained when a mass ratio of 0.2:1 of GO to melamine (nitrogen source) when a growth temperature of 700 °C [213] is employed. Li *et al.* [119] demonstrated that annealing GO at 500 °C under NH_3 atmosphere can reduce GO and dope the graphene with 5% nitrogen content.

Direct synthesis

Arc discharge approach

The arc discharge method has been employed to synthesize carbon-based materials such as carbon nanotubes [218]. It was shown that N-doped graphene synthesized from nano diamond transformation has higher nitrogen content as compared with those synthesized from graphite [219]. To synthesize N-doped graphene, it requires buffer gases as nitrogen sources [152]. Li *et al.* [152] reported N-doped multi-layered graphene sheet synthesized from arc-discharge using ammonia as a nitrogen precursor. They showed that the nitrogen content was approximately 1% which was consistent with what Rao *et al.* [219] discovered. Rao *et al.* [219] made use of ammonia and pyridine as nitrogen sources and the XPS data revealed that the samples had a nitrogen content of 1% and 0.6%, respectively. The arc discharge method is capable of synthesizing N-doped graphene in high purity and large quantities. However, the disadvantage of this method is that in the graphene structure, only a small quantity of nitrogen (Table 2.2) can be introduced [219]. By controlling parameters such as exposure time and plasma strength, the doping level could be optimized and regulated.

Table 2.2: Synopsis of heteroatom-doped graphene doping approaches.

Approaches	Advantages	Shortcomings	Ref.
CVD	• Easy to scale-up the reaction • Concurrently doping and growth of large sheet of graphene • Good reproducibility	• Sometimes, it can produce hazardous waste gases • Product may not be pure (due to hydrogen incorporation) • High process temperatures	[169,220-222]
Microwave-plasma CVD (MPCVD)	• Requires low temperature • Results in a high level of doping	• Slow and two-step process • Expensive and more complex	[223,224]
Arc discharge	• Mass-production	• Results in low doping level • Requires high voltage	[152,225]
Thermal annealing	• Easy to control doping level • Allows various choices of dopant precursors (solids, liquids, and gases)	• Requires high temperature • Results in low doping level	[226,227]
Plasma treatment	• Short reaction time • Consume low power	• Produces low yield	[228]

Chemical vapour deposition

Chemical vapour deposition is a versatile technique used in the synthesis of carbon-based nanostructures like graphene. It can produce large defect-free and few or single-layered graphene films [229]. It is highly dependent on the three parameters namely, growth temperature, catalyst, and precursor. CVD method works by decomposing hydrocarbon gases under high temperatures with the aid of a catalyst to form sp^2 carbon species. The catalytic growth mechanism makes the CVD method a suitable way to dope graphene films with different heteroatoms, especially to directly incorporate heteroatoms into the carbon lattices [230]. The doping occurs by reacting liquid, solid, or gaseous precursors that have desired foreign atoms along with graphite in the growth furnace. The CVD method is preferable because it is easy to scale-up the catalyzing process (Table 2.2), is independent of substrate size, and is known to produce high-quality N-doped graphene [208].

The N-doped graphene in the CVD can be synthesized using hydrocarbon gases [231] with metal single crystals (Ru, Co, Ni, and Cu foils) [232] at high temperatures [205]. Ni and Cu

foils are the most frequently used metal single crystals because of their unique solid solubility of carbon. Ni foil possesses a considerable solid solubility while Cu foil possesses a very limited solubility of carbon, therefore the carbon cannot diffuse to a great depth in the Cu substrate. However, Cu substrates are advantageous because of their graphene growth, which is self-limiting, meaning the graphene growth stops after one layer is formed.

Different precursors are used in the process of doping graphene such as liquid, solid and gaseous precursors. Nitrogen-containing functional groups could be doped in graphene by reacting graphene with nitrogen-containing reagents (urea, NH_3, and nitric acid) or through carbonizing/activating of nitrogen-rich carbon precursors, such as pentachloropyridine, polypyrrole, and pyrimidine. Other nitrogen-containing liquid precursors, such as acetonitrile and pyridine have also been used for the synthesis of N-doped graphene [233,234]. Some recent work has been based on gaseous nitrogen precursors such as ammonia [205]. Normally, the gaseous precursor works in conjunction with the other precursor (multi-precursor) while the liquid and solid precursors can function as a single precursor [235]. It should be noted that multi-precursors require multiple processes whereas the single precursors are more convenient and easier to control.

The problems with gaseous precursors are that they are hard to handle, transport, and thus expensive, compared with liquid/solid ones. Consequently, liquid precursors are more attractive for doped graphene growth [233,234]. The N-doped graphene is formed on the surface of the catalyst when the precursors separate and recombine through precipitation. This favours large-area and high-quality N-doped graphene when liquid precursors are employed [236]. The layer distribution of N-doped graphene varies in different studies depending on the type of nitrogen source used. The liquid precursors such as pyridine [234] and acetonitrile [233] are reported to produce monolayer N-doped graphene. Interestingly, N-doped graphene formed from gaseous nitrogen precursor (or gas mixtures), C_2H_4/NH_3 [237] is monolayer while a gas mixture of CH_4/NH_3 [238] produces few-layer nitrogen-doped graphene.

The formation of N-doped graphene depends on skeletal bonds of the liquid precursors [239], e.g., acrylonitrile contains a C-C single bond, C=C double bond, and C≡N triple bond. However, it cannot easily dope graphene. Pyridine contains C-C single and C=C double and C-N single and C=N double bonds. It is only C=C double bonds that have been shown to easily form N-doped graphene. This is because C-C bonds are easy to break at lower and higher temperatures while the C=C bond and C≡N bond are left at the surface of the catalyst. The C≡N bond is removed from the surface of the catalyst using high temperatures above 400 °C

resulting in volatile molecules, whereas, skeletal bonds in pyridine contain lower bond energies that cause an increase in the formation of N-doped graphene [236].

The doping level in the CVD method can be controlled by altering the flow rate and ratio of both carbon and nitrogen [240]. Wei *et al.* [205] reported that nitrogen decreases from 8.9 to 3.2 or 1.2% when NH_3/CH_4 ratio was reduced from 1:1 to 1:2 or 1:4, respectively. Further, the nitrogen bonding configuration in N-doped graphene differs with various studies. When Cu is used as a catalyst with a precursor of CH_4/NH_3 in a ratio of 1:1, then results in quaternary-N [205]. But when a catalyst Cu was used with CH_4/NH_3 (5:1) as a precursor, the N-doped graphene obtained mostly comprised of pyridinic-N [238]. Pyridinic-N is dominant when a different precursor (C_2H_4/NH_3) is used with Cu as a catalyst [240]. Zhang *et al.* [241] reported a low-cost synthesis of high-quality N-doped graphene with a nitrogen content of 3.72% (Table 2.3) and demonstrated that the bonding was primarily pyrrolic-N configuration. This N-doped graphene was synthesised from urea as a nitrogen source and methane as carbon source, on the Cu substrate using CVD.

Pyrolysis of GO and melamine in an argon atmosphere at 1050 °C has been reported to have a nitrogen content of 2.48% [242]. The decrease in temperature causes an increase in doping concentration. Lu *et al.* [208] reported that if the growth temperature in CVD is reduced, the atomic (nitrogen) percentage is raised from 2.1% to 5.6% when 1,3,5-triazine on Cu metal substrate is used (Table 2.3). Notably, research has revealed that nitrogen doping is highly dependent on the growth temperature and flow rate when the CVD method is employed [239,243].

Table 2.3: Synthesis methods of N-doped graphene and their nitrogen concentration.

Synthesis method	Precursors	Nitrogen content/%	Ref.
Thermal treatment	N^+ ion-irradiated graphene, NH_3	1.1	[209]
	GO, NH_3, argon	2.0 - 2.8	[210]
	GNR, NH_3	~2	[211]
	GO, melamine	7.1 - 10.1	[213]
	GO, amide/amine	10.9 - 13.4	[214]
Arc discharge	Multilayer graphene sheet, NH_3	1	[152]
	Graphite, NH_3, H_2, He	1	[219]
	Graphite, pyridine, H_2, He	0.6	[219]
	Nanodiamond, pyridine, He	1.4	[219]
CVD	Cu foil on Si substrate, CH_4, NH_3	1.2 - 8.9	[205]
	Cu foil, 1.3.5-triazine	2.1 - 5.6	[208]
	Cu foil, acetonitrile	~9	[233]
	Cu foil, pyridine	~24	[234]
	Cu foil, C_2H_4, NH_3	0 - 16	[240]
	Cu foil, CH_4, $CO(NH_2)_2$	3.72	[241]
	GO, melamine gel mixture	2.48	[242]

2.6.4 Boron-doped graphene

Boron is also an adjacent element to carbon in the periodic table and is suitable for doping. It can be chemically doped in the graphene lattice, just like nitrogen. Boron has one fewer valence electron than carbon. Three valence electrons participate in graphene doping bond formation with resultant single electron deficiency. This electron-deficient nature induces a p-doping effect and a downshift towards the Dirac point in the Fermi level. It has been forecast that the Fermi level is highly dependent on the doping level [244]. It decreases to approximately 0.65 eV when the doping level of boron is 2% and goes even higher when there is a higher doping level [219]. Boron doping induces p-type (positive) graphene. However, this doping may trigger chemical and electrochemical activity in the basal plane of graphene.

Boron-doped graphene (B-doped graphene) has two different bonding configurations i.e. either graphitic-boron (BC_3) or boron silane (BC_4) [245]. BC_3 configuration is obtained due to the

replacement of a carbon by boron in the hexagonal carbon lattice whereas the BC_4 configuration is acquired because of the edge site defects [245]. In-plane BC_3 (in-plane substitutional doping) has been reported to be more stable than out-of-plane doping [246]. The charge polarization occurs among the electron-deficient boron atom and neighbouring carbon atom. During doping, it retains the *sp²* planar structure and, resultantly, its conductivity because of the closeness of the sizes of boron and carbon. The lattice parameters are moderately changed due to the B–C bond (1.50 Å) being longer than the C-C bond (1.40-1.42 Å) in pristine graphene [247,248].

The synthesis of B-doped graphene using pure graphite at high temperature (>2000 °C), normally results in substitutional doping. However, when using GO at a lower temperature (900-1200 °C) produces more complex material with several different functional groups such as substitutional boron, borinic, borinic ester, boronic acid, and organo-borane (Figure 2.5) [245]. Tuning the level of boron doping in graphene induces different bandgaps of B-doped graphene from 0 to 0.54 eV [249]. Boron doping can induce more holes to the valence band of graphene which further enhances the carrier concentration in B-doped graphene (0.5 carriers per dopant) [147,250,251].
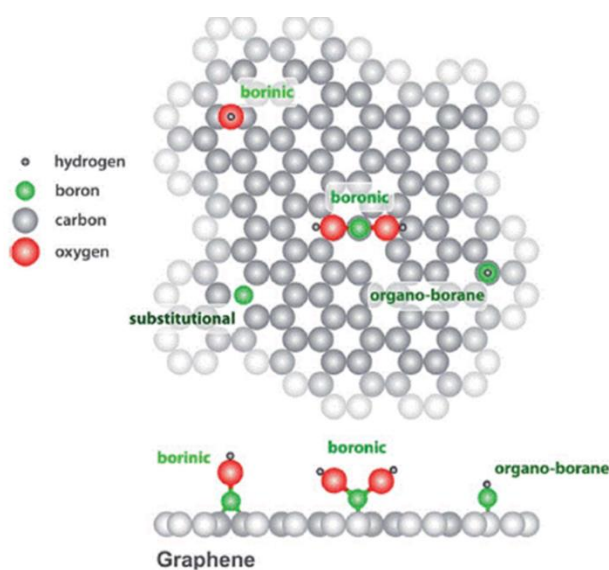
Figure 2.5: Ball model of B-doped graphene exhibiting the boron-induced defects [245].

The most frequently used methods range from solid-state reaction (gas-solid reactions) [251,252], liquid state reaction (hydrothermal/solvothermal synthesis) [253,254] to high temperature (CVD) [255,256]. These techniques can be split into top-down and bottom-up approaches. In the bottom-up approach, the arrangement of smaller components is more complex. For example, an atom can be assembled into molecules and molecules into the

nanostructure. This arrangement is achieved by covalent or non-covalent bonding. The top-down approach often uses microfabrication and nanofabrication methods whereby externally controlled tools are employed in the breaking down of the single crystal (bulk material) into an aqueous form or powder for the production of nanomaterials [257]. Irrespective of the approach adopted, the preparation of B-doped graphene requires a boron precursor and carbon precursor (graphite, GO, or rGO).

In the solid-state synthesis, Panchakarla *et al.* [258] were the first group to successfully dope graphene with boron. They used two methods during the synthesis of B-doped graphene. In the first method, B-doped graphene was synthesized using the arc discharge with graphite electrodes in the presence of different gases such as helium, hydrogen, and diborane. In the second method, B-doped graphene was synthesized by boron-packed graphite electrodes (3% B) with H_2 and He gases using arc discharge. The XPS revealed that boron was bonded to the sp^2 carbon network. The level of doping was found to be about 1.2 to 3.1% which was slightly different from 1.0 to 2.4% given by electron energy loss spectroscopy (EELS) used for confirmation. The Raman spectroscopy showed that the intensity ratio of D-band and G-band (I_D/I_G) of B-doped graphene was higher than the I_D/I_G ratio of undoped graphene and the G-band of B-doped graphene shifted to a higher frequency [258]. This shift was attributed to boron doping. In a case where B-doped graphene is synthesized at a lower growth temperature (900 – 1200 °C) different boron configurations such as boronic acids, boronic and borinic esters (Figure 2.5) are produced [258].

In 2016, Shaobo *et al.* [259] reported boron-doped reduced graphene oxide (B-rGO) synthesized from a facile dielectric barrier discharge (DBD) plasma approach using boric acid as a boron precursor under ambient conditions. The boron content in B-rGO was found to be 1.4%. Most reported B-doped graphene makes use of boron precursors; boron tribromide or diborane which are toxic and require special handling procedures. However, a greener approach has been demonstrated by Sheng *et al.* [260]. These authors employed less toxic boron trioxide vapour which was heated at a temperature of 1200 °C. The frequently used method for synthesis of B-doped graphene is based on the solid-state reaction between GO and boron trioxide or boric acid [260,261]. The materials are thermally annealed at a temperature between 900 and 1200 °C in an inert argon atmosphere. Typical doping levels obtained have been shown to range between 0.5 and 10% on photoemission spectroscopy measurements [260]. More recently, high-quality B-doped graphene was synthesized from SiC(001) single crystal by sublimation method. However, the boron content was very low (0.1%) [262].

Hydrothermal/solvothermal reaction approaches have been extensively used for doping graphene [253]. This approach tends to produce graphene materials with surface and morphology functionalization. Lu *et al.* [147] investigated a novel approach; Wurtz-type reductive coupling (WRC) reaction without the use of a transition metal catalyst. In this approach, B-doped graphene was synthesized by reacting tetrachloromethane, metallic potassium, and boron tribromide at temperatures between 150 and 210 °C for 10 min in a closed securely teflon-lined stainless-steel autoclave (solvent thermal process). The boron content in B-doped graphene was found to be 2.5% [147] when the XPS intensity measurement was used to quantitate atomic composition.

Comparatively, B-doped graphene is mostly synthesized using CVD approaches, and similarly, to N-doped graphene, Cu and Ni foils are used during the synthesis process. The boron precursors used can be liquid, solid, or gaseous. Gaseous boron precursors that have been investigated are 4-methoxyphenylboronic acid[256], diborane[250], and carborane [263]. Cattelan *et al.* [264] reported boron-doped graphene which had been synthesized using polycrystalline copper as a substrate, diborane, and methane as boron precursor and carbon precursor, respectively. The synthesis was carried out at a growth temperature of 950 °C and the boron content that was obtained was 2.5% [264].

Wu *et al.* [265] reported boron-doped single-layer graphene synthesized on copper at a growth temperature of 1000 °C in an argon carrier using the CVD technique. Boric acid and polystyrene were employed as boron and carbon precursors, respectively. Under these conditions, the obtained B-doped graphene had a boron content of about 5%. When a solid boron precursor such as phenylboric acid produced large monolayer polycrystalline graphene film from the CVD on copper foils under hydrogen gas stream at 950 °C [266]. Other boron precursors; include triphenylborane, boron trioxide, and ammonia borane.

2.6.5 Sulfur-doped graphene

Sulfur can be substitutionally doped into the graphene framework to modulate the chemical and electronic properties of graphene. Its bonding configuration is similar to that of oxygen, unlike nitrogen and boron doping effect, sulfur doping induces a negligible charge transfer that occurs in the C–S bond due to similar electronegativity between carbon ($\chi = 2.55$) and sulfur ($\chi = 2.58$). Figure 2.6 exhibits the different configurations being, C-SH, C-S-C, and C-SO$_x$-C (where x = 2, 3, or 4) [267]. The C–C bond length is shorter than that of the C-S bond (1.78 Å) [268], hence sulfur doping tends to provide a stable structure. It has been reported that the

sulfur doping in graphene takes place in two steps, firstly, formation of defect sites, secondly, double bond S=S rapture and the end-product (graphene sheet) change into a small-bandgap semiconductor or becomes more metallic compared with pristine graphene [269]. The two bands in the Fermi level are lifted in the band plot of sulfur-doped graphene (S-doped graphene) with one sulfur atom. This results in a bandgap of 0.3 eV with one S atom whereas containing two S atoms causes an increase in the metallic properties of graphene. S-doped graphene sheets are more resistive and more metallic as compared with pristine graphene. They are more resistive because of the sulfur and oxygen functionalities which causes the free carrier trapping.
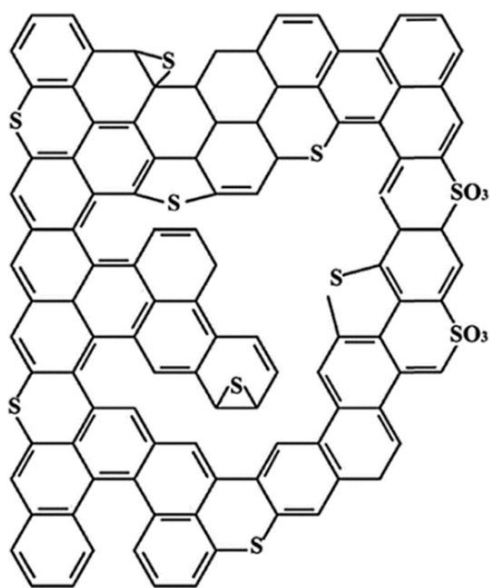
Figure 2.6: Bonding configuration of S-doped graphene [270].

Recently, various methods have been used in the synthesis of S-doped graphene. Sulfur atoms can be inserted into the graphene frameworks using CVD and thermal annealing of GO [271]. The sulfur-containing porous carbon material has been synthesized using infiltration of the carbon source into zeolite pores using the impregnation and CVD approach [272]. The thermal treatment approach has been successfully employed in the synthesis of S-doped graphene whereby graphene or GO is treated with sulfur dioxide [273], benzyl disulphide [267], hydrogen disulphide [274], and carbon disulphide [275]. These studies have shown that the thermal treatment approach produces a low sulfur content, even when the treatment temperature has been adjusted [276]. Poh *et al.* [273] reported that S-doped graphene is highly dependent on the type of sulfur precursor and type of GO or graphene used during the synthesis.

Xu *et al.* [169] reported that the CVD method can be used to synthesize S-doped graphene using thiophene as a sulfur precursor. The XPS analysis revealed that there was about 3.2% of sulfur content in S-doped graphene. However, Gao *et al.* [277] reported the synthesis of large-

area S-doped graphene using Cu substrate and hexane in the presence of sulfur *via* the CVD approach. Yet the sulfur content was very low, approximately 0.6%. Yang *et al.* [267] synthesized S-doped graphene *via* thermal annealing of GO and benzyl disulphide as a sulfur source. At different annealing temperatures of 600, 900, and 1050 °C sulfur contents of 1.53%, 1.35%, and 1.30% were obtained, respectively [267]. This shows that the annealing temperature affects the doping levels; lower temperatures tend to produce higher sulfur content. However, in 2015 Liu *et al.* [278] reported the use of similar sulfur-containing precursors (benzyl disulphide) and GO in the synthesis of S-doped graphene using the microwave-assisted solvothermal method and achieved a doping level of 2.3%. Liang *et al.* [274] reported the S-doped graphene that had been annealed at a temperature of 1000 °C with the gaseous sulfur source of H_2S gas on Si/SiO_2. Since then, different liquid organic material precursors such as hexane have been also employed in the presence of sulfur when the CVD method is used together with the copper substrate [277]. Hassani *et al.* [271] reported a high sulfur doping level of 5% (XPS) that was grown from CVD and sulfur powder as a sulfur precursor. Thus, the level of sulfur in S-doped graphene varies with synthetic technique and sulfur-containing precursor used.

2.6.6 Phosphorus-doped graphene

Phosphorus can also be used as a dopant and precursor to dope graphene. It belongs to group 15 elements below nitrogen. However, it is larger than nitrogen. Therefore, its doping causes greater structural distortion. The electronegativity of phosphorus ($\chi = 2.19$) is lower than of carbon ($\chi = 2.55$) which demonstrates higher electron-donating ability [279]. Phosphorus, though iso-valent to nitrogen, has a different doping effect due to higher electron-donating ability and more diffuse valance orbitals ($3s^2 3p^3$) [280]. Consequently, the polarity of the C-P bond is different from that of the C-N bond and this may be due to the more diffuse valance orbitals of phosphorus [281].

The large atomic radius of phosphorus does not appear in-plane of graphene [268] which significantly affects the bandgap phosphorus-doped graphene (P-doped graphene). Theoretically, the bandgap (0.53eV) of P-doped graphene is higher than those of both N-doped graphene (0.14 eV) and B-doped graphene (0.14 eV). Interestingly, doping with phosphorus is easier than with nitrogen since the formation energy of P-doped graphene is 7.1 eV/atom [268] while that of N-doped graphene is 8.0 eV/atom [219]. This suggests that phosphorus doping is energetically more favourable.

During doping, phosphorus can form a pyramidal-like bonding configuration along with three carbon atoms. This is due to strong hybridization between carbon 2p and phosphorus 3p. This is due to the change of hybridization of carbon from sp^2 to sp^3 [282]. In pyramidal-like bonding configuration, the phosphorus overhangs from the graphene plane and the P-C bond length (1.33 Å) increase by 24.6% compared with the C-C bond length of pristine graphene (Figure 2.7) [282]. Some and co-workers [283] reported the synthesis of highly air-stable P-doped graphene that constituted n-type behaviour. Recently, various techniques for substituting phosphorus atoms in the lattice of graphene have been investigated and reported such as CVD, inductively coupled plasma, and the most effective method is microwave plasma [284,285].
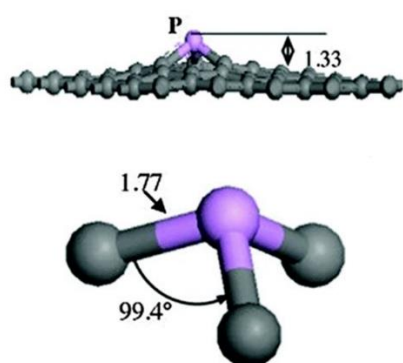
Figure 2.7: Geometric structure of P-doped graphene [282].

Zhang *et al.* [286] reported that P-doped graphene was synthesized using triphenylphosphine as phosphorus precursors and GO as carbon *via* thermal treatment resulting in phosphorus content of 1.81% on XPS measurement. The P-doped graphene has also been synthesized using post-thermal annealing of graphene/GO with triphenylphosphine (TPP) as a P-containing precursor under a protecting atmosphere [286,287]. Some *et al.* [283] reported that the P-doped graphene prepared from TPP under argon at 100 to 250 °C yielded a phosphorus content of 4.96%. Similar phosphorus-containing precursors were employed in the synthesis of P-doped graphene by Shin *et al.* [288] using an inductively coupled plasma technique to yield a phosphorus content of 2%.

Ionic liquids such as 1-butyl-3-methylimidazolium hexafluorophosphate have been employed in the synthesis of thermal annealed P-doped graphene as a phosphorus precursor [289]. During the thermal annealing process, different covalently bonded tetrahedral structures such as C_2PO_2, C_3PO, and CPO_3 were observed and consequently resulting in a charge redistribution in P-doped graphene. Dennis [290] reported that the bandgap opening relies purely on

phosphorus doping level, e.g. 0.5% resulted in a bandgap of 0.3 to 0.4 eV. *In situ* synthesis of P-doped graphene has been reported by Latorre-Sanchez *et al.* [291] where pyrolysis of natural alginate and dihydrogen phosphate ion was done under oxygen at a temperature of 900 °C. The P-doped graphene obtained had P-C and P-O bonds and an optical bandgap of 2.85 eV. It should be noted that P-doping gives rise to a magnetic moment ascribed to unpaired electron spin.

2.6.7 Halogen-doped graphene

Halogen (group 17 elements, namely, fluorine (F), chlorine (Cl), bromine (Br), and iodine (I)) are well known for their higher reactivity compared with other elements from groups 13 to 16. When the halogen is doped on the graphene lattice, it converts the sp^2 carbon bonding into an sp^3 state, which produces drastic distortions in the electronic and geometric structures of graphene [292]. It also enhances the active site of graphene, which modifies the graphitic carbon material, enabling doped graphene to be applied in various technological fields, namely, stem cells [293], photo-catalytic [294], DSSCs [295], and ORR [292]. Halogen-doped graphene is widely applied as an electro-catalyst for ORR in fuel cells. However, very few studies have been reported on its application in DSSCs.

The most reactive element of the halogen is fluorine. When F is bonded to graphene, it results in strong F-C bonds and the C-C bond length stretches between 1.57 and 1.58 Å [296]. The fluorine bonding causes an increase in the hydrophobicity of graphene [297]. Doping with Cl results in longer bond length and lower binding energy than H and F. This indicates that the covalent bond (Cl-C) is less stable compared with the C-H and C-F bonds [298]. Chlorine-doped graphene is reported to be thicker (1.1-1.7 nm) than fluorine-doped graphene due to its long bond length [298]. There are very few experimental and theoretical reports on bromine-doped graphene and iodine-doped graphene because of the thermodynamic instability related to their low electronegativity (F = 3.98, Cl = 3.16, Br = 2.96 and I = 2.66) and large sizes. Br and I tend to interact with graphene by physisorption without interrupting the sp^2 carbon network [299].

Halogen-doped graphene can be synthesized by ball milling [300], arc discharge [297], and microwave plasma [301] approaches. These approaches tend to produce differing doping levels of halogen-doped graphene. Halogen-doped graphene nanoplates were prepared by the ball milling approach in the presence of I, Br, and Cl [300]. A decrease in the halogen doping level of the halogen-doped graphene nanoplates was observed (Cl - 5.89%, Br - 2.78%, and I -

0.95%) due to the size and chemical reactivity of these elements. The arc discharge approach has been employed in the synthesis of fluorine-doped multi-layered graphene sheets which contained about 10% of F [297]. Bouša *et al.* [301] reported chemical modification of graphene by using various aryl halogens to produce halogen-doped graphene *via* the microwave plasma approach. XPS analysis revealed the successful covalent bonding of aryl molecules to the graphene basal plane. Different halogen doping levels were obtained, fluorine-doped graphene (5.06%) was reported to contain higher doping levels than chlorine-doped graphene (4.76%), bromine-doped graphene (3.86%), and iodine-doped graphene (3.50%).

2.6.8 Nitrogen and boron co-doped graphene

Previous studies had shown that heteroatoms can be co-doped in the synthesis of CNTs. Similar, to CNTs, graphene can also be co-doped with multiple species of foreign atoms. The co-doping of heteroatoms produces synergistic effects and creates new properties. Heteroatoms such as boron and nitrogen have similar sizes but generate opposite doping effects [302]. N, B co-doped graphene can be achieved by using two precursors (nitrogen and boron precursors) or a precursor that contains both nitrogen and boron in its structure. When they are simultaneously doped on graphene, they form boron nitride because of the phase separation between carbon and boron nitride [237,303]. This is ascribed to the larger binding site of C-C and B-N bonds as compared with that of N-C and B-C bonds. Doping by boron and nitrogen produces different bonding configurations and bond lengths, e.g., C-B (1.49 Å), C-N (1.35 Å), C-C (1.42 Å), and B-N (1.45 Å).

Figure 2.8 depicts the top views of five different structures, being pristine graphene, N-doped graphene, B-doped graphene, hexagonal boron nitride (h-BN), and boron and nitrogen co-doped graphene. The h-BN is well-known as white graphene. It is a dielectric that consists of a wide bandgap of approximately 5.9 eV. h-BN is synthesized in a similar way to other doped graphenes by using a CVD method. As-synthesized h-BN exhibits larger optical energy (5.5 eV) and elastic modulus (200-500 N m^{-2}) [304]. Boron and nitrogen co-doped graphene is more thermally stable than B-doped graphene, however, less thermally stable when compared with N-doped graphene [304].
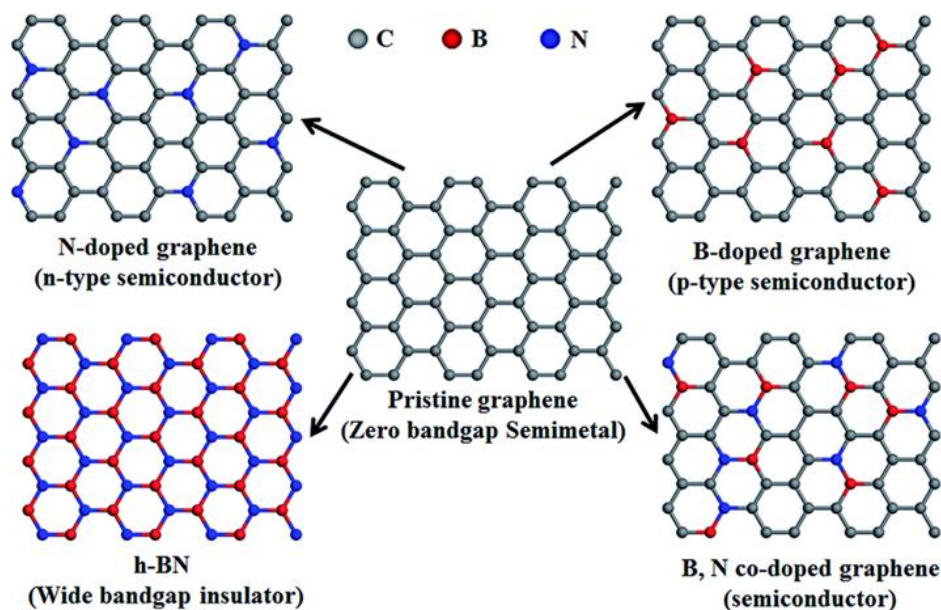
Figure 2.8: Schematic diagram of pristine graphene, N- and B-doped graphene, h-BN, and B, N co-doped graphene [304].

The co-doping tends to enhance the bandgap due to symmetry breaking [303]. Both nitrogen and boron produce a bandgap at the Dirac point however, they shift the Fermi level in different directions [303]. B, N co-doping is presumed to create a bandgap only at the Dirac point with no shifting in the Fermi level [76,246]. Various methods have been used in the synthesis of N- and B-doped graphene. Ci *et al.* [77] reported dual N and B co-doped graphene synthesized *via* CVD approach from ammonia borane and methane as the boron, nitrogen, and carbon precursors, respectively. The doping level was tuned by altering the reaction parameters. The N, B co-doped graphene with a high doping level, normally has a large area and N-B hybridized domain as demonstrated by XPS studies [77]. The hydrothermal approach has been reported by Wu *et al.* [305] where N, B co-doped graphene was synthesized using ammonia borane and GO, which resulted in nitrogen content of 3.0% and boron content of 3.0%. In 2013, Bepete *et al.* [306] reported the incorporation of a small BN domain (0.3-0.5%) using nitrogen gas and boric acid as nitrogen and boron precursors.

Co-doping with multiple species of foreign atoms produces different bonding configurations. Co-doping of phosphorus causes a pyridinic bonding of nitrogen on graphene [307] while the co-doping of sulfur promotes graphitic-N as dominant [169]. Porous P, N co-doped graphene has been synthesized using magnesium oxide-templating *in situ* CVD approach with methane and ammonium phosphate as nitrogen and phosphorus precursors [308]. The XPS analysis indicated phosphorus and nitrogen co-doped graphene formed had a nitrogen content of 2.6% with different nitrogen atoms configuration of pyrrolic-N, pyridinic-N, and graphitic-N,

however the phosphorus content (0.6%) was found to be less than that of nitrogen. The phosphorus atoms were covalently bonded with carbon in the various tetrahedral forms, being, C_2PO_2, C_3PO, and CPO_3. The level of doping and configuration of P and N co-doped graphene are affected by synthesis temperature in the CVD approach [309]. The synthesis temperature of 700 °C produced different nitrogen species in the sequence: pyridinic-N > pyrrolic-N > graphitic-N. P and N co-doped graphene synthesized at 800 °C and 900 °C had similar nitrogen species of pyrrolic-N and graphitic-N while those obtained at 1000 °C exhibited a graphitic-N. Higher temperature enhanced the number of phosphorus-carbon bonds and decreases the number of phosphorus-oxygen bonds. The increase in doping effect is due to the formation of more-stable bond configurations. However, the doping level for both nitrogen and phosphorus decrease as the temperature increases.

Very few reports exist on graphene that is simultaneously doped with nitrogen and sulfur [310]. Wang *et al.* [311] reported the interaction between sulfur and nitrogen in co-doped graphene. In their work, N and S co-doped graphene was prepared using a one-pot hydrothermal approach using amino acid and ly-cysteine as nitrogen and sulfur doping agents. The concurrent incorporation of nitrogen and sulfur atoms in the presence of oxygen alters the surface chemistry of carbon causing the increase in doping levels, whilst direct bonding between nitrogen and sulfur atoms was not fully demonstrated [311]. Xu *et al.* [169] reported N, S co-doped graphene synthesis from a nitrogen source of pyrimidine and sulfur source of thiophene at low temperature. The doping level of S and N atoms was found to be 0.7 to 2.0% and 3.7 to 5.7%, respectively. The use of multi-precursors is most easily controllable and convenient than single precursor doping methods. The N, S co-doped graphenes; are applied in lithium-ion batteries [312], supercapacitors [311], electrocatalytic oxygen reduction reactions [313,314], and exhibit promising performance.

2.7   DSSCs

Most research has been focusing on open-circuit voltage (V_{oc}), boosting the short-circuit current density (J_{sc}) and fill-factor (FF) to increase the efficiency of the cells. Enhancing the CE material causes the FF of the cell to increase, which is generally affected by the cell series resistance (R_s) and the slope of the tangent line to the current density (J) - voltage (V) curve at open-circuit voltage [308]. The charge carrier's transportation from the photoanode to the CE encounters varying resistance. The dominant charge transfer in DSSCs is at the CE/electrolyte interface. At the CE/electrolyte interface, the charge-transfer resistance and series resistance

are subjugated to the CEs. The series resistance of a solar cell dominates FF losses. A higher FF is due to smaller series resistance which generates higher power conversion efficiency.

2.7.1 Doped graphene as a counter electrode for DSSCs

The CE is used to minimize redox species in DSSCs, that act as mediators during the regeneration of the sensitizer occurring after electron injection. CEs are required to have a good catalytic activity to enhance the reduction of the electrolyte, hence should have lower sheet resistance, low cost, and high thermodynamic stability [315]. The reactions occurring at the CEs are highly dependent on the nature of the redox mediator being used for charge transfer between the CE and photoelectrode [315-317].

2.7.1.1 Oxygen-doped graphene in DSSCs

Graphene oxide and rGO as a CE are reported to have the good electrocatalytic ability in reducing the redox couple in DSSCs [93]. This is because they possess structural defects and oxygen-containing functional groups, for example, carbonyl, epoxide, and hydroxyl [318]. It was observed that the fabrication procedure of GO can also be regarded as a major factor in determining the performance of GO in DSSCs. DSSCs with graphene-based CE exhibited higher power conversion efficiency of approximately 90% compared with platinum-based CE [315]. Kavan *et al.* [319] demonstrated that increasing the number of oxygen-containing groups increases catalytic activation. Therefore, different materials of GO used in various procedures produced different power conversion efficiency. DSSCs fabricated from GO have been reported by Kumar [320] which produce a higher conversion efficiency of 5.58%. Recently, various researchers reported a reduction of GO to rGO chemically [321], thermally [322], electrochemically [323], and photothermally [324] and their application as GO or rGO-based CEs, exhibiting that rGO could be a better potential candidate for fabricating flexible and Pt-free DSSCs. Jang *et al.* [325] reported the use of rGO as CE that had been developed from the spin coating. This method resulted in a uniform morphology of rGO and high particle size, producing a power conversion efficiency of 3.99%.

Yeh *et al.* [192] investigated the effect of using GO and highly conductive rGO as CE. Highly conductive rGO yielded higher power conversion efficiency of 7.62% compared to a GO (0.03%). Highly conductive rGO exhibited a good electrocatalytic ability than GO because of its high standard heterogeneous rate of redox couple reduction and its electrochemical surface area. Recently, Sarker *et al.* [326] developed a high-efficiency DSSC with rGO as CE synthesized by doctor-blading a viscous rGO on fluorine-tin-oxide (FTO) substrate. The

DSSC-rGO electrode exhibited similar catalytic performance as platinum-based cells showing promising characteristics of replacing Pt.

2.7.1.2 Nitrogen-doped graphene in DSSCs

N-doped graphene has been employed in DSSCs for harvesting energy. N-doped graphene has exhibited gigantic electrocatalytic activity due to high charge polarization that occurs due to the difference in electronegativity between nitrogen and carbon [327]. It has been reported that N-doped graphene possesses a good electrocatalytic activity and high conductivity that can produce a conversion efficiency of more than 5% (Table 2.4). Metal-nitrogen-doped graphene or metal-free nitrogen graphene has been used as CE.

Table 2.4: Energy conversion efficiency for DSSCs with N-doped graphene as a CE.

Counter electrode	Jsc/mA cm^{-2}	Voc/V	FF	ŋ/%	Ref.
N-GR foam	15.84	0.77	0.58	7.07	[328]
N-GR	10.55	0.82	0.55	4.75	[329]
N-GR	12.32	0.71	0.60	6.12	[330]
Nanoplatelet-N-GR	14.02	0.89	0.74	9.05	[331]
N-GO/Pt	14.10	0.75	0.74	9.38	[332]
NGnP5	14.78	0.97	0.72	10.27	[331]
FeN/N-GR	18.83	0.74	0.78	10.86	[333]
N-GR	16.13	0.73	0.74	8.71	[333]
N-GR	13.43	0.64	0.59	5.07	[334]

Xue *et al.* [328] demonstrated that the use of (3D) N-doped graphene (nitrogen content of 7.6%) synthesized from freeze-drying of GO under ammonia gas treatment on DSSCs as a CE with an N719 as a dye sensitizer and I_3^-/I^- redox couple. It provided a power conversion efficiency of 7.07%. However, DSSCs had a poor FF of 0.58. The efficiency was slightly lower than that of platinum-based CEs because of the low fill factor [328]. This is due to the nitrogen-doping method that includes low-pressure drying and high-pressure synthesis. Further, ammonia gas treatment is toxic, therefore it is not suitable for mass production. However, N-doped graphene sheets which were synthesized in a similar method (hydrothermal reduction of GO) and with similar nitrogen precursor (ammonia) was reported by Wang *et al.* [330]. These N-doped graphene sheets had a nitrogen content of 2.5%. The N-doped graphene CE was created by drop-casting an N-doped graphene sheet solution onto a fluorine-doped tin oxide

glass substrate and the redox couple used was I_3^-/I^- redox couple. This DSSC produced a conversion efficiency of 6.12%.

In 2013, Shaocong *et al.* [335] demonstrated that doping graphene with nitrogen can enhance the power conversion efficiency of DSSCs (5.4% - N-doped graphene) whilst 5.1% – Pt improves catalytic activity and lowers the charge transfer resistance. They further demonstrated that N-doped graphene doped at different temperatures and increasing the nitrogen content do not affect the power conversion efficiency. The state of nitrogen doping was observed to play a major role in catalytic activity. Jeong *et al.* [151] found that pyrrolic-N has large binding energy toward ions in the solution, which may result in difficulty in the desorption of I^* to I^- for the iodine reduction reaction. Thus, the decrease of reaction sites would restrict the overall activity.

Yen *et al.* [329] reported a power conversion efficiency of 4.75% which was achieved when N-doped graphene prepared from the hydrothermal method was used as a CE in DSSCs. Later in 2012, nanoplatelet-NGR were employed as CE in DSSCs and they produced a power conversion efficiency of 9.05% and FF of 0.74, yet a different redox couple of $Co(bpy)_3^{3+/2+}$ and dye sensitizer of O-alkylated-JK-22 were used [336]. Graphene nanoplatelets doped with nitrogen at the edge, which are synthesized from the ball-milling method have been investigated [331]. The investigation was performed using six different NGnP/FTO CEs; NGnP1, NGnP2, NGnP3, NGnP4, NGnP5, and NGnP6 that have been fabricated from different deposition times, 2, 3, 5, 7, 9, and 11 min, respectively [331]. The NGnP CEs displayed excellent electrocatalytic performance for the redox couple ($Co(bpy)_3^{3+/2+}$) with lower charge transfer resistance [331]. As the deposition time increased, the energy conversion efficiency also increased. However, at the deposition time of 11 min, a decrease in efficiency was experienced. The highest power conversion efficiency of 10.27% was obtained from NGnP5 [331].

Metal-nitrogen-doped graphene CE produces a higher power conversion efficiency than metal-free nitrogen-doped graphene. Lin *et al.* [332] achieved an efficiency of 9.38% when N-doped graphene was used on Pt-sputtered fluorine-doped tin oxide substrate (NGR/Pt/FTO) as CE. This high efficiency was caused by the electron transfer effect which was supplied by NGR and the light-reflection effect from NGR/Pt/FTO which promoted the electron transfer from CE to the electrolyte (I_3^- ion) and light. In 2015, Xue *et al.* [334] report N-doped graphene nanoribbons (nitrogen content of 6.5% with a surface area of 751 cm^2 g^{-1}) which were

synthesized from thermal treatment of GO nanoribbons in ammonia gas and produced a power conversion efficiency of 5.07%.

Kim *et al.* [337] demonstrated that treating N-doped graphene with TiO_2 produced a power conversion efficiency of 9.32%. This is because the graphene/N-doped TiO_2 composite expands the absorption into the visible light region and increases the rate of electron transfer [337]. When N-doped graphene nanosheets with transition metal nitrides (iron nitride) core-shell nanoparticles are employed as CE material, exhibited a power conversion efficiency of 10.86% which was greater than that of DSSCs with platinum or N-doped graphene as CE being 9.93% or 8.72%, respectively [333]. In 2017, Yang *et al.* [338] reported that the electrochemical measurements of nitrogen-doped holey graphene (NHG) exhibited better electrochemical stability and higher catalytic activity concerning those of Pt, and DSSCs with optimized NHG demonstrate a power conversion efficiency of 9.07%, which was higher than the efficiency of 8.19% for Pt as the CE.

Recently, N-doped graphene on a Pt-sputtered fluorine-doped tin oxide substrate (NGR/Pt/FTO) as CEs achieved an efficiency of 9.38% *via* attributed to firstly, hole-cascading transport at the interface of electrolyte/CEs, as a result of controlling the valence band maximum of I^-/I_3^- redox couple and the Fermi level of Pt by nitrogen doping. Secondly, the extended electron transfer surface effect is provided by large-surface-area doped graphene. Thirdly, the high charge transfer efficiency is due to the superior catalytic characteristics of N-doped graphene. Finally, the superior light-reflection effect of NGR/Pt/FTO CEs facilitates the electron transfer from CEs to I_3^- ions of the electrolyte and light absorption of dye [332]. This lessens the loss that occurs at the interface of electrolyte/CE and causes an increase in power conversion efficiency of DSSCs [246].

2.7.1.3   Boron-doped graphene in DSSCs

In the meantime, there have been few reports based on the application of B-doped graphene as CE in DSSCs. Fang *et al.* [261] reported the use of B-doped graphene as CE in a DSSC which is based on an I_3^-/I^- redox couple. The B-doped graphene was fabricated from annealing of boron trioxide with GO at a temperature of 1200 °C for 4 h and resulted in a boron content of 1.0% [261]. This provided a high-power conversion efficiency of 6.73% [261]. The application of B-doped graphene as a CE with the $Co(2,2\text{-bipyridine})_3^{2+/3+}$ redox couple was reported to produce a higher power conversion efficiency than an I_3^-/I^- redox couple [339]. B-doped graphene exhibited higher electrocatalytic activity than Pt as CE in $Co(bpy)_3^{2+/3+}$ redox

couple [339]. Generally, B-doped graphene exhibits good electrochemical stability [339,340] and lower charge-transfer resistance [341]. DSSCs developed from B-doped graphene produced a power conversion efficiency of 9.21% which was higher than that of platinum CE (8.45%) [339].

2.7.1.4   Sulfur-doped graphene in DSSCs

Sulfur-reduced graphene oxide (SRGO) has been applied in DSSCs to produce a power conversion efficiency of 4.23% [342]. The SRGO has been fabricated from the one-step synthesis using a hydrothermal process with the use of mercaptoacetic acid. It had a sulfur content of 5.45% [342]. Meng *et al.* [343] reported the use of sulfur-doped porous graphene (SPG) in DSSCs as CE. SPG was synthesized from sulfur powder and poro-foaming agent *via* thermal annealing approach (800, 900, and 1000 °C). The annealing approach (especially, higher temperature - ≥ 900 °C) showed a better photovoltaic and electrochemical performance. The high-power conversion efficiency of 8.67% was achieved when as-made SPG was used as CE, outperforming the Pt (7.88%). Sulfur atom can tune the electronic structure of graphene and create a highly active site with a low change in carbon conjugation length. In 2017, Mustafa *et al.* [344] presented a new CE that consists of GO doped with poly(3,4-ethylenedioxythiophene) and TiO_2. Hence, a power conversion efficiency of 1.166% was achieved. The incorporation of poly(3,4-ethylenedioxythiophene)/GO (PEDOT-GO) with TiO_2 was found to produce more promising results than platinum CE (0.727%).

2.7.1.5   Phosphorus-doped graphene in DSSCs

P-doped graphene has been mostly applied in fuel cells [345], Li-ion batteries [286] and supercapacitors [346] as an electrode. Wang *et al.* [347] were the first to demonstrate that P-doped reduced GO can be employed as CE in DSSCs with I^-/I_3^- redox couple and it produced a power conversion efficiency of 6.26%. Ahn *et al.* [348] demonstrated that phosphorus-doped 3D graphene provides better performance than platinum as CE. P-doped 3D graphene produced a power conversion efficiency of 8.46% which was higher than that of platinum (6.01%). However, in 2017, Xu *et al.* [349] reported a higher power conversion efficiency of 7.08% fabricated from a P-doped porous graphene nanosheet with I^-/I_3^- redox couple. P-doped graphene nanosheet was synthesized using the CVD method and it had a surface area of 1627.8 $m^2\ g^{-1}$ [349].

2.7.1.6   Halogen-doped graphene in DSSCs

Recently, Jeon *et al.* [350] demonstrated that edge-selectively halogenated graphene nanoplatelets (XGnPs, X=Cl, Br, and I) and halogen contents of Cl, Br, and I in XGnPs as 3.18, 1.77, and 0.66%, respectively, used as CEs indicated enhanced electrocatalytic activities toward $Co(bpy)_3^{3+}$ reduction reaction in DSSCs with exceptional electrochemical stability. These authors further reported IGnP-CE to have the lowest charge-transfer resistance (R_{ct}) of 0.46 Ω cm^2 at the CE/electrolyte interface. It should be noted that this value is much lower than that of Pt-CE (0.81 Ω cm^2). It was also noted that in DSSCs with IGnP-CE had the highest FF (71.3%) and cell efficiency (10.31%), whereas those of DSSCs with Pt-CE were only 70.6% and 9.92%, respectively.   These characteristics could be inferred to emanate from an established balance between electrical conductivity for efficient charge transfer and charge polarization which enhances the reduction activity of redox couples simultaneously [351,352].

2.7.1.7   Heteroatom co-doped graphene in DSSCs

It has been reported that co-doping with two or more elements can generate a distinctive and synergistically increased electronic structure in the carbon matrix. It also causes an increase in the electrocatalytic activity of graphene because of the increase in spin densities and asymmetries of charge at the various sites of the double-doped graphene. A power conversion efficiency of 8.08% which is superior to 6.34% of Pt-CE was achieved when GO was reduced and doped with nitrogen and boron [166]. This B and N co-doped graphene was reported by Yu *et al.* [166] where the doped graphene was achieved *via* chemically grafting ionic liquid followed by thermal annealing.

Luo *et al.* [342] reported a co-doping of nitrogen and sulfur atoms in graphene which was fabricated using DL-penicillamine which possesses both atoms in its structure. The NSRGO had nitrogen and sulfur contents of 2.12% and 8.92%, respectively. The power conversion efficiency of NSRGO was compared with RGO, SRGO, and NRGO. NSRGO was found to exhibit a higher power conversion efficiency of 4.73% [342]. This is because the co-doping of heteroatoms provides more electrocatalytic active sites to ease the charge transfer between the cathode/electrolyte interface which leads to higher catalytical performance and an increase in photovoltaic performance[342]. However, a high power conversion efficiency of 7.42% had been demonstrated by Kannan *et al.* [353] which was higher than that of single atom-doped graphene (N or S-doped graphene CE). This high catalytic activity is ascribed to high charge polarization which produced the synergistic effect between the different electronegativities of

carbon and nitrogen. Furthermore, the structural distortion is produced by the larger atomic size of sulfur. The bifacial DSSCs with high transparent nitrogen-doped graphene, sulfur-doped, and nitrogen and sulfur dual-doped graphene-like carbon films as CEs exhibit drastically enhanced power conversion efficiency (PCE) of 3.74%, 3.86% and 4.22% under front-side illumination compared with that of pristine graphene as CE [354]. 3D N and S co-doped rGO was reported by Yu *et al.* [355] with an efficiency of 9.40% which was higher than that of platinum (9.10%). The high electrochemical performance was due to the synergistic effect of nitrogen and sulfur atoms in graphene.

Nitrogen and phosphorus belong in the same family; therefore, they show higher electron-donating ability which further shows stronger n-type behaviour [356]. The defects induced by co-doping (N and P) are predicated to bring about a highly localized state which is close to the Fermi level, especially for electrocatalysis [357]. Yu *et al.*[358] reported the use of N and P-doped graphene and single-component N or P-doped graphene in DSSCs. They produced a better performance along with a conversion efficiency of 8.57% which was higher than that of single-element N or P-doped graphene CE [358].

2.8   Density functional theory studies

Most frequently, density functional theory (DFT) calculations for DSSCs estimate the adsorption energies of atomic iodine under vacuum and explicit acetonitrile solvation conditions. Considering the pristine armchair and zigzag edges as well as the basal plane of graphene sheets, the I atom adsorption energies have been shown to be below the optimal range for the CE catalytic activity (-0.17, 0.17, and -0.49 eV, respectively) [359]. Recently, edge models involving double-coordinated Se (C-Se-C) or oxidized Se atoms also failed to support I atom adsorption. But, the I atom binding criterion for CE is effective for the single-coordinated Se-doping cases (C==Se), with adsorption energies of 0.77 and 0.48 eV for the armchair and zigzag edges, respectively [359,360]. For instance, the I_3^- /I^- ions have been shown to adsorb on the graphitic basal plane at distances of 3.18 to 3.37 Å [359]. This potentially possesses an n-type shift of the graphene band and significantly increases currents at finite bias voltages. It can thus, be argued that although the graphitic basal plane cannot drive an iodine reduction reaction on its own it has the good current-carrying capability, a necessary condition for high CE catalytic activity.

It is prudent to examine the dielectric function, absorption spectrum, and energy loss function of a single layer graphene sheet based on the density functional calculations. It has been shown

for light polarization parallel and perpendicular to the plane of the graphene sheet and compared with doped graphene, the available theoretical and experimental results appear the same. For example, it has been found that individual boron and nitrogen doping does not significantly affect the imaginary dielectric function and hence the absorption spectra. However, there is a significant red shift in absorption towards the visible range of radiation at high doping for the B/N co-doping[359] of graphene.

2.9　　Commercial, cost, and environmental perspectives

The exponential rise in commercial applications of optoelectronic materials of organic and nanostructured electronic origin, coupled with environmental concerns, motivates the quest for lower-cost approaches to sustainable electricity production. The present work examined DSSCs and specifically the use of heteroatom-doped graphene as a CE. This is a focussed interface engineering strategy that employs innovative nanostructures and interfaces processing to enhance device performance. There is limited literature on photochemical studies on the control of interface morphology, which complicates the determination of clear structure/function relationships in these very important devices. Several strategies are under investigation to achieve control of the interface morphology in organic donor/acceptor films [361]. This has seen an increase in sophisticated approaches for the design and optimization of solid-state photovoltaic devices. However, technological concerns about shelf-life and device stability when using liquid electrolytes need to be addressed. Generally, DSSCs rely on photoinduced charge separation at a dye-sensitized interface between a nanocrystalline, mesoporous metal oxide electrode, and a redox electrolyte. They are potentially a low-cost solar energy conversion technology but the challenge is achieving a rational optimization of materials and device designs [362]. The success of graphene-based materials used for energy applications wholly depends on the development and optimization of production methods. Of great interest is the optimized control of the sheet size and increasing the edge-to-surface ratio, which is vital for optimizing electrode performance in fuel cells and batteries. The frequently employed DSSC materials such as TiO_2 are inexpensive, easily available and safe to the environment. The raw materials are less prone to contamination and processable at ambient conditions, thus upscaling of manufacturing processes for mass production is even easier. The better performance of DSSCs under lower light intensities, makes them appealing for indoor applications, a major driver for any commercialization effort [363,364].

2.10   Conclusion

In summary, heteroatom-doped graphene materials have been investigated as efficient CEs for DSSCs. DSSCs show significant opportunities for research in renewable energy. In the DSSCs, the CE has good electrocatalytic activity and high electrical conductivity which is responsible for the collection of electrons from the external circuit and for catalyzing reduction reactions. Therefore, alternative CEs such as graphene and heteroatom-doped graphene, which are low-cost are preferentially used instead of high-cost platinum CEs. From the aforementioned studies, various heteroatom-doped graphene has revealed promising perspectives as CEs in DSSCs. Heteroatom-doped graphene as CE demonstrated significantly higher power conversion efficiency compared with platinum-based CE. Enhanced efficiency is due to improved electron transfers and dissociation of excitons at electrodes.

Various power efficiencies have been achieved from 2008 to 2018, depending on the heteroatom employed in the CE. To our knowledge, the efficiency of DSSCs depends on how the CE has been fabricated. When graphene is doped with heteroatoms such as O, N, B, S, and P modulation of electronic properties of graphene is observed. Heteroatom doping provides graphene with different structural, physicochemical, electromagnetic, and optical properties. The heteroatom-doped graphene properties depend on the doping configurations, type, and doping level. Doping configuration, doping level, and type differ in all heteroatom-doped graphenes due to various starting graphene materials, heteroatom precursor/source, doping temperature, and reaction time used in the synthesis method. Various synthesis approaches have been developed for heteroatom doping. Regardless of the enormous progress made so far, it is still a challenge to control heteroatom doping. The research based on graphene will continue to grow vigorously due to the wide application of heteroatom-doped graphene and new opportunities. It is foreseen that, sooner rather than later, after some improvement, such heteroatom-doped graphenes could be utilized for the necessities of society. In the near future, heteroatom-doped graphene could play a major role in solving the energy-related issues in various solar cells, apart from applying it as CE in DSSCs.

References

1.   K. Solangi, M. Islam, R. Saidur, N. Rahim and H. Fayaz, *Renew. Sust. Energy Rev.*, **2011**, 15, 2149-2163.
2.   S. Haehnlein, P. Bayer and P. Blum, *Renew. Sust. Energy Rev.*, **2010**, 14, 2611-2625.
3.   J. W. Lund, D. H. Freeston and T. L. Boyd, *Geothermics*, **2011**, 40, 159-180.

4.   C. Posten and G. Schaub, *J. Biotechnol.*, **2009**, 142, 64-69.

5.   A. Azarpour, S. Suhaimi, G. Zahedi and A. Bahadori, *Arab. J. Sci. Eng.*, **2013**, 38, 317-328.

6.   A. Raheem, S. A. Abbasi, A. Memon, S. R. Samo, Y. Taufiq-Yap, M. K. Danquah and R. Harun, *Energy Sustain. Soc.*, **2016**, 6, 16-29.

7.   C. Gokcol, B. Dursun, B. Alboyaci and E. Sunan, *Energy Policy*, **2009**, 37, 424-431.

8.   N. Komerath and P. Komerath, *Phys. Procedia*, **2011**, 20, 255-269.

9.   O. Okoro and T. Madueme, *Int. J. Sustain. Energy*, **2006**, 25, 23-31.

10.   M. C. Fuller, S. C. Portis and D. M. Kammen, *Environ. Sci. Policy Sustain. Dev.*, **2009**, 51, 22-33.

11.   K. Sangani, *Eng. Technol.*, **2007**, 2, 36-38.

12.   S. Sharma, K. K. Jain and A. Sharma, *Mater. Sci. Appl.*, **2015**, 6, 1145-1155.

13.   S. Zhang, X. Pan, H. Jiao, W. Deng, J. Xu, Y. Chen, P. P. Altermatt, Z. Feng and P. J. Verlinden, *IEEE J. Photovolt.*, **2016**, 6, 145-152.

14.   K. Chopra, P. Paulson and V. Dutta, *Prog. Photovolt. Res. Appl.*, **2004**, 12, 69-92.

15.   J. Major, R. Treharne, L. Phillips and K. Durose, *Nature*, **2014**, 511, 334-337.

16.   S. Khosroabadi, S. Keshmiri and S. Marjani, *J. Eur. Opt. Soc. Rapid Publ.*, **2014**, 9, 14052-14058.

17.   M. Kaur and H. Singh, *Int. J. Core Eng. Manag.*, **2016**, 3, 15-23.

18.   Q. Guo, G. M. Ford, W.-C. Yang, B. C. Walker, E. A. Stach, H. W. Hillhouse and R. Agrawal, *J. Am. Chem. Soc.*, **2010**, 132, 17384-17386.

19.   G. Li, R. Zhu and Y. Yang, *Nat. Photonics*, **2012**, 6, 153-159.

20.   Y. Liu, J. Zhao, Z. Li, C. Mu, W. Ma, H. Hu, K. Jiang, H. Lin, H. Ade and H. Yan, *Nat. commun.*, **2014**, 5, 5293-5301.

21.   J. D. Chen, C. Cui, Y. Q. Li, L. Zhou, Q. D. Ou, C. Li, Y. Li and J. X. Tang, *Adv. Mater.*, **2015**, 27, 1035-1041.

22.   W. Guter, J. Schöne, S. P. Philipps, M. Steiner, G. Siefer, A. Wekkeli, E. Welser, E. Oliva, A. W. Bett and F. Dimroth, *Appl. Phys. Lett.*, **2009**, 94, 223504-223508.

23.   M. Hosoya, H. Oooka, H. Nakao, S. Mori, T. Gotanda, N. Shida, M. Saito, Y. Nakano and K. Todori, *Abstract O-PV-6-2, Grand Renewable Energy Conference*, **2014**, 2, 21-37.

24.   L. Wei, P. Wang, Y. Yang, Z. Zhan, Y. Dong, W. Song and R. Fan, *Inorg. Chem. Front.*, **2018**, 5, 54-62.

25. M. Freitag, J. Teuscher, Y. Saygili, X. Zhang, F. Giordano, P. Liska, J. Hua, S. M. Zakeeruddin, J.-E. Moser and M. Grätzel, *Nat. Photonics*, **2017**, 11, 372-378.

26. S. Suhaimi, M. M. Shahimin, Z. Alahmed, J. Chyský and A. Reshak, *Int. J. Electrochem. Sci.*, **2015**, 10, 2859-2871.

27. A. M. Bagher, M. M. A. Vahid and M. Mohsen, *Am. J. Opt. Photonics*, **2015**, 3, 94-113.

28. Y. Chiba, A. Islam, Y. Watanabe, R. Komiya, N. Koide and L. Han, *Jpn. J. Appl. Phys.*, **2006**, 45, L638-L642.

29. A. Mishra, M. K. Fischer and P. Bäuerle, *Angew. Chem. Int. Ed.*, **2009**, 48, 2474-2499.

30. J. Wu, Z. Lan, J. Lin, M. Huang, Y. Huang, L. Fan and G. Luo, *Chem. Rev.*, **2015**, 115, 2136-2173.

31. M. Wu and T. Ma, *J. Phys. Chem. C*, **2014**, 118, 16727-16742.

32. D. Wei, *Int. J. Mol. Sci.*, **2010**, 11, 1103-1113.

33. A. Hagfeldt, G. Boschloo, L. Sun, L. Kloo and H. Pettersson, *Chem. Rev.*, **2010**, 110, 6595-6663.

34. P. Uthirakumar, *Solar cells - dye-sensitized devices: Fabrication of ZnO based dye-sensitized solar cells*, IntechOpen, India, 1st edn., **2011**,1, 437-455.

35. J. R. Durrant, S. A. Haque and E. Palomares, *Chem. Commun.*, **2006**, 31, 3279-3289.

36. F. Lenzmann, J. Krueger, S. Burnside, K. Brooks, M. Grätzel, D. Gal, S. Rühle and D. Cahen, *J. Phys. Chem. B*, **2001**, 105, 6347-6352.

37. Y. Kanai and C. J. Grossman, *Nano Lett.*, **2007**, 7, 1967-1972.

38. J. Stinchcombe, A. Pbnicaud, P. Bhyrappa, D. W. P. Boyd and A. C. Reed, *J. Am. Chem. Soc.*, **1993**, 115, 5212-5217.

39. L. Dai, *Acc. Chem. Res.*, **2013**, 46, 31-42.

40. C. Hu, D. Liu, Y. Xiao and L. Dai, *Prog. Nat. Sci.-Mater.*, **2018**, 28, 121-132.

41. M. J. Ju, I.-Y. Jeon, H. M. Kim, J. I. Choi, S.-M. Jung, J.-M. Seo, I. T. Choi, S. H. Kang, H. S. Kim, M. J. Noh, J.-J. Lee, H. Y. Jeong, H. K. Kim, Y.-H. Kim and J.-B. Baek, *Sci. Adv.*, **2016**, 56, 1-8.

42. A. Hauch and A. Georg, *Electrochim. Acta*, **2001**, 46, 3457-3466.

43. Z. Huang, X. Liu, K. Li, D. Li, Y. Luo, H. Li, W. Song, L. Chen and Q. Meng, *Electrochem. Commun.*, **2007**, 9, 596-598.

44. J. G. Nam, Y. J. Park, B. S. Kim and J. S. Lee, *Scr. Mater.*, **2010**, 62, 148-150.

45. A. Scalia, F. Bella, A. Lamberti, S. Bianco, C. Gerbaldi, E. Tresso and C. F. Pirri, *J. Power Sources*, **2017**, 359, 311-321.

46. J. Huo, J. Wu, M. Zheng, Y. Tu and Z. Lan, *RSC Adv.*, **2015**, 5, 83029-83035.

47. V.-D. Dao and H.-S. Choi, *ACS Appl. Mater. Interfaces*, **2015**, 8, 1004-1010.

48. Y. Xiao and G. Han, *J. Power Sources*, **2015**, 294, 8-15.

49. M. Moharana and A. Mallik, *Electrochim. Acta*, **2013**, 98, 1-10.

50. C. Zhong, W. B. Hu and Y. F. Cheng, *J. Power Sources*, **2011**, 196, 8064-8072.

51. Z. Tang, J. Wu, M. Zheng, J. Huo and Z. Lan, *Nano Energy*, **2013**, 2, 622-627.

52. M.-S. Wu, C.-Y. Chen, Y.-R. Chen and H.-C. Shih, *Electrochim. Acta*, **2016**, 215, 50-56.

53. Y.-C. Hsu, G.-L. Chen and R.-H. Lee, *J. Polym. Res.*, **2014**, 21, 440-449.

54. B. Anothumakkool, I. Agrawal, S. N. Bhange, R. Soni, O. Game, S. B. Ogale and S. Kurungot, *ACS Appl. Mater. Interfaces*, **2015**, 8, 553-562.

55. R. S. Moraes, E. Saito, D. M. G. Leite, M. Massi and A. S. da Silva Sobrinho, *Appl. Surf. Sci.*, **2016**, 364, 229-234.

56. X.-Y. Cheng, Z.-J. Zhou, Z.-L. Hou, W.-H. Zhou and S.-X. Wu, *Sci. Adv. Mater.*, **2013**, 5, 1193-1198.

57. J. S. Kang, M.-A. Park, J.-Y. Kim, S. H. Park, D. Y. Chung, S.-H. Yu, J. Kim, J. Park, J.-W. Choi and K. J. Lee, *Sci. Rep.*, **2015**, 5, 10450-10461.

58. J. Wu, Z. Lan, J. Lin, M. Huang, Y. Huang, L. Fan, G. Luo, Y. Lin, Y. Xie and Y. Wei, *Chem. Soc. Rev.*, **2017**, 46, 5975-6023.

59. F. Gong, H. Wang, X. Xu, G. Zhou and Z.-S. Wang, *J. Am. Chem. Soc.*, **2012**, 134, 10953-10958.

60. S. I. Cha, B. K. Koo, S. Seo and D. Y. Lee, *J. Mater. Chem.*, **2010**, 20, 659-662.

61. B. Lei, G. Li and X. Gao, *J. Mater. Chem. A*, **2014**, 2, 3919-3925.

62. M.-H. Yeh, L.-Y. Lin, C.-P. Lee, H.-Y. Wei, C.-Y. Chen, C.-G. Wu, R. Vittal and K.-C. Ho, *J. Mater. Chem.*, **2011**, 21, 19021-19029.

63. X. Fang, T. Ma, M. Akiyama, G. Guan, S. Tsunematsu and E. Abe, *Thin Solid Films*, **2005**, 472, 242-245.

64. M. Ikegami, K. Miyoshi, T. Miyasaka, K. Teshima, T. Wei, C. Wan and Y. Wang, *Appl. Phys. Lett.*, **2007**, 90, 153122-153126.

65. G. Li, J. Song, G. Pan and X. Gao, *Energy Environ. Sci.*, **2011**, 4, 1680-1683.

66. G. Yue, J. Wu, Y. Xiao, M. Huang, J. Lin, L. Fan and Z. Lan, *Electrochim. Acta*, **2013**, 92, 64-70.

67. Y.-L. Lee, C.-L. Chen, L.-W. Chong, C.-H. Chen, Y.-F. Liu and C.-F. Chi, *Electrochem. Commun.*, **2010**, 12, 1662-1665.

68. W. J. Lee, E. Ramasamy, D. Y. Lee and J. S. Song, *Sol. Energy Mater. Sol. Cells*, **2008**, 92, 814-818.

69. S.-S. Kim, Y.-C. Nah, Y.-Y. Noh, J. Jo and D.-Y. Kim, *Electrochim. Acta*, **2006**, 51, 3814-3819.

70. X. Fang, T. Ma, G. Guan, M. Akiyama, T. Kida and E. Abe, *J. Electroanal. Chem.*, **2004**, 570, 257-263.

71. G. Calogero, P. Calandra, A. Irrera, A. Sinopoli, I. Citro and G. Di Marco, *Energ Environ. Sci.*, **2011**, 4, 1838-1844.

72. M.-Y. Yen, C.-C. Teng, M.-C. Hsiao, P.-I. Liu, W.-P. Chuang, C.-C. M. Ma, C.-K. Hsieh, M.-C. Tsai and C.-H. Tsai, *J. Mater. Chem.*, **2011**, 21, 12880-12888.

73. K.-C. Huang, Y.-C. Wang, R.-X. Dong, W.-C. Tsai, K.-W. Tsai, C.-C. Wang, Y.-H. Chen, R. Vittal, J.-J. Lin and K.-C. Ho, *J. Mater. Chem.*, **2010**, 20, 4067-4073.

74. B. Zhang, D. Wang, Y. Hou, S. Yang, X. H. Yang, J. H. Zhong, J. Liu, H. F. Wang, P. Hu and H. J. Zhao, *Sci. Rep.*, **2013**, 3, 1836-1843.

75. E. Olsen, G. Hagen and S. Eric Lindquist, *Sol. Energy Mater. Sol. Cells*, **2000**, 63, 267-273.

76. X. Deng, Y. Wu, J. Dai, D. Kang and D. Zhang, *Phys. Lett.*, **2011**, 375, 3890-3894.

77. L. Ci, L. Song, C. Jin, D. Jariwala, D. Wu, Y. Li, A. Srivastava, Z. F. Wang, K. Storr, L. Balicas, F. Liu and P. M. Ajayan, *Nat. Mater.*, **2010**, 9, 430-435.

78. X. Xin, M. He, W. Han, J. Jung and Z. Lin, *Angew. Chem. Int. Ed.*, **2011**, 50, 11739-11742.

79. C. Yasuo, I. Ashraful, W. Yuki, K. Ryoichi, K. Naoki and H. Liyuan, *Jpn. J. Appl. Phys.*, **2006**, 45, L638-L642.

80. C.-T. Hsieh, B.-H. Yang and J.-Y. Lin, *Carbon*, **2011**, 49, 3092-3097.

81. K. Suzuki, M. Yamaguchi, M. Kumagai and S. Yanagida, *Chem. Lett.*, **2002**, 32, 28-29.

82. X. Hu, K. Huang, D. Fang and S. Liu, *Mater. Sci. Eng. B*, **2011**, 176, 431-435.

83. J. D. Roy-Mayhew and I. A. Aksay, *Chem. Rev.*, **2014**, 114, 6323-6348.

84. D. Chung, *J. Mater. Sci.*, **2002**, 37, 1475-1489.

85. M. J. Allen, V. C. Tung and R. B. Kaner, *Chem. Rev.*, **2010**, 110, 132-145.

86. K. S. Novoselov, A. K. Geim, S. V. Morozov, D. Jiang, Y. Zhang, S. V. Dubonos, I. V. Grigorieva and A. A. Firsov, *Science*, **2004**, 306, 666-669.

87. X. Miao, S. Tongay, M. K. Petterson, K. Berke, A. G. Rinzler, B. R. Appleton and A. F. Hebard, *Nano Lett.*, **2012**, 12, 2745-2750.

88. A. Aqel, K. Abou El-Nour, R. Ammar and A. Al-Warthan, *Arab. J. Chem.*, **2012**, 5, 1-23.

89. E. V. Castro, K. Novoselov, S. Morozov, N. Peres, J. L. Dos Santos, J. Nilsson, F. Guinea, A. Geim and A. C. Neto, *Phys. Rev. Lett.*, **2007**, 99, 216802-216806.

90. J. C. Meyer, A. K. Geim, M. I. Katsnelson, K. S. Novoselov, T. J. Booth and S. Roth, *Nature*, **2007**, 446, 60-63.

91. H. P. Boehm, R. Setton and E. Stumpp, *Pure Appl. Chem.*, **1994**, 66, 1893-1901.

92. W. Zhu, V. Perebeinos, M. Freitag and P. Avouris, *Phys. Rev. B*, **2009**, 80, 235402-235410.

93. M.-N. Lu, C.-Y. Chang, T.-C. Wei and J.-Y. Lin, *J. Nanomater.*, **2016**, 2016, 1-21.

94. M. Koshino and T. Ando, *Phys. Rev. B*, **2007**, 76, 085425.

95. T. Ohta, A. Bostwick, T. Seyller, K. Horn and E. Rotenberg, *Science*, **2006**, 313, 951-954.

96. Y. Zhang, T.-T. Tang, C. Girit, Z. Hao, M. C. Martin, A. Zettl, M. F. Crommie, Y. R. Shen and F. Wang, *Nature*, **2009**, 459, 820-823.

97. X. Tong, Q. Wei, X. Zhan, G. Zhang and S. Sun, *Catalysts*, **2016**, 7, 1-16.

98. J. Shen, Y. Zhu, X. Yang and C. Li, *Chem. Commun.*, **2012**, 48, 3686-3699.

99. S. Guo and S. Dong, *Chem. Soc. Rev.*, **2011**, 40, 2644-2672.

100. X. Yan, X. Cui and L.-s. Li, *J. Am. Chem. Soc.*, **2010**, 132, 5944-5945.

101. J. Duan, S. Chen, M. Jaroniec and S. Z. Qiao, *ACS Catal.*, **2015**, 5, 5207-5234.

102. K. A. Ritter and J. W. Lyding, *Nat. Mater.*, **2009**, 8, 235-242.

103. S. Morozov, K. Novoselov, M. Katsnelson, F. Schedin, D. Elias, J. A. Jaszczak and A. Geim, *Phys. Rev. Lett.*, **2008**, 100, 016602-016606.

104. P. Avouris, *Nano Lett.*, **2010**, 10, 4285-4294.

105. G. Xie, K. Zhang, B. Guo, Q. Liu, L. Fang and J. R. Gong, *Adv. Mater.*, **2013**, 25, 3820-3839.

106. C. Berger, Z. Song, X. Li, X. Wu, N. Brown, C. Naud, D. Mayou, T. Li, J. Hass and A. N. Marchenkov, *Science*, **2006**, 312, 1191-1196.

107. D. R. Cooper, B. D'Anjou, N. Ghattamaneni, B. Harack, M. Hilke, A. Horth, N. Majlis, M. Massicotte, L. Vandsburger and E. Whiteway, *ISRN Condens. Matter Phys.*, **2012**, 2012, 1-56.

108. A. C. Neto, F. Guinea, N. M. Peres, K. S. Novoselov and A. K. Geim, *Rev. Mod. Phys.*, **2009**, 81, 109-120.

109. J. Liu, J. Tang and J. J. Gooding, *J. Mater. Chem.*, **2012**, 22, 12435-12452.

110. S. Niyogi, E. Bekyarova, M. E. Itkis, H. Zhang, K. Shepperd, J. Hicks, M. Sprinkle, C. Berger, C. N. Lau and W. A. Deheer, *Nano Lett.*, **2010**, 10, 4061-4066.

111. Y.-C. Chang and W.-H. Chiang, *Adv. Struct. Mater.*, **2016**, 1, 103-133.

112. Y. Wen, C. Huang, L. Wang and D. Hulicova-Jurcakova, *Sci. Bull.*, **2014**, 59, 2102-2121.

113. J. Liang, Y. Huang, L. Zhang, Y. Wang, Y. Ma, T. Guo and Y. Chen, *Adv. Funct. Mater.*, **2009**, 19, 2297-2302.

114. M. A. Rafiee, J. Rafiee, Z. Wang, H. Song, Z. Yu and N. Koratkar, *ACS Nano*, **2009**, 3, 3884-3890.

115. J. Liu, W. Yang, H. M. Zareie, J. J. Gooding and T. P. Davis, *Macromolecules*, **2009**, 42, 2931-2939.

116. P. Sutter, J. T. Sadowski and E. A. Sutter, *J. Am. Chem. Soc.*, **2010**, 132, 8175-8179.

117. T. Sreeprasad, M. S. Maliyekkal, K. Deepti, K. Chaudhari, P. L. Xavier and T. Pradeep, *ACS Appl. Mater. Interfaces*, **2011**, 3, 2643-2654.

118. T. H. Han, W. J. Lee, D. H. Lee, J. E. Kim, E. Y. Choi and S. O. Kim, *Adv. Mater.*, **2010**, 22, 2060-2064.

119. X. Li, H. Wang, J. T. Robinson, H. Sanchez, G. Diankov and H. Dai, *J. Am. Chem. Soc.*, **2009**, 131, 15939-15944.

120. X. Yang, X. Zhang, Z. Liu, Y. Ma, Y. Huang and Y. Chen, *J. Phys. Chem. C*, **2008**, 112, 17554-17558.

121. A. V. Raghu, Y. R. Lee, H. M. Jeong and C. M. Shin, *Macromol. Chem. Phys.*, **2008**, 209, 2487-2493.

122. M. Steenackers, A. M. Gigler, N. Zhang, F. Deubel, M. Seifert, L. H. Hess, C. H. Y. X. Lim, K. P. Loh, J. A. Garrido and R. Jordan, *J. Am. Chem. Soc.*, **2011**, 133, 10490-10498.

123. J. Kim, L. J. Cote, F. Kim and J. Huang, *J. Am. Chem. Soc.*, **2009**, 132, 260-267.

124. L. Yan, Y. B. Zheng, F. Zhao, S. Li, X. Gao, B. Xu, P. S. Weiss and Y. Zhao, *Chem. Soc. Rev.*, **2012**, 41, 97-114.

125. G. M. Scheuermann, L. Rumi, P. Steurer, W. Bannwarth and R. Mülhaupt, *J. Am. Chem. Soc.*, **2009**, 131, 8262-8270.

126. M. J. McAllister, J.-L. Li, D. H. Adamson, H. C. Schniepp, A. A. Abdala, J. Liu, M. Herrera-Alonso, D. L. Milius, R. Car and R. K. Prud'homme, *Chem. Mater.*, **2007**, 19, 4396-4404.

127. S. Yang, L. Zhi, K. Tang, X. Feng, J. Maier and K. Müllen, *Adv. Funct. Mater.*, **2012**, 22, 3634-3640.

128. X. Wang, G. Sun, P. Routh, D.-H. Kim, W. Huang and P. Chen, *Chem. Soc. Rev.*, **2014**, 43, 7067-7098.

129. W. Gao, L. B. Alemany, L. Ci and P. M. Ajayan, *Nat. Chem.*, **2009**, 1, 403-408.

130. H. J. Shin, K. K. Kim, A. Benayad, S. M. Yoon, H. K. Park, I. S. Jung, M. H. Jin, H. K. Jeong, J. M. Kim and J. Y. Choi, *Adv. Funct. Mater.*, **2009**, 19, 1987-1992.

131. T. Szabó, O. Berkesi, P. Forgó, K. Josepovits, Y. Sanakis, D. Petridis and I. Dékány, *Chem. Mater.*, **2006**, 18, 2740-2749.

132. R. Balog, B. Jørgensen, L. Nilsson, M. Andersen, E. Rienks, M. Bianchi, M. Fanetti, E. Lægsgaard, A. Baraldi and S. Lizzit, *Nat. Mater.*, **2010**, 9, 315-319.

133. Z.-S. Wu, W. Ren, L. Xu, F. Li and H.-M. Cheng, *ACS Nano*, **2011**, 5, 5463-5471.

134. P. Blake, P. D. Brimicombe, R. R. Nair, T. J. Booth, D. Jiang, F. Schedin, L. A. Ponomarenko, S. V. Morozov, H. F. Gleeson and E. W. Hill, *Nano Lett.*, **2008**, 8, 1704-1708.

135. A. J. Samuels and J. D. Carey, *ACS Nano*, **2013**, 7, 2790-2799.

136. T. Wehling, K. Novoselov, S. Morozov, E. Vdovin, M. Katsnelson, A. Geim and A. Lichtenstein, *Nano Lett.*, **2008**, 8, 173-177.

137. W. Chen, D. Qi, X. Gao and A. T. S. Wee, *Prog. Surf. Sci.*, **2009**, 84, 279-321.

138. W. Chen, S. Chen, D. C. Qi, X. Y. Gao and A. T. S. Wee, *J. Am. Chem. Soc.*, **2007**, 129, 10418-10422.

139. F. Schedin, A. Geim, S. Morozov, E. Hill, P. Blake, M. Katsnelson and K. Novoselov, *Nat. Mater.*, **2007**, 6, 652-655.

140. J. Ristein, *Science*, **2006**, 313, 1057-1060.

141. O. Leenaerts, B. Partoens and F. Peeters, *Phys. Rev. B*, **2008**, 77, 125416-125422.

142. R. B. Pontes, A. Fazzio and G. M. Dalpian, *Phys. Rev. B*, **2009**, 79, 033412-033416.

143. H. Wang, Q. Wang, Y. Cheng, K. Li, Y. Yao, Q. Zhang, C. Dong, P. Wang, U. Schwingenschlögl, W. Yang and X. X. Zhang, *Nano Lett.*, **2012**, 12, 141-144.

144. F. Joucken, Y. Tison, J. Lagoute, J. Dumont, D. Cabosart, B. Zheng, V. Repain, C. Chacon, Y. Girard and A. R. Botello-Méndez, *Phys. Rev. B*, **2012**, 85, 161408-161413.

145. I.-Y. Jeon, Y.-R. Shin, G.-J. Sohn, H.-J. Choi, S.-Y. Bae, J. Mahmood, S.-M. Jung, J.-M. Seo, M.-J. Kim, D. Wook Chang, L. Dai and J.-B. Baek, *Proc. Natl. Acad. Sci. USA*, **2012**, 109, 5588-5593.

146. C.-K. Chang, S. Kataria, C.-C. Kuo, A. Ganguly, B.-Y. Wang, J.-Y. Hwang, K.-J. Huang, W.-H. Yang, S.-B. Wang and C.-H. Chuang, *ACS Nano*, **2013**, 7, 1333-1341.

147. X. Lu, J. Wu, T. Lin, D. Wan, F. Huang, X. Xie and M. Jiang, *J. Mater. Chem.*, **2011**, 21, 10685-10689.

148. D. Deng, X. Pan, L. Yu, Y. Cui, Y. Jiang, J. Qi, W.-X. Li, Q. Fu, X. Ma, Q. Xue, G. Sun and X. Bao, *Chem. Mater.*, **2011**, 23, 1188-1193.

149. P. Wu, Z. Cai, Y. Gao, H. Zhang and C. Cai, *Chem. Commun.*, **2011**, 47, 11327-11329.

150. P. Wu, Y. Qian, P. Du, H. Zhang and C. Cai, *J. Mater. Chem.*, **2012**, 22, 6402-6412.

151. H. M. Jeong, J. W. Lee, W. H. Shin, Y. J. Choi, H. J. Shin, J. K. Kang and J. W. Choi, *Nano Lett.*, **2011**, 11, 2472-2477.

152. N. Li, Z. Wang, K. Zhao, Z. Shi, Z. Gu and S. Xu, *Carbon*, **2010**, 48, 255-259.

153. E. J. Duplock, M. Scheffler and P. J. D. Lindan, *Phys. Rev. Lett.*, **2004**, 92, 225502-225520.

154. J. L. Cheng, C. Salazar and J. E. Sipe, *Phys. Rev. B*, **2013**, 88, 045438-045445.

155. A. G. Kannan, J. Zhao, S.-G. Jo, Y. S. Kang and D.-W. Kim, *J. Mater. Chem. A*, **2018**, 2, 12232-12239.

156. D. R. Dreyer, S. Park, C. W. Bielawski and R. S. Ruoff, *Chem. Soc. Rev.*, **2010**, 39, 228-240.

157. R. Garg, N. K. Dutta and N. R. Choudhury, *Nanomaterials*, **2014**, 4, 267-300.

158. D. W. Lee and J. W. Seo, *J. Phys. Chem. C*, **2011**, 115, 2705-2708.

159. O. C. Compton and S. T. Nguyen, *Small*, **2010**, 6, 711-723.

160. Y. L. Zhong, Z. Tian, G. P. Simon and D. Li, *Mater. Today*, **2015**, 18, 73-78.

161. B. C. Brodie, *Phil. Trans. R Soc. Lond.*, **1859**, 149, 249-259.

162. L. Staudenmaier, *Eur. J. Inorg. Chem.*, **1898**, 31, 1481-1487.

163. U. Hofmann and E. König, *Z. Anorg. Allg. Chem.*, **1937**, 234, 311-336.

164. W. S. Hummers Jr and R. E. Offeman, *J. Am. Chem. Soc.*, **1958**, 80, 1339-1339.

165. N. I. Zaaba, K. L. Foo, U. Hashim, S. J. Tan, W.-W. Liu and C. H. Voon, *Procedia Eng.*, **2017**, 184, 469-477.

166. H. Yu, B. Zhang, C. Bulin, R. Li and R. Xing, *Sci. Rep.*, **2016**, 6, 36143-36150.

167. D. C. Marcano, D. V. Kosynkin, J. M. Berlin, A. Sinitskii, Z. Sun, A. Slesarev, L. B. Alemany, W. Lu and J. M. Tour, *ACS Nano*, **2010**, 4, 4806-4814.

168. D. Chen, H. Feng and J. Li, *Chem. Rev.*, **2012**, 112, 6027-6053.

169. J. Xu, G. Dong, C. Jin, M. Huang and L. Guan, *ChemSusChem*, **2013**, 6, 493-499.

170. A. Ambrosi, C. K. Chua, A. Bonanni and M. Pumera, *Chem. Mater.*, **2012**, 24, 2292-2298.

171. I. K. Moon, J. Lee, R. S. Ruoff and H. Lee, *Nat. commun.*, **2010**, 1, 1-6.

172. E. Tegou, G. Pseiropoulos, M. K. Filippidou and S. Chatzandroulis, *Microelectron. Eng.*, **2016**, 159, 146-150.

173. N. Garino, A. Sacco, M. Castellino, J. A. Muñoz-Tabares, A. Chiodoni, V. Agostino, V. Margaria, M. Gerosa, G. Massaglia and M. Quaglio, *ACS Appl. Mater. Interfaces*, **2016**, 8, 4633-4643.

174. Y. Matsumoto, M. Koinuma, S. Y. Kim, Y. Watanabe, T. Taniguchi, K. Hatakeyama, H. Tateishi and S. Ida, *ACS Appl. Mater. Interfaces*, **2010**, 2, 3461-3466.

175. Y. H. Ng, A. Iwase, A. Kudo and R. Amal, *J. Phys. Chem. Lett.*, **2010**, 1, 2607-2612.

176. V. H. Pham, T. V. Cuong, S. H. Hur, E. Oh, E. J. Kim, E. W. Shin and J. S. Chung, *J. Mater. Chem.*, **2011**, 21, 3371-3377.

177. C. Nethravathi and M. Rajamathi, *Carbon*, **2008**, 46, 1994-1998.

178. S. Dubin, S. Gilje, K. Wang, V. C. Tung, K. Cha, A. S. Hall, J. Farrar, R. Varshneya, Y. Yang and R. B. Kaner, *ACS Nano*, **2010**, 4, 3845-3852.

179. D. Long, W. Li, L. Ling, J. Miyawaki, I. Mochida and S.-H. Yoon, *Langmuir*, **2010**, 26, 16096-16102.

180. A. Mathkar, D. Tozier, P. Cox, P. Ong, C. Galande, K. Balakrishnan, A. Leela Mohana Reddy and P. M. Ajayan, *J. Phys. Chem. Lett.*, **2012**, 3, 986-991.

181. M. F. R. Hanifah, J. Jaafar, M. Aziz, A. Ismail, M. Othman and M. A. Rahman, *Bull. Mater. Sci.*, **2015**, 38, 1569-1576.

182. S. Pei and H.-M. Cheng, *Carbon*, **2012**, 50, 3210-3228.

183. G. Eda and M. Chhowalla, *Adv. Mater.*, **2010**, 22, 2392-2415.

184. R. Maiti, A. Midya, C. Narayana and S. Ray, *Nanotechnology*, **2014**, 25, 495704-495714.

185. T. A. Pham, J. Kim, J. S. Kim and Y. T. Jeong, *Colloids Surf. A Physicochem. Eng. Asp.*, **2011**, 386, 195-199.

186. Z. Lei, L. Lu and X. Zhao, *Energy Environ. Sci.*, **2012**, 5, 6391-6399.

187. S. Stankovich, D. A. Dikin, R. D. Piner, K. A. Kohlhaas, A. Kleinhammes, Y. Jia, Y. Wu, S. T. Nguyen and R. S. Ruoff, *Carbon*, **2007**, 45, 1558-1565.

188. J. Zhang, H. Yang, G. Shen, P. Cheng, J. Zhang and S. Guo, *Chem. Commun.*, **2010**, 46, 1112-1114.

189. X. Fan, W. Peng, Y. Li, X. Li, S. Wang, G. Zhang and F. Zhang, *Adv. Mater.*, **2008**, 20, 4490-4493.

190. Z. Li, Y. Yao, Z. Lin, K.-S. Moon, W. Lin and C. Wong, *J. Mater. Chem.*, **2010**, 20, 4781-4783.

191. X. Mei and J. Ouyang, *Carbon*, **2011**, 49, 5389-5397.

192. M.-H. Yeh, L.-Y. Lin, L.-Y. Chang, Y.-A. Leu, W.-Y. Cheng, J.-J. Lin and K.-C. Ho, *ChemPhysChem*, **2014**, 15, 1175-1181.

193. L. J. Cote, R. Cruz-Silva and J. Huang, *J. Am. Chem. Soc.*, **2009**, 131, 11027-11032.

194. C. T. Chien, S. S. Li, W. J. Lai, Y. C. Yeh, H. A. Chen, I. Chen, L. C. Chen, K. H. Chen, T. Nemoto and S. Isoda, *Angew. Chem. Int. Ed.*, **2012**, 51, 6662-6666.

195. P. Wu, P. Du, H. Zhang and C. Cai, *Phys. Chem. Chem. Phys.*, **2013**, 15, 6920-6928.

196. Z. Xing, Z. Ju, Y. Zhao, J. Wan, Y. Zhu, Y. Qiang and Y. Qian, *Sci. Rep.*, **2016**, 6, 26146-26156.

197. C. Zhang, L. Fu, N. Liu, M. Liu, Y. Wang and Z. Liu, *Adv. Mater.*, **2011**, 23, 1020-1024.

198. Y. Shao, S. Zhang, M. H. Engelhard, G. Li, G. Shao, Y. Wang, J. Liu, I. A. Aksay and Y. Lin, *J. Mater. Chem.*, **2010**, 20, 7491-7496.

199. E. J. Biddinger, D. von Deak and U. S. Ozkan, *Top. Catal.*, **2009**, 52, 1566-1574.

200. C. Ewels and M. Glerup, *J. Nanosci. Nanotechnol.*, **2005**, 5, 1345-1363.

201. S. Kundu, T. C. Nagaiah, W. Xia, Y. Wang, S. V. Dommele, J. H. Bitter, M. Santa, G. Grundmeier, M. Bron and W. Schuhmann, *J. Phys. Chem. C*, **2009**, 113, 14302-14310.

202. M. Groves, A. Chan, C. Malardier-Jugroot and M. Jugroot, *Chem. Phys. Lett.*, **2009**, 481, 214-219.

203. A. Lherbier, X. Blase, Y.-M. Niquet, F. Triozon and S. Roche, *Phys. Rev. Lett.*, **2008**, 101, 036808-036812.

204. M. Wu, C. Cao and J. Z. Jiang, *Nanotechnology*, **2010**, 21, 505202-505209.

205. D. Wei, Y. Liu, Y. Wang, H. Zhang, L. Huang and G. Yu, *Nano Lett.*, **2009**, 9, 1752-1758.

206. A. Yanilmaz, A. Tomak, B. Akbali, C. Bacaksiz, E. Ozceri, O. Ari, R. T. Senger, Y. Selamet and H. M. Zareie, *RSC Adv.*, **2017**, 7, 28383-28392.

207. M. Du, J. Sun, J. Chang, F. Yang, L. Shi and L. Gao, *RSC Adv.*, **2014**, 4, 42412-42417.

208. Y.-F. Lu, S.-T. Lo, J.-C. Lin, W. Zhang, J.-Y. Lu, F.-H. Liu, C.-M. Tseng, Y.-H. Lee, C.-T. Liang and L.-J. Li, *ACS Nano*, **2013**, 7, 6522-6532.

209. B. Guo, Q. Liu, E. Chen, H. Zhu, L. Fang and J. R. Gong, *Nano Lett.*, **2010**, 10, 4975-4980.

210. D. Geng, Y. Chen, Y. Chen, Y. Li, R. Li, X. Sun, S. Ye and S. Knights, *Energy Environ. Sci.*, **2011**, 4, 760-764.

211. X. Wang, X. Li, L. Zhang, Y. Yoon, P. K. Weber, H. Wang, J. Guo and H. Dai, *Science*, **2009**, 324, 768-771.

212. H. Wang, T. Maiyalagan and X. Wang, *ACS Catal.*, **2012**, 2, 781-794.

213. Z.-H. Sheng, L. Shao, J.-J. Chen, W.-J. Bao, F.-B. Wang and X.-H. Xia, *ACS Nano*, **2011**, 5, 4350-4358.

214. A. Śliwak, B. Grzyb, N. Díez and G. Gryglewicz, *Appl. Surf. Sci.*, **2017**, 399, 265-271.

215. Y. Chen, B. Xie, Y. Ren, M. Yu, Y. Qu, T. Xie, Y. Zhang and Y. Wu, *Nanoscale Res. Lett.*, **2014**, 9, 646-654.

216. M. Alexander, V. Roumen, S. Koen, V. Alexander, Z. Liang, T. Gustaaf Van, V. Annick and H. Chris Van, *Nanotechnology*, **2008**, 19, 305604-305611.

217. I. Janowska, K. Chizari, O. Ersen, S. Zafeiratos, D. Soubane, V. Da Costa, V. Speisser, C. Boeglin, M. Houllé and D. Bégin, *Nano Res.*, **2010**, 3, 126-137.

218. J. Hutchison, N. Kiselev, E. Krinichnaya, A. Krestinin, R. Loutfy, A. Morawsky, V. Muradyan, E. Obraztsova, J. Sloan and S. Terekhov, *Carbon*, **2001**, 39, 761-770.

219. L. Panchakarla, K. Subrahmanyam, S. Saha, A. Govindaraj, H. Krishnamurthy, U. Waghmare and C. Rao, *Adv. Mater.*, **2009**, 21, 4726-4730.

220. S. M. Shinde, E. Kano, G. Kalita, M. Takeguchi, A. Hashimoto and M. Tanemura, *Carbon*, **2016**, 96, 448-453.

221. A. Capasso, T. Dikonimos, F. Sarto, A. Tamburrano, G. De Bellis, M. S. Sarto, G. Faggio, A. Malara, G. Messina and N. Lisi, *Beilstein J. Nanotechnol.*, **2015**, 6, 2028-2038.

222. A. Dadkhah, M. Faradonbeh, A. Rashidi, S. Tasharrofi and F. Mansourkhani, *J. Inorg. Organomet. Polym. Mater.*, **2018**, 28, 1609-1615.

223. N. Bundaleska, J. Henriques, M. Abrashev, A. M. Botelho do Rego, A. M. Ferraria, A. Almeida, F. M. Dias, E. Valcheva, B. Arnaudov, K. K. Upadhyay, M. F. Montemor and E. Tatarova, *Sci. Rep.*, **2018**, 8, 12595-12606.

224. A. Kumar, A. Voevodin, R. Paul, I. Altfeder, D. Zemlyanov, D. N. Zakharov and T. S. Fisher, *Thin Solid Films*, **2013**, 528, 269-273.

225. S. A. Shah, L. Cui, K. Lin, T. Xue, Q. Guo, L. Li, L. Zhang, F. Zhang, F. Hu, X. Wang, H. Wang, X. Chen and S. Cui, *RSC Adv.*, **2015**, 5, 29230-29237.

226. D. Li, X. Duan, H. Sun, J. Kang, H. Zhang, M. O. Tade and S. Wang, *Carbon*, **2017**, 115, 649-658.

227. M.-H. Jiang, D. Cai and N. Tan, *Int. J. Electrochem. Sci.*, **2017**, 12, 7154-7165.

228. M. Rybin, A. Pereaslavtsev, T. Vasilieva, V. Myasnikov, I. Sokolov, A. Pavlova, E. Obraztsova, A. Khomich, V. Ralchenko and E. Obraztsova, *Catrbon*, **2016**, 96, 196-202.

229. H. C. Lee, W.-W. Liu, S.-P. Chai, A. R. Mohamed, C. W. Lai, C.-S. Khe, C. Voon, U. Hashim and N. Hidayah, *Procedia Chem.*, **2016**, 19, 916-921.

230. H. Liu, Y. Liu and D. Zhu, *J. Mater. Chem.*, **2011**, 21, 3335-3345.

231. G. Nandamuri, S. Roumimov and R. Solanki, *Nanotechnology*, **2010**, 21, 145604-145609.

232. Z. Wang, P. Li, Y. Chen, J. Liu, H. Tian, J. Zhou, W. Zhang and Y. Li, *J. Mater. Chem. C*, **2014**, 2, 7396-7401.

233. A. L. M. Reddy, A. Srivastava, S. R. Gowda, H. Gullapalli, M. Dubey and P. M. Ajayan, *ACS Nano*, **2010**, 4, 6337-6342.

234. Z. Jin, J. Yao, C. Kittrell and J. M. Tour, *ACS Nano*, **2011**, 5, 4112-4117.

235. L. Van Nang, N. Van Duy, N. D. Hoa and N. Van Hieu, *J. Electron. Mater.*, **2016**, 45, 839-845.

236. G. Imamura and K. Saiki, *J. Phys. Chem. C*, **2011**, 115, 10000-10005.

237. L. Ci, L. Song, C. Jin, D. Jariwala, D. Wu, Y. Li, A. Srivastava, Z. Wang, K. Storr and L. Balicas, *Nat. Mater.*, **2010**, 9, 430-435.

238. L. Qu, Y. Liu, J.-B. Baek and L. Dai, *ACS Nano*, **2010**, 4, 1321-1326.

239. Y. J. Cho, H. S. Kim, S. Y. Baik, Y. Myung, C. S. Jung, C. H. Kim, J. Park and H. S. Kang, *J. Phys. Chem. C*, **2011**, 115, 3737-3744.

240. Z. Luo, S. Lim, Z. Tian, J. Shang, L. Lai, B. MacDonald, C. Fu, Z. Shen, T. Yu and J. Lin, *J. Mater. Chem.*, **2011**, 21, 8038-8044.

241. C. Zhang, W. Lin, Z. Zhao, P. Zhuang, L. Zhan, Y. Zhou and W. Cai, *Sci. China Phys. Mech.*, **2015**, 58, 107801-107806.

242. E. Bayram, G. Yilmaz and S. Mukerjee, *Appl. Catal. B*, **2016**, 192, 26-34.

243. W.-X. Lv, R. Zhang, T.-L. Xia, H.-M. Bi and K.-Y. Shi, *J. Nanoparticle Res.*, **2011**, 13, 2351-2360.

244. S. Mukherjee and T. Kaloni, *J. Nanoparticle Res.*, **2012**, 14, 1059-1064.

245. S. Agnoli and M. Favaro, *J. Mater. Chem. A*, **2016**, 4, 5002-5025.

246. P. Rani and V. Jindal, *RSC Adv.*, **2013**, 3, 802-812.

247.	R. H. Miwa, T. B. Martins and A. Fazzio, *Nanotechnology*, **2008**, 19, 155708-155716.

248.	R. Faccio, L. Fernández-Werner, H. Pardo, C. Goyenola, O. N. Ventura and Á. W. Mombrú, *J. Phys. Chem. C*, **2010**, 114, 18961-18971.

249.	Y.-B. Tang, L.-C. Yin, Y. Yang, X.-H. Bo, Y.-L. Cao, H.-E. Wang, W.-J. Zhang, I. Bello, S.-T. Lee and H.-M. Cheng, *ACS Nano*, **2012**, 6, 1970-1978.

250.	L. Zhao, M. Levendorf, S. Goncher, T. Schiros, L. Palova, A. Zabet-Khosousi, K. T. Rim, C. Gutierrez, D. Nordlund and C. Jaye, *Nano Lett.*, **2013**, 13, 4659-4665.

251.	Y. A. Kim, K. Fujisawa, H. Muramatsu, T. Hayashi, M. Endo, T. Fujimori, K. Kaneko, M. Terrones, J. Behrends and A. Eckmann, *ACS Nano*, **2012**, 6, 6293-6300.

252.	M. Endo, T. Hayashi, S.-H. Hong, T. Enoki and M. S. Dresselhaus, *J. Appl. Phys.*, **2001**, 90, 5670-5674.

253.	J. Borowiec and J. Zhang, *J. Electrochem. Soc.*, **2015**, 162, B332-B336.

254.	Z. Tian, C. Xu, J. Li, G. Zhu, J. Wu, Z. Shi and Y. Wang, *New J. Chem.*, **2015**, 39, 6907-6913.

255.	L. Zhao, M. Levendorf, S. Goncher, T. Schiros, L. Palova, A. Zabet-Khosousi, K. T. Rim, C. Gutiérrez, D. Nordlund and C. Jaye, *Nano Lett.*, **2013**, 13, 4659-4665.

256.	M. Ovezmyradov, I. V. Magedov, L. V. Frolova, G. Chandler, J. Garcia, D. Bethke, E. A. Shaner and N. G. Kalugin, *J. Nanosci. Nanotechnol.*, **2015**, 15, 4883-4886.

257.	J. M. Tour, *J. Chem. Mater.*, **2014**, 26, 163-171.

258.	L. Panchakarla, K. Subrahmanyam, S. Saha, A. Govindaraj, H. Krishnamurthy, U. Waghmare and C. Rao, *Adv. Mater.*, **2009**, 21, 4726-4730.

259.	S. Li, Z. Wang, H. Jiang, L. Zhang, J. Ren, M. Zheng, L. Dong and L. Sun, *Chem. Commun.*, **2016**, 52, 10988-10991.

260.	Z.-H. Sheng, H.-L. Gao, W.-J. Bao, F.-B. Wang and X.-H. Xia, *J. Mater. Chem.*, **2012**, 22, 390-395.

261.	H. Fang, C. Yu, T. Ma and J. Qiu, *Chem. Commun.*, **2014**, 50, 3328-3330.

262.	M. Telychko, P. Mutombo, M. Ondráček, P. Hapala, F. C. Bocquet, J. Kolorenč, M. Vondráček, P. Jelínek and M. Švec, *ACS Nano*, **2014**, 8, 7318-7324.

263.	D. Y. Usachov, A. V. Fedorov, A. E. Petukhov, O. Y. Vilkov, A. G. Rybkin, M. M. Otrokov, A. Arnau, E. V. Chulkov, L. V. Yashina and M. Farjam, *ACS Nano*, **2015**, 9, 7314-7322.

264.	M. Cattelan, S. Agnoli, M. Favaro, D. Garoli, F. Romanato, M. Meneghetti, A. Barinov, P. Dudin and G. Granozzi, *J. Chem. Mater.*, **2013**, 25, 1490-1495.

265. T. Wu, H. Shen, L. Sun, B. Cheng, B. Liu and J. Shen, *New J. Chem.*, **2012**, 36, 1385-1391.

266. H. Wang, Y. Zhou, D. Wu, L. Liao, S. Zhao, H. Peng and Z. Liu, *Small*, **2013**, 9, 1316-1320.

267. Z. Yang, Z. Yao, G. Li, G. Fang, H. Nie, Z. Liu, X. Zhou, X. a. Chen and S. Huang, *ACS Nano*, **2011**, 6, 205-211.

268. P. A. Denis, *Chem. Phys. Lett.*, **2010**, 492, 251-257.

269. P. A. Denis, R. Faccio and A. W. Mombru, *Chemphyschem*, **2009**, 10, 715-722.

270. Z. Yang, Z. Yao, G. Li, G. Fang, H. Nie, Z. Liu, X. Zhou, X. a. Chen and S. Huang, *ACS Nano*, **2012**, 6, 205-211.

271. F. Hassani, H. Tavakol, F. Keshavarzipour and A. Javaheri, *RSC Adv.*, **2016**, 6, 27158-27163.

272. Y. Xia, Y. Zhu and Y. Tang, *Carbon*, **2012**, 50, 5543-5553.

273. H. L. Poh, P. Šimek, Z. k. Sofer and M. Pumera, *ACS Nano*, **2013**, 7, 5262-5272.

274. C. Liang, Y. Wang and T. Li, *Carbon*, **2015**, 82, 506-512.

275. C. Bautista-Flores, J. Arellano-Peraza, R. Sato-Berrú, E. Camps and D. Mendoza, *Chem. Phys. Lett.*, **2016**, 665, 121-126.

276. W. Kiciński, M. Szala and M. Bystrzejewski, *Carbon*, **2014**, 68, 1-32.

277. H. Gao, Z. Liu, L. Song, W. Guo, W. Gao, L. Ci, A. Rao, W. Quan, R. Vajtai and P. M. Ajayan, *Nanotechnology*, **2012**, 23, 275605-275613.

278. Y. Liu, Y. Ma, Y. Jin, G. Chen and X. Zhang, *J. Electroanal. Chem.*, **2015**, 739, 172-177.

279. Z. W. Liu, F. Peng, H. J. Wang, H. Yu, W. X. Zheng and J. Yang, *Angew. Chem.*, **2011**, 123, 3315-3319.

280. D.-S. Yang, D. Bhattacharjya, M. Y. Song and J.-S. Yu, *Carbon*, **2014**, 67, 736-743.

281. E. Cruz-Silva, F. Lopez-Urias, E. Munoz-Sandoval, B. G. Sumpter, H. Terrones, J.-C. Charlier, V. Meunier and M. Terrones, *ACS Nano*, **2009**, 3, 1913-1921.

282. H.-m. Wang, H.-x. Wang, Y. Chen, Y.-j. Liu, J.-x. Zhao, Q.-h. Cai and X.-z. Wang, *Appl. Surf. Sci.*, **2013**, 273, 302-309.

283. S. Some, J. Kim, K. Lee, A. Kulkarni, Y. Yoon, S. Lee, T. Kim and H. Lee, *Adv. Mater.*, **2012**, 24, 5481-5486.

284. Z. Sun, Z. Yan, J. Yao, E. Beitler, Y. Zhu and J. M. Tour, *Nature*, **2010**, 468, 549-552.

285. W.-C. Yen, H. Medina, J.-S. Huang, C.-C. Lai, Y.-C. Shih, S.-M. Lin, J.-G. Li, Z. M. Wang and Y.-L. Chueh, *J. Phys. Chem. C*, **2014**, 118, 25089-25096.

286. C. Zhang, N. Mahmood, H. Yin, F. Liu and Y. Hou, *Adv. Mater.*, **2013**, 25, 4932-4937.

287. Y. Wen, B. Wang, C. Huang, L. Wang and D. Hulicova-Jurcakova, *Chem. Eur. J.*, **2015**, 21, 80-85.

288. D.-W. Shin, T. S. Kim and J.-B. Yoo, *Mater. Res. Bull.*, **2016**, 82, 71-75.

289. R. Li, Z. Wei, X. Gou and W. Xu, *RSC Adv.*, **2013**, 3, 9978-9984.

290. P. A. Denis, *Comput. Mater. Sci.*, **2013**, 67, 203-206.

291. M. Latorre-Sánchez, A. Primo and H. García, *Angew. Chem. Int. Ed.*, **2013**, 52, 11813-11816.

292. K. Kakaei and A. Balavandi, *J. Colloid Interf. Sci.*, **2016**, 463, 46-54.

293. K. Yang, Y. Li, X. Tan, R. Peng and Z. Liu, *Small*, **2013**, 9, 1492-1503.

294. R. Kalyani and K. Gurunathan, *J. Mater. Sci. Mater. Electron*, **2016**, 27, 10634-10641.

295. I. C. Ciobotaru, S. Polosan and C. C. Ciobotaru, *Inorganica Chim. Acta*, **2018**, 483, 448-453.

296. R. Zbořil, F. Karlický, A. B. Bourlinos, T. A. Steriotis, A. K. Stubos, V. Georgakilas, K. Šafářová, D. Jančík, C. Trapalis and M. Otyepka, *Small*, **2010**, 6, 2885-2891.

297. B. Shen, J. Chen, X. Yan and Q. Xue, *RSC Adv.*, **2012**, 2, 6761-6764.

298. J. Wu, L. Xie, Y. Li, H. Wang, Y. Ouyang, J. Guo and H. Dai, *J. Am. Chem. Soc.*, **2011**, 133, 19668-19671.

299. A. Yaya, C. Ewels, I. Suarez-Martinez, P. Wagner, S. Lefrant, A. Okotrub, L. Bulusheva and P. Briddon, *Phys. Rev. B*, **2011**, 83, 045411-045417.

300. I.-Y. Jeon, H.-J. Choi, M. Choi, J.-M. Seo, S.-M. Jung, M.-J. Kim, S. Zhang, L. Zhang, Z. Xia and L. Dai, *Sci. Rep.*, **2013**, 3, 1810-1817.

301. D. Bouša, M. Pumera, D. Sedmidubský, J. Šturala, J. Luxa, V. Mazánek and Z. Sofer, *Nanoscale*, **2016**, 8, 1493-1502.

302. R. Sharma, S. Khan, V. Goyal, V. Sharma and K. S. Sharma, *Chem. Flat. Mater.*, **2017**, 1, 20-33.

303. B. Muchharla, A. Pathak, Z. Liu, L. Song, T. Jayasekera, S. Kar, R. Vajtai, L. Balicas, P. M. Ajayan and S. Talapatra, *Nano Lett.*, **2013**, 13, 3476-3481.

304. L. Ma, A. H. C. Hart, S. Ozden, R. Vajtai and P. M. Ajayan, *Faraday Discussions*, **2014**, 173, 9-46.

305. Z. S. Wu, A. Winter, L. Chen, Y. Sun, A. Turchanin, X. Feng and K. Müllen, *Adv. Mater.*, **2012**, 24, 5130-5135.

306. G. Bepete, D. Voiry, M. Chhowalla, Z. Chiguvare and N. J. Coville, *Nanoscale*, **2013**, 5, 6552-6557.

307. C. H. Choi, M. W. Chung, H. C. Kwon, S. H. Park and S. I. Woo, *J. Mater. Chem. A*, **2013**, 1, 3694-3699.

308. S. Thomas, T. Deepak, G. Anjusree, T. Arun, S. V. Nair and A. S. Nair, *J. Mater. Chem. A*, **2014**, 2, 4474-4490.

309. Y. Xue, B. Wu, H. Liu, J. Tan, W. Hu and Y. Liu, *Phys. Chem. Chem. Phys.*, **2014**, 16, 20392-20397.

310. Z.-L. Wang, D. Xu, H.-G. Wang, Z. Wu and X.-B. Zhang, *ACS Nano*, **2013**, 7, 2422-2430.

311. T. Wang, L.-X. Wang, D.-L. Wu, W. Xia and D.-Z. Jia, *Sci. Rep.*, **2015**, 5, 9591-9599.

312. Z. Yang, K. Qian, J. Lv, W. Yan, J. Liu, J. Ai, Y. Zhang, T. Guo, X. Zhou and S. Xu, *Sci. Rep.*, **2016**, 6, 27957-27967.

313. T. Xing, Y. Zheng, L. H. Li, B. C. C. Cowie, D. Gunzelmann, S. Z. Qiao, S. Huang and Y. Chen, *ACS Nano*, **2014**, 8, 6856-6862.

314. J. Li, Y. Zhang, X. Zhang, J. Huang, J. Han, Z. Zhang, X. Han, P. Xu and B. Song, *ACS Appl. Mater. Interfaces*, **2017**, 9, 398-405.

315. J. D. Roy-Mayhew, D. J. Bozym, C. Punckt and I. A. Aksay, *ACS Nano*, **2010**, 4, 6203-6211.

316. G. Boschloo and A. Hagfeldt, *Acc. Chem. Res.*, **2009**, 42, 1819-1826.

317. B. E. Hardin, H. J. Snaith and M. D. McGehee, *Nat. Photonics*, **2012**, 6, 162-169.

318. V.-D. Dao, L. L. Larina, H. Suh, K. Hong, J.-K. Lee and H.-S. Choi, *Carbon*, **2014**, 77, 980-992.

319. L. Kavan, J. H. Yum and M. Grätzel, *ACS Nano*, **2010**, 5, 165-172.

320. K. K. Devarepally, *Meet. Abstr.*, **2016**, MA2016-01, 775-782.

321. H. Zheng, C. Y. Neo, X. Mei, J. Qiu and J. Ouyang, *J. Mater. Chem.*, **2012**, 22, 14465-14474.

322. H.-S. Jang, J.-M. Yun, D.-Y. Kim, D.-W. Park, S.-I. Na and S.-S. Kim, *Electrochim. Acta*, **2012**, 81, 301-307.

323. X. Xu, D. Huang, K. Cao, M. Wang, S. M. Zakeeruddin and M. Grätzel, *Sci. Rep.*, **2013**, 3, 1489-1496.

324. C. Nagavolu, K. Susmitha, M. Raghavender, L. Giribabu, K. B. S. Rao, C. Smith, C. Mills, S. Silva and V. Srikanth, *Solar Energy*, **2016**, 137, 143-147.

325. H.-S. Jang, J.-M. Yun, D.-Y. Kim, S.-I. Na and S.-S. Kim, *Surf. Coat. Technol.*, **2014**, 242, 8-13.

326. S. Sarker, K.-S. Lee, H. W. Seo, Y.-K. Jin and D. M. Kim, *Solar Energy*, **2017**, 158, 42-48.

327. M. Zhang and L. Dai, *Nano Energy*, **2012**, 1, 514-517.

328. Y. Xue, J. Liu, H. Chen, R. Wang, D. Li, J. Qu and L. Dai, *Angew. Chem. Int. Ed.*, **2012**, 51, 12124-12127.

329. M.-Y. Yen, C.-K. Hsieh, C.-C. Teng, M.-C. Hsiao, P.-I. Liu, C.-C. M. Ma, M.-C. Tsai, C.-H. Tsai, Y.-R. Lin and T.-Y. Chou, *RSC Adv.*, **2012**, 2, 2725-2728.

330. G. Wang, Y. Fang, Y. Lin, W. Xing and S. Zhuo, *Mater. Res. Bull.*, **2012**, 47, 4252-4256.

331. M. J. Ju, I.-Y. Jeon, J. C. Kim, K. Lim, H.-J. Choi, S.-M. Jung, I. T. Choi, Y. K. Eom, Y. J. Kwon, J. Ko, J.-J. Lee, H. K. Kim and J.-B. Baek, *Adv. Mater.*, **2014**, 26, 3055-3062.

332. C.-A. Lin, C.-P. Lee, S.-T. Ho, T.-C. Wei, Y.-W. Chi, K. P. Huang and J.-H. He, *ACS Photonics*, **2014**, 1, 1264-1269.

333. J. Balamurugan, T. D. Thanh, N. H. Kim and J. H. Lee, *Adv. Mater. Interfaces*, **2016**, 3, 1500348-1500358.

334. Y. Xue, J. M. Baek, H. Chen, J. Qu and L. Dai, *Nanoscale*, **2015**, 7, 7078-7083.

335. S. Hou, X. Cai, H. Wu, X. Yu, M. Peng, K. Yan and D. Zou, *Energy & Environ. Sci.*, **2013**, 6, 3356-3362.

336. M. J. Ju, J. C. Kim, H.-J. Choi, I. T. Choi, S. G. Kim, K. Lim, J. Ko, J.-J. Lee, I.-Y. Jeon and J.-B. Baek, *ACS Nano*, **2013**, 7, 5243-5250.

337. S.-B. Kim, J.-Y. Park, C.-S. Kim, K. Okuyama, S.-E. Lee, H.-D. Jang and T.-O. Kim, *J. Phys. Chem. C*, **2015**, 119, 16552-16559.

338. W. Yang, X. Xu, L. Hou, X. Ma, F. Yang, Y. Wang and Y. Li, *J. Mater. Chem. A*, **2017**, 5, 5952-5960.

339. S.-M. Jung, I. T. Choi, K. Lim, J. Ko, J. C. Kim, J.-J. Lee, M. J. Ju, H. K. Kim and J.-B. Baek, *Chem. Mater.*, **2014**, 26, 3586-3591.

340. A. Ambrosi, C. K. Chua, A. Bonanni and M. Pumera, *Chem. Rev.*, **2014**, 114, 7150-7188.

341. L. Wang, Z. Sofer, P. Šimek, I. Tomandl and M. Pumera, *J. Phys. Chem. C*, **2013**, 117, 23251-23257.

342. Q. Luo, F. Hao, S. Wang, H. Shen, L. Zhao, J. Li, M. Grätzel and H. Lin, *J. Phys. Chem. C*, **2014**, 118, 17010-17018.

343.   X. Meng, C. Yu, X. Song, Z. Liu, B. Lu, C. Hao and J. Qiu, *J. Mater. Chem. A*, **2017**, 5, 2280-2287.

344.   M. N. Mustafa, S. Shafie, Z. Zainal and Y. Sulaiman, *J. Nanomater.*, **2017**, 2017, 1-9.

345.   M. Kaukonen, A. V. Krasheninnikov, E. Kauppinen and R. M. Nieminen, *ACS Catal.*, **2013**, 3, 159-165.

346.   P. Karthika, N. Rajalakshmi and K. Dhathathreyan, *J. Nanosci. Nanotechnol.*, **2013**, 13, 1746-1751.

347.   Z. Wang, P. Li, Y. Chen, J. He, J. Liu, W. Zhang and Y. Li, *J. Power Sources*, **2014**, 263, 246-251.

348.   H.-J. Ahn, I.-H. Kim, J.-C. Yoon, S.-I. Kim and J.-H. Jang, *Chem. Commun.*, **2014**, 50, 2412-2415.

349.   X. Xu, W. Yang, B. Chen, C. Zhou, X. Ma, L. Hou, Y. Tang, F. Yang, G. Ning, L. Zhang and Y. Li, *Appl. Surf. Sci.*, **2017**, 405, 308-315.

350.   I.-Y. Jeon, H. M. Kim, I. T. Choi, K. Lim, J. Ko, J. C. Kim, H.-J. Choi, M. J. Ju, J.-J. Lee, H. K. Kim and J.-B. Baek, *Nano Energy*, **2015**, 13, 336-345.

351.   D. Yu, E. Nagelli, F. Du and L. Dai, *J. Phys. Chem. Lett.*, **2010**, 1, 2165-2173.

352.   S. Das, P. Sudhagar, V. Verma, D. Song, E. Ito, Y. Lee Sang, S. Kang Yong and W. Choi, *Adv. Funct. Mater.*, **2011**, 21, 3729-3736.

353.   A. G. Kannan, J. Zhao, S. G. Jo, Y. S. Kang and D.-W. Kim, *J. Mater. Chem. A*, **2014**, 2, 12232-12239.

354.   X. Xu, W. Yang, Y. Li, Z. Tu, S. Wu, X. Ma, F. Yang, L. Zhang, S. Chen and A. Wang, *Chem. Eng. J.*, **2015**, 267, 289-296.

355.   Z. Yu, Y. Bai, Y. Wang, Y. Liu, Y. Zhao, Y. Liu and K. Sun, *Chem. Eng. J.*, **2017**, 311, 302-309.

356.   Y. Wen, T. E. Rufford, D. Hulicova-Jurcakova and L. Wang, *Chem. Sust. Energy Mater.*, **2016**, 9, 513-520.

357.   D. Yu, Y. Xue and L. Dai, *J. Phys. Chem. Lett.*, **2012**, 3, 2863-2870.

358.   C. Yu, Z. Liu, X. Meng, B. Lu, D. Cui and J. Qiu, *Nanoscale*, **2016**, 8, 17458-17464.

359.   P. Rani, G. S. Dubey and V. K. Jindal, *Physica E: Low Dimens. Sys. Nanostruct.*, **2014**, 62, 28-35.

360.   D. W. Chang, H.-J. Choi, I.-Y. Jeon and J.-B. Baek, *J. Chem. Soc. Japan*, **2013**, 13, 224-238.

361.   K. Sivula, Z. T. Ball, N. Watanabe and J. M. J. Fréchet, *Adv. Mater.*, **2005**, 18, 206-210.

362.   B. C. O'Regan and J. R. Durrant, *Acc. Chem. Res.*, **2009**, 42, 1799-1808.

363.   J. Gong, K. Sumathy, Q. Qiao and Z. Zhou, *Renew. Sust. Energy Rev.*, **2017**, 68, 234-246.

364.   F. Bonaccorso, L. Colombo, G. Yu, M. Stoller, V. Tozzini, A. C. Ferrari, R. S. Ruoff and V. Pellegrini, *Science*, **2015**, 347, 1246501-1246511.

CHAPTER 3

materials

Effect of Doping Temperatures and Nitrogen Precursors on the Physicochemical, Optical, and Electrical Conductivity Properties of Nitrogen-Doped Reduced Graphene Oxide

Nonjabulo P. D. Ngidi, Moses A. Ollengo [ID] and Vincent O. Nyamori *

School of Chemistry and Physics, University of KwaZulu-Natal, Westville Campus, Private Bag X54001, Durban 4000, South Africa; nonjabulongidi@gmail.com (N.P.D.N.); mosesollengo@gmail.com (M.A.O.)
* Correspondence: nyamori@ukzn.ac.za; Tel.: +27-31-2608256; Fax: +27-31-2603091

check for updates

Abstract: The greatest challenge in graphene-based material synthesis is achieving large surface area of high conductivity. Thus, tuning physico-electrochemical properties of these materials is of paramount importance. An even greater problem is to obtain a desired dopant configuration which allows control over device sensitivity and enhanced reproducibility. In this work, substitutional doping of graphene oxide (GO) with nitrogen atoms to induce lattice–structural modification of GO resulted in nitrogen-doped reduced graphene oxide (N-rGO). The effect of doping temperatures and various nitrogen precursors on the physicochemical, optical, and conductivity properties of N-rGO is hereby reported. This was achieved by thermal treating GO with different nitrogen precursors at various doping temperatures. The lowest doping temperature (600 °C) resulted in less thermally stable N-rGO, yet with higher porosity, while the highest doping temperature (800 °C) produced the opposite results. The choice of nitrogen precursors had a significant impact on the atomic percentage of nitrogen in N-rGO. Nitrogen-rich precursor, 4-nitro-o-phenylenediamine, provided N-rGO with favorable physicochemical properties (larger surface area of 154.02 m^2 g^{-1}) with an enhanced electrical conductivity (0.133 S cm^{-1}) property, making it more useful in energy storage devices. Thus, by adjusting the doping temperatures and nitrogen precursors, one can tailor various properties of N-rGO.

Keywords: reduced graphene oxide; nitrogen-doping; chemical vapor deposition; physicochemical properties; optical properties; electrical conductivity

Effect of doping temperatures and nitrogen precursors on the physicochemical, optical, and electrical conductivity properties of nitrogen-doped reduced graphene oxide

Nonjabulo P. D. Ngidi, Moses A. Ollengo and Vincent O. Nyamori

School of Chemistry and Physics, University of KwaZulu-Natal, Westville Campus, Private Bag X54001, Durban 4000, South Africa

Graphical abstract
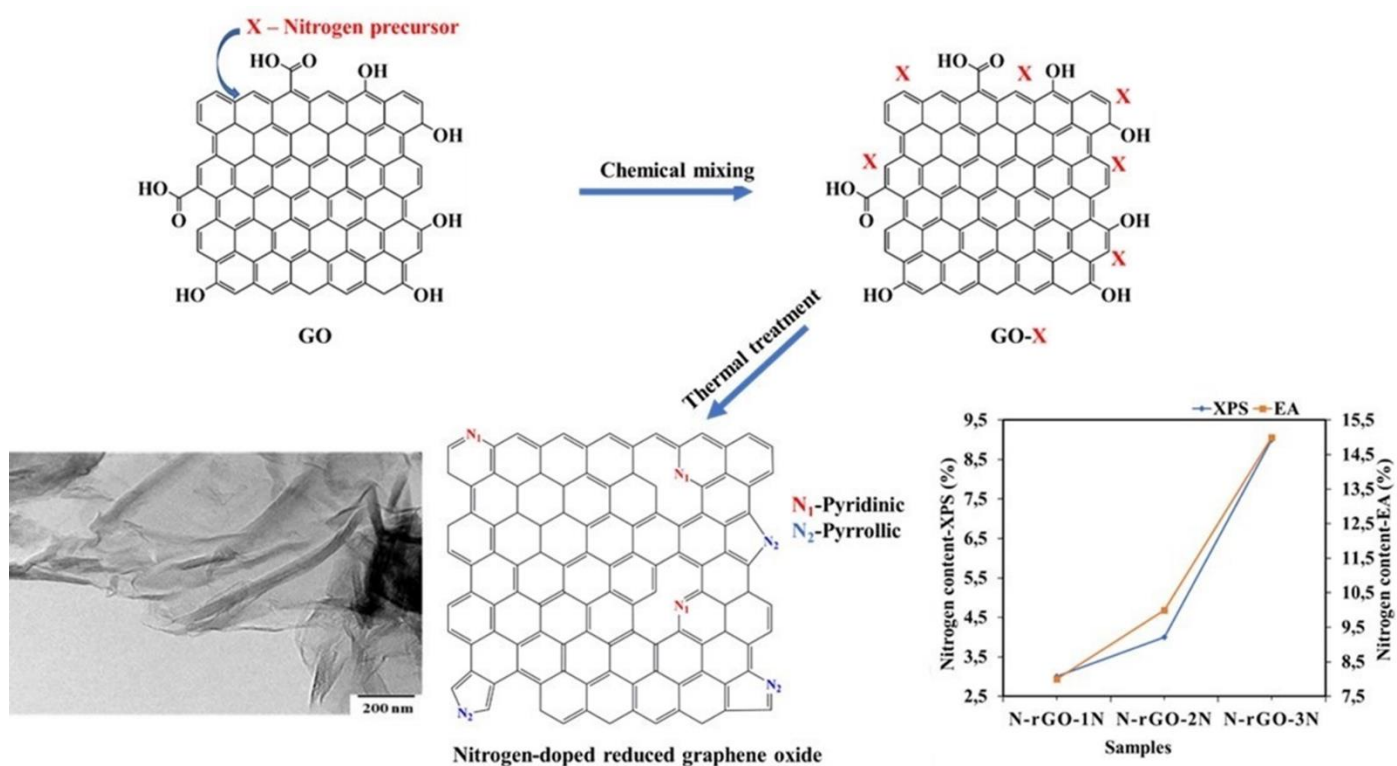
Abstract

The greatest challenge in graphene-based materials synthesis is achieving a large surface area and high conductivity. Thus, tuning the physico-electrochemical properties of these materials is of paramount importance. An even greater problem is to obtain the desired dopant configuration which allows control over device sensitivity and enhanced reproducibility. In this work, substitutional doping of graphene oxide (GO) with nitrogen atoms to induce lattice-structural modification of GO, resulted in nitrogen-doped reduced graphene oxide (N-rGO). The effect of doping temperatures and various nitrogen precursors on the physicochemical, optical, and conductivity properties of N-rGO is hereby reported. This was achieved by thermal treating GO with different nitrogen precursors at various doping temperatures. The lowest doping temperature (600 °C) resulted in less thermally stable N-rGO, yet with higher porosity, whilst the highest doping temperature (800 °C) produced the opposite results. The choice of nitrogen precursors had a significant impact on the atomic percentage of nitrogen in N-rGO with favourable physicochemical properties (larger surface area of 154.02 m^2 g^{-1}) with an enhanced electrical conductivity (0.133 S cm^{-1}) property, making it more useful in energy storage devices. Thus, by adjusting the doping temperatures and nitrogen precursors, one can tailor various properties of N-rGO.

Keywords

3.1   Introduction

Functionalization of carbon-based materials, such as graphene and carbon nanotubes for different purposes is gaining a lot of attention in the field of material science. This interest arises because of their low cost, unique stable physicochemical properties, and broad applications. The former includes energy harvesting devices [1], supercapacitors [2], sensors [3], field-effect transistors [4] and medical uses [5]. Certain extrinsic properties, such as electrical conductivity, high chemical stability and a zero-band gap, enable some carbon-based materials to perform as semi-metals and semiconductors [6]. Graphene, for instance, has a zero-band gap that needs to be manipulated for use in various applications such as solar cells. Graphene is a transparent material with a low coefficient of light absorption. Therefore, when graphene is applied in solar cells, it tends to produce a lower power conversion efficiency than solar cells based on heteroatom-doped graphene [7]. Most studies have shown that doped graphene can absorb a single photon; this can excite several electrons and do so proportionally to the degree of doping. The photon excites an electron, which then rapidly falls back down to its ground state of energy. The fallen electron then excites two more electrons as a knock-on effect. This indicates that a DSSC using doped graphene could show significant efficiency in converting light to electricity.[7]. Thus, creating a well-tuned and sizeable bandgap to improve the coefficient of light absorption of graphene is a great challenge but with enormous interest.

The bandgap of graphene can be tuned by altering the surface chemistry through substitutional doping [8]. This can be achieved by using selected heteroatoms to tune and enhance the band structure and conductivity [9,10]. Various heteroatoms that have commonly been employed in substitutional doping include boron [11-13] and nitrogen [14-16]. This is because they possess similar atomic radii and sizes to carbon and impact interesting electron chemistry within the graphene framework [17]. These heteroatoms have a significant effect on the electrical properties of graphene which is shown by a p-type conductivity for boron whereas nitrogen results in n-type conductivity [18]. In the case of strong p-type doping, it can be conferred by the interaction with the environment, hence, nitrogen-doping does not always confer n-type conductivity unless graphene is encapsulated [19]. The nitrogen atom is mostly used in the chemical doping of graphene or graphene oxide (GO). This is because the nitrogen atom acts as a defect site in the crystal structure of graphene and these defective centres can enhance the electrochemical activity of graphene or GO [20].

Nitrogen-doping suppresses the density of the state of graphene near the Fermi level and results in bandgap opening. Furthermore, nitrogen-doping tends to introduce strong electron donor states and

leads to n-type or p-type semiconductor behaviour depending on the bonding configuration. The conductivity and carrier mobilities of nitrogen-doped graphene are lower than pristine graphene due to the presence of nitrogen atoms and defects introduced during the nitrogen-doping process which are capable of functioning as scattering centres that hinder the electron or hole transport [21]. Boron-doping in graphene results in p-type doping and is also highly favourable. This is because the B-C bond is about 0.5% longer than the C-C bond while the N-C bond is about the same as the C-C bond in length, enabling the formation of a relaxed structure of boron-doped graphene. Boron-doping tends to introduce more holes into the valence band of graphene resulting in a high carrier concentration. Boron-doped graphene is reported to have high conductivity compared to pristine graphene [22] and nitrogen-doped graphene [23], due to the large density of state near the Fermi level.

Doping GO with nitrogen results in nitrogen-doped reduced graphene oxide (N-rGO). The ideal physicochemical properties of N-rGO for optoelectrical applications include a large surface area and high chemical stability. These physicochemical properties of N-rGO can be significantly enhanced by improving the atomic percentage of nitrogen [24] and the bonding configuration [25]. Various bonding configurations of nitrogen in N-rGO have been reported, e.g., pyrrolic-N [25], pyridinic-N [26], quaternary-N [27,28] and oxide-N [29]. These bonding configurations impart various effects on the carrier concentration which tend to produce well-defined band structures in doped GO [30].

The mechanism of formation of N-rGO is still a fascinating phenomenon because it is not well understood and there is more that can be done to manipulate it. Therefore, synthetic procedures for N-rGO need a certain level of control regarding the required extent of doping and the bonding configuration of nitrogen. Different synthetic approaches have been employed in the *in-situ* synthesis of N-rGO, such as arc discharge [31], plasma method [32], thermal annealing [33] and chemical vapour deposition (CVD) [34,35]. The CVD approach is mostly preferred because it is easier to scale-up and produces relatively high-quality N-rGO. Scientific reports on the synthesis of N-rGO *via* the CVD approach indicate that the most used materials are metal catalysts (Cu, Ni, Co or Fe) [36,37] and organic molecules [38].

In the CVD synthesis of N-rGO, several factors including the type of carrier gas, doping temperature and nitrogen precursor (used either as a solid, liquid or in the gaseous phase), influence the nitrogen content and properties of the final product [39,40]. Nang *et al.* [41] and Panchakarla *et al.* [42] reported the use of dimethylformamide and pyridine, respectively, as liquid nitrogen precursors for the synthesis of N-rGO, with the former achieving a very low

nitrogen content of 0.64%. The drawback of liquid nitrogen precursors is that they are expensive, highly flammable and dangerous when used in the CVD method.

The alternative to liquid and gaseous nitrogen precursors is solid nitrogen precursors. The use of solid nitrogen precursors, such as monoethanolamine [43], urea [33,44], 1,3,5-triazine [24], pentachloropyridine [36] and the combination of imidazole and melamine [45] have been reported and observed to result in high doping levels. Lu *et al.* [24] reported the CVD synthesis of a few-layered nitrogen-doped graphene oxide containing atomic percentages of between 2.1 and 5.6% nitrogen by making use of the carbon and nitrogen precursor 1,3,5-triazine and Cu foil as a catalyst. Doped graphene films with a higher nitrogen content of approximately 5.6% were obtained at a doping temperature of 990 °C, with melamine [46] as a solid nitrogen precursor. The use of the solid nitrogen precursor, pentachloropyridine, in the synthesis of nitrogen-doped graphene was reported by Wan *et al.* [36] to yield a nitrogen content between 4.4 and 7.5%. Solid nitrogen precursors are cost-effective and are easy to handle compared with liquid and gaseous nitrogen precursors.

In this work, we report for the first time, the effect of different doping temperatures and solid nitrogen precursors on the physicochemical (nitrogen content, crystallinity, thermal stability, and bonding configuration), optical (bandgap energy and charge recombination) and electrical conductivity properties of N-rGO. The synthesis of N-rGO (Figure 3.1) was achieved by liquid exfoliation of GO, high-temperature vapour reduction of GO and doping it with nitrogen atoms from various solid nitrogen precursors (4-nitroaniline, 4-aminophenol and 4-nitro-*o*-phenylenediamine). These nitrogen precursors were chosen because they possess a different number of nitrogen atoms on their structures or frameworks, and therefore the effect of the number of nitrogen atoms contained in the nitrogen precursor was also investigated.
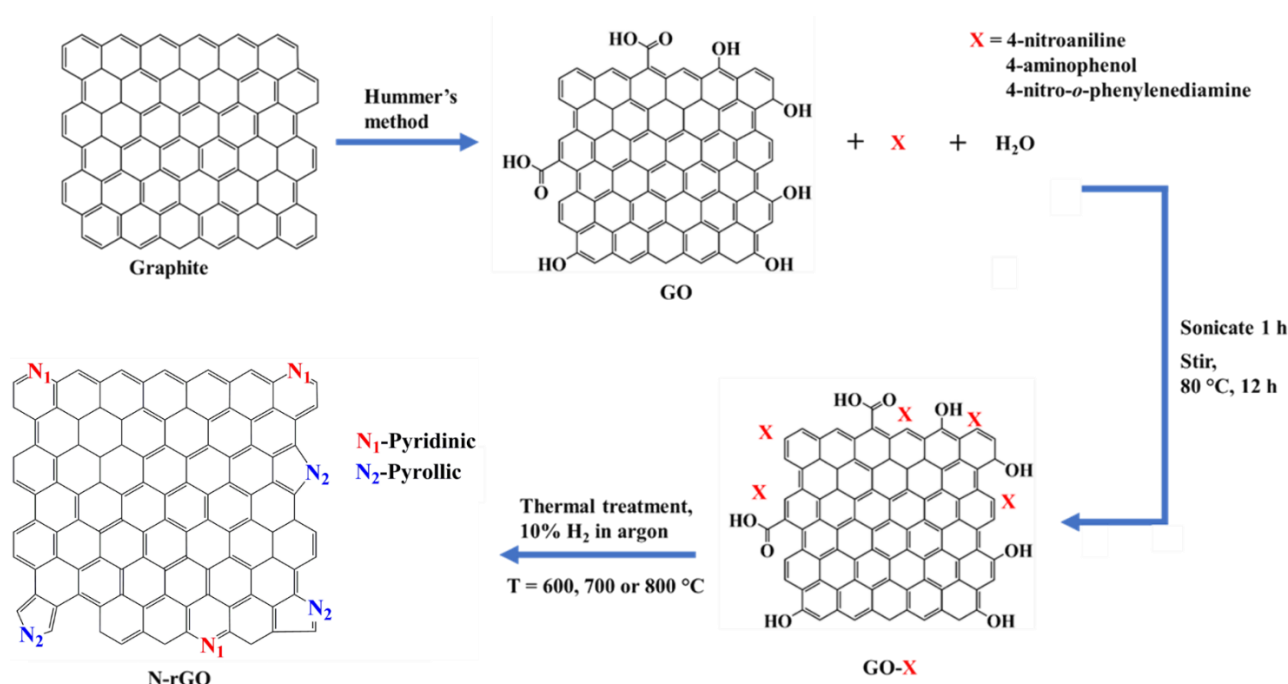
Figure 3.1: Schematic diagram of the conversion of graphite to N-rGO.

3.2 Materials and methods

3.2.1 Materials and instrumentation

Graphite powder (99.99% - trace metal basis), sodium nitrate (99%), potassium permanganate (99%), 4-nitroaniline (≥99%), 4-aminophenol (≥99%) and 4-nitro-*o*-phenylenediamine (≥99%) were purchased from Sigma-Aldrich, South Africa. These chemicals were of analytical grade and were used without further purification. Hydrogen peroxide (100%) was purchased from Merck Laboratory Supplies, South Africa. Sulphuric acid (98%) was purchased from Promark Chemicals, South Africa. Double distilled water was obtained from a double distiller, Glass Chem water distiller model Ws4lcd was supplied by Shalom Laboratory Supplies, South Africa. A gas mixture of 10% hydrogen in argon (v/v) was purchased from Afrox Limited Gas Co., Durban, South Africa. Weighing of N-rGO was done on an electronic weighing balance, Mettler AE 200, Mundelein, IL USA. Ultrasonication was performed in a digital ultrasonic water bath (400 W) obtained from Shalom Laboratory Supplies, Durban, South Africa.

3.2.2 Synthesis of N-rGO

A modified Hummer's method was used to synthesize graphene oxide (GO) [47]. In brief, approximately 1 g of graphite powder and 1 g of sodium nitrate were mixed with 50 mL of concentrated sulphuric acid in a 500 mL round-bottom flask placed in an ice bath and stirred

for 30 min. After that, 6 g of potassium permanganate was added slowly to the mixture with the temperature kept at 5 °C to prevent explosion and excessive heating. Thereafter, the mixture was stirred for 3 h at a temperature of 35 °C and then further treated with 200 mL of 3% hydrogen peroxide while stirring for 30 min. The resulting GO was washed with double distilled water until a pH of 6 was achieved. The product was then filtered and dried in the oven for 24 h at a temperature of 80 °C.

The synthesized GO was simultaneously reduced (using 10% hydrogen in argon as a reducing agent) and doped with different nitrogen precursors, namely 4-nitroaniline, 4-aminophenol and 4-nitro-*o*-phenylenediamine. This was done by mixing 70 mg of GO and 30 mg of nitrogen precursor in 50 mL double distilled water, followed by sonication (25 °C) for 1 h. The mixture was further stirred and heated for 6 h at a temperature of 100 °C to remove the excess water. After drying, the resulting black solid was heat-treated in a ceramic quartz boat placed in a tube furnace (Elite Thermal Systems Ltd, Model TSH12/50/160) in a mixture of 10% hydrogen in argon (v/v) at a flow rate of 100 mL min^{-1}. The doping temperature of the furnace was set at each of 600, 700 and 800 °C, for each nitrogen precursor. The carrier gas flow rate and the doping temperature were maintained constant throughout the synthesis period of 2 h. After 2 h, the furnace was allowed to cool naturally to room temperature and N-rGO was collected and subsequently characterized.

3.2.3 Physicochemical characterization

The surface morphology of N-rGO was investigated by field emission scanning electron microscopy (FE-SEM, Carl Zeiss Ultra Plus, Cambridge, UK). Briefly, the aluminium stub sample holders were coated with a piece of sticky carbon tape; after that, the N-rGO was sprinkled on the carbon tape and gold-coated thrice before SEM analysis. The microstructural features of the N-rGO were evaluated using high-resolution–transmission electron microscopy (HR-TEM, JOEL JEM model 1010, Peabody, MA, USA), and set at an accelerating voltage of 100 kV at different magnifications.

The crystallinity or graphitic nature of the N-rGO was investigated with a Delta Nu Advantage 532^{TM} Raman spectrometer (Laramie, WY, USA) equipped with NuSpec^{TM} software (1.0., Microsoft Publisher, Redmond, WA, USA) and operated at a wavelength (λ) of 514.5 nm. The functional groups present in the N-rGO were investigated with a PerkinElmer Spectrum 100 Fourier transform infrared (FTIR) spectrometer (Akron, OH, USA) equipped with an attenuated total reflectance (ATR) accessory. Approximately 0.22 g of the N-rGO was pressed

into a pellet for about 2 min, under a pressure of 10 Tons. The pellets were then placed on the diamond crystal for analysis.

The thermal stability of N-rGO was measured with a TA Instruments Q series^{TM} thermal analysis instrument (DSC/thermogravimetric analysis (TGA) (SDT-Q600), New Castle, PA, USA) in the air flowing at a rate of 50 mL min^{-1} and heated from room temperature up to 1000 °C at a ramping rate of 10 °C min^{-1}. N-rGO were further characterized by X-ray photoelectron spectroscopy (XPS, Quantum 2000 with an X-ray source of monochromatic Al K$_\alpha$ (1486.7 eV)), Chanhassen, MN, USA) to investigate the surface chemical composition of carbon and nitrogen.

A Micromeritics Tristar II 3020 surface area and porosity analyser (Norcross, GA, USA) were used to determine the textural properties of N-rGO. Typically, a mass of approximately 0.1 g of N-rGO was degassed at 90 °C for 1 h, the temperature was then raised to 160 °C and the sample was further degassed for 12 h using Micromeritics Vacprep 061 (sample degas system), before fitting N-rGO in the Micromeritics Tri-star II instrument for analysis. The textural properties of the N-rGO were investigated at a temperature of -196 °C with N$_2$ as the adsorbate. The specific surface areas were calculated with the Brunauer, Emmett and Teller (BET) model and the pore volumes were obtained by applying the Barrett-Joyner-Halenda (BJH) model.

The phase characteristics of the synthesized N-rGO were determined by X-ray powder diffraction (XRD, Rigaku/Dmax RB, The Woodlands, TX, USA) and the measurements were performed with graphite monochromated high-density with a θ-θ scan in locked coupled mode, using a Cu k$_\alpha$ radiation source (λ = 0.15406 nm). The absorbance of N-rGO was recorded with an ultraviolet-visible spectrophotometer (UV-Vis, Shimadzu, UV-1800 Roodepoort, South Africa). The GO and N-rGO were firstly dispersed in ethanol absolute and then sonicated for 30 minutes before UV-Visible spectrophotometric analysis. Charge recombination analysis of N-rGO was investigated with a PerkinElmer LS 55 spectrofluorometer (Akron, OH, USA) fitted with a solid sample accessory. Excitation was performed at 310 nm, and the emission spectrum was recorded from 450 - 550 nm with an excitation slit and emission slit at 5 nm and 2 nm, respectively (slid position). The electrical conductivity of N-rGO was determined by a Four-point probe (Keithley 2400 source-meter, Beaverton, OR, USA) measurements which were carried out on pellets with a thickness of 0.2 mm formed from N-rGO (0.03 g).

3.3　　Results and discussion

The physicochemical characteristics of N-rGO synthesized with different nitrogen precursors and at different doping temperatures of 600, 700 and 800 °C are presented. Both factors influence the level of nitrogen-doping, morphology, crystallinity, thermal stability, optical and electrical conductivity properties of N-rGO.

3.3.1　Morphology

The nitrogen atoms from the different nitrogen precursors were successfully introduced into the GO lattice. N-rGO synthesized from: 4-aminophenol is represented by N-rGO-1N, 4-nitroaniline is represented by N-rGO-2N while 4-nitro-*o*-phenylenediamine is represented by N-rGO-3N. N-rGO in the SEM images showed a thick and overlapping sheet structure (Supplementary Materials – Figure S3.1). This was attributed to flake-like structures. A similar observation for SEM images of N-rGO was reported by Jiang *et al.* [48]. Further details of the structures were evaluated by HR-TEM. For comparison, Figure 3.2 presents the HR-TEM images and the selected area electron diffraction (SAED) patterns of GO and N-rGO. Both GO and N-rGO exhibited a wrinkled structure (Figure 3.2 (a)), which increased after doping (Figure 3.2 (c)). The more wrinkled structure in N-rGO is caused by the stimulation of defects such as pores, holes and cavities which were introduced during the process of doping [49]. The different doping temperatures and nitrogen precursors revealed no effect on the morphology of N-rGO.
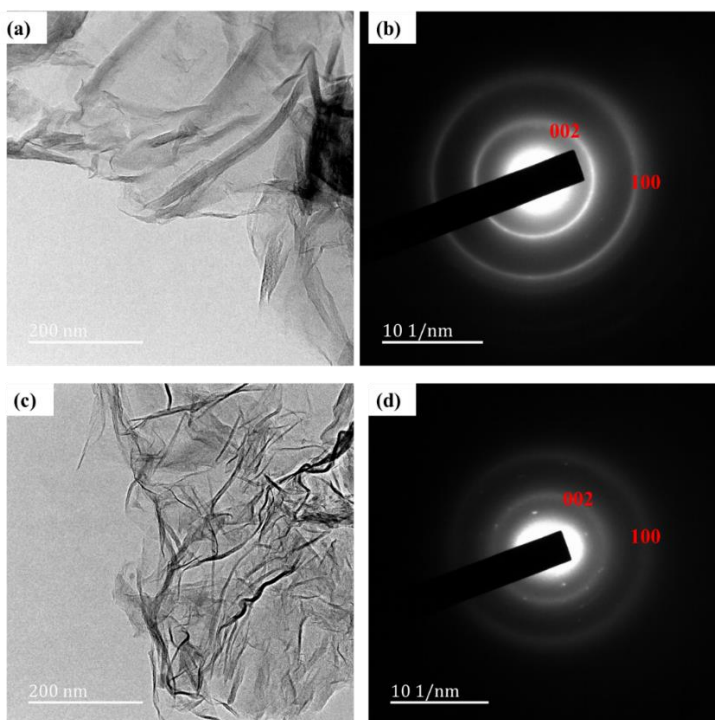
Figure 3.2: HR-TEM image of (a) GO, (b) SAED pattern of GO, (c) HR-TEM image of N-rGO-1N-600 °C and (d) SAED pattern of N-rGO-1N-600 °C.

The SAED patterns recorded to study the crystalline structures of GO and N-rGO revealed two diffraction rings that were associated with the (002) and (100) planes for both GO (Figure 3.2 (b)) and N-rGO (Figure 3.2 (d)). The presence of hexagonal diffraction spots in the electron diffraction pattern observed indicates that N-rGO has a well-ordered structure while the occurrence of structural distortion after doping is revealed by the ring-like diffraction pattern. The observed disorder might be due to the introduction of functional groups, and the overlapping graphene sheets [50]. The diffraction spots in hexagonal positions in N-rGO are reflective of the preservation of the original honey-comb-like atomic structure of graphene [51]. The GO also shows a ring-like structure (distortion) which is due to ring spacing (Figure 3.2 (b)).

The different interlayer spacings (d_{002} spacing) on the edge of GO and at the cross-sections of layers of N-rGO as observed in the HR-TEM images (Figure 3.3 (a) and (b)) showed that the carbon atom layers were not identical; this is indicative that the N-rGO consists of few-layers of graphene sheets (Table 3.1). After nitrogen-doping, the d_{002} spacing was found to decrease. For example, the d_{002} spacing of N-rGO-1N-600 °C was found to be 0.37 nm which is smaller than that of GO (0.47 nm). The decrease in d_{002} spacing after nitrogen-doping was attributed

to the reduction of oxygen functional groups such as carboxyl, epoxy and hydroxyl groups [52].
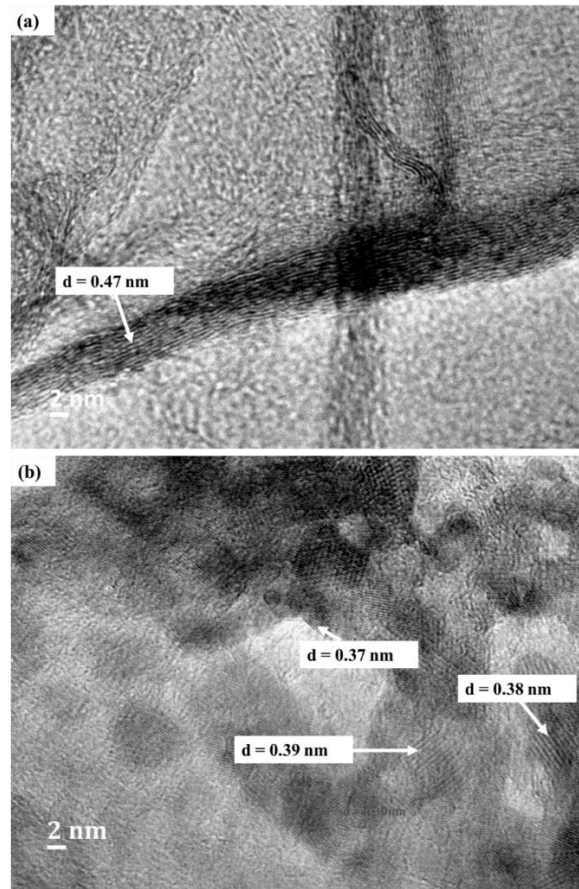
Figure 3.3: The d_{002} inter-layer spacing of (a) GO and (b) N-rGO-1N-600 °C.

Table 3.1: Comparison of the d_{002} inter-layer spacing of GO and N-rGO synthesized at different temperatures and with different nitrogen precursors.

Sample	Inter-layer spacing/nm
GO	0.47 ± 0.03
N-rGO-1N-600 °C	0.39 ± 0.01
N-rGO-1N-700 °C	0.40 ± 0.02
N-rGO-1N-800 °C	0.44 ± 0.02
N-rGO-2N-600 °C	0.38 ± 0.01
N-rGO-2N-700 °C	0.39 ± 0.01
N-rGO-2N-800 °C	0.40 ± 0.02
N-rGO-3N-600 °C	0.36 ± 0.01
N-rGO-3N-700 °C	0.38 ± 0.01
N-rGO-3N-800 °C	0.39 ± 0.01

The d_{002} spacing of N-rGO varied with different doping temperatures and nitrogen precursors used. The d_{002} spacing was found to increase with an increase in doping temperature. For instance, N-rGO-1N-600 °C, N-rGO-1N-700 °C and N-rGO-1N-800 °C have d_{002} spacings of 0.39, 0.40 and 0.44 nm, respectively. The smaller d_{002} spacing observed at a lower doping temperature (600 °C) is attributed to structural strains and the less crystalline nature of N-rGO. A larger d_{002} spacing was observed for N-rGO-1N synthesized from the nitrogen precursor, 4-aminophenol, at 800 °C. The interlayer spacing increased due to the distortion introduced by the inclusion of nitrogen. Such intercalation structural distortion has been widely reported for different carbon nanomaterials, such as carbon nanotubes [53]. Therefore, Raman spectroscopy was further used to investigate the effect of various temperatures and nitrogen precursors on the graphitic nature (structural properties) of N-rGO.

3.3.2 Structural properties

The structural and electronic properties of N-rGO were investigated by Raman spectroscopy. Two major peaks, namely the G-band peak (between 1580 and 1606 cm^{-1}) which originates from the Raman E_{2g} mode, and the D-band peak (between 1347 and 1363 cm^{-1}) which is the disorder-induced band, were observed. The intensities of the D-band of N-rGO-3N-600 °C and N-rGO-3N-700 °C; and the G-bands of N-rGO-1N-600 °C and N-rGO-1N-700 °C, are of the same value (Table 3.2). However, their I_D/I_G ratios are different. This indicates that the nitrogen dopant distribution in N-rGO was not homogeneous [54].

Table 3.2: Crystallinity analysis of N-rGO.

Sample	D-band/cm^{-1}	G-band/cm^{-1}	I_D/I_G	I_{2D}/I_G	L_a/nm
GO	1355 ± 1	1601 ± 1	0.82	0.0589	5.37
N-rGO-1N-600 °C	1354 ± 1	1585 ± 1	1.04	0.0199	4.20
N-rGO-1N-700 °C	1360 ± 1	1585 ± 1	0.88	0.0212	5.00
N-rGO-1N-800 °C	1363 ± 1	1575 ± 1	0.86	0.0287	5.11
N-rGO-2N-600 °C	1357 ± 1	1603 ± 1	1.08	0.0159	4.07
N-rGO-2N-700 °C	1356 ± 1	1602 ± 1	1.02	0.0207	4.31
N-rGO-2N-800 °C	1360 ± 1	1601 ± 1	0.85	0.0253	5.37
N-rGO-3N-600 °C	1355 ± 1	1606 ± 1	1.77	0.0103	2.49
N-rGO-3N-700 °C	1355 ± 1	1605 ± 1	1.40	0.0197	3.14
N-rGO-3N-800 °C	1361 ± 1	1602 ± 1	0.88	0.0212	5.00

The G-bands for all N-rGO samples showed a slight shift in frequency for all doping temperatures. A shift in the D-band (from 1354 to 1363 cm^{-1}) of N-rGO-1N was observed as the doping temperature was increased. This was due to the change in the bond length and symmetry of the C-C and C=C bonds in the graphene lattice and compressive stress on graphene during the annealing process [55]. The asymmetric line shape and shift of the G-band (from 1601 to 1606 cm^{-1}) of GO and N-rGO-3N-600 °C, may be due to the increase in the percentage of nitrogen incorporated. Results showed that the changes in the D- and G-bands are associated with the increase in defects/dopant concentration.

It has been shown that relaxation or the change of lattice constant is highly asymmetric with lattice constant increasing by 0.32% with 2% in boron substitution and decreases very slightly with N-substitution [42]. Panchakarla *et al.* [42] have shown that the inter-planar separation reduces by almost 2.7% in B-doped bilayer reduced graphene oxide while it remains almost unchanged in N-doped bilayers. However, there is a resultant large decrease and a slight increase in a frequency shift in G-band with either B or N substitution. Boron affords a homogeneous distribution as such, disorder or the number of possible configurations increases with the concentration of dopant atoms and results in more prominent peaks of the D-band compared to nitrogen. However, G-band stiffens both with boron and nitrogen doping and the intensity of the D-band is higher with respect to that of the G-band in all the doped samples.

The intensities of the G- and D-bands differ, and this is evident in the I_D/I_G ratio of N-rGO (Table 3.2). The I_D/I_G ratio is an indication of the degree of disorder and graphitic nature of N-rGO. A broader width of the D-band, narrower width of the G-band and a larger I_D/I_G ratio, suggest that N-rGO possesses many defective sites and different bonding structures (*e.g.*, C-O, C-N) in the graphene lattice [56]. The I_D/I_G ratios of all N-rGO decreased with an increase in doping temperature (from 600 to 800 °C) for the same nitrogen precursor. The larger I_D/I_G ratios observed at the lowest doping temperature of 600 °C imply a higher level of disorder (lower crystallinity). The highest doping temperature of 800 °C resulted in highly crystalline N-rGO because more amorphous products in N-rGO were reduced. Similar observations were reported by Capasso *et al.* [57]. Table 3.2 also shows the increase in defects upon an increase in nitrogen content (nitrogen precursor) in the graphene oxide lattice. In the case of N-rGO-3N that was obtained from a nitrogen precursor with the largest number of nitrogen atoms, a marked shift in the G-band was observed. This is due to the increase in nitrogen atoms introduced in bond formation within the sp^2 carbon lattice of the GO. N-rGO-3N samples were

observed to be less crystalline, with I_D/I_G ratios of 1.77, 1.40 and 0.88 at doping temperatures of 600, 700 and 800 °C, respectively. While other N-rGO-1N and N-rGO-2N samples which were synthesized from 4-aminophenol and 4-nitroaniline, respectively, were more crystalline.

Apart from the characteristic D-band and G-band, GO and N-rGO have a third peak; 2D-band. The 2D-band represent the second order of the D-band, which is alluded to as an overtone of the D-band. Its occurrence is due to two phonon lattice vibrational processes, however, it is not associated with the defect, like D-band. Therefore, the 2D-band is regarded as a strong band in graphene even when there is no presence of the D-band. The observed 2D band peak of GO had higher intensity compared to N-rGO, 2D-band. The intensity ratios of the G-band and 2D-band (I_{2D}/I_G ratio) have been used to investigate the electron concentration of the N-rGO. Results showed that the I_{2D}/I_G ratio changes as the number of nitrogen atoms in the graphene lattice increases (Table 3.2). The different nitrogen precursors have different nitrogen atoms insertion capacity into rGO thus, the change in I_{2D}/I_G.

The I_D/I_G ratio of all N-rGO tends to increase as the I_{2D}/I_G ratio decreases. A similar trend was also reported by Zafar *et al.* [54]. This is because N-rGO consists of an extra scattering effect that arises from nitrogen induced electron doping. The 2D-band is mostly dependent on the electron/hole scattering rate which is influenced by lattice and charge carrier doping. Therefore, the I_D/I_G ratio would increase the electron-defect elastic scattering rate, while the I_{2D}/I_G ratio would increase the electron-electron inelastic scattering (Coulomb interaction). However, the evaluation of the doping level of N-rGO using the I_{2D}/I_G ratio and blue-shifting of G-band is complicated because the G-band and 2D-band features are greatly affected by strains, defects, and a number of layers.

The crystallite size (L_a) of N-rGO, which depends on the I_D/I_G ratio, was calculated with the aid of an equation:

$$HWHM = 71 - 5.2\,L_a \qquad\qquad (1)$$

where HWHM stands for the half-width at a half maximum which is the half of the full width at half maximum (FWHM) when the function is symmetric, and this was reported by Mallet-Ladeira *et al.* [58] (which is an alternative to the Tuinstra-Koenig (TK) law). The crystallite size decreases remarkably with an increase in the I_D/I_G ratio of N-rGO. N-rGO synthesized at the lowest temperature (600 °C) produced N-rGO with a smaller crystallite size than that prepared at the highest temperature (800 °C). The crystallite sizes of N-rGO vary with the type

of nitrogen precursor used. Smaller crystallite size of 2.49 nm was observed in N-rGO-3N while N-rGO-2N and N-rGO-1N had a crystallite size of 4.07 and 4.20 nm, respectively, at 600 °C. The crystallite size of GO (5.37 nm) was larger than that of N-rGO which indicates that thermal treatment and the type of nitrogen precursor affected the crystallite size of N-rGO. Previous studies have reported a link between the increase in I_D/I_G ratio and smaller crystallite size which is due to the formation of small crystals during reduction [50].

3.3.3 Thermal stability

The decomposition behaviour of N-rGO was investigated by the thermogravimetric analysis (TGA). The synthesized N-rGO exhibited different thermal stabilities. TGA weight loss curves of N-rGO-1N, N-rGO-2N and N-rGO-3N are shown in Figures 3.4 (a), (b) and (c), respectively.
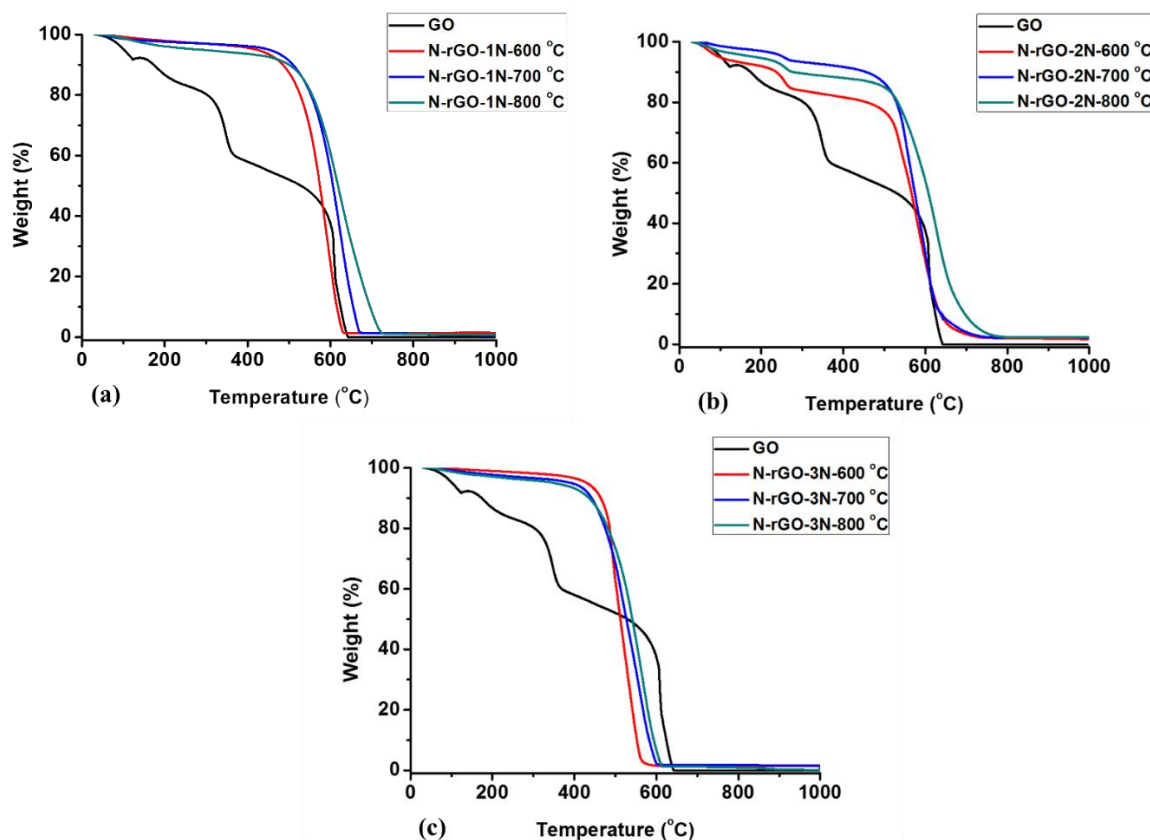
Figure 3.4: TGA thermograms of (a) N-rGO-1N, (b) N-rGO-2N and (c) N-rGO-3N.

The thermogram of GO showed a sequence of reaction steps because of the different oxygen-containing functional groups present in GO. These include carbonyl (C=O), hydroxyl (C-OH), epoxide (C-O-C) and single-bonded oxygen at the surface (C-O) [59,60]. The oxygen functional groups have different thermal decomposition temperatures. The thermogram of GO

revealed that the decomposition occurred in different reaction steps, namely, the initial step, second step and final step. The initial step represents the rapid decline in GO weight, and this occurred before 100 °C and ended at 320 °C. The weight loss of around 100 °C is due to the evolution of water (H_2O). The water lost in this step was physically absorbed between the layers of GO. The weight loss above 100 to 320 °C is attributed to the loss of CO_x groups (carbon monoxide and carbon dioxide) [61]. The second step was a slow step where the GO continues to decompose, possibly due to the loss of sp^2 carbon atoms in a hexagonal structure, that occurs between the decomposition temperatures of 320 and 645 °C. The drastic weight loss between 320 and 645 °C is caused by the loss of labile oxygen-containing functional groups such as hydroxyl and epoxy groups due to their bond strength [62]. The final step exhibits a slower reduction in mass that ends at 1000 °C, signalling complete decomposition of GO to char.

All N-rGO samples were found to have different decomposition temperatures. The N-rGO synthesized at the higher doping temperatures (700 and 800 °C) showed no massive mass loss in the decomposition range of 100 - 300 °C, revealing the efficient removal of oxygen functional groups during the thermal process in the synthesis. All the thermograms (Figure 3.4) showed that N-rGO synthesized at the highest doping temperature (800 °C) were more thermally stable while samples prepared at the lowest doping temperature (600 °C) displayed the lower thermal stability. The most stable N-rGO were synthesized at doping temperature of 800 °C with decomposition temperatures of 591, 577 and 520 °C for N-rGO-1N, N-rGO-2N and N-rGO-3N, respectively. At a doping temperature of 600 °C, N-rGO-1N, N-rGO-2N and N-rGO-3N showed decomposition temperatures of 545, 536 and 488 °C, respectively. The nitrogen precursor 4-aminophenol produced N-rGO-1N that are more structured with fewer defects resulting in higher thermal stability. On the other hand, the other nitrogen precursors, namely, 4-nitroaniline and 4-nitro-*o*-phenylenediamine produced, N-rGO of lower thermal stability which suggests that the samples contain a greater extent of nitrogen-doping. There is a distinct decomposition pattern of N-rGO-2N around 300 to 500 °C which is associated with the removal of stable functionalities. A similar observation was reported by Khandelwal *et al.* [63]. The thermal stability of N-rGO samples correlates to its lower crystallinity, which is supported with microscopic studies and Raman spectroscopy analysis (Table 4.2). The thermal stability of N-rGO is also associated with nitrogen bonding configuration (nitrogen functionalities) in a graphene network. Kumar *et al.* [64] reported that pyridinic-N configurations are mostly dominant at lower doping temperatures. Whereas, at higher doping

temperature, graphitic-N is more dominant, and this results in more thermal stable N-rGO (with graphitic-N). This is evidence of a temperature-dependent nitrogen configuration doping in N-rGO. Hence, it is possible to achieve selective configurative nitrogen doping, a major breakthrough in tuning physicochemical properties of N-rGO.

3.3.4 Surface chemistry

3.3.4.1 Surface area and porosity

The surface areas, pore volumes and pore size distributions of N-rGO obtained at varying doping temperatures are shown in Table 3.3. All as-synthesized N-rGO exhibited different surface areas and pore volumes/sizes. GO had a surface area of 59.46 m^2 g^{-1}, but after thermal annealing and doping with nitrogen, the surface area and pore volume increased. Thermal annealing during doping of GO caused additional exfoliation which resulted in increased surface areas and pore volumes in N-rGO due to perforations of the sheets [65].

Table 3.3: A comparison of the surface areas and porosities of N-rGO synthesized at different temperatures and with different nitrogen precursors.

Sample	Surface area/m^2 g^{-1}	Pore volume/cm^3 g^{-1}	Pore size/nm
GO	59.46	0.0564	11.39
N-rGO-1N-600 °C	87.52	0.1876	15.11
N-rGO-1N-700 °C	74.98	0.1652	17.32
N-rGO-1N-800 °C	65.05	0.1083	19.84
N-rGO-2N-600 °C	110.55	0.4324	24.89
N-rGO-2N-700 °C	99.21	0.3003	26.45
N-rGO-2N-800 °C	90.34	0.2537	27.53
N-rGO-3N-600 °C	154.02	0.5029	25.96
N-rGO-3N-700 °C	130.67	0.4986	28.89
N-rGO-3N-800 °C	95.08	0.2835	34.67

The effect of doping temperatures and nitrogen precursors on the surface areas, pore volumes and pore sizes were investigated. It was observed that for all precursors, N-rGO synthesized at the highest doping temperature (800 °C) had a smaller surface area than N-rGO synthesized at the lowest doping temperature (600 °C). However, it has been reported that higher doping temperatures during the synthesis of N-rGO create smaller nanocrystalline graphene sheets, porous structures, large surface areas and more defects [66]. In this work, the low surface area

is caused by the collapse of the carbon skeleton structure during the annealing process. Thereby, reducing the surface area of N-rGO.

Apart from doping temperatures, the surface area was also influenced by the nitrogen content in N-rGO. The largest surface area (154.02 m^2 g^{-1}) was observed for the nitrogen precursor 4-nitro-o-phenylenediamine (N-rGO-3N-600 °C) while, the smaller surface area (65.05 m^2 g^{-1}) was obtained for N-rGO-1N-800 °C which was synthesized from 4-aminophenol. The high surface area in N-rGO-3N and N-rGO-2N may suggest a high percentage of the pyridinic-N site in these N-rGO [67]. A good trend of BET surface area and pore sizes was observed in N-rGO samples. This illustrated that the surface area and pore volume increase with an increase in nitrogen content of N-rGO. This is because of the formation of extra pores on the surface of GO after doping, which is associated with extra exfoliation and perforation on the sheets [49,68].

The nitrogen adsorption-desorption isotherms (Figure 3.5) for these materials can be classified as Type IV isotherms [69]. The type IV isotherms were accompanied by well-defined H_3 hysteresis loops which are associated with capillary condensation. For N-rGO-1N-600 °C, N-rGO-2N-600 °C and N-rGO-3N-600 °C, the H_3 type hysteresis loops ranged from 0.49, 0.46 and 0.45 P/P_o, respectively, to 1.0 P/P_o. This demonstrates the presence of micro-and mesoporous structures within the N-rGO layers with plate-like slit-shaped pores [70].
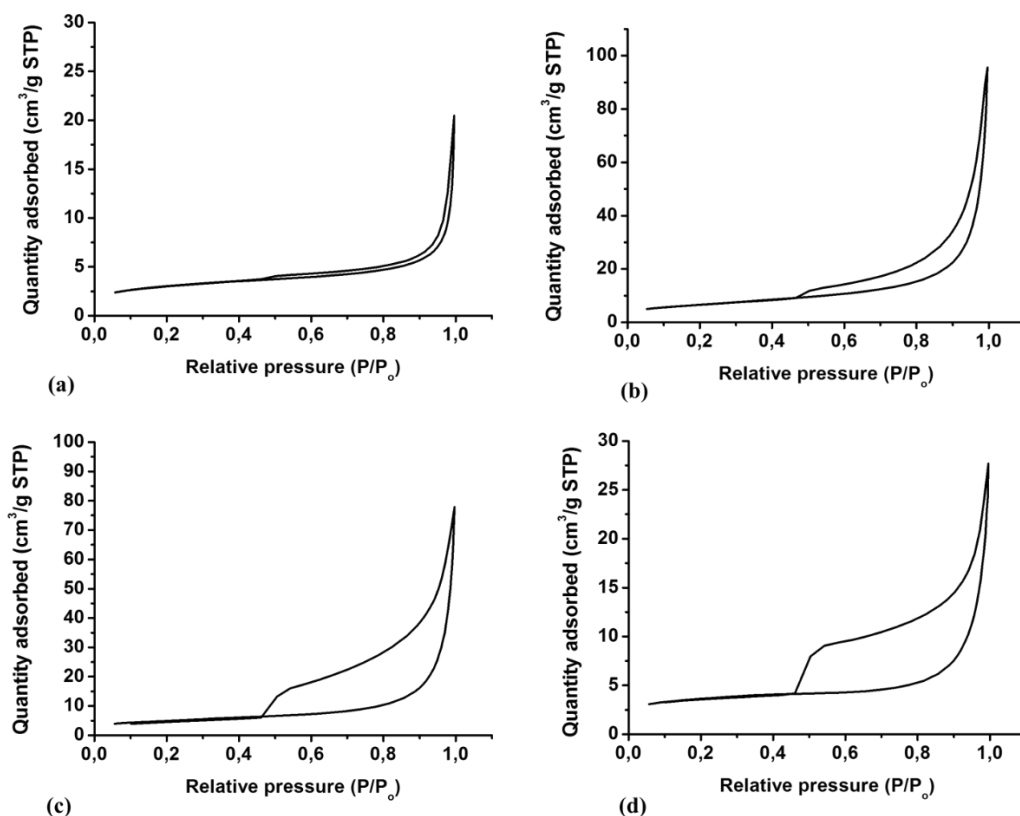
Figure 3.5: N_2 adsorption-desorption isotherms of (a) GO, (b) N-rGO-1N-600 °C, (c) N-rGO-2N-600 °C and (d) N-rGO-3N-600 °C.

3.3.4.2 Functional groups

N-rGO and GO were characterized using FTIR spectroscopy to investigate the effect of doping temperatures and nitrogen precursors on the functional groups present in the N-rGO. The FTIR spectral patterns of all the N-rGO samples were used to identify the presence of different functional groups, by comparison with that of GO (Figure 3.6).
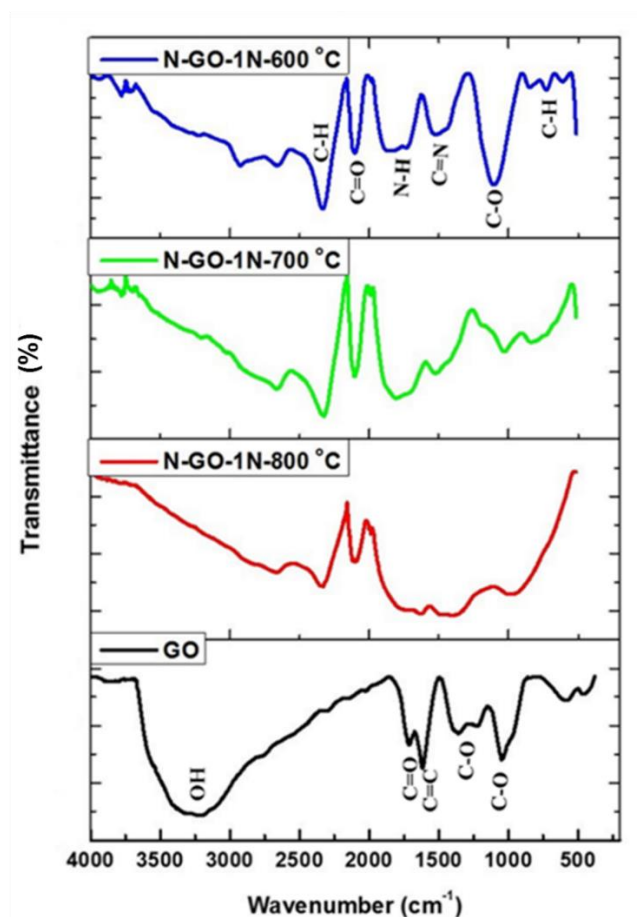
Figure 3.6: FTIR spectra of GO and N-rGO-1N at doping temperatures of 600, 700 and 800 °C.

The FTIR spectrum of GO showed different functional groups including hydroxyl (O-H), carbonyl (C=O), (C=C) and (C-O), indexed at 3157, 1733, 1614 and 1255/1155 cm^{-1}, respectively, which are similar to those previously reported [71]. After nitrogen-doping of GO, peaks for C=N stretching vibrations and N-H bending vibrations occurred at 1348 and 1660 cm^{-1}, respectively. Higher doping temperatures tend to reduce the peak for the O-H stretching vibration. The C-H stretching vibration peak is observed at 2489 cm^{-1} while the peak at 650 cm^{-1} (fingerprint region) is assigned to the C-H bending vibration (hybridized *sp^2* bonding). The FTIR spectra of N-rGO synthesized from other nitrogen precursors (4-nitroaniline and 4-nitro-*o*-phenylenediamine) revealed the presence of similar functional groups as for N-rGO-1N synthesized from 4-aminophenol.

3.3.4.3   Nitrogen contents

Elemental analysis (CHNS/O) of the N-rGO samples prepared was performed to study the relationship between the nitrogen precursors and the elemental composition of N-rGO. All the synthesized N-rGO samples contained different compositions carbon, oxygen and nitrogen

(Table 3.4). The highest doping temperature for each nitrogen precursor produced N-rGO with lower nitrogen content, while the lowest doping temperature resulted in the largest nitrogen content for all nitrogen precursors. Thus, a doping temperature of 600 °C was found to be the best temperature for the nitrogen-doping of GO. A similar trend was reported by Song *et al.* [56] where GO was doped by hydrothermal treatment with ammonia as the nitrogen precursor at doping temperatures of 160, 190, 220, 250 and 280 °C. Thus, the largest nitrogen content occurred at a doping temperature of 160 °C.

Table 3.4: Elemental composition of N-rGO.

Sample	Elemental analysis	
	Nitrogen/%	Oxygen/%
GO	-	42.985 ± 5
N-rGO-1N-600 °C	8.351 ± 5	1.496 ± 5
N-rGO-1N-700 °C	7.053 ± 5	1.255 ± 5
N-rGO-1N-800 °C	6.982 ± 5	0.464 ± 5
N-rGO-2N-600 °C	10.204 ± 5	0.789 ± 5
N-rGO-2N-700 °C	7.697 ± 5	0.613 ± 5
N-rGO-2N-800 °C	7.490 ± 5	0.239 ± 5
N-rGO-3N-600 °C	15.431 ± 5	3.475 ± 5
N-rGO-3N-700 °C	11.981 ± 5	3.029 ± 5
N-rGO-3N-800 °C	9.578 ± 5	1.082 ± 5

Varying the nitrogen precursors was found to influence the level of doping of N-rGO. 4-nitro-*o*-phenylenediamine which contains the most nitrogen atoms in its structure (3 N atoms per molecule), resulted in high nitrogen content than for the other nitrogen precursors. The nitrogen content of N-rGO-3N synthesized from 4-nitro-*o*-phenylenediamine at temperatures of 600, 700 and 800 °C was 15.431, 11.981 and 9.578%, respectively. As the nitrogen content in N-rGO increased, the oxygen content was also found to increase. The decrease in oxygen content from a doping temperature of 600 to 800 °C was attributed to deoxygenation in N-rGO. Higher oxygen content was observed in the N-rGO-3N-600 °C. This is because 4-nitro-*o*-phenylenediamine contains more oxygen atoms in its structure than the other precursors, therefore, during the doping process, oxygen was also introduced. A correlation was observed between the crystallinity and elemental composition of N-rGO. Less crystalline N-rGO was found to contain a higher nitrogen content. This is exemplified by N-rGO-3N-600 °C with a

greater density of defects (high I_D/I_G ratio) and nitrogen content. An increase in nitrogen-doping also resulted in a decrease in crystallite size (Table 3.2). This is consistent with the findings reported by Zhang *et al.* [72].

The nitrogen bonding configuration in N-rGO affects the electronic properties [73]. Thus, the incorporation of nitrogen in GO and the C-N bonding configurations were investigated using XPS (Figure 3.7). The trend in nitrogen content observed from the XPS analysis correlates with the results obtained from elemental analysis (Table 3.4). The C 1s and N 1s peaks in N-rGO appear at about 284 and 400 ± 0.1 eV, respectively. The C 1s spectra (Supplementary Materials – Table S1) of N-rGO synthesized from different nitrogen precursors show a slight shift in the binding energies of the peaks that correspond to C=C, C-N, C-O, carboxylate (O=C-O) and carbonyl (C=O) bonds. Zhang *et al.* [74] and Sheng *et al.* [75] reported that the C-O bonding configuration disappears after the doping and annealing process. However, this was not the case here since the C-O bonding peak remained, and this indicates that most oxygen groups in N-rGO were not completely removed. N-rGO-3N-600 °C showed C, O, and N peaks with percentage compositions of 81.5, 9.5 and 8.5%, respectively. N-rGO-3N-600 °C had a higher nitrogen content and lower carbon and oxygen content than N-rGO-1N-600 °C and N-rGO-2N-600 °C.
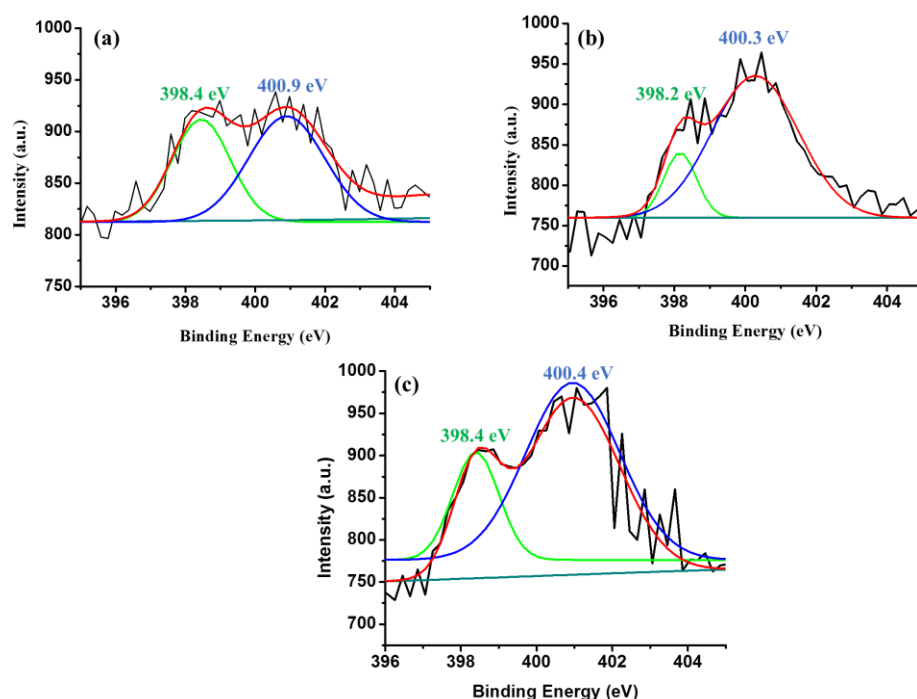
Figure 3.7: XPS high-resolution N 1s spectra of (a) N-rGO-1N-600 °C, (b) N-rGO-2N-600 °C and (c) N-rGO-3N-600 °C.

Nitrogen-doped reduced graphene oxide is reported to contain the three most desired, nitrogen bonding configurations namely, pyrrolic-N, pyridinic-N and graphitic-N with different components of N 1s at 399.8 - 401.2 eV, 398.1 - 99.3 eV and 401.1 - 402.7 eV, respectively [76,77]. However, these N 1s positions vary in comparatively wide ranges in different studies. Figure 3.7 shows a comparison of the different XPS spectra and the presence of various nitrogen (N 1s) species in N-rGO. The N 1s spectra of all N-rGO samples were fitted into two peaks, namely, pyrrolic-N and pyridinic-N. The N 1s spectra for N-rGO-1N-600 °C and N-rGO-2N-600 °C are lower in intensity, therefore it was not possible to determine the percentage of each bonding configuration. However, the N 1s spectrum for N-rGO-3N-600 °C was fitted into two N 1s peaks, namely pyrrolic-N at 400.4 ± 0.1 eV with a 46% content and pyridinic-N at 398.4 ± 0.1 eV with a 54% constant. These results suggest that N-rGO-3N-600 °C possesses a greater content of pyridinic-N than pyrrolic-N. An increase of pyridinic-N in N-rGO is related to lower thermal stability and higher surface area. This suggests that there are more defects in N-rGO-3N-600 °C. The lower pyrrolic-N content in N-rGO-3N-600 °C is due to the lower stability of pyrrolic-N which occurs in carbon materials that are doped at lower temperatures [78].

The doping temperatures control the type of nitrogen bonding configuration. For example, low doping temperatures are reported to produce N-rGO in which pyrrolic-N and pyridinic-N dominate [56]. Lu *et al.* [24] also noted that N-rGO synthesized at low temperatures acquired a higher degree of microstructural disorder associated with the higher nitrogen content. Moreover, it was found that the quality of the resulting N-rGO microstructure was directly dependent on the doping temperature.

3.3.5 Phase composition

The structure and phase compositions of all N-rGO were investigated by powder-XRD. The X-ray diffractograms of GO, N-rGO-1N-600 °C, N-rGO-2N-600 °C and N-rGO-3N-600 °C are presented in Figure 3.8. In the case of GO, a diffraction peak was observed at 13.8° (2θ). However, all the samples with nitrogen are devoid of this peak at 2θ = 13.8°. This may be due to the deoxidization of oxygen-containing functional groups in the N-rGO structure. The (004) diffraction peak indicates the crystallinity of the synthesized GO and N-rGO. The diffractograms of N-rGO-1N-600 °C, N-rGO-2N-600 °C and N-rGO-3N-600 °C have a broad diffraction peak at 25.1°, 25.5° and 25.6°, respectively, indicating a high graphitic degree. The nitrogen-rich sample, N-rGO-3N-600 °C have a higher shift of the 2θ angle compared with N-

rGO-1N-600 °C and N-rGO-2N-600 °C. The 2θ angle shift may be caused by strain, stress, defects and dislocation induced in the crystal lattice during nitrogen-doping.
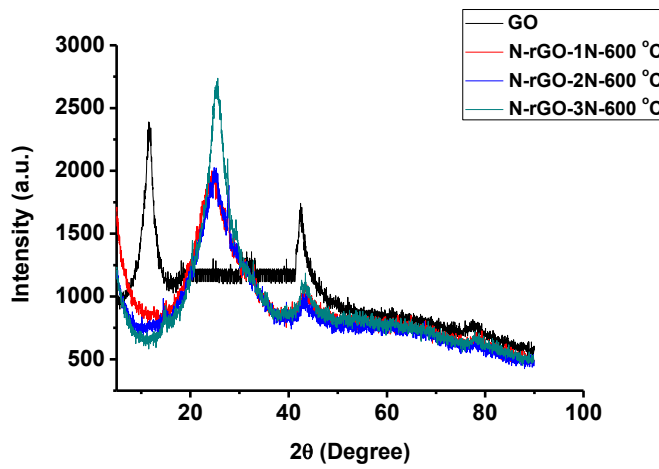
Figure 3.8: Powder X-ray diffractograms of GO, N-rGO-1N-600 °C, N-rGO-2N-600 °C and N-rGO-3N-600 °C.

Microstructural parameters (lattice dimensions, dislocation density and micro-strain) were determined from the diffraction 2θ angles and the Scherrer equation. Table 3.5 shows various XRD parameters for N-rGO.

Table 3.5: Powder-XRD-parameters for N-rGO prepared at a doping temperature of 600 °C.

Sample	$2\theta/°$	FWHM/β_{hkl}	Inter-layer spacing/nm	Crystallite size/nm
GO	13.8	2.12	0.640	3.93
N-rGO-1N-600 °C	25.1	7.8	0.186	1.09
N-rGO-2N-600 °C	25.5	10.8	0.183	0.79
N-rGO-3N-600 °C	25.6	11.4	0.182	0.75

FWHW = full width at half maximum

The peak intensity and peak width of 2θ vary significantly depending on the doping of GO. The FWHM of 2θ of N-rGO increased with increased nitrogen content, which in turn depended on the nitrogen precursor. However, the shift in 2θ causes a decrease in the d_{002} spacing which is associated with a reduction of epoxy, hydroxyl, and carboxyl functional groups on the GO framework. For instance, the broad (002) peak and decrease in crystallinity in N-rGO-3N-600 °C is due to the increased nitrogen content. Increasing the nitrogen content causes an increase in a structural strain of N-rGO-3N-600 °C, thus resulting in enhanced surface defects of the graphite layer which probably led to the broadening of the FWHM of the peak. The increase

of FWHM observed concurred with the decrease in thermostability from TGA analysis (Figure 3.4). These changes also correspond to the variations in lattice distortions and d_{002} spacings. For example, the d_{002} spacing of GO (0.640 nm) was larger than those of N-rGO and this correlates with the increase in nitrogen content. N-rGO-3N-600 °C with a higher nitrogen content of 8.5% had a d_{002} spacing of 0.182 nm, while a lower nitrogen content (3.0%) in N-rGO-1N-600 °C resulted in a d_{002} spacing of 0.186 nm. The d_{002} spacings of the N-rGO samples obtained from XRD correspond with those determined from HR-TEM analysis (Table 3.1). Hence, it can be concluded that nitrogen-doping influences the d_{002} spacing. The crystallite sizes of the synthesized N-rGO also tend to decrease with higher nitrogen content in N-rGO, which indicates an increase in the number of defects induced. These observations of crystallite size (XRD) correlate with the calculated crystallite sizes from Raman spectroscopy (Table 3.2). N-rGO-3N-600 °C had a smaller crystallite size (0.75 nm) than either GO or the other N-rGO (N-rGO-1N and N-rGO-2N).

3.3.6 Optical properties

The optical properties of the N-rGO were investigated by UV-Vis spectrophotometry. From the work reported by Loryuenyong *et al.* [79], the maximum absorption wavelength of GO was reported to be around 230 - 270 nm. In Figure 3.9, GO exhibited a maximum absorption peak at 234 nm that is associated with π-π* and n-π* transitions of C=C and C=O bonds, respectively [80]. In contrast, N-rGO shows an absorption peak at 262 - 275 nm. The shift to a longer wavelength indicates the deoxygenation and restoration of the electronic π-conjugation of GO [81]. The peaks between 260 - 275 nm in the N-rGO spectra are attributed to π-π* transitions of the double bonds. The introduction of more lone electrons creates more n-π* transitions which tend to shift absorption to longer wavelength (since energy is inversely proportional to the wavelength). This shows a characteristic of sp^2 hybridization bands and lone pairs of nitrogen. A significant increase in absorbance was noted which shifted towards the visible light range as the nitrogen content increased. This shift also enables N-rGO to have a better capability of light-harvesting compared with GO. This is because freer electrons are easier to excite than bound (π-electrons) and therefore π-π* are fewer than n-π*, hence the shift to longer wavelength, a phenomenon which is required for light-harvesting. Mohamed *et al.* [82] reported that heteroatom-doped graphene with an absorption frequency ranging from 300 - 650 nm had limited photocatalytic activity resulting in a lower light-harvesting capability. The nitrogen-rich sample (N-rGO-3N-600 °C) exhibited a slightly shift in absorption peak.
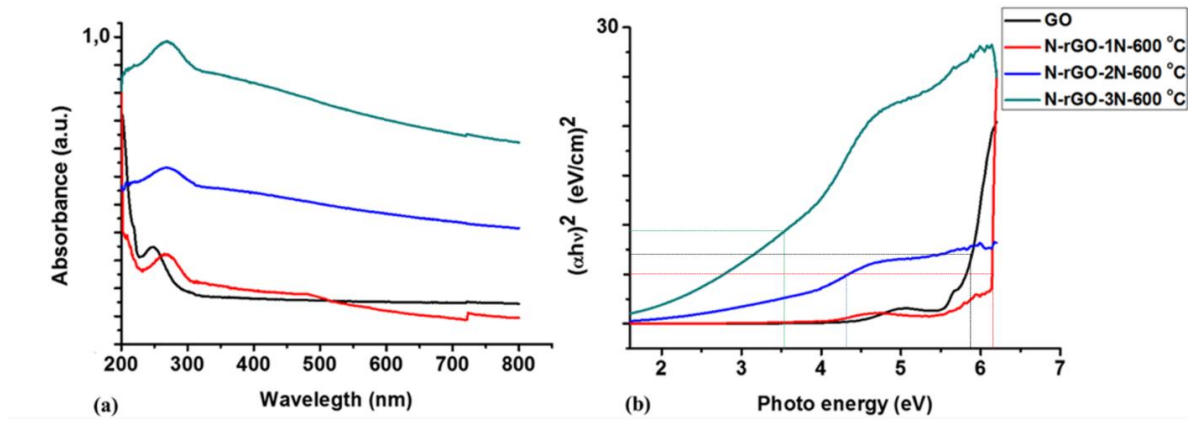
Figure 3.9: (a) UV-Vis absorption spectra and (b) Tauc plots for GO, N-rGO-1N-600 °C, N-rGO-2N-600 °C and N-rGO-3N-600 °C.

In the Tauc plot for N-rGO and GO (Figure 3.9 (b)), N-rGO exhibited two absorption edges that correspond to rGO. The optical bandgaps obtained from the Tauc plots are: 5.9 eV for GO, 6.2 eV for N-rGO-1N-600 °C, 4.4 eV for N-rGO-2N-600 °C and 3.5 eV for N-rGO-3N-600 °C. To further confirm the trend displayed in the Tauc plots, the optical bandgap (Table 3.6) was also recalculated by Planck's quantum equation:

$$E = \frac{hc}{\lambda} \qquad (2)$$

$$= \frac{1.2 \, X 10^{-6}}{\lambda}$$

where, h represents Planck's constant, c is the speed of light, and λ is a absorption wavelength [83]. N-rGO-3N-600 °C showed a slight decrease in energy bandgap (4.5 eV). While N-rGO with lower nitrogen content, *i.e.* N-rGO-1N-600 °C and N-rGO-2N-600 °C had a bandgap of 4.8 and 4.6 eV, respectively.

Table 3.6: Energy bandgap of N-rGO from a doping temperature of 600 °C obtained from Planck's quantum equation.

Sample	Wavelength/nm	Bandgap energy/eV
GO	234	5.3
N-rGO-1N-600 °C	262	4.8
N-rGO-2N-600 °C	271	4.6
N-rGO-3N-600 °C	275	4.5

The decrease in bandgap energies of N-rGO may be due to compensation of the bandgap states associated with the incorporation of dopant atoms, and this resulted in the Fermi level moving up in the direction of the conduction band edge [84]. This implies that higher nitrogen content in N-rGO induces a lower rate of electron-hole (e^-/h^+) recombination than for N-rGO with lower nitrogen content. The large bandgaps for N-rGO-1N-600 °C and N-rGO-2N-600 °C indicate that lower nitrogen content may not be ideal for light-harvesting. Smaller bandgap energies can lead to enhancement of visible light trapping than larger bandgap energies. The e^-/h^+ recombination of N-rGO was therefore investigated by photoluminescence spectroscopy. A comparison of the e^-/h^+ recombination dynamics of N-rGO is presented in Figure 3.10.
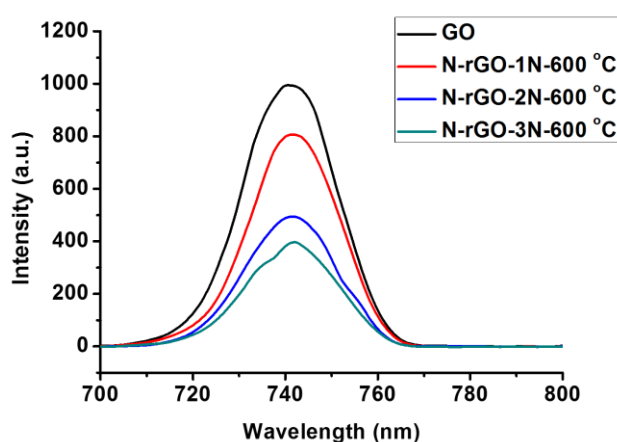
Figure 3.10: A comparison of the photoluminescence spectra of N-rGO.

The intra-bandgap, which is associated with local defect functions as a trap for free carriers, affects the recombination and electron transport [85]. All N-rGO from different nitrogen precursors luminescence at e^-/h^+ recombination rate of 745 nm as shown in Figure 3.10. However, their photoluminescence peak intensities are different. The variation of nitrogen precursor showed the enhancement of photoluminescence peak intensity. Van Khai *et al.* [86] reported that the doping temperatures tend to cause a shift in wavelength, which is due to the presence of quaternary-N, whereas the presence of pyrrolic-N and pyridinic-N was closely related to the enhancement of photoluminescence peak intensity. Therefore, the enhanced photoluminescence intensity in N-rGO corresponds to the decrease density of pyrrolic-N. Whereas, the increased density of pyridinic-N may be correlated with the decrease of non-radiative recombination. N-rGO-1N-600 °C with a lower nitrogen content had a higher photoluminescence peak intensity while N-rGO-3N-600 °C with a higher nitrogen content was

of lower intensity. This further suggests that N-rGO-3N-600 °C has a lower rate of a e^-/h^+ recombination.

3.3.7   Electrical conductivity properties

To study the effect of nitrogen content on the electrical conductivity of N-rGO, the current-voltage (I–V) characteristics (Figure 3.11) was used. All the N-rGO samples exhibited a linear I-V relationship. However, the I-V slope of the GO sample is almost close to zero. This is due to high oxygen content (oxygen functional group) which cause GO to behave like an insulating material [87]. Generally, the structure of GO is amorphous because of distortions from the sp^3-oxygen (C–O–C, C–OH and COOH). Additionally, because of the random dispersion, the sp^2-hybridized benzene rings are isolated by sp^3-hybridized rings, in this way promoting the insulating characteristics. In the case of N-rGO, the I–V slope significantly increased, demonstrating that the electrical conductivity of N-rGO was enhanced. The enhanced electrical conductivity can be attributed to the reduction of oxygen functional groups and restoration of the sp^2 carbon network.
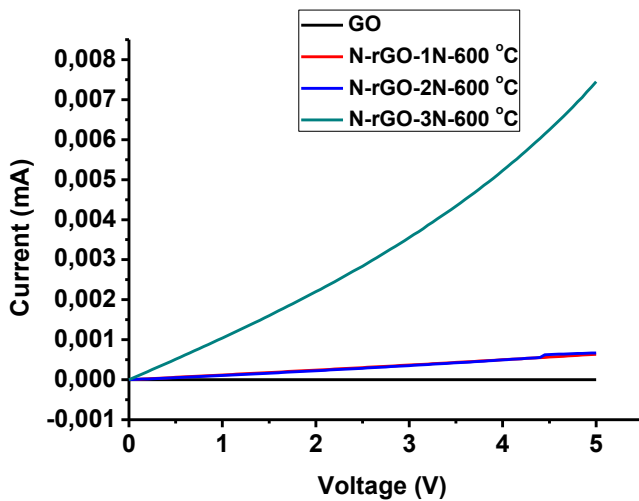
Figure 3.11: Current-voltage curve of N-rGO at doping temperature of 600 °C.

The electrostatic investigation on the effect of nitrogen-doping on the electrical bandgap of GO was carried out by firstly, determining resistivity (ρ), using the four-probes relation:

$$\rho = \left(\frac{\pi}{\ln 2}\right)\left(\frac{V}{I}\right) t \qquad (3)$$

where V is the voltage between the two inner probes, I is the current into and out of the sheet between the two outer probes, and t is the sheet thickness [88]. The obtained ρ was then used in the estimation of the electrical bandgap (E_g) as follows:

$$E_g = 2k \frac{\Delta \ln \rho}{\Delta T^{-1}} \qquad (4)$$

where $\frac{\Delta \ln \rho}{\Delta T^{-1}}$ is a slope on $\ln \rho$ versus T-1 plot and k is the Boltzmann constant (0.000086 eV/K) and T is the temperature in Kelvin. It was generally observed that nitrogen-doping has the effect of reducing the electrical bandgap of GO structure (Table 3.7). However, N-rGO-1N-700 °C and N-rGO-2N-800 °C had non-linear relations an indication of two conductive regimes. This can be attributed to dominant N configuration, doping concentration and the respective temperatures. A doping temperature of 700 °C produced N-rGO with lower dopant concentration, and a pyrrolic-N configuration was dominant. A higher conjugation on average is expected and therefore much lower electrical bandgap compared to the pyridinic-N configuration at the same temperature.

Table 3.7: Effect of nitrogen-doping temperature on the electrical bandgap of GO.

Sample	Resistivity/Ω mm^{-1}	Conductivity/mmS m^{-1}	Bandgap/eV
GO	7.89	0.127	3.24
N-rGO-1N-600 °C	4.92	0.203	2.50
N-rGO-2N-600 °C	4.63	0.216	2.40
N-rGO-3N-600 °C	5.00	0.200	2.52
N-rGO-1N-700 °C	3.29	0.304	1.86
N-rGO-2N-700 °C	5.04	0.198	2.53
N-rGO-3N-700 °C	4.93	0.203	2.50
N-rGO-1N-800 °C	4.59	0.218	2.39
N-rGO-2N-800 °C	8.03	0.125	3.26
N-rGO-3N-800 °C	4.63	0.216	2.40

The electrical conductivities are shown in Table 3.8, obtained from four-point probe measurements, this is exhibiting an increase in conductivity with an increase in nitrogen content. N-rGO-3N-600 °C sample exhibited the highest electrical conductivity and excellent ultra-low electrical resistivity. So far, the mechanism of enhancement of electrical conductivity of N-rGO is not yet understood. It is believed that the interaction of N-C and interfacial

structure are key variables of controlling electrical conduction. The high electrical conductivity in N-rGO-3N-600 °C may be attributed to the restoration of the π-electrons conjugated network in graphene, prompting more formation of percolation pathways within the sp^2 carbon atoms. The dominant nitrogen bonding configuration in N-rGO-3N-600 °C is pyridinic-N, which allows electrons within the π-graphene structure, lower stone-wall defects, creating high electron percolation pathways and quite a low conduction gap, hence, enhanced conductivity. Therefore, N-rGO-3N-600 °C that was synthesized have basal pyridinic-N than edge substitution, due to the availability of electrons within conduction space, elevating the density of state near the Dirac point. Thus, creates a specialized band around the Dirac point. The created band gives rise to a finite density of states near the Dirac point and enhance the electrical conductivity. Hence, it can be suggested that the electrical conductivity of N-rGO might be dependent on the nitrogen content which is incorporated into the structure of GO. Consequently, N-rGO-3N-600 °C serves as a promising material for various applications such as electronic and opto-electronic devices.

Table 3.8: Electrical conductivity of the N-rGO at doping temperature of 600 °C.

Sample	Sheet resistance/Ω sq^{-1}	Bulk resistivity/Ω cm	Electrical conductivity/S cm^{-1}
GO	9.147×10^6	8.289×10^4	1.210×10^{-5}
N-rGO-1N-600 °C	8.764×10^3	794.6	1.260×10^{-3}
N-rGO-2N-600 °C	8.769×10^3	554.9	1.820×10^{-3}
N-rGO-3N-600 °C	830.5	7.500	1.330×10^{-1}

3.4 Conclusion

In conclusion, N-rGO has been successfully synthesized from solid nitrogen precursors (4-aminophenol, 4-nitroaniline and 4-nitro-*o*-phenylenediamine). The incorporation of the N atom into the GO lattice at various doping temperatures caused a significant effect on the physicochemical properties such as surface morphology, surface chemistry, surface area and porosity. Microscopic studies showed a more wrinkled-like structure on N-rGO than for GO due to the presence of nitrogen atoms in the GO framework. By lowering the doping temperature, higher nitrogen content was incorporated into the GO lattice. The nitrogen content of N-rGO varied for different nitrogen precursors. N-rGO exhibited lower thermal stability as the level of nitrogen-doping increased, due to more defects and distortions

experienced in the N-rGO structure. The enhancement of surface area and a high degree of disorder on N-rGO were attributed to the removal of oxygen-containing functional groups.

N-rGO-1N-600 °C, N-rGO-2N-600 °C and N-rGO-3N-600 °C had a nitrogen content of 3.0, 3.7 and 8.5%, respectively. The nitrogen-rich precursor, 4-nitro-o-phenylenediamine, led to higher doping of N-rGO. N-rGO-3N-600 °C was found to have the highest nitrogen content of 8.5% and a high surface area of 154.02 m^2 g^{-1} though it was less crystalline and manifested low thermal stability. The peak fitting of N 1s in all N-rGO samples produced two major components of pyridinic-N and pyrrolic-N with different nitrogen content. N-rGO showed good absorption and luminescence in the near UV region. The photoluminescence peak intensity and bandgap values were highly dependent on nitrogen content. Higher nitrogen content in N-rGO exhibited a smaller optical bandgap of 4.5 eV with lower photoluminescence peak intensity. N-rGO-3N-600 °C exhibited higher electrical conductivity of 0.133 S cm^{-1}.

References

1. M. Ye, Z. Zhang, Y. Zhao and L. Qu, *Joule*, **2018**, 2, 245-268.
2. S. D. Lee, H. S. Lee, J. Y. Kim, J. Jeong and Y. H. Kahng, *Mater. Res. Express*, **2017**, 4, 085601-085610.
3. Y. Yao and J. Ping, *Trends Anal. Chem.*, **2018**, 105, 75-88.
4. K. Bhatt, C. Rani, M. Vaid, A. Kapoor, P. Kumar, S. Kumar, S. Shriwastawa, S. Sharma, R. Singh and C. Tripathi, *Pramana-J. Phys.*, **2018**, 90, 71-76.
5. S. Priyadarsini, S. Mohanty, S. Mukherjee, S. Basu and M. Mishra, *J. Nanostructure Chem.*, **2018**, 8, 123-137.
6. G. Lu, K. Yu, Z. Wen and J. Chen, *Nanoscale*, **2013**, 5, 1353-1368.
7. M. Czerniak-Reczulska, A. Niedzielska and A. Jędrzejczak, *Adv. Mater. Sci.*, **2015**, 15, 67-81.
8. H. Liu, Y. Liu and D. Zhu, *J. Mater. Chem.*, **2011**, 21, 3335-3345.
9. R. L. D. Whitby, *ACS Nano*, **2014**, 8, 9733-9754.
10. D. Chen, L. Tang and J. Li, *Chem. Soc. Rev.*, **2010**, 39, 3157-3180.
11. V. Thirumal, A. Pandurangan, R. Jayavel and R. Ilangovan, *Synth. Met.*, **2016**, 220, 524-532.
12. S. Li, Z. Wang, H. Jiang, L. Zhang, J. Ren, M. Zheng, L. Dong and L. Sun, *Chem. Commun.*, **2016**, 52, 10988-10991.

13. D. Y. Usachov, A. V. Fedorov, O. Y. Vilkov, A. E. Petukhov, A. G. Rybkin, A. Ernst, M. M. Otrokov, E. V. Chulkov, I. I. Ogorodnikov and M. V. Kuznetsov, *Nano Lett.*, **2016**, 16, 4535-4543.

14. M. Megawati, C. K. Chua, Z. Sofer, K. Klimova and M. Pumera, *Phys. Chem. Chem. Phys.*, **2017**, 19, 15914-15923.

15. Z. Xing, Z. Ju, Y. Zhao, J. Wan, Y. Zhu, Y. Qiang and Y. Qian, *Sci. Rep.*, **2016**, 6, 26141-26150.

16. W. Cai, C. Wang, X. Fang, L. Yang and X. Chen, *Appl. Phys. Lett.*, **2015**, 106, 253101-253105.

17. X. Wang, G. Sun, P. Routh, D.-H. Kim, W. Huang and P. Chen, *Chem. Soc. Rev.*, **2014**, 43, 7067-7098.

18. C. N. R. Rao, K. Gopalakrishnan and A. Govindaraj, *Nano Today*, **2014**, 9, 324-343.

19. D. Usachov, O. Vilkov, A. Gruneis, D. Haberer, A. Fedorov, V. Adamchuk, A. Preobrajenski, P. Dudin, A. Barinov and M. Oehzelt, *Nano Lett.*, **2011**, 11, 5401-5407.

20. M. P. Kumar, T. Kesavan, G. Kalita, P. Ragupathy, T. N. Narayanan and D. K. Pattanayak, *RSC Adv.*, **2014**, 4, 38689-38697.

21. A. Ambrosi, C. K. Chua, N. M. Latiff, A. H. Loo, C. H. A. Wong, A. Y. S. Eng, A. Bonanni and M. Pumera, *Chem. Soc. Rev.*, **2016**, 45, 2458-2493.

22. T. Lin, F. Huang, J. Liang and Y. Wang, *Energy Environ. Sci.*, **2011**, 4, 862-865.

23. H. L. Poh, P. Šimek, Z. Sofer, I. Tomandl and M. Pumera, *J. Mater. Chem. A*, **2013**, 1, 13146-13153.

24. Y.-F. Lu, S.-T. Lo, J.-C. Lin, W. Zhang, J.-Y. Lu, F.-H. Liu, C.-M. Tseng, Y.-H. Lee, C.-T. Liang and L.-J. Li, *ACS Nano*, **2013**, 7, 6522-6532.

25. T. Wang, L.-X. Wang, D.-L. Wu, W. Xia and D.-Z. Jia, *Sci. Rep.*, **2015**, 5, 9591-9599.

26. Z. Luo, S. Lim, Z. Tian, J. Shang, L. Lai, B. MacDonald, C. Fu, Z. Shen, T. Yu and J. Lin, *J. Mater. Chem.*, **2011**, 21, 8038-8044.

27. S. Zhang, S. Tsuzuki, K. Ueno, K. Dokko and M. Watanabe, *Angew. Chem. Int. Ed.*, **2015**, 54, 1302-1306.

28. W. He, C. Jiang, J. Wang and L. Lu, *Angew. Chem. Int. Ed.*, **2014**, 53, 9503-9507.

29. S. Park, Y. Hu, J. O. Hwang, E.-S. Lee, L. B. Casabianca, W. Cai, J. R. Potts, H.-W. Ha, S. Chen and J. Oh, *Nat. Commun.*, **2011**, 3, 638-638.

30. L. Zhao, R. He, K. T. Rim, T. Schiros, K. S. Kim, H. Zhou, C. Gutiérrez, S. Chockalingam, C. J. Arguello and L. Pálová, *Science*, **2011**, 333, 999-1003.

31. N. Li, Z. Wang, K. Zhao, Z. Shi, Z. Gu and S. Xu, *Carbon*, **2010**, 48, 255-259.

32. X. Zhang, A. Hsu, H. Wang, Y. Song, J. Kong, M. S. Dresselhaus and T. Palacios, *ACS Nano*, **2013**, 7, 7262-7270.

33. X.-j. Li, X.-x. Yu, J.-y. Liu, X.-d. Fan, K. Zhang, H.-b. Cai, N. Pan and X.-p. Wang, *Chin. J. Chem. Phys.*, **2012**, 25, 321-326.

34. H. Wang, Y. Zhou, D. Wu, L. Liao, S. Zhao, H. Peng and Z. Liu, *Small*, **2013**, 9, 1316-1320.

35. T. Wu, H. Shen, L. Sun, B. Cheng, B. Liu and J. Shen, *New J. Chem.*, **2012**, 36, 1385-1391.

36. S. Zhou, N. Liu, Z. Wang and J. Zhao, *ACS Appl Mater Interfaces*, **2017**, 9, 22578-22587.

37. N. Guo, Y. Xi, S. Liu and C. Zhang, *Sci. Rep.*, **2015**, 5, 12051-12058.

38. D. Du, P. Li and J. Ouyang, *ACS Appl Mater Interfaces*, **2015**, 7, 26952-26958.

39. A. Zabet-Khosousi, L. Zhao, L. Pálová, M. S. Hybertsen, D. R. Reichman, A. N. Pasupathy and G. W. Flynn, *J. Am. Chem. Soc.*, **2014**, 136, 1391-1397.

40. H. Wang, T. Maiyalagan and X. Wang, *ACS Catal.*, **2012**, 2, 781-794.

41. L. Van Nang, N. Van Duy, N. D. Hoa and N. Van Hieu, *J. Electron. Mater.*, **2016**, 45, 839-845.

42. L. Panchakarla, K. Subrahmanyam, S. Saha, A. Govindaraj, H. Krishnamurthy, U. Waghmare and C. Rao, *Adv. Mater.*, **2009**, 21, 4726-4730.

43. J. F. Bao, N. Kishi and T. Soga, *Mater. Lett.*, **2014**, 117, 199-203.

44. C. Zhang, W. Lin, Z. Zhao, P. Zhuang, L. Zhan, Y. Zhou and W. Cai, *Sci. China Phys. Mech.*, **2015**, 58, 107801-107805.

45. R. Vishwakarma, G. Kalita, S. M. Shinde, Y. Yaakob, C. Takahashi and M. Tanemura, *Mater. Lett.*, **2016**, 177, 89-93.

46. Z. Wang, P. Li, Y. Chen, J. Liu, H. Tian, J. Zhou, W. Zhang and Y. Li, *J. Mater. Chem. C*, **2014**, 2, 7396-7401.

47. W. S. Hummers Jr and R. E. Offeman, *J. Am. Chem. Soc.*, **1958**, 80, 1339-1339.

48. M.-H. Jiang, D. Cai and N. Tan, *Int. J. Electrochem. Sci.*, **2017**, 12, 7154-7165.

49. K. Yokwana, S. C. Ray, M. Khenfouch, A. T. Kuvarega, B. B. Mamba, S. D. Mhlanga and E. N. Nxumalo, *J. Nanosci. Nanotechnol.*, **2018**, 18, 5470-5484.

50. N. A. Kumar, H. Nolan, N. McEvoy, E. Rezvani, R. L. Doyle, M. E. Lyons and G. S. Duesberg, *J. Mater. Chem. A*, **2013**, 1, 4431-4435.

51. P. Pham, *J. Carbon Res.*, **2018**, 4, 1-34.

52. M.-Y. Yen, C.-K. Hsieh, C.-C. Teng, M.-C. Hsiao, P.-I. Liu, C.-C. M. Ma, M.-C. Tsai, C.-H. Tsai, Y.-R. Lin and T.-Y. Chou, *RSC Adv.*, **2012**, 2, 2725-2728.

53. P. Ayala, R. Arenal, M. Rümmeli, A. Rubio and T. Pichler, *Carbon*, **2010**, 48, 575-586.

54. Z. Zafar, Z. H. Ni, X. Wu, Z. X. Shi, H. Y. Nan, J. Bai and L. T. Sun, *Carbon*, **2013**, 61, 57-62.

55. B. J. Matsoso, K. Ranganathan, B. K. Mutuma, T. Lerotholi, G. Jones and N. J. Coville, *RSC Adv.*, **2016**, 6, 106914-106920.

56. J.-h. Song, C.-M. Kim, E. Yang, M.-H. Ham and I. Kim, *RSC Adv.*, **2017**, 7, 20738-20741.

57. A. Capasso, T. Dikonimos, F. Sarto, A. Tamburrano, G. De Bellis, M. S. Sarto, G. Faggio, A. Malara, G. Messina and N. Lisi, *Beilstein J. Nanotechnol.*, **2015**, 6, 2028-2038.

58. P. Mallet-Ladeira, P. Puech, C. Toulouse, M. Cazayous, N. Ratel-Ramond, P. Weisbecker, G. L. Vignoles and M. Monthioux, *Carbon*, **2014**, 80, 629-639.

59. S. Pei and H.-M. Cheng, *Carbon*, **2012**, 50, 3210-3228.

60. M. Mowry, D. Palaniuk, C. C. Luhrs and S. Osswald, *RSC Adv.*, **2013**, 3, 21763-21775.

61. N. Justh, B. Berke, K. László and I. M. Szilágyi, *J. Therm. Anal. Calorim.*, **2018**, 131, 2267-2272.

62. B. Y. S. Chang, N. M. Huang, M. N. An'amt, A. R. Marlinda, Y. Norazriena, M. R. Muhamad, I. Harrison, H. N. Lim and C. H. Chia, *Int. J. Nanomedicine*, **2012**, 7, 3379-3387.

63. M. Khandelwal and A. Kumar, *Dalton Trans.*, **2016**, 45, 5180-5195.

64. A. Kumar, A. Ganguly and P. Papakonstantinou, *J. Phys. Condens. Matter*, **2012**, 24, 235501-235506.

65. H. C. Youn, S. M. Bak, M. S. Kim, C. Jaye, D. A. Fischer, C. W. Lee, X. Q. Yang, K. C. Roh and K. B. Kim, *ChemSusChem*, **2015**, 8, 1875-1884.

66. S. Liu, W. Peng, H. Sun and S. Wang, *Nanoscale*, **2014**, 6, 766-771.

67. C.-M. Chen, J.-Q. Huang, Q. Zhang, W.-Z. Gong, Q.-H. Yang, M.-Z. Wang and Y.-G. Yang, *Carbon*, **2012**, 50, 659-667.

68. C. Fu, C. Song, L. Liu, X. Xie and W. Zhao, *Int. J. Electrochem. Sci.*, **2016**, 11, 3876-3886.

69. K. S. Sing, *Pure Appl. Chem.*, **1985**, 57, 603-619.

70. X. Qiao, S. Liao, C. You and R. Chen, *Catalysts*, **2015**, 5, 981-991.

71. M. F. R. Hanifah, J. Jaafar, M. Aziz, A. F. Ismail, M. A. Rahman and M. H. D. Othman, *J. Teknol.*, **2015**, 74, 189-192.

72. C. Zhang, L. Fu, N. Liu, M. Liu, Y. Wang and Z. Liu, *Adv. Mater.*, **2011**, 23, 1020-1024.

73. J. Zhang, C. Zhao, N. Liu, H. Zhang, J. Liu, Y. Q. Fu, B. Guo, Z. Wang, S. Lei and P. Hu, *Sci. Rep.*, **2016**, 6, 28330-28340.

74. W. Zhang, C.-T. Lin, K.-K. Liu, T. Tite, C.-Y. Su, C.-H. Chang, Y.-H. Lee, C.-W. Chu, K.-H. Wei, J.-L. Kuo and L.-J. Li, *ACS Nano*, **2011**, 5, 7517-7524.

75. Z.-H. Sheng, L. Shao, J.-J. Chen, W.-J. Bao, F.-B. Wang and X.-H. Xia, *ACS Nano*, **2011**, 5, 4350-4358.

76. F. Baldovino, A. Quitain, N. P. Dugos, S. A. Roces, M. Koinuma, M. Yuasa and T. Kida, *RSC Adv.*, **2016**, 6, 113924-113932.

77. F. Chen, L. Guo, X. Zhang, Z. Y. Leong, S. Yang and H. Y. Yang, *Nanoscale*, **2017**, 9, 326-333.

78. M. Chen, L.-L. Shao, Y.-X. Guo and X.-Q. Cao, *Chem. Eng. J.*, **2016**, 304, 303-312.

79. V. Loryuenyong, K. Totepvimarn, P. Eimburanapravat, W. Boonchompoo and A. Buasri, *Adv. Mater. Sci. Eng.*, **2013**, 2013, 1-5.

80. A. Jamil, F. Mustafa, S. Aslam, U. Arshad and M. A. Ahmad, *Chin. Phys. B*, **2017**, 26, 086501-086508.

81. R. Vinoth, S. Ganesh Babu, D. Bahnemann and B. Neppolian, *Sci. Adv. Mater.*, **2015**, 7, 1-7.

82. M. Mokhtar Mohamed, M. A. Mousa, M. Khairy and A. A. Amer, *ACS Omega*, **2018**, 3, 1801-1814.

83. D. Bhatnagar, S. Singh, S. Yadav, A. Kumar and I. Kaur, *Mater. Res. Express*, **2017**, 4, 015101-015110.

84. R. Marschall and L. Wang, *Catal. Today*, **2014**, 225, 111-135.

85. C. H. Chuang, Y. F. Wang, Y. C. Shao, Y. C. Yeh, D. Y. Wang, C. W. Chen, J. W. Chiou, S. C. Ray, W. F. Pong, L. Zhang, J. F. Zhu and J. H. Guo, *Sci. Rep.*, **2014**, 4, 4521-4527.

86. T. Van Khai, H. G. Na, D. S. Kwak, Y. J. Kwon, H. Ham, K. B. Shim and H. W. Kim, *Carbon*, **2012**, 50, 3799-3806.

87. T. Van Khai, H. G. Na, D. S. Kwak, Y. J. Kwon, H. Ham, K. B. Shim and H. W. Kim, *J. Mater. Chem.*, **2012**, 22, 17992-18003.

88.   S. Bose, T. Kuila, M. E. Uddin, N. H. Kim, A. K. T. Lau and J. H. Lee, *Polymer*, **2010**, 51, 5921-5928.

Appendix: Supporting information for Chapter 3
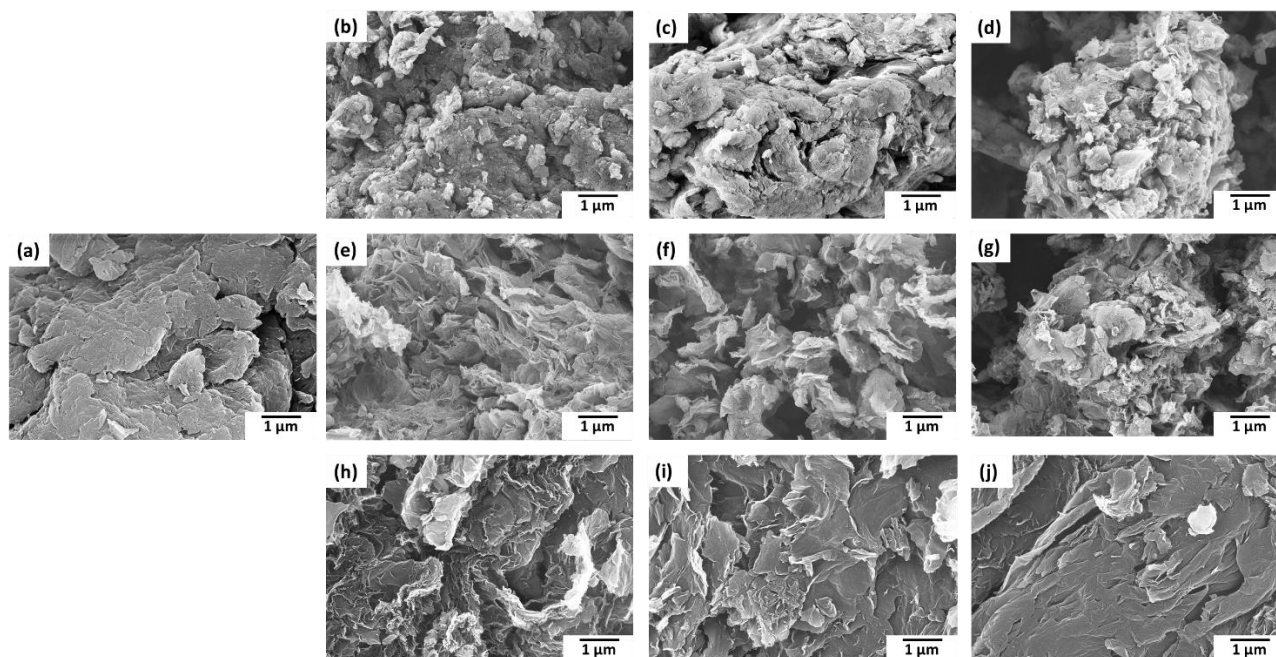
Figure S3.1: SEM images of (a) GO, (b) N-rGO-1N-600 °C, (c) N-rGO-1N-700 °C, (d) N-rGO-1N-800 °C, (e) N-rGO-2N-600 °C, (f) N-rGO-2N-700 °C, (g) N-rGO-2N-800 °C, (h) N-rGO-3N-600 °C, (i) N-rGO-3N-700 °C and (j) N-rGO-3N-800 °C.

Table S3.1: Atomic percentage (%) of N 1s and C 1s peak binding energy (eV).

Sample	Element	Atomic %	Peak binding energy (eV)	Compound (s)	Peak area %
N-rGO-1N	C	84.5	284.8 ± 0.1 eV	C-C	76
			285.6 ± 0.1 eV	C-N	2
			286.4 ± 0.1 eV	C-O	16
			287.7 ± 0.1 eV	C=O	3
			289.0 ± 0.1 eV	O-C=O	3
	O	10.6	532.6 ± 0.1 eV	Organic O	100
	N	3.0	-	-	-
N-rGO-2N	C	83.7	284.9 ± 0.1 eV	C-C	77
			285.0 ± 0.1 eV	C-N	3
			286.5 ± 0.1 eV	C-O	14
			287.8 ± 0.1 eV	C=O	3
			289.1 ± 0.1 eV	O-C=O	3
	O	10.7		Organic O	100
	N	3.7	-	-	-
N-rGO-3N	C	81.5	284.7 ± 0.1 eV	C-C	76
			285.2 ± 0.1 eV	C-N	4
			286.3 ± 0.1 eV	C-O	14
			287.6 ± 0.1 eV	C=O	2
			288.9 ± 0.1 eV	O-C=O	4
	O	9.5	532.2 ± 0.1 eV	Organic O	100
	N	8.5	398.4 ± 0.1 eV	Organic N	54
			400.4 ± 0.1 eV	Organic N	46

CHAPTER 4

Check for updates

Tuning the properties of boron-doped reduced graphene oxide by altering the boron content†

Nonjabulo P. D. Ngidi, (iD) Moses A. Ollengo (iD) and Vincent O. Nyamori (iD) *

The design and fabrication of electronic devices based on graphene nanomaterials are dependent on the tuning of Fermi levels. This can be achieved by doping graphene oxide (GO) with an electron-withdrawing (p-type) or electron-donating (n-type) species that causes changes in the electron density and enhances the electrochemical properties. In this research, the effect of boron content on the optical, electrochemical, and conductivity properties of GO was investigated. Boron-doped reduced graphene oxide (B-rGO) was synthesized *via* a chemical vapor deposition method by using GO and varying amounts of boric anhydride, as a boron precursor, at a doping temperature of 600 °C. The B-rGO samples were characterized by standard spectroscopic techniques. B-rGO had a sheet structure with various graphene islands and disordered regions. The highest boron content incorporated into the reduced GO framework was 7.12%. B-rGO samples manifested strong absorption in the ultraviolet region. An electronic band structure with a low charge resistance of 20.23 Ω and enhanced electrical conductivity properties of 5.920 S cm^{-1} was observed and noted to be dependent on the concentration of boron incorporated. All the B-rGO samples demonstrated a p-type conductivity behaviour which is attributed to an increase in the density of states near the Fermi level. This work opens a new avenue for the fabrication of solar cells based on p-type B-rGO.

Tuning the properties of boron-doped reduced graphene oxide by altering the boron content

Nonjabulo P. D. Ngidi, Moses A. Ollengo, and Vincent O. Nyamori

School of Chemistry and Physics, University of KwaZulu-Natal, Westville Campus, Private Bag X54001, Durban 4000, South Africa

Graphical abstract
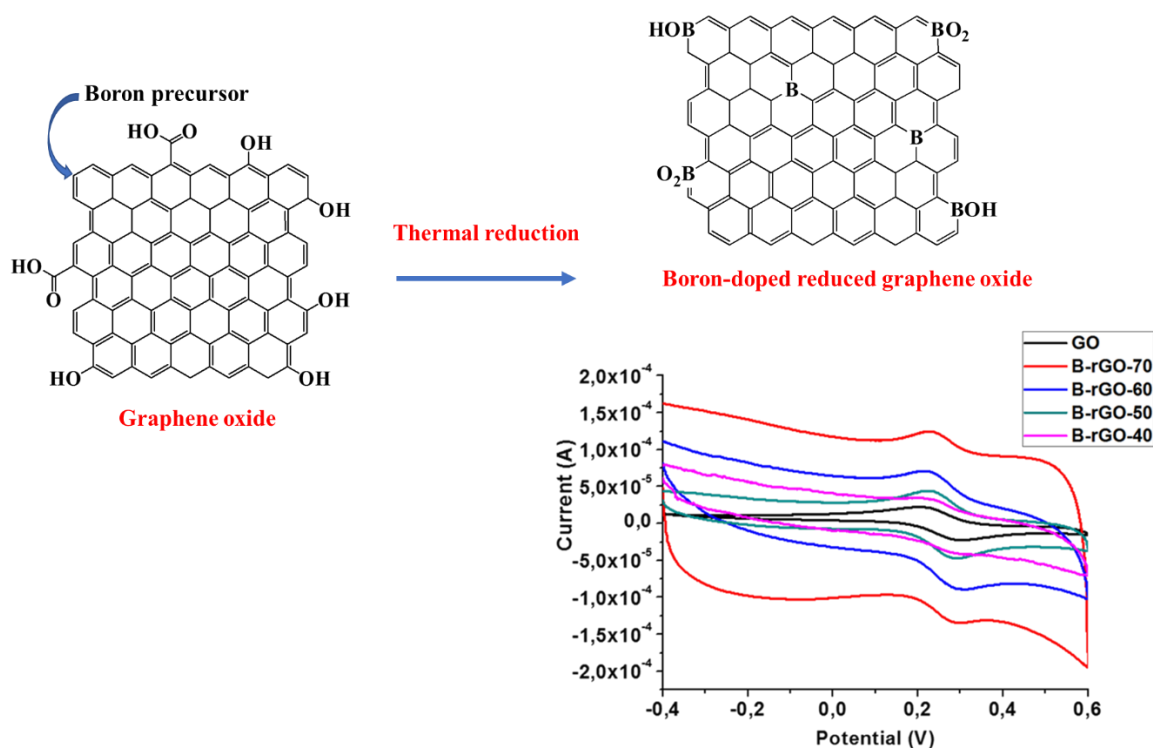
Abstract

The design and fabrication of electronic devices based on graphene nanomaterials are dependent on the tuning of Fermi levels. This can be achieved by doping graphene oxide (GO) with an electron-withdrawing (*p*-type) or electron-donating (*n*-type) species that causes changes in the electron density and enhances the electrochemical properties. In this research, the effect of boron content on the optical, electrochemical, and conductivity properties of GO was investigated. Boron-doped reduced graphene oxide (B-rGO) was synthesized *via* a chemical vapor deposition method by using GO and varying amounts of boric anhydride, as a boron precursor, at a doping temperature of 600 °C. The B-rGO samples were characterized by standard spectroscopic techniques. B-rGO had a sheet structure with various graphene islands and disordered regions. The highest boron content incorporated into the reduced GO framework was 7.12%. B-rGO samples manifested strong absorption in the ultraviolet region. An electronic band structure with a low charge resistance of 20.23 Ω and enhanced electrical conductivity properties of 5.920 S cm^{-1} was observed and noted to be dependent on the concentration of boron incorporated. All the B-rGO samples demonstrated a *p*-type conductivity behaviour which is attributed to an increase in the density of states near the Fermi level. This work opens a new avenue for the fabrication of solar cells based on *p*-type B-rGO.

Keywords

Reduced graphene oxide; Boron-doped; Chemical vapor deposition; Electronic structure; Electrochemical properties

4.1   Introduction

Graphene-based nanomaterials have been widely researched for different potential applications. It is of interest to understand how to modify their electronic structure, through the introduction of heteroatoms or the creation of defects, to fabricate suitable graphene-based materials with appropriate physical, chemical, and electronic properties [1]. The modification of the electronic structure of graphene causes electron modulation to tune its optoelectronic properties for a specific application, such as energy conversion and storage [2,3]. The modification of the carbon sp^2 lattice in graphene results in the formation of covalent bonds with functional groups or other molecules [4]. Exploratory and theoretical investigations on graphene doping demonstrate the possibility of synthesizing *p-* and *n*-type semiconductors *via* the substitution of carbon with various heteroatoms in the graphene framework [5-8]. Thus, various heteroatoms have been doped into the graphene lattice, for example, nitrogen, boron, sulfur, phosphorus, and many different metals.

Boron is one of the heteroatoms that can initiate novel and complementary properties prompting specific applications in solar cells [9]. This is evident from DFT calculations that show that the boron atom can efficiently displace the carbon atom from the graphene lattice and that the energy barrier to dope a boron atom into the graphene lattice is lower than that of a nitrogen atom [10]. The boron atom is less electronegative than a carbon atom and, during doping, it induces a *p*-type conductivity in graphene [11]. Boron-doping in the graphene framework leads to redistribution of electron density, where the electron-deficient boron sites provide enhanced binding capability. This occurs because when boron substitutes carbon in the hexagonal sp^2-bonded structure, it introduces holes as charge carriers which imposes a characteristic bandgap and produces excellent conductivity [2,12,13]. Jia *et al.* [14] reported a higher ratio of *sp*-hybridized carbon to sp^2-hybridized carbon (4:1) which has also showed excellent electrochemical electrode performance and enhanced photocatalytic properties.

In general, boron-doping is advantageous for various applications, such as supercapacitors [15], hydrogen storage [16], potassium-ion batteries [17,18], field emissions [19], gas sensing [20], photo- and heterogeneous-catalysis [21], biomedical applications [22], and solar cells [23]. To investigate the electronic properties of graphene-modified by boron-doping, the total density of states of boron-doped graphene oxide (B-GO) is used. Notably, the Fermi level (E_F) of graphene corresponds with the Dirac point. Boron has one less electron than carbon, thus it can easily displace a carbon atom. Also, the close covalent atomic radii of 85 pm for boron

and 70 pm for carbon allow boron to displace carbon even when the process is linked with a large activation energy barrier such as 2.6 – 2.8 eV [24,25]. This exchange occurs when the interlayer spacing (d_{002}) of epitaxial graphene is bigger, thus, the moiré resulting from the overlaid epitaxial graphene and lattices imposes a potential, inducing Dirac cone replica and leads to the opening of the bandgap in the band structure [26,27]. The B-GO isomers that are formed from various chosen doping sites have been observed to differ in the bandgap, bond length, and stability [28]. The bandgap is observed to be at its greatest when dopants are placed at the same sublattice point of graphene because of the consolidated impact of the symmetrical breaking of sublattices. However, when the dopants are placed at adjacent sublattice positions, it results in a closed bandgap.

The two facets, bandgap, and *p*-type characteristics have been investigated mostly *via* experimental and theoretical approaches. In theoretical computations, boron-doping in a graphene lattice is assumed to substitute the carbon atom, resulting in two outcomes. Firstly, this introduces chirality in the basal plane, and at this point, bandgap oscillations vanish rapidly as a function of the chiral angle [29]. Secondly, carbon substitution by a single boron atom has the potential to induce spontaneous magnetization, independent of the site of substitution [24], arising from a spin polarization, and results in a lower bandgap near the Fermi energy [29,30]. The induced magnetic moment is localized at the substitution site [30,31].

Experimentally, boron-doping can be achieved by different approaches such as hydrothermal or solvothermal synthesis [32-34], high-temperature chemical vapor deposition (CVD) [35], and plasma treatment [36]. These techniques can also be divided into *in situ* and *ex situ* methods. Plasma treatment, which is an *in situ* approach, has been reported to be an efficient route for boron-doping. However, with this method, it is possible to increase the number of defects on the graphene-based nanomaterials, and this further attenuates its electrical conductivity. The issue with *in situ* approaches is that impurities from the metal catalyst precursors inhibit the investigation of the exclusive contribution from the doped material. On the other hand, in the case of *ex situ* approaches, there are also disadvantages, and this includes the requirement of very high temperatures and additional time or steps to obtain efficient boron-doped samples.

Hydrothermal and solvothermal approaches have been used in the synthesis of graphene-based materials, especially in boron-doped graphene. These approaches are performed in a sealed autoclave at temperatures exceeding the boiling points of organic solvents and are not time-

consuming. Thermal exfoliation is also preferable because of its cost-effective, easier to scale-up, and produces large quantities of graphene [37,38]. CVD is a frequently used approach. However, the issue with the CVD method, is that during the doping process, the dopant precursors are not completely exhausted, hence, they may cause contamination and compromise the characteristic electrocatalytic properties. Therefore, purification is required; hot distilled water [2] can be used to remove excess or unreacted boron precursors from doped graphene. Alternatively, for large-scale purification, sodium hydroxide [39], ethanol [40], or hydrochloric acid [15] can be used to remove boron precursors. Normally, NaOH is used because it is effective, easily available, and relatively easy to separate B_2O_3 in B-rGO. The CVD approach is carried out with a certain boron precursor at elevated temperatures [40]. When graphene oxide (GO) or reduced graphene oxide (rGO) are doped with boron, they tend to yield more complex structures such as boronic esters, borinic esters, and boronic acids [11]. The issue with boron-doping is to regulate the boron concentration, bonding configuration, and electron transport properties.

Panchakarla *et al*. [41] reported that a boron content of 2% tends to cause a Fermi level shift of 0.65 eV, exhibiting a *p*-type conductivity. Recently, studies on the synthesis of boron-doped reduced graphene oxide (B-rGO) have focused on the use of various boron precursors and methodologies. In 2016, Thirumal *et al*. [15] reported B-rGO with a doping content of 2.56% by using hydrothermal reduction of boric acid as a boron precursor. However, in 2018, Mannan *et al*. [33] used a similar method to synthesize B-rGO and achieved a boron content of between 1.64 and 1.89%. The difference in boron content was caused by the use of various reactants and reaction conditions (boron precursor, temperature, time, and pressure) during the boron-doping procedure. This suggests that different reactants and reaction conditions result a varying boron content in B-rGO.

In this paper, the conditions for the preparation of B-rGO were optimized, thus, GO was doped with varying amounts of boron (using boric anhydride, B_2O_3 as a precursor) at a doping temperature of 600 °C, by using the CVD approach. Boric anhydride has been widely reported as a boron precursor and tends to result in better doping in graphene [33,42], thus, in this case, it was used. In literature, most of the synthesis of boron doping has been done in higher doping temperatures such as 1200 °C [43], 1000 °C [3], and 700 °C [40]. Thus, the novelty of this work is based on the attempt to introduce different doping percentages in B-rGO at a relatively

lower doping temperature and to determine how the different amounts of boron-doping affect the surface energy, and electrochemical, optical, and conductivity properties.

4.2 Experimental approach

4.2.1 Materials and instrumentation

Boric anhydride (B_2O_3, ≥98%), a boron standard solution (9995 mg ± 20 mg L^{-1}), graphite powder (99.99% trace metal basis), and sodium hydroxide (NaOH, ≥97%) were purchased from Sigma-Aldrich, South Africa. A gas mixture of 10% hydrogen in argon (v/v) was purchased from Afrox Limited Gas Company, South Africa. A digital ultrasonic water bath (400 W), which was supplied by Shalom Laboratory Supplies, South Africa, was used for sonication. Double distilled water was obtained from a double distiller (Glass Chem water distiller model Ws4lcd, supplied by Shalom Laboratory Supplies, South Africa).

4.2.2 Synthesis of B-rGO

GO was synthesized by a modified Hummers' method [44]. B-rGO was synthesized through thermal annealing of GO in the presence of various amounts of B_2O_3. The doping temperature was varied (600, 700, and 800 °C) during the synthesis, and a doping temperature of 600 °C was found to be the optimum doping temperature for B-rGO, thus this article focuses on 600 °C. The synthesis at 600 °C was performed in triplicate. In a typical procedure, GO was first mixed mechanically with different masses of B_2O_3 (40, 50, 60, and 70 *wt.*%, which herein are denoted as B-rGO-40, B-rGO-50, B-rGO-60, and B-rGO-70, respectively). After mechanical mixing, the mixture was transferred into a corundum crucible and, thereafter, placed in the centre of a quartz tube (length 850 mm, inner diameter 27 mm) under a continuous flow of 10% hydrogen in argon. The heating system used was a tube furnace (Elite Thermal Systems Ltd., TSH12/50/610) fitted with a temperature controller (Eurotherm 2416). The furnace was heated from room temperature to 600 °C at an increasing rate of 10 °C min^{-1}. After the furnace had reached 600 °C, the temperature was held constant for two hours, and, thereafter, the sample was allowed to cool naturally to room temperature under an argon atmosphere. For purification, the product obtained (0.5 g) was refluxed at a temperature of 100 °C in a 3 M NaOH aqueous solution for two hours to remove unreacted B_2O_3. The sample was then filtered through a sintered glass funnel under vacuum and washed with double distilled water. Thereafter, the product was dried in an oven at 60 °C for 24 hours. Then, FTIR spectroscopy was used to verify that all the unreacted B_2O_3 had been successfully removed

4.2.3   Characterization

The surface morphology of the synthesized B-rGO was characterized by a field emission scanning electron microscope (FE-SEM, Carl Zeiss Ultra Plus). Further morphological and structural characterizations were performed with a high-resolution transmission electron microscope (HR-TEM, JOEL JEM model 1010).   A Fourier transform infrared spectrophotometer (FTIR, PerkinElmer Spectrum 100) equipped with an attenuated total reflection (ATR) accessory was used to investigate the presence of various functional groups in B-rGO. Briefly, the sample, B-rGO, was pressed into a pellet under a pressure of 10 Tons and thereafter placed on a diamond crystal for analysis. In the case of Raman spectroscopy, a DeltaNu Advantage 532^{TM} Raman spectrophotometer, with an excitation source of an Nd:YAG solid-state crystal class 3b diode, was used to determine the graphitic nature or crystallinity of B-rGO. The excitation wavelength (λ) was 514.5 nm, and Nuspec^{TM} software was used to generate the Raman spectra.

The boron content in B-rGO was determined by electron dispersive X-ray spectroscopy (EDS, Oxford instrument - INCA 4.15) and inductively coupled plasma-optical emission spectrometry (ICP-OES, PerkinElmer Optima 5300 DV). Briefly, 10 mg of each B-rGO sample was digested in a mixture of 30% (v/v) hydrogen peroxide and concentrated sulfuric acid (ratio 3:1, respectively) until the black solid of B-rGO dissolved. The digested mixture was quantitatively transferred to a 100 mL volumetric flask and the solution was made up to the mark with double distilled water. Standard solutions of boron were prepared with different concentrations, i.e. 10, 20, 30, 40, 50, 60, 70, 80, 90, and 100 mg L^{-1}, from a commercial boron standard solution. All the standard solutions and B-rGO samples were filtered through 0.45 μm syringe filters and transferred into ICP vials for analysis.

The surface area and porosity (textural characteristics) of the samples were investigated with a Micromeritics TriStar II 3020 analyzer. Approximately 0.2 g of B-rGO was degassed for 1 h at 90 °C, after which the temperature was raised to 160 °C and further degassed for 12 h in a Micromeritics Vacprep 061 sample degassing system. After degassing, the B-rGO samples were fitted in the Micromeritics TriStar II instrument. The pore volumes were obtained with the Barrett-Joyner-Halenda (BJH) model, while the specific surface area was calculated with the Brunauer–Emmett–Teller (BET) isothermal model.

Thermal stability was investigated using a TA Instruments Q Series™ thermal analysis instrument (DSC/TGA (SDT-Q600)). The B-rGO samples were heated from ambient temperature to 1000 °C at a rate of 10 °C min^{-1} under airflow. X-ray powder diffraction (XRD, Rigaku/Dmax RB) was used to investigate the phase composition of B-rGO with graphite monochromated high-intensity Cu K$_\alpha$ radiation (λ = 0.154 nm) and a θ-θ scan in a locked coupled-mode. Optical properties were determined with a UV-Visible spectrophotometer (Shimadzu, UV-Vis-1800). The GO and B-rGO samples were first dispersed in ethanol absolute and then sonicated for 30 min before analysis. A PerkinElmer LS 55 spectrofluorometer fitted with a solid sample accessory was used to investigate the charge recombination of B-rGO. Excitation was performed at 310 nm, and the emission spectrum was recorded from 450 to 550 nm with the excitation slit and emission slit set at 5 nm and 2 nm, respectively.

Electrical conductivity was determined from four-point probe measurements using a Keithley 2400 source-meter. The B-rGO samples were first formed into a pellet with a thickness of 0.02 mm. Cyclic voltammetry (CV) was conducted on a Metrohm 797 VA Computrace electrochemical workstation with a 57970110-dosing processor potentiostat (Metrohm, Switzerland). Electrochemical impedance spectroscopy (EIS, CHI 600E work station, CHI Instruments) was used to determine the electrochemical properties of B-rGO. A three electrode system was used, namely, a counter electrode (platinum wire, Pt), reference electrode (Ag/AgCl), and working electrode which was prepared by casting the B-rGO sample onto a glassy carbon electrode. A ferro/ferricyanide ($[Fe(CN)6]^{3-/4-}$) redox couple was used as the electrolyte. The CV was performed at a scan rate of 100 mV s^{-1} with a potential range from -0.4 to 0.6 V. The electrodes for electron impedance spectroscopy (EIS) were prepared similarly and the impedance was measured in a frequency range of 1 – 1000 Hz with a potential amplitude of 10 mV s^{-1}.

4.3   Results and discussion

In this work GO and four samples of rGO doped with different amounts of boron were prepared and characterized.

4.3.1   Boron content

The ICP-OES and EDS (Table 4.1 and Supplementary data - Figure S4.1) were used to confirm the targeted boron wt.% for each B-rGO sample prepared. The boron concentrations

determined from ICP-OES were used to further calculate the wt.% doping in the B-rGO. The boron content present in B-rGO was quite low relative to the targeted boron wt.%, this is because the replacement of a carbon atom with a boron atom is difficult. The boron content present (express as mass percentage concentration (%m/m) in B-rGO was found to be between 3.36 and 7.12%, and this followed the trend of the wt.% of boron precursor (boric anhydride) used. For example, sample B-rGO-70 which had the highest amount of boric anhydride provided the highest percentage of boron from ICP-OES analysis, whilst B-rGO-40, with the least wt.% of the boron precursor, gave the lowest readings. With this clear trend, it is, therefore, possible to tune the boron concentration of the synthesized B-rGO samples by varying the amount of boron precursor used.

Table 4.1: Quantitative analysis of boron in B-rGO samples.

Sample	Boron/(m/m)%
GO	-
B-rGO-70	7.12 ± 0.4
B-rGO-60	5.98 ± 1.1
B-rGO-50	4.60 ± 0.4
B-rGO-40	3.36 ± 0.1

4.3.2   Functional groups

Figure 4.1 shows the FTIR spectra of GO and B-rGO in the range of $200 - 4000$ cm^{-1}. In Figure 4.1 (a) it is seen that at least five peaks in the spectrum of GO show distinctive characteristics. The five characteristic peaks were observed at 1051, 1240, 1615, 1750, and 3250 cm^{-1}, which are assigned to the stretching vibration of alkoxy (C-O), epoxy (C-O-C), aromatic (C=C), carbonyl (C-O), and hydroxyl (OH) groups, respectively [45-47]. However, after boron-doping, the hydroxyl peak became sharper and is shifted from 3250 cm^{-1} to 3150 cm^{-1} due to the consequent reduction of GO and incorporation of boron atoms into the GO lattice. Other new peaks were observed at 1102, 1180, and 1383 cm^{-1} which were attributed to the stretching vibration of C-O, B-C, and B-O bonds, respectively [33,48].

Since boron is less electronegative than carbon, it tends to act as an electron acceptor in the vicinity of C-B bonds. The bond length of boron-boron is equal to 1.56 Å at 300-1000 K. Therefore, it is 10% longer than the carbon-carbon bond (1.41 Å). As a result, certain perturbations of the honeycomb framework of graphene are unavoidable. Thus, the position in

which the dopant atoms are situated is very important, because a higher symmetry of the nanostructure can reimburse for perturbation effects. The C-B bond length is 1.52 Å. There is a small difference in the electronegativity between carbon (2.55) and boron (2.04), therefore the bonds are expected to be weakly polar. The heat of formation indicates a change of enthalpy during the formation of one mole of the compound from its simple substances. Higher temperatures tend to enhance the heat of formation. The increase in heat of formation lowers the thermodynamic stability [49]. The covalent bond length between boron and carbon, and electron relaxing void introduced by boron (HOLE) by lowering the overall states, have the consequence of a slight red-shift as opposed to the expected blue-shift. Thus, from the spectral analyses, it can be suggested that boron functionalities have been incorporated into the GO network [33].
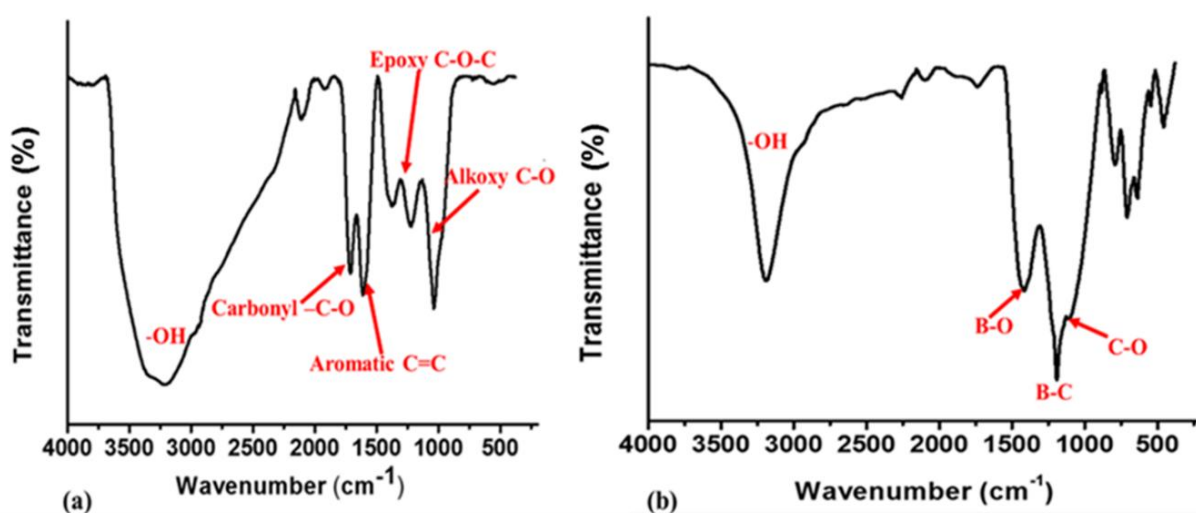
Figure 4.1: ATR-FTIR spectra of (a) GO and (b) B-rGO-40.

4.3.3 Morphology

The 2-D structural morphologies of the B-rGO samples are shown in Figure 4.2. The GO sample has a planar-like, 2-D structure, while the B-rGO samples have a wrinkled undulated structure, which did not show much difference from the surface morphology of GO, other than that more corrugations were observed. The difference is due to the boron doping effect and deformation upon exfoliation in the carbon framework [23,50]. Similar observations have been reported by other researchers [2,42,51,52]. Also, boron-doping resulted in a decrease in the interlayer spacing (d_{002} spacing) of GO, as can be seen in Figure 4.2 (c) and (d).

127
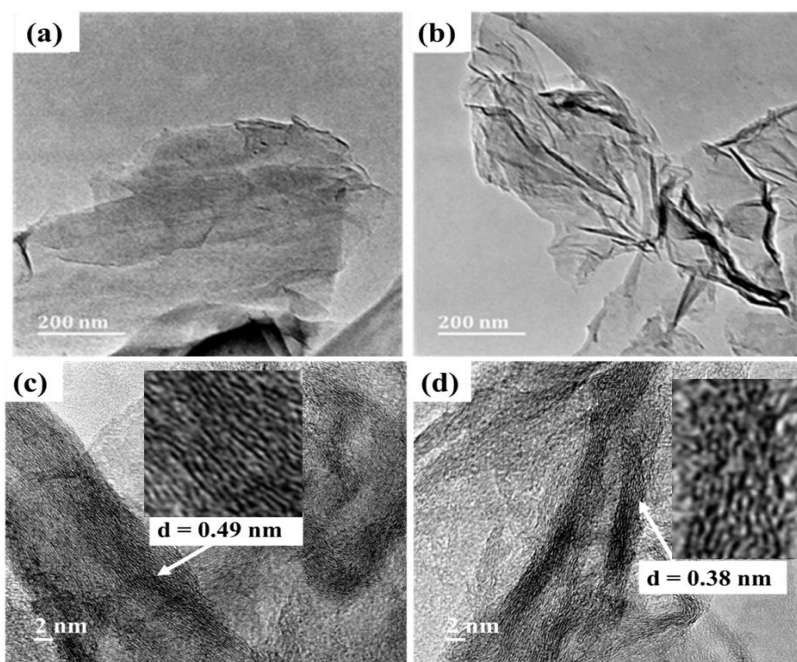
Figure 4.2: HR-TEM images of (a) GO and (b) B-rGO, and interlayer spacing of (c) GO and (d) B-rGO.

Figure 4.3 shows SEM images of GO and various B-rGO samples. Images (b) to (e) reveal that the B-rGO samples contain randomly aggregated few-layers of ultra-fine sheets which are closely packed. A closer view shows that the nanosheets of B-rGO were randomly stacked together, displaying a flake-like structure. This was caused by the thermal annealing of GO and reduction of oxygen functional groups which resulted in a few fine layers of GO sheets [53]. Further structural properties of B-rGO samples were investigated by spectroscopic methods and are also discussed herein.
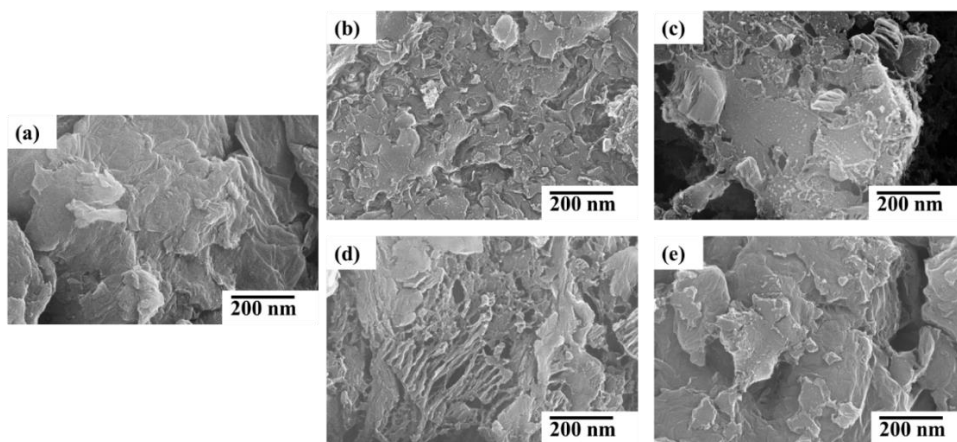
Figure 4.3: SEM images of (a) GO, (b) B-rGO-70, (c) B-rGO-60, (d) B-rGO-50 and (e) B-rGO-40.

128

4.3.4 Crystallinity

Figure 4.4 (a) shows the Raman spectra of B-rGO which reveal the D- and G-bands at 1341 and 1592 cm^{-1}, respectively. The intensity of the D- and G-bands of B-rGO manifested a frequency down-shift compared with those of GO. The broadening of both D- and G-bands for B-rGO indicates the incorporation of the boron functional group and loss of crystalline nature [33,54]. In this work, an increase in intensity and broadening of the D-band was observed, which reveals a loss of crystallinity of B-rGO as the boron concentration increases. The ratio of I_D/I_G for the D- and G-bands was measured to deduce the disorder and defects present in the B-rGO samples [55] (see Table 4.2). Thus, the lower I_D/I_G ratio represents a higher degree of crystallinity while the higher I_D/I_G ratio suggests that the materials have a lower degree of crystallinity.
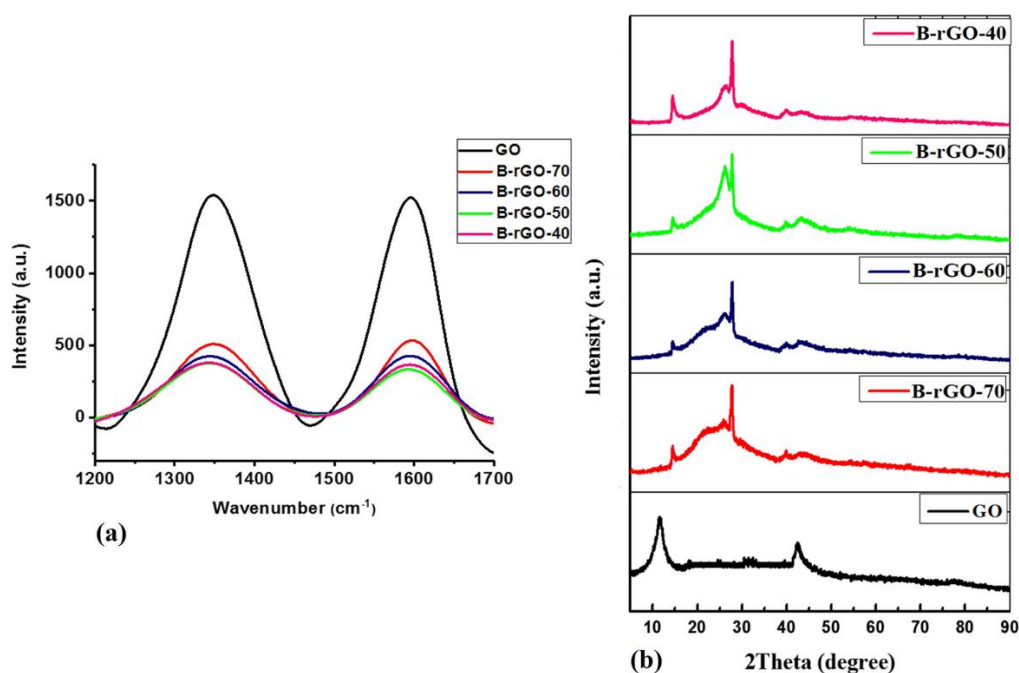
Figure 4.4: (a) Raman spectra and (b) Powder X-ray diffractograms of GO and B-rGO.

As seen in Table 4.2, the I_D/I_G ratios for GO, B-rGO-70, B-rGO-60, B-rGO-50, and B-rGO-40 were 0.99, 1.33, 1.28, 1.26, and 1.23, respectively. The increment of the I_D/I_G ratio after boron-doping in GO has been reported by several researchers [33,35,56,57]. The increase in I_D/I_G ratio for B-rGO samples is attributed to a lower degree of crystallinity or disruption in the GO framework [58], which suggests the introduction of boron into the GO lattice and the introduction of more defects. The defects are due to boron-doping in the GO lattice and the

harsh oxidation of graphite. The increase in boron concentration resulted in a higher I_D/I_G ratio, demonstrating the formation and increase in the amount of sp^3 hybridization and defects in the graphene sheet, which lead to changes in structural and electrical properties [59].

B-rGO-70 had the highest I_D/I_G ratio of 1.33 of all the B-rGO samples, due to its higher boron content. Also, the crystallite size (L_a) of B-rGO was observed to decrease with the increase in boron concentration (Table 4.2). The crystallite size was calculated with the use of equation 1:

$$HWHM = 71 - 5.2\, L_a \qquad (1)$$

where *HWHM* represents the half-width at a half maximum which is half of the full width at half maximum (FWHM) when the function is symmetric, this equation was reported by Mallet-Ladeira *et al.* [60]. Further structural analysis of the B-rGO samples was performed by powder-XRD.

Table 4.2: Crystallinity of GO and B-rGO.

Sample	D-band/$\pm$ 1 cm^{-1}	G-band/$\pm$ 1 cm^{-1}	I_D/I_G	L_a/nm
GO	1350	1590	0.99	4.44
B-rGO-70	1348	1594	1.33	3.31
B-rGO-60	1345	1593	1.28	3.43
B-rGO-50	1342	1591	1.26	3.49
B-rGO-40	1341	1592	1.23	3.58

The diffractograms of the GO and B-rGO samples exhibited graphitic diffraction patterns which are shown in Figure 4.4 (b). GO showed a strong peak at a 2θ angle of 11° (*d* = 0.770 nm) which is assigned to the non-functionalized GO [61]. The shift from 11° to 15° after boron doping suggests that oxygen functional groups were reduced in the occurrence of exfoliation with boron functionalities [33,41]. For B-rGO, the broad peaks were between 25° and 27° (*d* = 0.352 - 0.330 nm). The shift in the 2θ peak (between 25 and 27°, corresponding to the (002) plane) to the left and its broadness demonstrated that the boron-doping resulted in a hexagonal crystal structure [15]. This broadening is attributed to stress, strain, and defects induced during boron-doping. This suggests that the B-rGO samples had a lower degree of crystallinity and graphitization. These results correlate with the Raman spectroscopy analysis (Table 4.2). The reduction of GO is caused by the use of 10% hydrogen in argon. During the reaction, hydrogen

and oxygen are combined and form water and it is all blown out of the exhaust pipe of the furnace, hence there will be less oxygen and more reduced graphene oxide. The observed decrease in interlayer spacing is an additional indication that the boron atom has been successfully incorporated into the GO lattice [62], and this is consistent with HR-TEM studies, as seen in Figure 4.2 (c) and (d).

Table 4.3 shows the powder-XRD parameters (interlayer spacing and crystallite size) calculated from Scherrer's equation. An increase in boron content causes an increase in the structural strain of B-rGO samples by enhancing the surface defects of the graphite layer, which results in broadening of the full width at half maximum (FWHM) of the peaks. This is an indication of a significant increase in the number of defects which is induced with an increase in the incorporation of the boron atom into the GO lattice. Also, the crystallite size (L_a) decreased from 2.97 to 0.64 nm with increasing boron content. Hence, based on the interlayer spacing and crystallite size calculations, the B-rGO-70 sample had the lowest degree of crystallinity or graphitization, and the smallest crystallite size.

Table 4.3: Powder-XRD-parameters of GO and B-rGO.

Sample	2θ/degree	FWHM/β_{hkl}	Interlayer spacing/nm	Crystallite size (L_a)/nm
GO	11.5	2.81	0.770	2.97
B-rGO-70	25.3	13.2	0.352	0.64
B-rGO-60	25.4	11.0	0.350	0.77
B-rGO-50	25.9	7.74	0.344	1.11
B-rGO-40	26.9	6.88	0.330	1.24

4.3.5 Textural properties

The surface area and porosity of the B-rGO samples varied with boron content (Table 4.4). The boron-doping on the GO sheets tends to increase the surface area of B-rGO and this is due to the substitutional incorporation of boron atoms which provides defect-like small pores in the basal plane of the GO sheet, thereby inhibiting the formation of the graphitic structure [2]. The enhancement of surface area after boron-doping has been reported by Singh *et al.* [42], which was due to the open space between the two-dimensional nano-sheets. The increase in surface area and porosity with an increase in boron content as determined by the BET and BJH analysis respectively correlates with the results obtained from SEM images. However, when comparing

the porosity and surface area of B-rGO, it is noted that both the pore volumes and surface area increase, whilst the pore sizes decrease, with increasing boron content. This is because of the defects created during boron-doping which lead to the weakening of the π-π interactions between the GO sheets and consequently change the structural morphology by forming more wrinkled and folded sheets [63].

Table 4.4: Textural characteristics of GO and B-rGO.

Sample	Surface area/m^2 g^{-1}	Pore volume/cm^3 g	Pore size/nm
GO	55.00	0.2827	25.2
B-rGO-70	130.0	0.3710	5.20
B-rGO-60	84.13	0.2783	7.10
B-rGO-50	68.74	0.2032	13.8
B-rGO-40	64.61	0.1169	20.4

It is envisaged that boron-doping tends to create defects on the GO surface and also generates pores/holes resulting from the evolution of carbon dioxide and carbon monoxide during the thermal reduction treatment. This causes folding and crumpling of GO sheets due to their inherent smaller mechanical resistivity [64]. Therefore, the porous structure is increased by boron content. For example, Table 4.4 reveals that the B-rGO-70 sample had the largest BET-surface area and this was attributed to the greatest amount of boron in the sample and extra pores on the surface of GO, which is related to extra exfoliation and perforation on the GO sheets. On the other hand, the smaller surface area of B-rGO-40 may have been caused by the chemical reduction of GO which is associated with π-π stacking between rGO sheets, and this resulted in agglomeration [61]. The enhancement in agglomeration is due to Van der Waals forces from π-π interactions and is evident from the decrease in pore volume in B-rGO-40. The pore size was obtained from the spaces between GO sheets and it varied with boron content. Also, the pores observed for B-rGO samples were mesoporous, a phenomenon that can cause a fast charge-discharge process, known as ionic diffusion.

The adsorption isotherms of GO and B-rGO are typical type IV adsorption-desorption isotherms as seen in Supplementary data (Figure S4.2), and thus the samples are classified as type IV mesoporous materials with interconnected pore systems [65]. All samples exhibited H3-type hysteresis loops between ≈ 0.45 and 1.0 P/P$_o$ with various sizes of cavitation. It was observed that cavitation increases with boron content and this type of hysteresis loop is

characteristic of materials consisting of plate-like particles with slit-shaped pores. The observed hysteresis loops are consistent with the morphological structures observed in the SEM images.

4.3.6 Thermal stability

The thermal stability and purity of the samples as inferred from the TGA thermograms and derivatives weights are exhibited in Figure 4.5. The thermogram of GO demonstrates a succession of reaction steps due to the presence of diverse oxygen-containing functional groups (hydroxyl (C-OH), carbonyl (C=O), epoxide (C-O-C), and single-bonded oxygen (C-O)) [66,67]. However, after doping such reaction steps were not observed, evidencing that the reduction of oxygen-functional groups was successful. The thermograms showed the least amount of residual mass (4% weight) which in all cases was assigned to the presence of char.
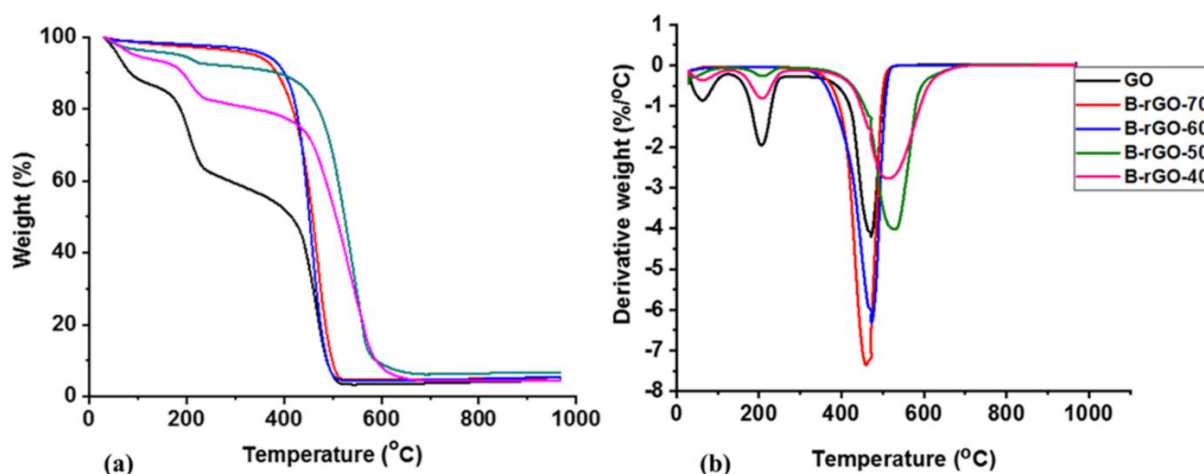
Figure 4.5: Thermal stability studies represented as (a) TGA thermograms and (b) derivatives weights for GO and B-rGO.

The thermogram of GO showed a weight loss at 200 °C which was due to the loss of water and the removal of oxygen-containing groups in the sample (Figure 4.5). In contrast, the B-rGO-70 and B-rGO-60 samples did not show this weight loss. One major peak at $400 - 550$ °C was observed for B-rGO and it showed the maximum decomposition temperature. The increase in the thermal stability of some B-rGO samples (B-rGO-40 and B-rGO-50) was observed after boron-doping. Duan *et al.* [68] demonstrated that doping graphene with a heteroatom can enhance the thermal stability of graphene. The heteroatom-doping sometimes tends to block the combustion sites and depress the formation of CO_x [69]. However, when comparing the

B-rGO samples, the thermal stability decreases with an increase in boron content (Table 4.5), with B-rGO-70 being the least thermally stable. This was attributed to defects induced during boron-doping, as supported by the observed TEM and SEM images where the B-rGO sheets were more folded. When nanomaterials are not crystalline, they are easy to break because they are not well-structured and this, results in a less stable material. The thermal stability of the B-rGO samples also correlates with their lower crystallinity as seen from the Raman spectroscopy analysis (Table 4.2).

Table 4.5: Decomposition temperatures of GO and B-rGO.

Sample	Decomposition Temp./°C
GO	473
B-rGO-70	462
B-rGO-60	470
B-rGO-50	524
B-rGO-40	520

4.3.7 Optical properties

Figure 4.6 (a) shows the UV-Vis absorption spectra of B-rGO in the wavelength range of 200-800 nm. The synthesized GO exhibited a major absorption peak at 242 nm which is associated with a $\pi \rightarrow \pi^*$ electron transition in the C-C bonds [70,71]. The incorporation of boron resulted in an absorption shift from 275 to 303 nm. As the boron content increased, an enhanced electronic conjugation in the reduced B-rGO samples was observed.
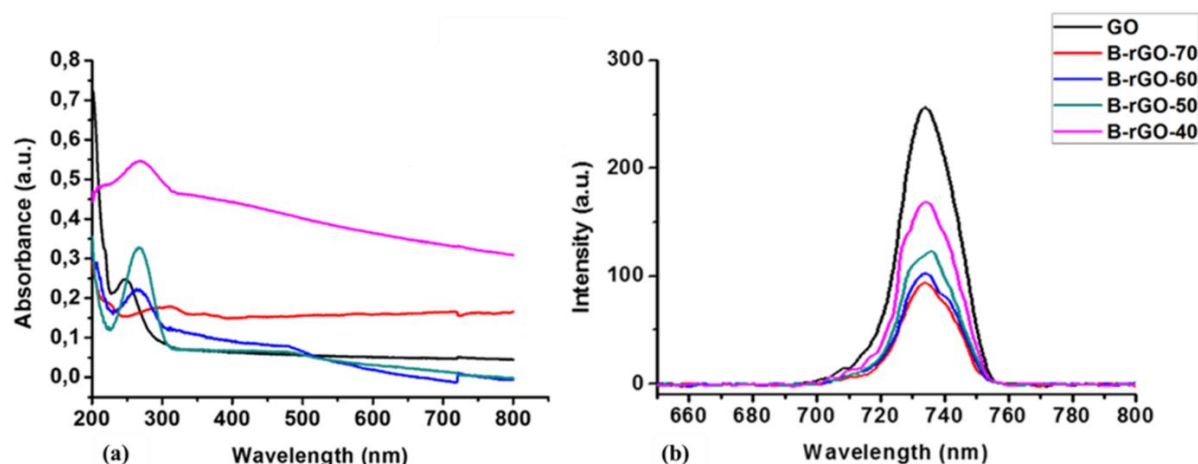
Figure 4.6: (a) UV-Vis absorption and (b) Photoluminescence spectra for GO and B-rGO.

The bandgap energies for the nanomaterials were extrapolated from Tauc's plot (Supplementary data – Figure S4.3) and are shown in Table 4.6. The *x*-axis intercept of the Tauc's plot to estimate the bandgap does not start at zero. Normally, the plot of *(αhv)²* versus photon energy *(hv)* gives a straight line in a certain region. The extrapolation of this straight line to the (hv)-axis gives the value of the indirect optical bandgap *(E_g)*. In this case and according to the plots in the Supplementary data (Figure S4.3), tangents to the curves were drawn at linear segments to minimize the contribution of the phonons, and the intersection value (in eV) at the *x*-axis gives the direct bandgap energy according to Tauc's equation.

The absorption maxima in the UV-Vis absorption spectra of B-rGO are different because of the differences in the densities of states around the Fermi level and, thus, extrapolation in the Tauc's plots resulted in different bandgap values. The decrease in bandgap is a clear indication that the synthesized GO has been successfully reduced and doped with boron. Also, the decrease in bandgap energies resulted in the Fermi level moving up in the direction of the conduction band edge. The shift of the absorption edge or widening of the energy bandgap is due to the Moss-Burstein effect [72] which originates from the lifting of the Fermi level into the conduction band potential because of the enhancement in the charge carrier concentration. It is also due to the decrease in shallow-level trap concentration close to the conduction band potential. It should be noted that the bandgap is dominated by π–π* and σ–σ* interband transitions, generally represented as E_g σ–σ*(E_g π–π*), however, the contributions arising from the Penn gap E_o σ–σ*(E_o π–π*) and broadening C σ–σ*(C π–π*) affects the expected shift in the presence of the "hole" imposing dopant, due to the enhanced transition of π-electrons (in p_z-type orbitals) to π* anti-bonding states and, subsequently, to vacant orbitals in boron. This phenomenon can be argued to render electrons labile and susceptible to external field effects.

Table 4.6: Energy bandgaps of GO and B-rGO.

Sample	λ_{max} absorption/nm	Bandgap energy/eV
GO	242	3.9
B-rGO-70	303	2.5
B-rGO-60	275	2.7
B-rGO-50	275	2.7
B-rGO-40	275	2.9

The variation in bandgap energy is due to the σ–σ* transition which comes from the σ–bonded electrons participating in the covalent bonds of both sp^3 and sp^2 carbon atoms. In a dopant environment, this determines electron oscillation strength S σ–σ* (S π–π*). However, the doping concentration and dopant configuration, as stated earlier, are varied and nonlinear. It can be argued that the observed trend arises from varied Tauc joined density of states and the classical Lorentzian dispersions in the neighbourhoods of the bandgap which is dependent on C- and B-hybridization in the B-rGO matrix. This is so because there is a strong correlation between the strength and the energy position of the oscillating electrons. Applying Tauc-Lorentz formalism becomes plausible because it averages the contributions of the π–π* and σ–σ* transitions resulting in energy values, which are not consistent with expected tight-binding molecular dynamics and are strongly correlated to the strength of electron binding energies.

To further investigate the optical properties, the band potentials were calculated by using the Butler and Ginley equations:

$$E_{VB} = X - E_e + 0.5\, E_g \tag{1}$$

$$E_{CB} = E_{VB} - E_g \tag{2}$$

where E_{VB} represents the valence band potential, E_{CB} represents the conduction band potential, E_g is the energy bandgap from (Table 4.6), X is the electronegativity of the semiconductor, and E_e is the energy of free electrons on the hydrogen scale (~ 4.5 eV) [73]. Table 4.7 shows the calculated band potentials of B-rGO. The values of $(\alpha h\nu)^2$ for $E < E_g$ appear non-zero due to intense multiple reflections from the film/substrate interface due to the low optical absorption originating from the weak π–π⋆ transition and at higher photon energy the optical absorption increases due to the major σ–σ⋆ transition. The change in the valence and conduction band potential after boron-doping was attributed to the Moss-Burstein effect. This is because of the high dopant concentration in B-rGO, thus the lower state of the conduction band is occupied by the excess electrons (carriers) from the boron (impurities) atoms, therefore the electrons require additional energy to be promoted from the valence band potential to the conduction band potential (empty state).

Table 4.7: Band potentials for GO and B-rGO.

Sample	Valence band potential/eV	Conduction band potential/eV
GO	-1.66	-5.56
B-rGO-70	-2.74	-5.24
B-rGO-60	-2.64	-5.34
B-rGO-50	-2.64	-5.34
B-rGO-40	-2.59	-5.39

It is not possible to consider flat band potentials in view of the varied dopant concentration and configuration, and thus the change in conduction band potential is subject to the density of states and dispersion around the Fermi level. The conduction band of B-rGO-40 is greater due to more movement of partially filled electrons. Thus, it has a greater energy level. The valence band potential value for B-rGO-70 is greater because of the π-state which disappears near the Fermi level due to bonding between the π- and boron-related state, causing electron transfer from graphene to boron. Boron-doping tended to enhance the valence band potential of GO and a new hybridized band was formed between -2.24 and -2.74 eV under the Dirac point. This affected the energy state of adjacent bands which gave rise to charge redistribution. As a result, an electric charge, equivalent but opposite in sign to the charge, captured at the surface state, was generated inside B-rGO, leading to the formation of a space charge layer near the surface. The thickness of the space charge layer increased with decreasing concentration of the mobile charge carriers, and this was observed with increasing boron concentration. Thus, the work function of GO can be altered or tuned just by varying the doping concentration of boron.

The charge separation rate of electron-hole (charge) recombination of B-rGO was investigated by means of photoluminescence spectroscopy. The photoluminescence spectra of the B-rGO samples at an excitation wavelength of 340 nm are shown in Figure 4.6 (b). It was observed that the intensity of the B-rGO peaks decreased drastically as compared with that of GO. This indicated that the electron-hole pair recombination has been successfully reduced with a prolonged lifetime of photogenerated carriers and this is due to the synergistic effect of B-rGO. B-rGO-70 with higher boron content tends to induce a lower rate of charge recombination as compared with the other samples that had lower boron content. These observations corroborate the effect of varying boron content in B-rGO and the energy bandgap (Figure 4.6 (a)). However, there was no significant change in the photoluminescence spectra of the B-rGO and GO samples, indicating that the permissible excited states generally do not change.

4.3.8 Electrochemical properties

The current and resistance of B-rGO samples were measured with a four-point probe and, thus, the electrical conductivity (σ) and resistivity (ρ) could be determined at room temperature from the following equations:

$$\sigma = \frac{1}{\rho} \tag{3}$$

$$\rho = \left(\frac{\pi}{\ln 2}\right)\left(\frac{V}{I}\right) t \tag{4}$$

where t represents the thickness of the pellet, I is the current and V represents the change in voltage [74]. The values obtained are recorded in Table 4.8. The GO sample showed the highest resistivity, while the B-rGO samples exhibited much lower resistivities, due to the boron-doping effect. This was consistent with Poh *et al.* [75] who reported a similar decreasing trend in resistivity after doping graphene with boron.

Table 4.8: Electrical conductivity of GO and B-rGO.

Sample	Sheet resistance/Ω sq^{-1}	Bulk resistivity/Ω cm	Electrical conductivity/S cm^{-1}
GO	2.415×10^7	2.188×10^6	4.570×10^{-7}
B-rGO-70	1.863×10^1	1.692×10^{-1}	5.920
B-rGO-60	3.100×10^1	2.810×10^{-1}	3.560
B-rGO-50	5.179×10^1	4.694×10^{-1}	2.135×10^{-1}
B-rGO-40	5.780×10^3	5.238×10^1	1.913×10^{-2}

The I–V characteristics of the B-rGO samples through basic conductivity estimations are shown in Figure 4.7. The I-V slope of GO was found to be close to zero, which implies that GO is an insulating material. The slight deviation of B-rGO-40 from a straight line demonstrated it is a non-Ohmic conductor. Increasing the boron content, produced a curved line passing through the origin, which indicated that B-rGO-50, B-rGO-60 and B-rGO-70 have semiconductor field-effect characteristics. Thus, simultaneous reduction and doping of GO affords semi-conducting behavior. An increase in the I-V slope suggests that B-rGO has a higher electrical conductivity than GO. These results are in agreement with those reported by Van Khai *et al.* [76].
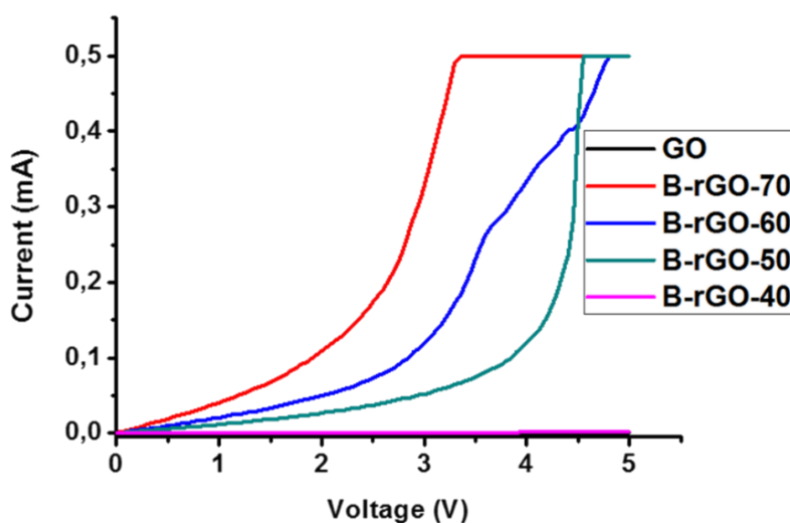
Figure 4.7: Current-voltage characteristics of GO and B-rGO.

Among the B-rGO samples, B-rGO-70 was found to exhibit the largest conductivity, while B-rGO-40 showed the smallest conductivity. The enhancement in conductivity after doping with boron is caused by an increase in hole-type charge carriers in the GO network and is also due to the change of bonding configuration. It was seen that the conductivity increased with boron content in B-rGO, implying that all the B-rGO samples exhibited semi-conducting properties. These electrical conductivity behaviours are associated with the electron acceptor properties of the boron atom. From Figure 4.7, it can be deduced that B-rGO-40 showed a significant decrease in free carrier mobility, whilst the highest mobility of free carriers was in B-rGO-70. Based on the rigid band model, it can be inferred that the holes created and pore sizes on B-rGO-40 (BET results - Table 4.4) serve as a trap for free electrons. Thus, one can assume a decrease in free carrier mobility lowers the electrical conductivity. Generally, boron-doping caused a shift in the Fermi level away from the Dirac point (graphene) and resulted in a finite density of states at zero energy [77]. The Fermi level shift is highly dependent on the doping concentration of boron atoms. The finite density of state at zero energy is caused by the increase of quasi-particle weight in semi-conductors by impurity doping. Therefore, the electrical conductivity of B-rGO is expected to increase when boron doping increases and is consistent with the electronic band structure (Table 4.7).

The Hall effect measurement results for carrier densities and mobilities of B-rGO are shown in Table 4.9. The trend in resistivity was determined from the Hall effect and it correlates with the trend of the resistivity obtained from the four-point probe measurements shown in Table

4.8. The Hall coefficient is negative which serves as an indication that all the B-rGO samples synthesized are *p*-type semiconductors. The carrier mobilities tended to vary with boron concentration for the B-rGO samples. B-rGO-70 manifested a *p*-type semiconducting behaviour with excellent carrier mobility (0.311 cm^2 V^{-1} s^{-1}). Carrier mobility is a very important parameter for semiconductor materials. Higher mobility usually leads to better device performance. Graphene has been reported to have the highest carrier mobility among all the semiconductors because of the low effective mass. The high mobility of graphene-based materials can also stem from its one atom thickness in which the electron has a smaller scattering (due to its high confinement). Therefore, it is believed that the variation of boron content overcomes the low conductivity of GO.

Table 4.9: Hall effect measurements for B-rGO at a constant field of 1160 G.

Sample	Resistivity/Ω cm	Hall coefficient/cm^3 C^{-1}	Carrier density/cm^{-3}	Carrier mobility/cm^2 V^{-1} s^{-1}
B-rGO-70	0.2560	-0.0796	12.560	0.311
B-rGO-60	0.9691	-0.245	4.082	0.253
B-rGO-50	2.990	-0.323	3.096	0.108
B-rGO-40	5.806	-0.517	1.934	0.089

4.3.8.1 Electrode potential characteristics

Figure 4.8 (a) shows the CV curves for all the B-rGO samples over the optimized potential range. All the curves are almost quasi-rectangular in shape. The [Fe(CN)6]$^{3-/4-}$ redox probe current on GO was smaller than those of the B-rGO samples. Furthermore, the potential difference between the reduction and oxidation peaks of the [Fe(CN)6]$^{3-/4-}$ redox couple tends to decrease after boron-doping, due to the good electron transfer capability of B-rGO. All the B-rGO samples displayed good current responses and this was attributed to the different boron functionalities present in B-rGO, which further enhanced semi-conductivity. B-rGO-40 shows pseudo-characteristics with a narrower rectangular shape than the other B-rGO samples. This is because of the switching of the current. It is deduced that a lower boron-doping concentration in GO presented some pseudo-characteristics and resulted in poor rate capacities. The redox current of the [Fe(CN)6]$^{3-/4-}$ redox probe was further enhanced with B-rGO-70. This further demonstrates that the variation of boron concentration effectively improved the electron transfer capability.
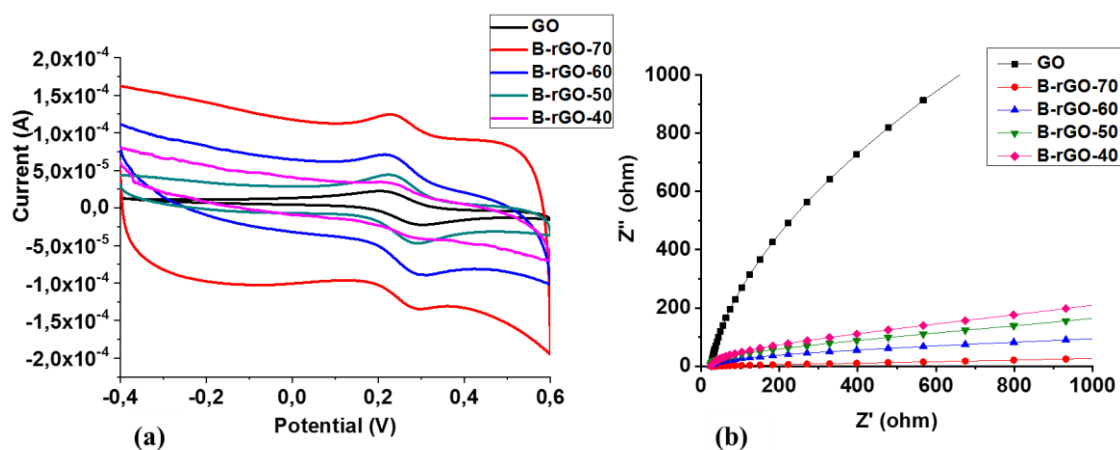
Figure 4.8: (a) Cyclic voltammograms curves and (b) Nyquist plots in the high-frequency region for GO and B-rGO samples.

The high boron content in B-rGO-70 improved its capacitance which could be credited to an enhanced BET surface area (Table 4.4) and better electrical conductivity properties (Table 4.8). Consequently, the contribution through the electrochemical double-layer capacitance (EDLC) increased. The detailed mechanism of the Faradaic reaction is not yet understood in B-rGO. However, this pseudo-capacitive behaviour is due to the Faradaic redox reaction that is provided from the boron-containing enriched carbons [78]. Thus, improving the surface wetting by electrolytes enhances the electron capability. This concurs with other reports in that heteroatoms tend to cause an increment in the wettability of carbon-based electrodes and they enhance capacitance [2,79,80].

4.3.8.2 Interfacial charge transfer characteristics

In the Nyquist plot, GO shows a small semi-circle at the high-frequency region (Figure 4.8 (b)). However, after doping with various boron concentrations, the semi-circle disappears. This phenomenon is attributed to the mass transfer characteristics, which are predominant in the B-rGO samples, and corroborates the sharp increase in conductivity observed (Figure 4.7). In Figure 4.8 (b), the ascending order of slopes was B-rGO-70, B-rGO-60, B-rGO-50, B-rGO-40, and GO. This demonstrates that B-rGO-70 has a lower mass flow than B-rGO-40. The lower mass flow is due to morphological and structural modification, and reduction of oxygen-containing functional groups. The low mass flow is very beneficial in energy storage devices due to its minimized energy wastage by reducing unwanted heat during charging and discharging processes.

141

A larger Faradaic charge transfer resistance (R_{ct}) was observed in GO (Table 4.10) due to the high number of oxygen-containing groups that lower its electrochemical characteristics. After boron-doping, R_{ct} decreased in all of the B-rGO samples. Thus, increasing the boron concentration in B-rGO leads to a lower R_{ct}. B-rGO-70 exhibited the lowest R_{ct} of 20.23 Ω, which correlates to the absence of a semi-circle in the Nyquist plot. The lower R_{ct} suggests that B-rGO-70 has less charge transfer resistance than the other B-rGO samples. This further demonstrates that B-rGO-70 can be a better conductive material with a higher electron conduction network because of the synergistic effect. These results correlate with the trend in electrical conductivity properties of B-rGO (Table 4.8), making these materials more suitable for application in dye-sensitized solar cells as counter electrodes.

Table 4.10: Resistance values for GO and B-rGO obtained by fitting the impedance spectra.

Sample	R_{ct}/Ω
GO	75.18
B-rGO-70	20.23
B-rGO-60	32.90
B-rGO-50	40.01
B-rGO-40	40.86

4.4   Conclusion

Boron atoms were successfully doped into the GO lattice at various boron concentrations. The boron content in B-rGO increased with boric anhydride concentration and reached its highest doping level of 7.12%, which imposed a significant change in the physicochemical, optical, electrochemical, and conductivity properties. B-rGO-70 had the largest BET surface area which enhanced the capacitance but also caused it to be the least thermally stable. B-rGO samples showed strong absorption in the ultraviolet region. The doped materials showed a significant difference in their electronic properties, suggesting that the greater the degree of boron doping in graphene, the greater is the conductivity. The chaotic surface morphology of B-rGO-70, with an open porous structure and a high surface area, tends to enhance its electrical conductivity. B-rGO-70 showed a typical semiconductor characteristic, with a sheet resistance of 1.863×10^1 Ω sq^{-1}. It also had the lowest R_{ct} of 20.23 Ω, which is an indicator of good electron transport through the electrode-electrolyte interface, which is a promising feature for the design and fabrication of electronic nanodevices.

References

1. N. Chen, X. Huang and L. Qu, *Phys. Chem. Chem. Phys.*, **2015**, 17, 32077-32098.

2. D.-Y. Yeom, W. Jeon, N. D. K. Tu, S. Y. Yeo, S.-S. Lee, B. J. Sung, H. Chang, J. A. Lim and H. Kim, *Sci. Rep.*, **2015**, 5, 9811-9817.

3. L. Wang, Z. Sofer, P. Šimek, I. Tomandl and M. Pumera, *J. Phys. Chem. C*, **2013**, 117, 23251-23257.

4. S. Maharubin, X. Zhang, F. Zhu, H.-C. Zhang, G. Zhang and Y. Zhang, *J. Nanomater.*, **2016**, 2016, 6375962.

5. M.-L. Yang, N. Zhang, K.-Q. Lu and Y.-J. Xu, *Langmuir*, **2017**, 33, 3161-3169.

6. A. Omidvar, *Mater. Chem. Phys.*, **2017**, 202, 258-265.

7. N. Rohaizad, Z. Sofer and M. Pumera, *Electrochem. Commun.*, **2020**, 112, 106660.

8. S. M. Tan, H. L. Poh, Z. Sofer and M. Pumera, *Analyst*, **2013**, 138, 4885-4891.

9. Z. Zhai, H. Shen, J. Chen, X. Li and Y. Li, *ACS Appl. Mater. Interfaces*, **2020**, 12, 2805-2815.

10. L. Pan, Y. Que, H. Chen, D. Wang, J. Li, C. Shen, W. Xiao, S. Du, H. Gao and S. T. Pantelides, *Nano Lett.*, **2015**, 15, 6464-6468.

11. S. Agnoli and M. Favaro, *J. Mater. Chem. A*, **2016**, 4, 5002-5025.

12. L. Ferrighi and C. Di Valentin, *Surf. Sci.*, **2015**, 634, 68-75.

13. Y.-B. Tang, L.-C. Yin, Y. Yang, X.-H. Bo, Y.-L. Cao, H.-E. Wang, W.-J. Zhang, I. Bello, S.-T. Lee and H.-M. Cheng, *ACS Nano*, **2012**, 6, 1970-1978.

14. Z. Jia, Z. Zuo, Y. Yi, H. Liu, D. Li, Y. Li and Y. Li, *Nano Energy*, **2017**, 33, 343-349.

15. V. Thirumal, A. Pandurangan, R. Jayavel and R. Ilangovan, *Synth. Met.*, **2016**, 220, 524-532.

16. S. S. Samantaray, V. Sangeetha, S. Abinaya and S. Ramaprabhu, *Int. J. Hydrog. Energy*, **2018**, 43, 8018-8025.

17. Y. Liu, Z. Tai, J. Zhang, W. K. Pang, Q. Zhang, H. Feng, K. Konstantinov, Z. Guo and H. K. Liu, *Nat. Commun.*, **2018**, 9, 3641-3610.

18. S. Gong and Q. Wang, *J. Phys. Chem. C*, **2017**, 121, 24418-24424.

19. X. Wu, Y. Wang and P. Yang, *Phys. Lett. A*, **2017**, 381, 2004-2009.

20. R. Lv, G. Chen, Q. Li, A. McCreary, A. Botello-Méndez, S. Morozov, L. Liang, X. Declerck, N. Perea-López and D. A. Cullen, *Proc. Natl. Acad. Sci. USA*, **2015**, 112, 14527-14532.

21.   W. Cheng, X. Liu, N. Li, J. Han, S. Li and S. Yu, *RSC Adv.*, **2018**, 8, 11222-11229.

22.   T. Zhang, H. Zhao, G. Fan, Y. Li, L. Li and X. Quan, *Electrochim. Acta*, **2016**, 190, 1150-1158.

23.   H. Fang, C. Yu, T. Ma and J. Qiu, *Chem. Commun.*, **2014**, 50, 3328-3330.

24.   A. J. Du, S. C. Smith and G. Q. Lu, *Chem. Phys. Lett.*, **2007**, 447, 181-186.

25.   L. Tsetseris and S. T. Pantelides, *Carbon*, **2014**, 67, 58-63.

26.   T. M. Dieb, Z. Hou and K. Tsuda, *J. Chem. Phys.*, **2018**, 148, 241716-241717.

27.   I. Pletikosić, M. Kralj, P. Pervan, R. Brako, J. Coraux, A. N'diaye, C. Busse and T. Michely, *Phys. Rev. Lett.*, **2009**, 102, 056808.

28.   P. Rani and V. Jindal, *RSC Adv.*, **2013**, 3, 802-812.

29.   V. Barone, O. Hod and E. G. Scuseria, *Nano Lett.*, **2006**, 6, 2748 - 2754.

30.   R. Q. Wu, L. Liu, G. W. Peng and Y. P. Feng, *Appl. Phys. Lett.*, **2005**, 86, 122510-122513.

31.   Y. W. Son, M. L. Cohen and S. G. Louie, *Phys. Rev. Lett.*, **2006**, 97, 216801-216804.

32.   B. Quan, S.-H. Yu, D. Y. Chung, A. Jin, J. H. Park, Y.-E. Sung and Y. Piao, *Sci. Rep.*, **2014**, 4, 5631-5636.

33.   M. Mannan, Y. Hirano, A. Quitain, M. Koinuma and T. Kida, *J. Mater. Sci. Eng.*, **2018**, 7, 492-496.

34.   J. Borowiec and J. Zhang, *J. Electrochem. Soc.*, **2015**, 162, B332-B336.

35.   E. Romani, D. Larrude, M. da Costa, G. Mariotto and F. Freire, *J. Nanomater.*, **2017**, 2017, 1-8.

36.   S. Li, Z. Wang, H. Jiang, L. Zhang, J. Ren, M. Zheng, L. Dong and L. Sun, *Chem. Commun.*, **2016**, 52, 10988-10991.

37.   R. A. Thearle, N. M. Latiff, Z. Sofer, V. Mazánek and M. Pumera, *Electroanalysis*, **2017**, 29, 45-50.

38.   L. Wang, Z. Sofer, J. Luxa and M. Pumera, *J. Mater. Chem. C*, **2014**, 2, 2887-2893.

39.   S. Ge, J. He, C. Ma, J. Liu, F. Xi and X. Dong, *Talanta*, **2019**, 199, 581-589.

40.   M. Sahoo, K. Sreena, B. Vinayan and S. Ramaprabhu, *Mater. Res. Bull.*, **2015**, 61, 383-390.

41.   L. Panchakarla, K. Subrahmanyam, S. Saha, A. Govindaraj, H. Krishnamurthy, U. Waghmare and C. Rao, *Adv. Mater.*, **2009**, 21, 4726-4730.

42.   M. Singh, S. Kaushal, P. Singh and J. Sharma, *J. Photochemi. Photobiol. A Chem.*, **2018**, 364, 130-139.

43. Z.-H. Sheng, H.-L. Gao, W.-J. Bao, F.-B. Wang and X.-H. Xia, *J. Mater. Chem.*, **2012**, 22, 390-395.

44. W. S. Hummers Jr and R. E. Offeman, *J. Am. Chem. Soc.*, **1958**, 80, 1339-1339.

45. H. Yu, B. Zhang, C. Bulin, R. Li and R. Xing, *Sci. Rep.*, **2016**, 6, 36141-36147.

46. P. Ranjan, S. Agrawal, A. Sinha, T. R. Rao, J. Balakrishnan and A. D. Thakur, *Sci. Rep.*, **2018**, 8, 12001-12013.

47. N. I. Zaaba, K. L. Foo, U. Hashim, S. J. Tan, W.-W. Liu and C. H. Voon, *Procedia Eng.*, **2017**, 184, 469-477.

48. X. Mu, B. Yuan, X. Feng, S. Qiu, L. Song and Y. Hu, *RSC Adv.*, **2016**, 6, 105021-105029.

49. V. V. Chaban and O. V. Prezhdo, *Nanoscale*, **2016**, 8, 15521-15528.

50. Z.-S. Wu, W. Ren, L. Xu, F. Li and H.-M. Cheng, *ACS Nano*, **2011**, 5, 5463-5471.

51. F. Wu, Y. Xing, L. Li, J. Qian, W. Qu, J. Wen, D. Miller, Y. Ye, R. Chen, K. Amine and J. Lu, *ACS Appl. Mater. Interfaces*, **2016**, 8, 23635-23645.

52. S. S. Balaji, M. Karnan, J. Kamarsamam and M. Sathish, *ChemElectroChem.*, **2019**, 6, 1492-1499.

53. A. T. Smith, A. M. LaChance, S. Zeng, B. Liu and L. Sun, *Nano Mater. Sci.*, **2019**, 1, 31-47.

54. Y. Hishiyama, H. Irumano, Y. Kaburagi and Y. Soneda, *Phys. Rev. B*, **2001**, 63, 245406-245411.

55. R. Beams, L. G. Cançado and L. Novotny, *J. Phys. Condens. Matter.*, **2015**, 27, 083002-083026.

56. S. Srivastava, S. K. Jain, G. Gupta, T. Senguttuvan and B. K. Gupta, *RSC Adv.*, **2020**, 10, 1007-1014.

57. Y. Bleu, F. Bourquard, V. Barnier, Y. Lefkir, S. Reynaud, A. S. Loir, F. Garrelie and C. Donnet, *Appl. Surf. Sci.*, **2020**, 513, 145843.

58. P. Han and A. Manthiram, *J. Power Sources*, **2017**, 369, 87-94.

59. L. G. Cançado, A. Jorio, E. M. Ferreira, F. Stavale, C. A. Achete, R. B. Capaz, M. V. d. O. Moutinho, A. Lombardo, T. Kulmala and A. C. Ferrari, *Nano Lett.*, **2011**, 11, 3190-3196.

60. P. Mallet-Ladeira, P. Puech, C. Toulouse, M. Cazayous, N. Ratel-Ramond, P. Weisbecker, G. L. Vignoles and M. Monthioux, *Carbon*, **2014**, 80, 629-639.

61. J. Zhang, H. Yang, G. Shen, P. Cheng, J. Zhang and S. Guo, *Chem. Comm.*, **2010**, 46, 1112-1114.

62. Y. Wang, C. Wang, Y. Wang, H. Liu and Z. Huang, *ACS Appl. Mater. Interfaces*, **2016**, 8, 18860-18866.

63. R. Nankya, J. Lee, D. O. Opar and H. Jung, *Appl. Surf. Sci.*, **2019**, 489, 552-559.

64. C.-M. Chen, J.-Q. Huang, Q. Zhang, W.-Z. Gong, Q.-H. Yang, M.-Z. Wang and Y.-G. Yang, *Carbon*, **2012**, 50, 659-667.

65. J. Lee, R. Nankya, A. Kim and H. Jung, *Electrochim. Acta*, **2018**, 290, 496-505.

66. F. Najafi and M. Rajabi, *Int. Nano Lett.*, **2015**, 5, 187-190.

67. J. Long, S. Li, J. Liang, Z. Wang and B. Liang, *Poly. Compos.*, **2019**, 40, 723-729.

68. X. Duan, S. Indrawirawan, H. Sun and S. Wang, *Catal. Today*, **2015**, 249, 184-191.

69. B. Frank, J. Zhang, R. Blume, R. Schlögl and D. S. Su, *Angew. Chem. Int. Ed.*, **2009**, 48, 6913-6917.

70. S. Schöche, N. Hong, M. Khorasaninejad, A. Ambrosio, E. Orabona, P. Maddalena and F. Capasso, *Appl. Surf. Sci.*, **2017**, 421, 778-782.

71. G. Jayalakshmi, K. Saravanan, B. Panigrahi, B. Sundaravel and M. Gupta, *Nanotechnology*, **2018**, 29, 185701-185722.

72. Z. M. Gibbs, A. LaLonde and G. J. Snyder, *New J. Phys.*, **2013**, 15, 075020-075039.

73. M. A. Butler and D. S. Ginley, *J. Electrochem. Soc.*, **1978**, 125, 228-232.

74. S. Bose, T. Kuila, M. E. Uddin, N. H. Kim, A. K. T. Lau and J. H. Lee, *Polymer*, **2010**, 51, 5921-5928.

75. H. L. Poh, P. Šimek, Z. Sofer, I. Tomandl and M. Pumera, *J. Mater. Chem. A*, **2013**, 1, 13146-13153.

76. T. Van Khai, H. G. Na, D. S. Kwak, Y. J. Kwon, H. Ham, K. B. Shim and H. W. Kim, *Chem. Eng. J.*, **2012**, 211, 369-377.

77. H. Mousavi and R. Moradian, *Solid State Sci.*, **2011**, 13, 1459-1464.

78. J. Han, L. L. Zhang, S. Lee, J. Oh, K.-S. Lee, J. R. Potts, J. Ji, X. Zhao, R. S. Ruoff and S. Park, *ACS Nano*, **2012**, 7, 19-26.

79. J. Segalini, B. Daffos, P.-L. Taberna, Y. Gogotsi and P. Simon, *Electrochim. Acta*, **2010**, 55, 7489-7494.

80. R. Baronia, J. Goel, G. Gautam, D. Singh and S. K. Singhal, *J. Nanosci. Nanotechnol.*, **2019**, 19, 3832-3843.
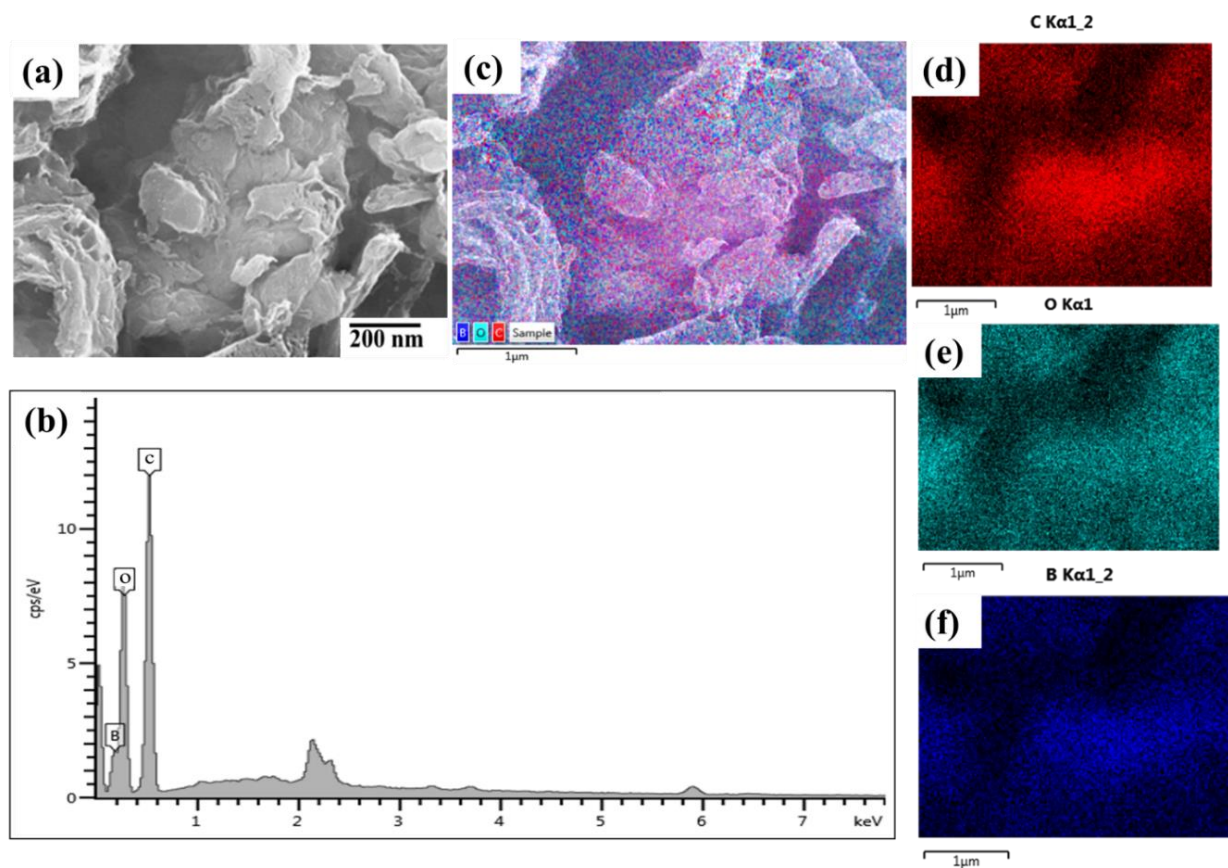
Figure S4.1: EDS measurement conducted at the selected area (a) SEM image of B-rGO-70, (b) EDS result, elemental mapping of (c) B-rGO, (d) carbon, (e) oxygen, and (f) boron.
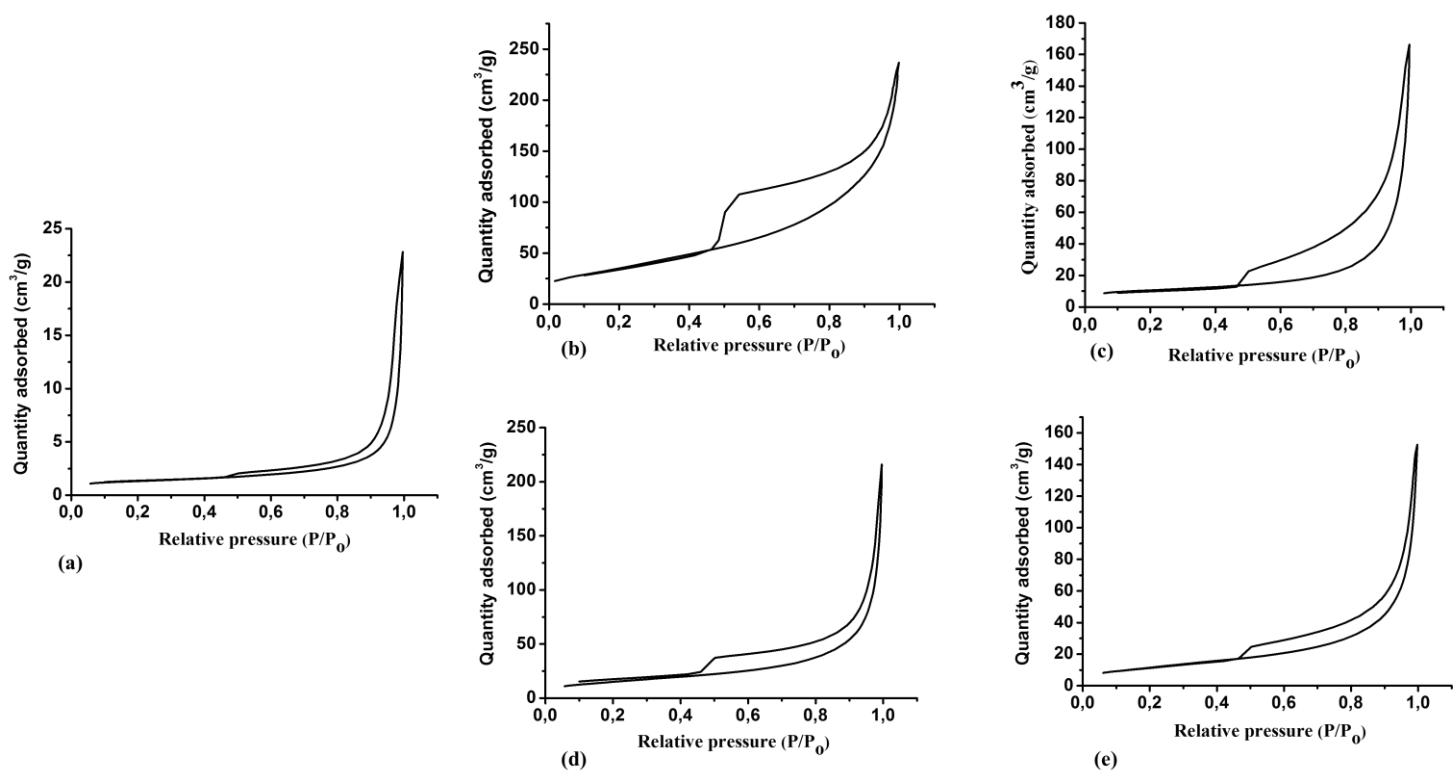
Figure S4.2: N_2 adsorption-desorption isotherms for (a) GO, (b) B-rGO-70, (c) B-rGO-60, (d) B-rGO-50 and (e) B-rGO-40.
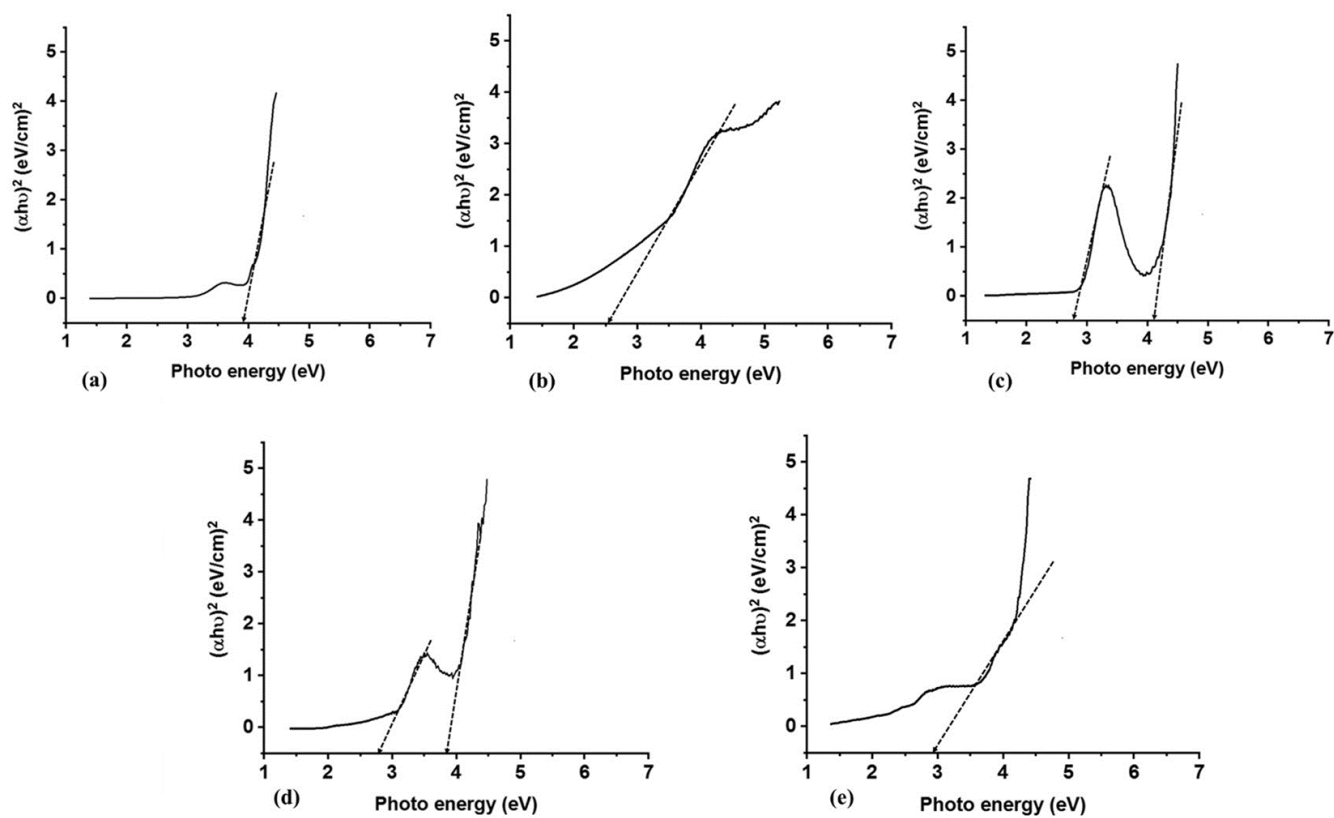
Figure S4.3: Tauc's plot for (a) GO, (b) B-rGO-70, (c) B-rGO-60, (d) B-rGO-50, and (e) B-rGO-40.

CHAPTER 5

Enhanced performance by heteroatom-doped reduced graphene oxide-TiO₂-based nanocomposites as photoanodes in dye-sensitized solar cells

Nonjabulo P. D. Ngidi, Edigar Muchuweni and Vincent O. Nyamori

School of Chemistry and Physics, University of KwaZulu-Natal, Westville Campus, Private Bag X54001, Durban 4000, South Africa

Graphical abstract
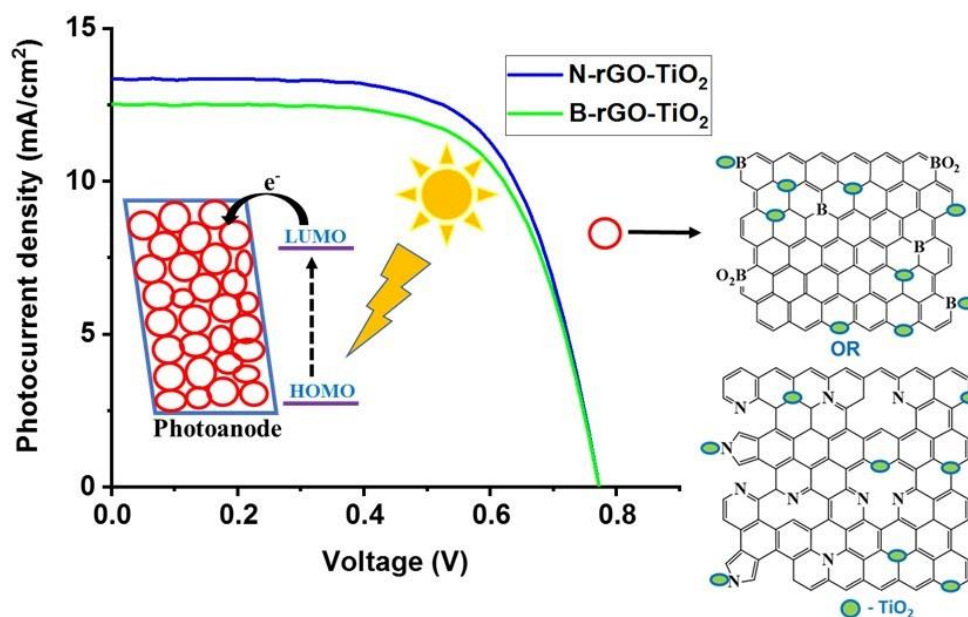
Abstract

The photoanode in a dye-sensitised solar cell (DSSC) plays a crucial role in achieving a high power conversion efficiency (PCE). It supports the sensitizer and acts as a transporter of photo-excited electrons from the sensitizer to the external circuit. These two functions are enhanced by a large surface area and a fast charge transport rate. Typically, the photoanode consists of titanium dioxide (TiO_2) nanoparticles. If the nanoparticles are deposited on a carbonaceous substrate, it facilitates the transport of photogenerated electrons. This study compared the photoanode performance of boron- or nitrogen-doped reduced graphene oxide (B- or N-rGO) nanocomposites integrated with TiO_2. All nanocomposites exhibited mainly the anatase TiO_2 phase, and N-rGO-TiO_2 exhibited the lowest bandgap of 2.1 eV, which was attributed to the formation of Ti-O-C and Ti-O-N bonds. Also, N-rGO-TiO_2 displayed good charge carrier separation ability and electron transfer. The low TiO_2 content in the nanocomposites led to the suppression of electron-hole recombination, reduction in the bandgap energy, and improvement in electron transport, resulting in higher current density. Two photo-harvesting dyes (sensitisers) were investigated, i.e., eosin B and Sudan II. A higher light-harvesting efficiency was obtained from eosin B, indicating the presence of more dye molecules anchored onto the TiO_2. Photoanodes fabricated from N-rGO-TiO_2 and B-rGO-TiO_2 showed enhanced photo-exciton generation, higher short-circuit current densities, and significantly better PCEs of 3.94 and 2.55%, respectively, than their undoped rGO-TiO_2 counterparts (1.78%). This work demonstrates that heteroatom-doped rGO-TiO_2 based nanocomposites can improve the rate of transportation and collection of electrons, thereby enhancing the performance of DSSCs.

Keywords

Titania-based nanocomposite; Reduced graphene oxide; Boron-doped; Nitrogen-doped; Photoanode

5.1   Introduction

In recent years, dye-sensitised solar cells (DSSCs) have been widely investigated compared with their silicon-based counterparts. DSSCs exhibit specific advantages, such as low manufacturing cost, easy fabrication, and compatibility with flexible substrates. However, DSSCs have issues that lower their power conversion efficiencies (PCEs), such as poor charge extraction, leakage currents, electron-hole recombination, and instability. To address these drawbacks, various studies have been dedicated to the engineering and manufacturing of devices that could satisfy the standards of the photovoltaic cell market. However, the low PCEs of DSSCs have remained a major obstacle. Thus, recent advancements in DSSC components, especially photoanodes, have been shown to enhance device performance.

In DSSCs, the primary factor controlling the PCE and electron flow is charge carrier recombination, which is the major drawback of nanostructured semiconductor materials, inferable from their surface defects [1]. Hence, various researchers have reported different approaches to restrict charge recombination and improve PCE [2,3]. Such approaches involve the use of nanocrystalline materials from zero-dimensional (nanoparticles) [4], one-dimensional nanostructures (such as nanowires, nanorods, and nanotubes) [5,6], and two-dimensional nanostructures (nanosheets) [7], to suppress electron-hole recombination.

Graphene, a 2D sheet of carbon crystals, has remarkable properties that allow it to be applied in DSSCs as a photoanode or counter electrode (CE). Graphene-based nanomaterials have been mostly used as a CEs in DSSCs, resulting in enhanced PCEs (0.5 to 7.7%) [8]. However, although graphene as a photoanode has been reported to improve the fill factor (FF), it reduces the PCE of DSSCs [9]. The challenge with graphene is the restacking of its sheets. Thus, various approaches have been applied to enhance the electronic and physicochemical properties of graphene by stacking an optimum amount of metal oxide, as a cost-effective and efficient photocatalyst in DSSCs. Metal oxides offer the highest diffusion length; however, the issue of electron-hole recombination still lingers, hindering the performance of DSSCs [10]. Thus, surface modification of metal oxides with graphene or graphene oxide (GO) has been attempted and resulted in improved PCEs [11]. The combination of graphene or GO with a metal oxide tends to produce a synergistic effect of interface modification on the charge transport in the graphene or GO hybrid system. Thus, it enhances the electrical conductivity and PCE of the DSSCs.

The most researched metal oxide is TiO_2, which has attracted significant attention due to its low-cost, nontoxicity (low environmental impact), excellent chemical stability, ease of fabrication, small bandgap, and good performance under ultraviolet light [12]. The presence of oxygen vacancies in TiO_2 makes it an n-type semiconductor. TiO_2 can be classified into three crystalline phases: anatase, rutile, and brookite [13]. These polymorphs have different thermodynamic stability. The polymorph with the least thermodynamic stability is brookite, which is acquired through complex preparation procedures and exists as a mixture with one of the other polymorphs [14]. Rutile is the most thermodynamically stable polymorph with a bandgap of 3.02 eV [15]. Anatase is a more active polymorph with a larger bandgap and is a better photocatalyst when compared with rutile [16,17]. It also has an improved photocarrier lifetime, high oxidative power, and exhibits excellent conductivity; thus, it has been widely used in DSSCs [18] and photocatalytic [19] applications.

Various TiO_2-based nanocomposites have been used as a photoanode in DSSCs, resulting in better PCE [20,21]. For example, the fabrication of TiO_2/reduced graphene oxide (rGO) nanocomposites and their application in DSSCs as photoanodes have been reported by Daulay *et al.* [22]. The optimum performance was obtained from the lowest rGO loading, yet the highest loading of rGO exhibited a lower PCE of 0.9%. Therefore, discovering better approaches remains a crucial quest for preventing back-reaction with electrolyte species and enhancing electron transport. Thus, further investigations on various TiO_2-based nanocomposites as photoanodes in DSSCs are still required.

This work presents a comparative analysis of the physicochemical, optical, and electrical conductivity properties of TiO2 coated with heteroatom-doped rGO, particularly boron-doped reduced graphene oxide (B-rGO) or nitrogen-doped reduced graphene oxide (N-rGO), *via* a hydrothermal reaction. In addition, the use of two photo-harvesting dyes, eosin B and Sudan II, was investigated in DSSCs. These dyes were chosen because they show excellent absorption at around 400 - 700 nm (visible region) and adsorb strongly onto the TiO_2 surface. The effect of the heteroatoms (nitrogen and boron atoms) in rGO and TiO_2 concentration on the photovoltaic performance of TiO_2-based nanocomposites as a photoanode was investigated. This study proposes a promising strategy to control the various properties of heteroatom-doped rGO-TiO_2-based nanocomposites as potential photoanodes in DSSCs.

5.2   Experimental

5.2.1   Materials

Boron standard solution (999.5 ± 20 mg L^{-1}), titanium(IV) oxide (P25) powder (TiO$_2$, ≥21 nm, 99.5%), absolute ethanol (99.5%), titanium standard (1000 ± 4 mg L^{-1} AR), eosin B (97%) and Sudan II (90%) were brought from Sigma-Aldrich, South Africa.

5.2.2   Synthesis of the heteroatom-doped rGO nanocomposites and device fabrication

The synthesis of GO was carried out in our laboratory, as reported elsewhere [23], whereas rGO, B-rGO, and N-rGO were synthesised by thermal treatment method using chemical vapour deposition (CVD) [24,25].   Heteroatom-doped rGO-TiO$_2$ based nanocomposites were synthesised using the hydrothermal method at 200 °C [26].   The nanocomposite was subsequently washed with double-distilled water and dried for 24 h in an oven at 60 °C. The TiO$_2$-based nanocomposite was further calcined in a CVD at a temperature of 350 °C for 1 h to decompose the unreacted titanium (IV) oxide (P25) powder completely and, thereafter, further characterised. DSSCs fabrication was performed in a similar way to that reported by Ngidi *et al*. [26].

5.2.3   Characterisation

The microstructure and surface morphology of the nanocomposites were determined by high-resolution transmission electron microscopy (HR-TEM, JEOL JEM 1010 model) and field emission-scanning electron microscopy (FE-SEM, Carl Zeiss Ultra Plus), respectively. The Renishaw inVia Raman microscope was used to investigate the graphitic nature of the nanocomposites. The TiO$_2$ and boron content present in the nanocomposites was investigated by PerkinElmer Optima 5300 DV, inductively coupled plasma-optical emission spectrometry (ICP-OES), while the other elements present in the nanocomposites were detected by the Elementar vario EL cube CHNSO elemental analyser. Various functional groups and phase compositions were quantified by the PerkinElmer Spectrum 100 Fourier transform infrared (FTIR) and powder X-ray diffraction (XRD, Bruker AXS, CuK$_\alpha$ radiation source, λ = 0.154 nm), respectively. A TA Instruments Q series^{TM} thermal analyzer DSC/TGA (Q600) instrument was employed to investigate the thermal stability of the nanocomposites.

A Micromeritics Tristar II 3020 porosity and surface area analyser was used to investigate the textural characteristics of the nanocomposites. Each nanocomposite (0.1000 g) was degassed

for 12 h at 160 °C in a Micromeritics Vacprep 061 device before the nanocomposite was placed in the Micromeritics Tristar II instrument for analysis. The Barrett-Joyner-Halenda (BJH) and Brunauer, Emmett, and Teller (BET) models were used to measure the pore volumes and surface areas of the nanocomposites, respectively. The optical properties of TiO_2-based nanocomposites were analysed with a Shimadzu ultraviolet-visible spectrophotometer. The PerkinElmer LS 55 spectrofluorometer was employed to investigate charge carrier recombination of the nanocomposites. Electrical conductivity was determined using the four-point probe equipment with a Keithley 2400 SourceMeter. The Hall effect was used to investigate the type of semiconductor nanocomposite and charge carrier mobility. This was carried out using the Ecopia Hall effect measurement system at a constant magnetic field strength of 1160 T.

The electrochemical behaviours of pure TiO_2 and heteroatom-doped rGO-TiO_2-based nanocomposites were investigated using a VersaSTAT3F potentiostat/galvanostat electrochemical workstation (cyclic voltammetry (CV) and electrochemical impedance spectroscopy (EIS)). The EIS data were analysed using ZSimpWin software. A reference electrode (Ag/AgCl), working electrode (mixture of nanocomposite), counter electrode (platinum wire (Pt)), and an electrolyte (potassium hydroxide, KOH) were used. The nanocomposite mixture was prepared as reported by Ngidi *et al.* [26]. The CV was carried out at a scan rate of 100 mV s^{-1} with a potential range from -1.0 to 1.0 V. A solar simulator (Oriel Instruments LCS-100) was used to carry out the DSSCs photovoltaic measurements. The characterisation of DSSCs was performed on an active area of 0.96 cm^2 under light illumination (AM 1.5 G, 100 mW cm^{-2}).

5.3   Results and discussion

The nanocomposites synthesised in this study were assigned as reduced graphene oxide-titania (rGO-TiO_2), nitrogen-doped reduced graphene oxide-titania (N-rGO-TiO_2), and boron-doped reduced graphene oxide-titania (B-rGO-TiO_2). The physicochemical, optical, and electrical properties of the nanocomposites are discussed in the subsequent sub-sections, followed by the photovoltaic properties of the fabricated DSSCs.

5.3.1   Chemical state and composition

The quantification of the elemental composition of titanium was performed by ICP-OES (Table 5.1) and EDX (Supplementary Data - Figure S5.1), while the presence of other elements was evaluated using an elemental analyser (Supplementary Data - Table S5.1). The nitrogen and

boron content in the nanocomposites was lower compared to N-rGO and B-rGO (Supplementary Data - Table S5.1 and Table S5.2). The titanium content in rGO-TiO$_2$, N-rGO-TiO$_2$, and B-rGO-TiO$_2$ was found to be 30.0, 29.2, and 28.8%, respectively. The higher titanium content in rGO-TiO$_2$ is attributed to more interfacial cross-link formation (hydrogen bonds between rGO and TiO$_2$, and the Ti−O−C covalent bonds) [27]. rGO with low oxygen content has considerable interaction energies, thus showing larger energy gain. In the case of B-rGO-TiO$_2$, a lower titanium content than that of rGO-TiO$_2$ was achieved because of the agglomeration of titanium nanoparticles caused by the boron atoms incorporated in the interstitial sites as B^{3+}, thus resulting in more formation of B-O bonds instead of B-O-Ti [28]. N-rGO-TiO$_2$ had a higher content of titanium than B-rGO-TiO$_2$, suggesting more interstitial N (Ti-O-N) formation. The elemental analysis also verified the reduction of oxygen functional groups in N-rGO. The presence of different functional groups in the nanocomposites was further investigated using ATR-FTIR.

Table 5.1: TiO$_2$ wt.% loading and ICP-OES values.

Sample	TiO$_2$ loading/wt.%	ICP-OES Titanium/%
rGO-TiO$_2$	50	30.0
N-rGO-TiO$_2$	50	29.2
B-rGO-TiO$_2$	50	28.8

5.3.2 Surface functional groups

The ATR-FTIR spectrum of TiO$_2$ (Figure 5.1 (a)) revealed the presence of several characteristic peaks, e.g., the O-H stretching vibration at 3453 cm^{-1} and its bending vibration at 1691 cm^{-1}, and the Ti-O stretching band of 680 cm^{-1}. All the heteroatom-doped rGO-TiO$_2$-based nanocomposites showed a peak between 500 - 950 cm^{-1}, which is associated with the anatase phase of TiO$_2$ because of the Ti-O-C and Ti-O-Ti stretching and vibration modes [29,30]. The broad peak, which is assigned to the stretching vibration of the hydroxyl group between 3500 to 3000 cm^{-1}, is found on the TiO$_2$ nanoparticle surface [31]. All the nanocomposites exhibited a reduction of the -OH group after thermal treatment. A weak peak was observed around 1403 cm^{-1}, which was assigned to Ti-O-N present in the N-rGO-TiO$_2$, while the peaks around 1401 cm^{-1} revealed the presence of boron due to Ti-O-B bonds on B-rGO-TiO$_2$. The FTIR spectral results are consistent with the elemental analysis results, thus providing evidence that the integration of TiO$_2$ with heteroatom-doped rGO was successful**.**
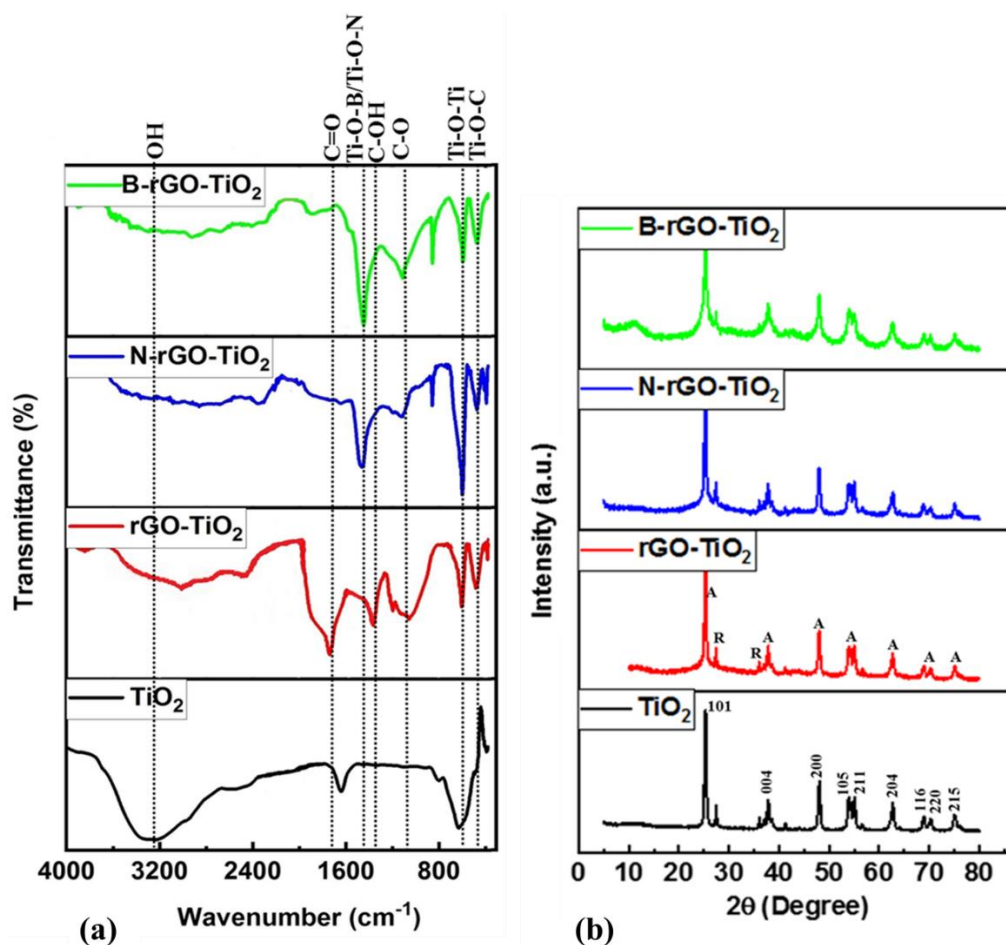
Figure 5.1: (a) ATR-FTIR spectra and (b) powder X-ray diffractograms of the TiO_2-based nanocomposites.

5.3.3 Surface morphology

The microstructure of the nanocomposites was determined by TEM and HR-TEM, while the morphology was examined using FE-SEM. All nanocomposites showed "flower-like" structures, with a few thick layers which consisted of a folded edge covered with TiO_2 nanoparticles, as shown in Figures 5.2 (a) – (c). The layers of rGO-TiO_2 were agglomerated to form larger flakes inside the TiO_2 matrix. The agglomeration of the nanocomposites is reported to bring a negative factor that affects the PCE of the DSSCs [32]. The agglomeration in rGO-TiO_2 originates from excess TiO_2 not anchored on the nanocomposite surface. The integration of heteroatom-doped rGO nanomaterials with a low amount of TiO_2 enables the coverage of more TiO_2 reactive sites in a three-dimensional matrix, which will further assist in improving the charge transport in DSSCs.
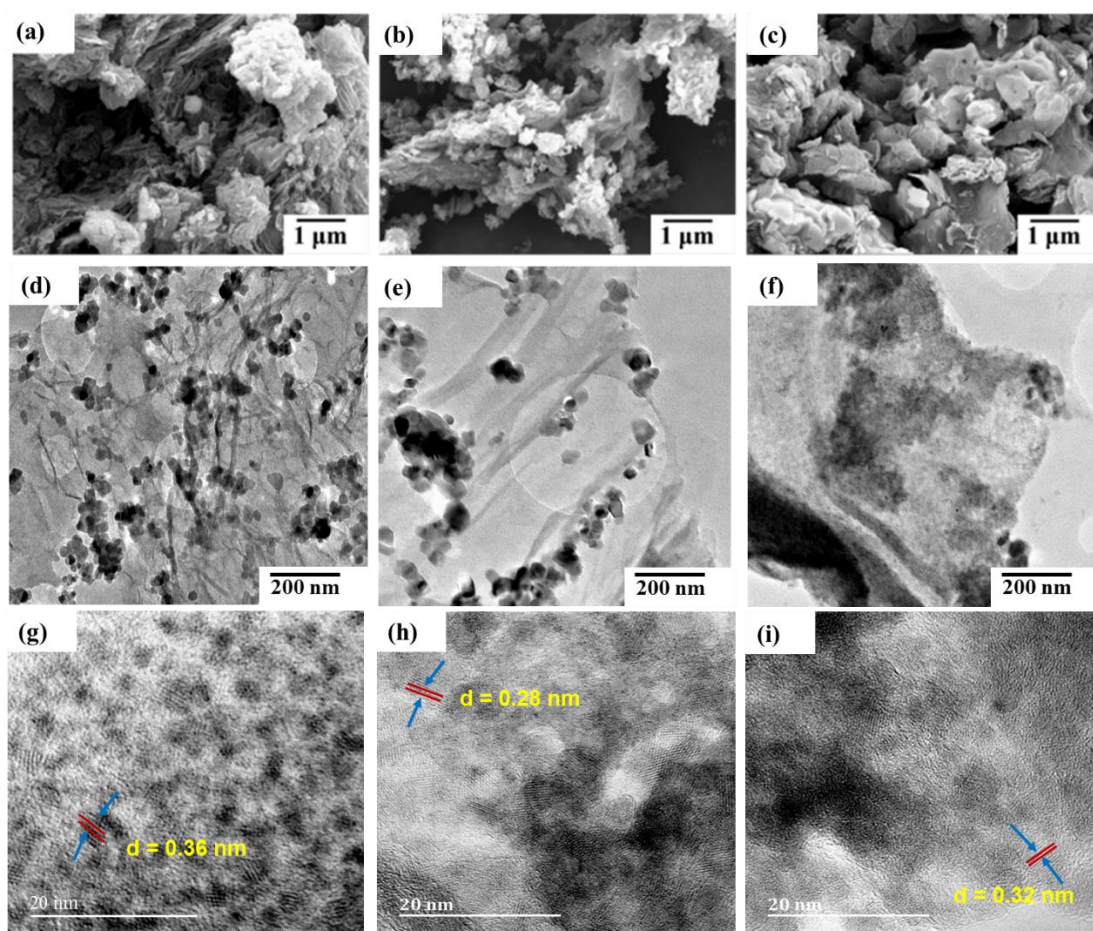
Figure 5.2: FE-SEM images of (a) rGO-TiO$_2$, (b) N-rGO-TiO$_2$, (c) B-rGO-TiO$_2$, TEM images of (d) rGO-TiO$_2$, (e) N-rGO-TiO$_2$, (f) B-rGO-TiO$_2$, HR-TEM images of (g) rGO-TiO$_2$, (h) N-rGO-TiO$_2$ and (i) B-rGO-TiO$_2$.

In Figure 5.2 (d), a large sheet was observed with some nanoparticles of TiO$_2$ clustered together on the GO sheet. The TiO$_2$ nanoparticles were observed as small fine particles agglomerated and embedded on the edges or surfaces of GO layers. This is attributed to the presence of Ti^{4+}, which is regarded as a hard Lewis acid, and serves as a template for nucleation. The spreading of TiO$_2$ nanoparticles on the surface is ascribed to the low TiO$_2$ content in N-rGO-TiO$_2$ and B-rGO-TiO$_2$. These loose TiO$_2$ nanoparticles would help enhance electron transfer between the nanocomposite and the dye on the photoanode in DSSCs.

The HR-TEM images in Figures 5.2 (g) to (i) revealed the measured interlayer spacings for the crystalline planes. The interlayer spacing of the nanocomposites between the adjacent lattice fringes is indexed to the (101) plane of anatase TiO$_2$, thus confirming that the anatase TiO$_2$ nanoparticles are enclosed by two square facets and eight isosceles trapezoidal [33].

5.3.4 Phase composition

The pristine TiO_2 and its nanocomposite samples exhibited a noticeable amount of anatase TiO_2 and a negligible amount of rutile TiO_2, which had X-ray diffractograms characteristic of rutile phase peaks at 2θ values of 27.6° and 36.4° [34]. In comparison, the anatase TiO_2 exhibited well-defined peaks at 2θ values of 25.0°, 37.5°, and 48.1° (Figure 5.1 (b)) as expected [34]. The diffractograms revealed that all the nanocomposites preferred the anatase phase of TiO_2 because of its higher Fermi energy level [35,36]. The 2θ values of 25°, 37°, 48°, 54.4°, 55°, 63°, 68.9°, 70.1°, and 75° were assigned to the (101), (004), (200), (105), (211), (204), (116) (220) and (215) anatase titania planes, respectively [37,38]. The 2θ values of 27.6° and 36.4° for rutile TiO_2 were attributed to the (110) and (101) planes, respectively [39]. These characteristic peaks are verified by the reported 21-1276 JCPDS data [40].

The well-known peak of GO at 24.5° was concealed by an anatase titania peak at 25° in rGO-TiO_2. The N-rGO and B-rGO materials (Supplementary Data – Figure S5.2) usually show a diffraction peak at 25°; however, it should be noted that such a peak overlaps with that of the anatase phase of TiO_2 due to the stacking disorder attributed to the intercalation of TiO_2 particles into stacked B-rGO or N-rGO. The (101) peak becomes broader for B-rGO-TiO_2 and N-rGO-TiO_2 due to stress and strain, proving the success of nitrogen or boron doping. Thus, these diffractograms also confirm the distribution of anatase TiO_2 within the heteroatom-doped rGO.

Table 5.2 shows the P-XRD parameters, such as the 2θ value and interlayer spacing, of the nanocomposites. The 2θ value of 25.3° for rGO-TiO_2 yielded a 0.34 nm interlayer spacing, which was smaller compared to TiO_2. However, the N-rGO-TiO_2 and B-rGO-TiO_2 nanocomposites showed an interlayer spacing that was smaller than that of rGO-TiO_2. This indicates that the particles supported on the heteroatom-doped rGO (N-rGO-TiO_2 - 0.28 nm and B-rGO-TiO_2 - 0.32 nm) were finer and more uniform than those of rGO-TiO_2. The smaller interlayer spacing may also be ascribed to the splitting of bigger nanoparticles during the hydrothermal synthesis and the loss of oxygen-containing groups. Smaller particle sizes result in a larger surface area, which enhances charge transportation and consequently suppresses the recombination of photoinduced electrons and holes. The calculated average interlayer spacing values are consistent with those from HR-TEM (Figure 5.2 (g) - (i)). The existence of TiO_2 in the nanocomposites was further elucidated by Raman spectroscopic analysis.

Table 5.2: P-XRD parameters and the I_D/I_G ratio of the nanocomposites.

Sample	2θ/degree	Interlayer spacing/nm	I_D/I_G
TiO_2	25.0	0.36	-
rGO-TiO_2	25.3	0.34	1.31
N-rGO-TiO_2	25.9	0.28	1.55
B-rGO-TiO_2	25.5	0.32	1.39

5.3.5 Defects on the graphitic structure

Raman spectroscopy was employed to investigate the crystallinity of the heteroatom-doped rGO-TiO_2-based nanocomposites (Figure 5.3). The spectrum for pure TiO_2 shows distinct characteristic peaks at 142, 399, 521, and 640 cm^{-1}, which correspond to the $E_{g(1)}$, $B_{1g(1)}$, ($B_{1g(2)}$ + A_{1g}), and $E_{g(2)}$ modes, respectively [41,42]. After integrating TiO_2 with heteroatom-doped rGO, the intensity of these peaks was reduced due to defects induced during nanocomposite formation. These peaks reveal that anatase TiO_2 is present, as observed in the P-XRD analysis (Figure 5.1 (b)). All nanocomposites exhibited two prominent peaks at around 1352 and 1609 cm^{-1}, which were the characteristic features of the D- and G-bands, respectively. The D-band arises due to in-plane or edge sp^3 defects and cluttered/disordered carbon, and it corresponds to the A_{1g} symmetry mode [43], while the G-band is attributed to in-plane vibrations of the ordered sp^2-bonded carbon atoms, and provides data about the doubly degenerate E_{2g} mode of the Brillonium zone centre [44,45]. Raman line shapes are affected by various factors, particularly non-stoichiometric oxygen insufficiencies or the disorder prompted by pressure, phonon confinement impacts, and minor phases [46]. The phonon confinement impact is regularly based on the sample particle size (small particle size reduces the intensity of the peak and causes peak broadening), whereas the effect of the surface pressure is caused by the interface stress and the surrounding particles, and thus, enhances the shifts of Raman lines.
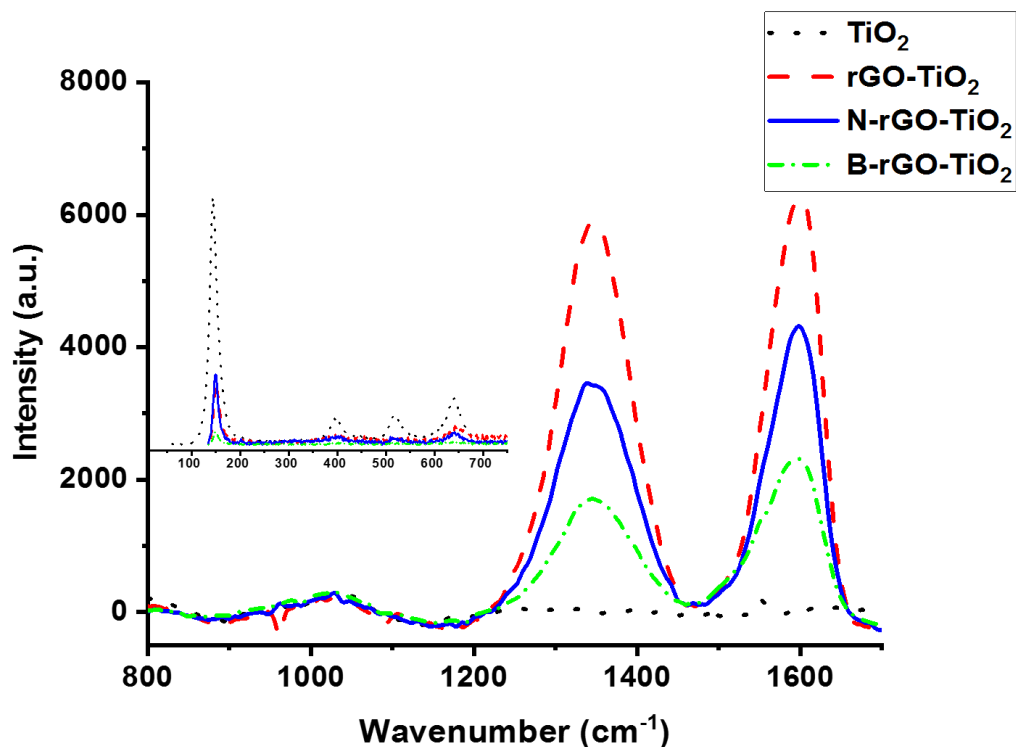
Figure 5.3: Raman spectra of the TiO$_2$-based nanocomposites.

The D-band of B-rGO-TiO$_2$ and N-rGO-TiO$_2$ showed a slight decrease in wavenumber when compared with that of rGO-TiO$_2$. The increase of the D-band wavenumber is reported to be due to hole doping, while its decrease is associated with electron doping [47], whereas the G-band is reported to be independent of doping defects. It was observed that the D-band peak intensity of B-rGO-TiO$_2$ was lower than that of N-rGO-TiO$_2$ and rGO-TiO$_2$ due to the increase in hole doping. The peak observed at 1051 cm^{-1} may be attributed to various factors, such as the presence of smaller particle size, hydroxylation of titania from the rGO sheet, and a new Ti-OH bond. Cao *et al.* [48] reported similar observations in rGO-TiO$_2$.

The ratio of the D- and G-band peak intensities, characterised as I_D/I_G, represents the structural order of the nanocomposites. It indicates the defects present in the nanocomposites and also shows a strong dependence on charge carrier density [49]. Thus, the smaller the I_D/I_G ratio, the greater the regularity. B-rGO-TiO$_2$ and rGO-TiO$_2$ had I_D/I_G ratios of 1.31 and 1.39, respectively, which were lower than 1.55 for N-rGO-TiO$_2$. N-rGO-TiO$_2$ had the highest I_D/I_G ratio because of the sp^2 disorder in the graphitic carbon nanocomposites, which is enhanced when integrating the TiO$_2$ nanoparticles and N-rGO [50]; thus, confirming the presence of a strong (Ti-O-C) chemical bond as observed in the FTIR analysis (Figure 5.1 (a)). The

161

elemental, FTIR, and Raman analyses confirmed the incorporation of TiO_2 into heteroatom-doped rGO.

5.3.6 Surface area and porosity

The pore sizes and specific surface areas obtained from nitrogen adsorption-desorption isotherms are shown in Table 5.3. A larger surface area was observed in rGO-TiO_2 compared to pure TiO_2, which was attributed to the impact of rGO, which has a low density of < 2 g cm^{-3}, while TiO_2 has a density of 4.038 g cm^{-3} and thus, the nanocomposite showed an increase in the surface area [51]. Both B-rGO-TiO_2 and N-rGO-TiO_2 exhibited a larger surface area than rGO-TiO_2. This is due to the better incorporation of TiO_2 nanoparticles on the heteroatom-doped rGO surface. The larger surface area in N-rGO-TiO_2 is attributed to the embedding of the dopant TiO_2 network and the presence of a large surface area in N-rGO. TiO_2 nanoparticles were equitably dispersed on N-rGO sheets without agglomeration. Thus, this feature suggests that incorporating TiO_2 into N-rGO easily formed the Ti-O-C bond at the surface defects and functional groups [52]. B-rGO-TiO_2 showed a smaller surface area than the other TiO_2-based nanocomposites, which could be caused by the agglomeration given by the carbonaceous material [53]. The type of moieties of TiO_2 present in the nanocomposites also plays a crucial role in surface area determination. All the TiO_2-based nanocomposites had larger surface areas, which was due to the presence of TiO_2 in the anatase phase. The presence of anatase TiO_2 on the TiO_2-based nanocomposites has also been revealed by the analyses of the P-XRD and Raman (Figure 5.1 (b) and 5.2). Therefore, the surface areas of TiO_2-based nanocomposites highly depend on the titanium content and type of surface properties of the anatase particles [53,54].

Table 5.3: A comparison of textural characteristics of the TiO_2-based nanocomposites.

Sample	Surface area/m^2 g^{-1}	Pore size/nm
TiO_2	34.2	29.56
rGO-TiO_2	121.3	15.48
N-rGO-TiO_2	133.6	9.14
B-rGO-TiO_2	126.8	11.32

The BJH analysis in Table 5.3 demonstrated that the nanocomposites had pore sizes of around (9.1 - 15.5 nm), which are considered mesoporous composites [55]. The pore size distribution of rGO-TiO_2 was lower than that of TiO_2 because of the presence of rGO in the nanocomposite. A similar observation was reported by Ates *et al.* [56]. However, Leal *et al.* [57] reported a

lower pore size distribution for TiO$_2$ than with rGO-TiO$_2$, which was attributed to changes in crystal structure and morphology *via* thermal treatment, thus forming a flower-like crystal. When comparing the nanocomposites, the pore size was observed to vary based on the titanium content. B-rGO-TiO$_2$ has a higher porosity than N-rGO-TiO$_2$, owing to the presence of TiO-O produced on the surface, which increases the particle size. The porous structure on the nanocomposites can enable the diffusion and transfer of dye molecules on the photoanode of DSSCs, which will enhance the dye loading amount. A higher dye loading amount is reported to be beneficial for improving the absorption of sunlight by the photoanode, thus enhancing the PCE of DSSCs [58]. As observed in Figure 5.4 the distinct hysteresis loop at $0 < P/P_o < 1$ indicates that the nanocomposites belong to the type IV category. The adsorption isotherm of N-rGO-TiO$_2$ rises because of the capillary condensation in the mesoporous channels or cages.
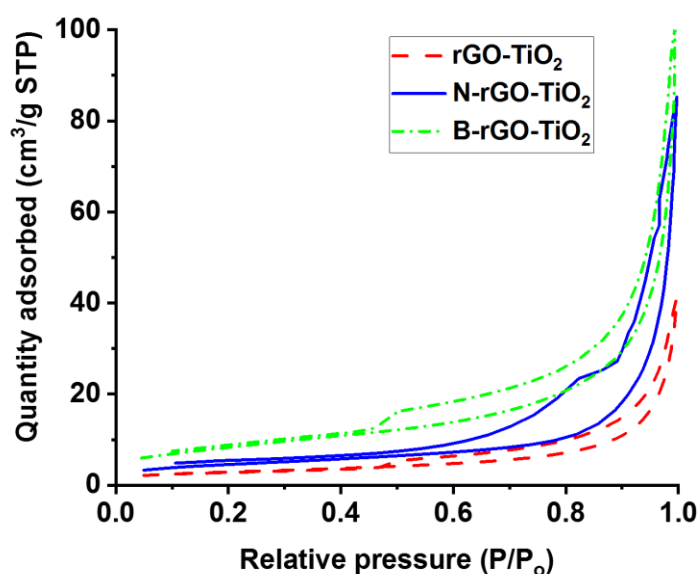
Figure 5.4: N$_2$ adsorption-desorption isotherms for the nanocomposites.

5.3.7 Thermal stability

The thermograms of the nanocomposites are shown in Figure 5.5 over a 25 - 1000 °C temperature range. All the thermograms of the nanocomposites exhibited a weight loss from 25 to 200 °C, which was attributed to moisture or water losses, even though the nanocomposites were dried overnight to remove moisture. This suggests that the nanocomposites are hygroscopic. The decomposition temperature between 200 and 400 °C represents a loss of amorphous carbon and other functional groups. Above 400 °C, the thermograms showed the decomposition of other structured carbonaceous materials or the decomposition of the graphene carbon skeleton. The N-rGO-TiO$_2$ and B-rGO-TiO$_2$ nanocomposites exhibited two steps of

163

weight loss, which were accompanied by the decomposition steps of GO, thus accentuating the incorporation of TiO_2 on the surface of GO.
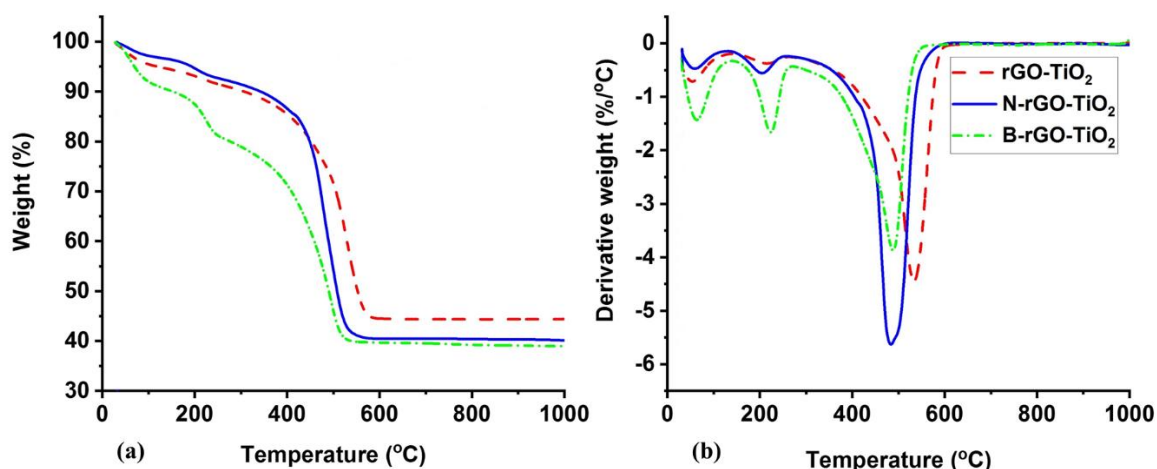
Figure 5.5: (a) TGA thermograms and (b) derivative weight loss curves for the TiO_2-based nanocomposites.

The rGO-TiO_2 nanocomposite had higher thermal stability than the other TiO_2-based nanocomposites because the oxygen-containing functional groups were reduced during the hydrothermal process. It also demonstrated higher thermal stability than the heteroatom-doped rGO-TiO_2-based nanocomposites (Table 5.4) owing to the strong interaction between TiO_2 and rGO formed after the hydrothermal process, thus, indicating the existence of a more thermally stable Ti-O-C interaction. A similar observation was reported by Vallejo *et al.* [54] and Chang *et al.* [59] for the synthesis of GO-TiO_2.

Table 5.4: Thermal stabilities and residual content of the nanocomposites.

Sample	Decomposition temperature/°C	Residual content/%
rGO-TiO₂	525.9	45
N-rGO-TiO₂	484.8	41
B-rGO-TiO₂	488.7	40

The thermograms show that the nanocomposites did not decompose completely due to residual titanium dioxide, which is shown by a straight line after 500 °C. Table 5.4 revealed that the nanocomposites have a residual TiO_2 content of about 40, 41, and 45% in B-rGO-TiO_2, N-rGO-TiO_2, and rGO-TiO_2, respectively. This indicates that approximately 50% of the mass of the nanocomposites is carbon and oxygen-functional groups. The variation of the thermal

stability and residual TiO_2 content of these nanocomposites indicates a different titanium content. From the thermograms, the order of residual titanium content is rGO-TiO_2 > N-rGO-TiO_2 > B-rGO-TiO_2, which correlates with the order of ICP-OES titanium values (Table 5.1).

5.3.8 Optical properties

The optical behaviour of the nanocomposites was investigated by UV-Visible spectroscopy and was recorded in the 300 - 700 nm wavelength range (Figure 5.6 (a)). The absorption band of TiO_2 appeared at 345 nm, which falls in the range of 340 - 355 nm, which is also mostly reported by other researchers [60,61]. The shift of the absorption band to 366 nm in rGO-TiO_2 was associated with the inherent bandgap absorption of TiO_2, originating from the valence band (O_{2p}) to the conduction band (Ti_{3d}). However, the absorption band of the heteroatom-doped rGO-TiO_2-based nanocomposites was further shifted to a longer wavelength between 360 - 385 nm due to the presence of various heteroatoms in the nanocomposites. The oxygen vacancy states in TiO_2 are substituted by the heteroatoms (boron or nitrogen atom) from B-rGO or N-rGO, enhancing the visible light activity. The formation of Ti^{3+} species between the TiO_2 conduction and valence bands during the incorporation of TiO_2 into N-rGO or B-rGO also contributes to enhancing the absorption edge toward the visible-light region [61].
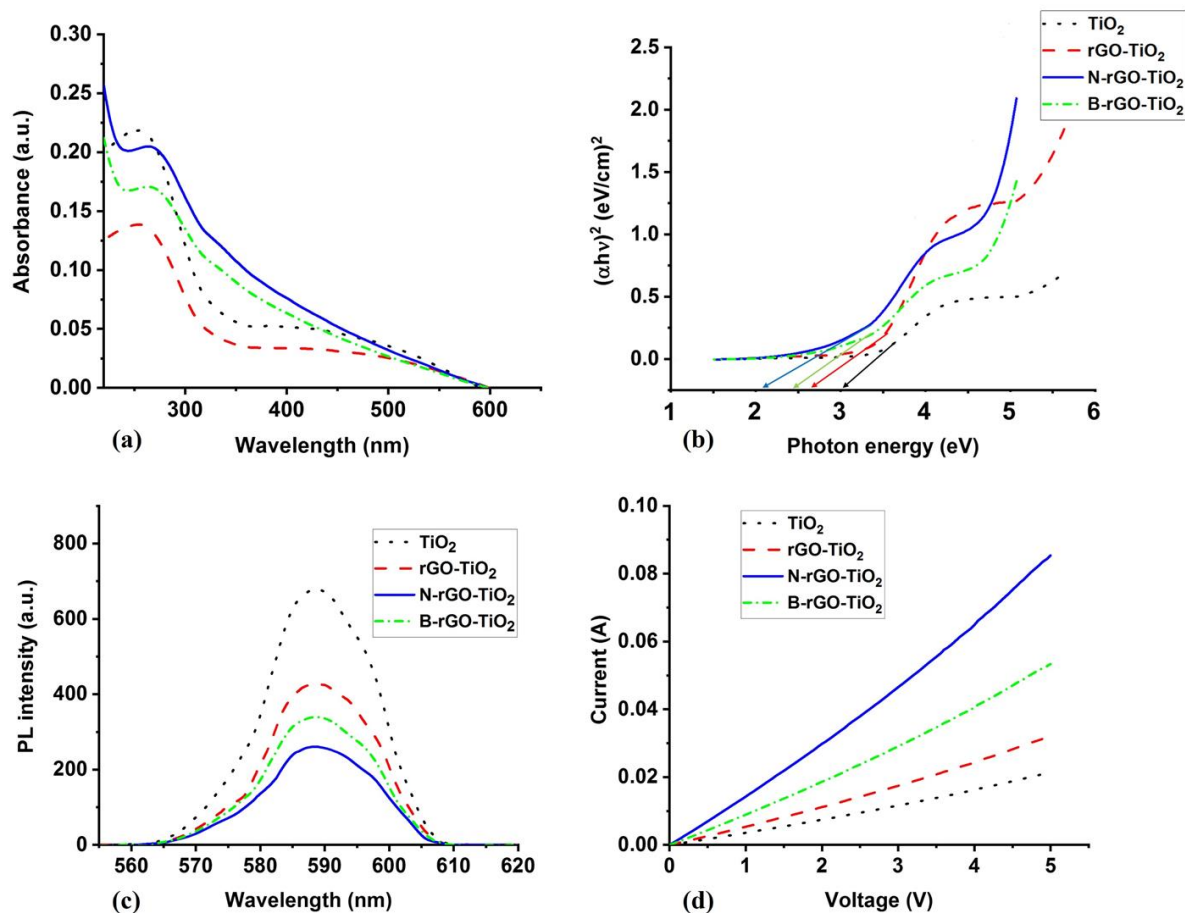
Figure 5.6: (a) UV-Vis absorption spectra, (b) Tauc's plots, (c) photoluminescence spectra, and (d) current-voltage characteristics of the TiO_2-based nanocomposites.

The UV-Vis absorption spectra were further analyzed using Tauc's plot function (Figure 5.6 (b)) to calculate the energy bandgap. Pure TiO_2 had an energy bandgap of 3.0 eV, while the absorption edge of the nanocomposites showed a shift to a longer wavelength. The threshold wavelength (366 nm) of rGO-TiO_2 corresponds to a bandgap of 2.7 eV, comparable with those previously reported [62,63]. In both heteroatom-doped rGO-TiO_2-nanocomposites, the results demonstrated that boron or nitrogen doping could drastically reduce the TiO_2 bandgap (N-rGO-TiO_2 and B-rGO-TiO_2 have bandgaps of 2.1 and 2.4 eV, respectively). This trend indicates less energy is needed to free outer shell electrons and convert them to mobile charge carriers than in pure TiO_2. The smaller bandgap is associated with larger surface areas and slower electron-hole recombination rates on the TiO_2 surface. The interfacial cross-link formation (strong hydrogen bonds between rGO or heteroatom-doped rGO and TiO_2 and Ti−O−C covalent bonds) and the decrease in oxygen functional groups affect the electronic properties of heteroatom-doped rGO or pristine rGO. Thus, the electronic structure of the TiO_2-based

nanocomposites changes from semi-metallic to semiconducting with an indirect bandgap. The lowest rGO-TiO$_2$ unoccupied band is positioned below the TiO$_2$ conduction band and largely localized on the carbon and oxygen orbitals of rGO, which brings some contributions to the rGO-bonded Ti atoms. For the heteroatom-doped rGO-based nanocomposites, the lowest unoccupied band serves as a photoelectron trap and hinders electron-hole recombination.

B-rGO-TiO$_2$ has a smaller energy bandgap than that of rGO-TiO$_2$ due to boron doping that led to more formation of Ti^{3+}. The visible light absorption in N-rGO-TiO$_2$ could have originated from the bandgap narrowing due to the mixing of O$_{2p}$ states with N$_{2p}$ or the introduction of a mid-bandgap level and nitrogen doping-induced oxygen vacancies. Therefore, the introduction of heteroatom-doped rGO into TiO$_2$ assists in reducing or modulating the bandgap, thus, resulting in better optical properties. These results indicate that heteroatoms on doped rGO encourage the separation of photoinduced charge carriers, which is crucial for photoanode applications.

5.3.9 Electron-hole transition

The recombination rate between photogenerated holes and photoinduced electrons in heteroatom-doped rGO-TiO$_2$-based nanocomposites was determined using photoluminescence spectroscopy (PL). The PL spectra are shown in Figure 5.6 (c) for pure TiO$_2$ and the nanocomposites with a 590 nm excitation wavelength. The intensity of the PL spectra tends to vary with the nanocomposite type. A lower PL intensity serves as an indication of less charge recombination. The reduction in PL intensity is attributed to the rapid transportation of photogenerated electrons and simultaneous prevention of charge carrier recombination by the nanocomposites, which is significant in improving the PCE of DSSCs.

When compared with TiO$_2$, all the TiO$_2$-based nanocomposites showed lower PL intensities due to the fast movement of electrons from the TiO$_2$ conduction band to heteroatom-doped rGO or pristine rGO. B-rGO-TiO$_2$ and N-rGO-TiO$_2$ showed a much lower PL intensity, attributed to the movement of excited electrons from the valence band to the conduction band for onward transfer to the heteroatom-doped rGO sheet due to its higher electronic conductivity, which prevents direct electron-hole recombination. Such rapid movement of electrons and holes in B-rGO-TiO$_2$ and N-rGO-TiO$_2$ leads to the reduction of the photoexcited electron-hole pair recombination rate. It also suggests that the Ti ions act as charge separators at a particular level rather than acting as recombination centres. Incorporating heteroatom-doped rGO into TiO$_2$ creates an indirect optical transition (IOT) because of the formation of a

hybrid interface, thus resulting in hole transfer from TiO$_2$ to heteroatom-doped rGO (localized *sp^2* domains), which suppresses the recombination of charge carriers.

5.3.10 Electrical properties

Figure 5.6 (d) shows the *I-V* characteristics of the nanocomposites determined using fundamental electrical conductivity measurements. The integration of rGO or heteroatom-doped rGO with TiO$_2$ led to an enhancement in the *I-V* slope, thus, implying that nanocomposites exhibited semiconducting properties. When comparing the nanocomposites, N-rGO-TiO$_2$ exhibited a steeper *I-V* slope, suggesting an enhanced electrical conductivity in N-rGO-TiO$_2$ compared to its B-rGO-TiO$_2$ and rGO-TiO$_2$ counterparts. The higher electrical conductivity correlates with the larger surface area, narrower bandgap, and lower electron-hole recombination obtained for N-rGO-TiO$_2$. Thus, TiO$_2$, attached to heteroatom-doped rGO, forms an interfacial contact by chemical bonding or electrostatic attraction, which provides electron transfer pathways.

The electrical properties of the nanocomposites were further investigated using the Hall effect. The Hall effect principle is highly dependent on the effect of an electric current and applied magnetic field to a semiconductor sample plate. Thus, a distortion in the magnetic field of charge carriers occurs, leading to the separation of electrons to one side of the sample plate and holes to the other side, giving rise to the Hall voltage [64]. The charge carrier density (*n*) and mobilities (μ) of pure TiO$_2$ and TiO$_2$-based nanocomposites were investigated using the Hall effect [65], and the results are tabulated in Table 5.5. Equations (1) and (2) were used to calculate the values of *n* and μ, respectively:

$$n = \frac{1}{R_H} \tag{1}$$

$$\mu = \frac{R_H}{\rho} \tag{2}$$

where ρ is the resistivity and R_H represents the Hall coefficient. The sign of the Hall coefficient indicates the nature of the majority carriers in a material. The rGO-TiO$_2$ and N-rGO-TiO$_2$ nanocomposites exhibited p-type conductivity, indicating that holes are the majority carriers. However, a negative Hall coefficient was observed for B-rGO-TiO$_2$, indicating that electrons are the majority carriers, i.e., n-type conductivity. These charge carrier characteristics are due to changes in the electronic structure of GO as a result of heteroatom-doping and incorporation of TiO$_2$. The resistivity value of pure TiO$_2$ was 1.79×10^{-3} Ω cm, which agrees with literature

values [66,67]. All nanocomposites exhibited a lower resistivity value compared to pure TiO_2. This was attributed to the presence of electrically conductive graphene-based materials in the nanocomposites and suggests that these nanocomposites are a promising material for application in DSSCs. Heteroatom-doped $rGO-TiO_2$ nanocomposites had higher charge carrier mobilities compared to $rGO-TiO_2$ and TiO_2, with $N-rGO-TiO_2$ having the highest carrier mobility of 0.692 cm^2 V^{-1} s^{-1}. Higher carrier mobility is beneficial for better DSSCs performance.

Table 5.5: Electrical properties of the TiO_2 and nanocomposites measured using Hall effect.

Sample	Resistivity/ Ω cm	Hall coefficient/cm^3 C^{-1}	Carrier density/cm^{-3}	Carrier mobility/cm^2 V^{-1} s^{-1}
TiO_2	1.79×10^{-3}	2.21×10^{-4}	4.52×10^3	0.124
$rGO-TiO_2$	9.01×10^{-4}	3.38×10^{-4}	2.98×10^3	0.375
$N-rGO-TiO_2$	8.59×10^{-6}	5.94×10^{-6}	1.68×10^5	0.692
$B-rGO-TiO_2$	4.20×10^{-5}	-2.26×10^{-5}	4.42×10^4	0.538

5.3.11 Electrochemical properties

The electrochemical behaviours of pure TiO_2 and heteroatom-doped $rGO-TiO_2$-based nanocomposites were investigated using cyclic voltammetry with a potential range of -1.0 to 1.0 V at a scan rate of 100 mVs^{-1}, as shown in Figure 5.7 (a). TiO_2 exhibited a rectangular behaviour with a reversible nature, which suggests the prominence of non-faradic behaviour. Earlier studies based on TiO_2 have witnessed this non-faradic behaviour [68,69]. $rGO-TiO_2$ had the least rectangular curve compared to other nanocomposites, inferring the presence of lower capacitance due to the repealing of the interaction of the $rGO-TiO_2$ electrode and electrolyte (KOH ions) [70]. $N-rGO-TiO_2$ displayed the most rectangular behaviour due to higher-level charge separation and electrochemical conductivity, implying a higher capacitance. All the nanocomposites are more similar to the electric double-layer capacitor (EDLC) behaviour.
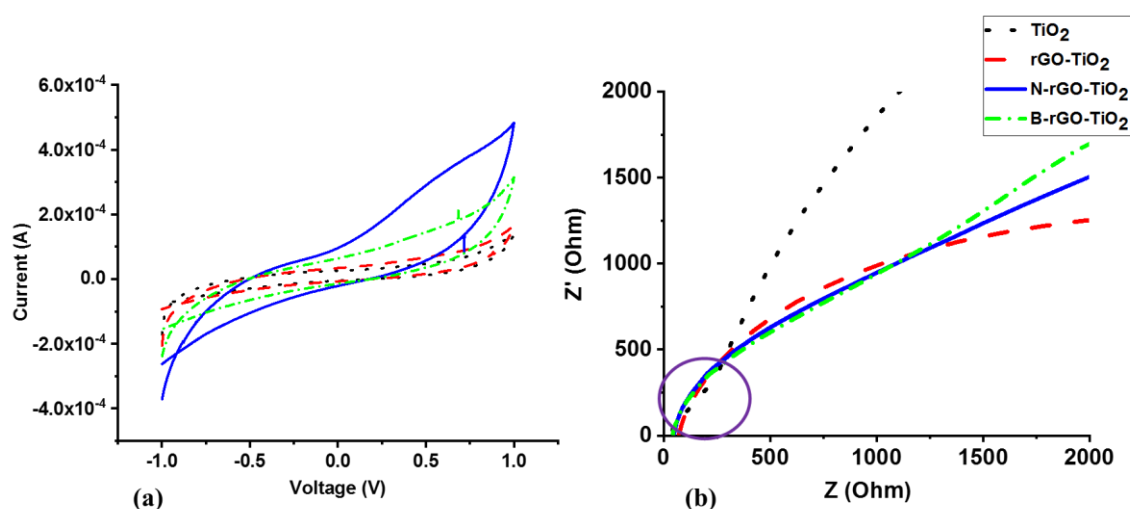
Figure 5.7:   (a) Cyclic voltammograms and (b) Nyquist plots of the TiO$_2$-based nanocomposites.

The EIS technique was used to investigate the ion transport behaviours of the pure TiO$_2$ and TiO$_2$-based nanocomposites. The Nyquist plots for pure TiO$_2$ and nanocomposites are shown in Figure 5.7 (b) and exhibited a slight semicircle arc in the high-frequency region, which is associated with low charge-transfer resistance (R$_{ct}$), and the slope of the straight line in the low frequency is due to diffusion-limited process [71]. The Warburg impedance in the Nyquist plot is indicated by the 45° slope, which originates from the frequency dependence of ion transport in the KOH (electrolyte) [72]. The Warburg region for the electrode serves as an indication of higher ion diffusion resistance. All the nanocomposites lack the semicircle, indicating that the resistance is negligible, subsequently proposing a phenomenal charge reversal with a change in voltage. This might be credited to a larger surface area and higher electrical conductivity, enabling more sites for improved catalytic activity.

5.3.12 Photovoltaic performance of the fabricated DSSCs

This section entails the light-harvesting experiments for evaluating the dye and the various nanocomposite photoanodes. Sudan II and eosin B dyes were chosen because they can harvest sunlight over a broad-spectrum of wavelengths (Supplementary Data – Figure S5.3). They both have large molecular weight and contain =O and -H functional groups responsible for easy anchoring on the surface of the metal oxide in order to improve electron transfer. The J$_{sc}$ and V$_{oc}$ for these DSSCs follow the pattern eosin B > Sudan II. The high J$_{sc}$ and V$_{oc}$ values in eosin B-based DSSCs are due to more generation and collection of light-generated carriers (Table 5.6). The low FF (15.2%) in Sudan II-based DSSCs was due to poor photogenerated

electron injection from the dye molecules to the TiO_2 photoanode. Although most photogenerated electrons from the dye molecule excited state rapidly move to the TiO_2 conduction band after irradiation, the electrons move back to recombine with the oxidized dye molecules and the electrolyte. This increases the dark current and charge recombination, mainly in the electrolyte, and subsequently causes a decrease in the PCE [73]. The eosin B-based DSSCs displayed a better PCE than the Sudan II-based DSSCs, which was attributed to the higher photogenerated electron transport rate. Thus, eosin B was then chosen and further used with the nanocomposite-based photoanodes.

The PCE of DSSCs highly depends on dye molecule properties, such as light-harvesting efficiency, electron injection rate, and oxidized dye regeneration efficiency. Thus, to enhance the DSSC performance, dye molecules ought to have high light-harvesting efficiency, an optimized electron injection efficiency, and a fast oxidized dye regeneration reaction. The eosin B dye has a higher potential for electron injection and has a higher capability for oxidized dye regeneration (Figure 5.8 (a)). Therefore, the number of photogenerated electrons in DSSCs is influenced by the type of dye and dye loading. Thus, incorporating graphene-based materials, with a larger specific surface area, into TiO_2 can improve dye adsorption on the photoanode [74].

The effect of varying the dye loading concentration (10, 50, and 100 mg L^{-1}) was tested in DSSCs. The PCE was low at lower dye loading concentrations due to relatively low photon absorption, low charge generation, and poor charge collection in the devices. However, a higher concentration (100 mg L^{-1}) of eosin B resulted in higher V_{oc}, J_{sc}, and PCE values (Supplementary data – Table S5.3 and Figure S5.4) due to high photon absorption on the semiconductor surface. Hence, this work focused more on the results obtained using 100 mg L^{-1} loading, which was discovered to be the optimum dye loading concentration.

Table 5.6: Light-harvesting performance of the TiO_2 and nanocomposite based DSSCs.

Photoanode	Dyes	V_{oc}/V	J_{sc}/mA cm^{-2}	FF/%	PCE/%
TiO_2	Sudan II	0.54	4.5	15.2	0.10 ± 0.01
TiO_2	eosin B	0.55	7.86	36.8	0.65 ± 0.03
rGO-TiO_2	eosin B	0.70	11.67	48.6	1.78 ± 0.05
N-rGO-TiO_2	eosin B	0.78	13.82	60.3	3.94 ± 0.01
B-rGO-TiO_2	eosin B	0.78	12.50	55.1	2.55 ± 0.02

A remarkable improvement was observed in the J_{sc}, V_{oc}, FF, and PCE of the nanocomposites. The nanocomposites exhibited higher FF values, probably due to the dominancy of the electron injection process, since TiO_2 integrated with rGO or heteroatom-doped rGO has a higher electron injection driving force than that of pristine TiO_2. The V_{oc} of DSSCs relies upon the energy difference between the TiO_2 conduction band and electrolyte redox potential. V_{oc} is reported to be affected by the difference between the Fermi level in the photoanode and the Nernst potential of the I^-/I_3^- electrolyte, while J_{sc} is affected by the dye adsorption, light scattering, and electron transfer efficiency [75]. Compared with pristine TiO_2, the addition of rGO tends to raise the conduction band of TiO_2, thus enhancing the V_{oc} of rGO-TiO_2 [76]. The excited electrons in the conduction band of TiO_2 prompt a higher electron population in the conduction band of ITO, thereby enhancing the J_{sc} [77]. The enhanced J_{sc} could be attributed to the improvement in dye loading, which increases photon absorption, resulting in the faster injection of electrons to the TiO_2 conduction band. The incorporation of rGO into TiO_2 also provides a proper energy level alignment between TiO_2 and ITO, which facilitates the acceleration of photogenerated electrons from the TiO_2 conduction band to an ITO electrode for onward transportation to an external circuit. This, in turn, enhanced the PCE from 0.65% for DSSCs based on pristine TiO_2 to 1.78% for the rGO-TiO_2-based devices.

When comparing the PCE of rGO-TiO_2-based DSSCs obtained from this study with previously reported values, it was observed that the literature reported values were both lower and higher, mainly due to the usage of different rGO-TiO_2 synthesis techniques that resulted in rGO-TiO_2 photoanodes with different properties. For example, Baharin *et al.* [78] synthesised rGO-TiO_2 nanocomposites using the thermal treatment method and employed them as photoanodes to fabricate DSSCs, which had a lower PCE (1.21%) compared to this study. Another lower PCE (0.48%) of rGO-TiO_2-based DSSCs was reported by Omar *et al.* [79]. Conversely, a higher PCE of 4.43% for rGO-TiO_2-based DSSCs was obtained by Patil *et al.* [80], where an indoline-based organic dye reportedly played a significant role in improving the device stability, electronic properties, spectral response and PCE. Patil *et al.* [80] demonstrated that the rGO content in rGO-TiO_2 provides more active sites for higher dye adsorption, consequently improving the DSSC performance. Rouhani *et al.* [81] reported a much higher PCE of 6.06%, which was attributed to the larger surface area of rGO-TiO_2 that assisted in improving photon harvesting and led to higher V_{oc} and J_{sc} values. Kumar *et al.* [82] also reported a PCE of 6.89%, higher than the PCE obtained in this study. Their rGO-TiO_2 was more beneficial for improving the charge transport rate and light collection efficiency.
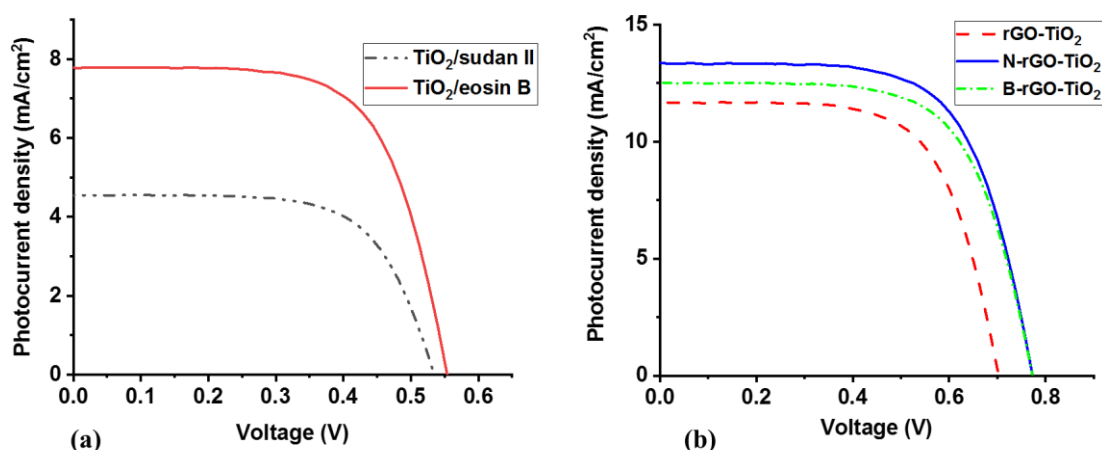
Figure 5.8: *J-V* characteristics of the (a) Sudan II and eosin B dyes and (b) TiO_2-based nanocomposites in DSSCs.

The addition of heteroatom-doped rGO to TiO_2 suppresses electron-hole recombination and enhances the J_{sc}. This is because B-rGO and N-rGO have higher electron mobility rates. Thus, B-rGO or N-rGO in the nanocomposites acts as a bridge that speeds up the transportation of electrons to the electron collector, thereby suppressing electron-hole recombination in the TiO_2 photoanode. From Table 5.6, the PCE of rGO-TiO_2-based DSSCs was higher than that of the TiO_2-based DSSCs. Such an increase in PCE is comparable with previous studies [83,84]. N-rGO-TiO_2-based DSSCs exhibited the largest J-V curve (Figure 5.8 (b)), corresponding to the highest PCE of 3.94%, attributed to the larger surface area and high electrical conductivity of the nanocomposite. The higher V_{oc} of N-rGO-TiO_2-based DSSCs could be credited to the low doping level of TiO_2. The higher doping level of TiO_2 sometimes causes the conduction and valence bands to shift and bring about a bandgap narrowing effect, thus resulting in a decrease in the V_{oc} [85], as observed in rGO-TiO_2. B-rGO-TiO_2 had a lower doping level of TiO_2 than rGO-TiO_2, yet its PCE was low, and this was due to the presence of more B-O instead of B-O-Ti, which resulted in the poor conductivity of B-rGO-TiO_2. In this study, incorporating heteroatom-doped rGO into TiO_2 resulted in a wider absorption region, a higher light-to-electron conversion rate, reduced back electron transfer process, and facilitated the efficient transportation of photoelectrons from the photoanode to the ITO electrode, which subsequently led to an enhanced PCE of the DSSCs. The *J-V* curves in Figure 5.8 (b) also showed that the photovoltaic performance of the nanocomposites was better than that of pristine rGO and heteroatom-doped rGO (Supplementary Data - Figure S5.5 and Table S5.4).

173

5.4   Conclusion

DSSCs containing various TiO_2-based nanocomposites as photoanodes were successfully fabricated, and two light-harvesting dyes, eosin B and Sudan II, were evaluated. The hydrothermal synthetic method resulted in anatase TiO_2-based nanocomposites. The integration of TiO_2 with heteroatom-doped rGO significantly enhanced the photoelectronic properties of the resulting photoanodes and reduced the recombination effect in DSSCs. The decrease in electron-hole recombination is attributed to the increase in charge carrier transport. B-rGO-TiO_2 and N-rGO-TiO_2 exhibited large surface areas, which resulted in higher dye adsorption. Apart from the large surface area, B-rGO-TiO_2 and N-rGO-TiO_2 also exhibited superior electrical conductivity, which led to faster electron transfer in the DSSCs. The J_{sc} values of DSSCs fabricated from heteroatom-doped rGO-TiO_2-based nanocomposites were enhanced due to a significant increase in photoabsorption. However, the rGO-TiO_2-based DSSCs resulted in relatively lower performance, with a V_{oc} of 0.75 V, J_{sc} of 11.67 mA cm^{-2}, and PCE of 1.78%. A relatively higher J_{sc} of 13.82 mA cm^{-2} and PCE of 3.94% were observed in DSSCs utilising the N-rGO-TiO_2 photoanode. Also, the low titanium content in B-rGO-TiO_2 and N-rGO-TiO_2 offered improved optical properties and higher electrical conductivity, which enhanced the PCE of B-rGO-TiO_2- and N-rGO-TiO_2-based DSSCs, thereby outperforming the DSSCs based on pristine rGO-TiO_2 photoanodes. Therefore, heteroatom-doped rGO-TiO_2-based nanocomposites have excellent potential to be used as photoanodes in DSSCs.

References

1.   A. Bakhshayesh, M. Mohammadi and D. Fray, *Electrochim. Acta*, **2012**, 78, 384-391.

2.   K. Al-Attafi, A. Nattestad, H. Qutaish, M.-S. Park, L. K. Shrestha, K. Ariga, S. X. Dou and J. Ho Kim, *Sci. Technol. Adv. Mater.*, **2021**, 22, 100-112.

3.   P. Gnida, P. Jarka, P. Chulkin, A. Drygała, M. Libera, T. Tański and E. Schab-Balcerzak, *Materials*, **2021**, 14, 1633-1650.

4.   G. Zamiri and S. Bagheri, *J. Colloid Interface Sci.* , **2018**, 511, 318-324.

5.   V. Kumar, R. Gupta and A. Bansal, *ACS Appl. Nano Mater.*, **2021**, 4, 6212-6222.

6.   F. M. Al-Marzouki, S. Abdalla and S. Al-Ameer, *Adv. Mater. Sci. Eng.*, **2016**, 2016, 4928710-4928724.

7.   Y. Meng, Y. Lin and Y. Lin, *J. Mater. Sci.: Mater. Electron*, **2013**, 24, 5117-5121.

8. Y. Zhang, H. Li, L. Kuo, P. Dong and F. Yan, *Curr. Opin. Colloid Interface Sci.*, **2015**, 20, 406-415.

9. S. Sharma, B. Siwach, S. Ghoshal and D. Mohan, *Renew. Sust. Energ. Rev.*, **2017**, 70, 529-537.

10. N. Kopidakis, N. Neale, K. Zhu, J. Van De Lagemaat and A. Frank, *Appl. Phys. Lett.*, **2005**, 87, 202106-202110.

11. Y. Lai, H. Zhuang, K. Xie, D. Gong, Y. Tang, L. Sun, C. Lin and Z. Chen, *New J. Chem.*, **2010**, 34, 1335-1340.

12. J. Nowotny, M. A. Alim, T. Bak, M. A. Idris, M. Ionescu, K. Prince, M. Z. Sahdan, K. Sopian, M. A. M. Teridi and W. Sigmund, *Chem. Soc. Rev.*, **2015**, 44, 8424-8442.

13. M. Bellardita, A. Di Paola, B. Megna and L. Palmisano, *Appl. Catal. B: Environ.*, **2017**, 201, 150-158.

14. X. Che, L. Li, J. Zheng, G. Li and Q. Shi, *J. Chem. Thermodyn.*, **2016**, 93, 45-51.

15. Y. Wang, T. Sun, X. Liu, H. Zhang, P. Liu, H. Yang, X. Yao and H. Zhao, *Phys. Rev. B*, **2014**, 90, 045301-045306.

16. T. Luttrell, S. Halpegamage, J. Tao, A. Kramer, E. Sutter and M. Batzill, *Sci. Rep.*, **2014**, 4, 4041-4048.

17. Q. Zhang and C. Li, *Nanomaterials (Basel)*, **2020**, 10, 911-918.

18. A. Aboulouard, B. Gultekin, M. Can, M. Erol, A. Jouaiti, B. Elhadadi, C. Zafer and S. Demic, *J. Mater. Res. Technol.*, **2020**, 9, 1569-1577.

19. A. K. Mohapatra and J. Nayak, *Optik*, **2018**, 156, 268-278.

20. N. Yang, J. Zhai, D. Wang, Y. Chen and L. Jiang, *ACS Nano*, **2010**, 4, 887-894.

21. A. Kim, J. Kim, M. Y. Kim, S. W. Ha, N. T. T. Tien and M. Kang, *Bull Korean Chem. Soc.*, **2012**, 33, 3355-3360.

22. S. Daulay, A. Madsuha, E. Rosa and A. Yuwono, *J. Phys. Conf. Ser.*, **2019**, 1402, 055101-055107.

23. L. Shahriary and A. A. Athawale, *Int. J. Renew. Energy Environ. Eng.*, **2014**, 2, 58-63.

24. N. P. D. Ngidi, M. A. Ollengo and V. O. Nyamori, *Materials*, **2019**, 12, 3376-3400.

25. N. P. D. Ngidi, M. A. Ollengo and V. O. Nyamori, *New J. Chem.*, **2020**, 44, 16864-16876.

26. N. P. D. Ngidi, E. Muchuweni and V. O. Nyamori, *RSC Adv.*, **2022**, 12, 2462-2472.

27. P. N. O. Gillespie and N. Martsinovich, *ACS Appl Mater Interfaces*, **2019**, 11, 31909-31922.

28. E. Finazzi, C. Di Valentin and G. Pacchioni, *J. Phys. Chem. C*, **2009**, 113, 220-228.

29. Q. Huang, S. Tian, D. Zeng, X. Wang, W. Song, Y. Li, W. Xiao and C. Xie, *ACS Catal.*, **2013**, 3, 1477-1485.

30. S. Ida, P. Wilson, B. Neppolian, M. Sathish, A. R. Mahammed Shaheer and P. Ravi, *Ultrason. Sonochemistry*, **2020**, 64, 104866-104907.

31. S. Delekar, H. Yadav, S. Achary, S. Meena and S. Pawar, *Appl. Surf. Sci.*, **2012**, 263, 536-545.

32. U. Mehmood, K. Harrabi, I. A. Hussein and S. Ahmed, *IEEE J. Photovolt.*, **2016**, 6, 196-201.

33. L.-L. Tan, W.-J. Ong, S.-P. Chai and A. R. Mohamed, *Nanoscale Res. Lett.*, **2013**, 8, 465-474.

34. S. Phromma, T. Wutikhun, P. Kasamechonchung, T. Eksangsri and C. Sapcharoenkun, *Appl. Sci.*, **2020**, 10, 993-1006.

35. J. Ge, Y. Ping, G. Liu, G. Qiao, E. J. Kim and M. Wang, *Mater. Lett.*, **2016**, 181, 216-219.

36. J. Guo, S. Zhu, Z. Chen, Y. Li, Z. Yu, Q. Liu, J. Li, C. Feng and D. Zhang, *Ultrason. Sonochem.*, **2011**, 18, 1082-1090.

37. P. M. Martins, C. G. Ferreira, A. R. Silva, B. Magalhães, M. M. Alves, L. Pereira, P. A. A. P. Marques, M. Melle-Franco and S. Lanceros-Méndez, *Compos. B. Eng.*, **2018**, 145, 39-46.

38. C. Hou, Q. Zhang, Y. Li and H. Wang, *J. Hazard. Mater.*, **2012**, 205, 229-235.

39. H. Arami, M. Mazloumi, R. Khalifehzadeh and S. K. Sadrnezhaad, *Mater. Lett.*, **2007**, 61, 4559-4561.

40. Y.-w. Jun, M. F. Casula, J.-H. Sim, S. Y. Kim, J. Cheon and A. P. Alivisatos, *J. Am. Chem. Soc.*, **2003**, 125, 15981-15985.

41. J. S. Chen, Y. L. Tan, C. M. Li, Y. L. Cheah, D. Luan, S. Madhavi, F. Y. C. Boey, L. A. Archer and X. W. Lou, *J. Am. Chem. Soc.*, **2010**, 132, 6124-6130.

42. H. M. Yadav and J.-S. Kim, *J. Alloys Compd.*, **2016**, 688, 123-129.

43. M. S. Dresselhaus, A. Jorio, M. Hofmann, G. Dresselhaus and R. Saito, *Nano Lett.*, **2010**, 10, 751-758.

44. D. Liang, C. Cui, H. Hu, Y. Wang, S. Xu, B. Ying, P. Li, B. Lu and H. Shen, *J. Alloys Compd.*, **2014**, 582, 236-240.

45. Y. Zhang, N. Zhang, Z.-R. Tang and Y.-J. Xu, *Phys. Chem. Chem. Phys.*, **2012**, 14, 9167-9175.

46. S. Bagwasi, B. Tian, J. Zhang and M. Nasir, *Chem. Eng. J.*, **2013**, 217, 108-118.

47.   J. Liu, Q. Li, Y. Zou, Q. Qian, Y. Jin, G. Li, K. Jiang and S. Fan, *Nano Lett.*, **2013**, 13, 6170-6175.

48.   S. Cao, T. Liu, Y. Tsang and C. Chen, *Appl. Surf. Sci.*, **2016**, 382, 225-238.

49.   L. G. Cançado, A. Jorio, E. M. Ferreira, F. Stavale, C. A. Achete, R. B. Capaz, M. V. d. O. Moutinho, A. Lombardo, T. Kulmala and A. C. Ferrari, *Nano Lett.*, **2011**, 11, 3190-3196.

50.   Y. Wang, Z. Shi and J. Yin, *ACS Appl Mater Interfaces*, **2011**, 3, 1127-1133.

51.   A. Rosy and G. Kalpana, *Bull. Mater. Sci.*, **2018**, 41, 81-88.

52.   M. S. A. Sher Shah, A. R. Park, K. Zhang, J. H. Park and P. J. Yoo, *ACS Appl Mater Interfaces*, **2012**, 4, 3893-3901.

53.   V. Štengl, S. Bakardjieva, T. M. Grygar, J. Bludská and M. Kormunda, *Chem. Cent. J.*, **2013**, 7, 41-53.

54.   W. Vallejo, A. Rueda, C. Díaz-Uribe, C. Grande and P. Quintana, *R. Soc. Open Sci.*, **2019**, 6, 181821-181838.

55.   T. Lavanya, M. Dutta and K. Satheesh, *Sep. Purif. Technol.*, **2016**, 168, 284-293.

56.   M. Ates, Y. Bayrak, H. Ozkan, O. Yoruk, M. Yildirim and O. Kuzgun, *J. Polym. Res.*, **2019**, 26, 49-65.

57.   J. F. Leal, S. M. A. Cruz, B. T. A. Almeida, V. I. Esteves, P. A. A. P. Marques and E. B. H. Santos, *Environ. Sci.: Water Res. Technol.*, **2020**, 6, 1018-1027.

58.   L. Wei, P. Wang, Y. Yang, Z. Zhan, Y. Dong, W. Song and R. Fan, *Inorg. Chem. Front.*, **2018**, 5, 54-62.

59.   B. Y. S. Chang, N. M. Huang, M. N. An'amt, A. R. Marlinda, Y. Norazriena, M. R. Muhamad, I. Harrison, H. N. Lim and C. H. Chia, *Int J Nanomedicine*, **2012**, 7, 3379-3387.

60.   M. Atif, W. Farooq, A. Fatehmulla, M. Aslam and S. M. Ali, *Materials*, **2015**, 8, 355-367.

61.   S. K. Kuriechen, S. Murugesan and S. Paul Raj, *J. Catal.*, **2013**, 2013, 1-6.

62.   M. Nasr, S. Balme, C. Eid, R. Habchi, P. Miele and M. Bechelany, *J. Phys. Chem. C*, **2017**, 121, 261-269.

63.   M. Ruidíaz-Martínez, M. A. Álvarez, M. V. López-Ramón, G. Cruz-Quesada, J. Rivera-Utrilla and M. Sánchez-Polo, *Catalysts*, **2020**, 10, 520-545.

64.   N. T. Padmanabhan, P. Ganguly, S. C. Pillai and H. John, *Mater. Today Energy*, **2020**, 17, 100447-100457.

65. A. Haque, M. Abdullah-Al Mamun, M. Taufique, P. Karnati and K. Ghosh, *IEEE Trans. Semicond. Manuf.*, **2018**, 31, 535-544.

66. N. Musila, M. Munji, J. Simiyu, E. Masika, R. Nyenge and M. Kineene, *Traektoriâ Nauki= Path of Science*, **2018**, 4, 3006-3012.

67. A. A. Daniyan, L. E. Umoru and B. Olunlade, *Journal of Minerals and Materials Characterization and Engineering*, **2013**, 1, 138-144.

68. D. J. Ahirrao, H. M. Wilson and N. Jha, *Appl. Surf. Sci.*, **2019**, 491, 765-778.

69. P. Naresh Kumar Reddy, D. P. M. D. Shaik, V. Ganesh, D. Nagamalleswari, K. Thyagarajan and P. Vishnu Prasanth, *Ceram. Int.*, **2019**, 45, 16251-16260.

70. S. Britto, V. Ramasamy, P. Murugesan, R. Thangappan and R. Kumar, *Diam. Relat. Mater.*, **2022**, 122, 108798-108809.

71. H. Han, T. Song, E.-K. Lee, A. Devadoss, Y. Jeon, J. Ha, Y.-C. Chung, Y.-M. Choi, Y.-G. Jung and U. Paik, *ACS Nano*, **2012**, 6, 8308-8315.

72. J. Yan, T. Wei, W. Qiao, B. Shao, Q. Zhao, L. Zhang and Z. Fan, *Electrochim. Acta*, **2010**, 55, 6973-6978.

73. H. Cheema and K. S. Joya, *Titanium Dioxide: Material for a Sustainable Environment*, **2018**, 20, 387-420.

74. Y.-H. Nien, H.-H. Chen, H.-H. Hsu, P.-Y. Kuo, J.-C. Chou, C.-H. Lai, G.-M. Hu, C.-H. Kuo and C.-C. Ko, *Vacuum*, **2019**, 167, 47-53.

75. Z. Xiang, X. Zhou, G. Wan, G. Zhang and D. Cao, *ACS Sustain. Chem. Eng.*, **2014**, 2, 1234-1240.

76. H. Ding, S. Zhang, J.-T. Chen, X.-P. Hu, Z.-F. Du, Y.-X. Qiu and D.-L. Zhao, *Thin Solid Films*, **2015**, 584, 29-36.

77. R. Ramamoorthy, K. Karthika, A. Maggie Dayana, G. Maheswari, V. Eswaramoorthi, N. Pavithra, S. Anandan and R. Victor Williams, *J. Mater. Sci.: Mater. Electron*, **2017**, 28, 13678-13689.

78. A. Baharin, S. K. Sahari, R. Kemat and N. E. A. Azhar, *Int. J. Nanoelectron. Mater.*, 13, 159-168.

79. A. Omar, M. S. Fakir, K. S. Hamdan, N. H. Rased and N. A. Rahim, *Pigment Resin Technol.*, **2020**, 49, 315-324.

80. J. V. Patil, S. S. Mali, J. S. Shaikh, A. P. Patil, P. S. Patil and C. K. Hong, *Synth. Met.*, **2019**, 256, 116146-116155.

81. S. Rouhani, M. Hosseinnezhad, N. Sohrab, K. Gharanjig, A. Salem and Z. Ranjbar, *Prog. Color Color. Coat.*, **2022**, 15, 123-131.

82.   K. A. Kumar, K. Subalakshmi and J. Senthilselvan, *Mater. Sci. Semicond. Process*, **2019**, 96, 104-115.

83.   S. P. Lim, A. Pandikumar, N. M. Huang and H. N. Lim, *Int. J. Energy Res.*, **2015**, 39, 812-824.

84.   G. Cheng, M. S. Akhtar, O. B. Yang and F. J. Stadler, *ACS Appl. Mater. Interface*, **2013**, 5, 6635-6642.

85.   B. Xu, G. Wang and H. Fu, *Sci. Rep.*, **2016**, 6, 23395-23409.

Appendix: Supporting information for Chapter 5
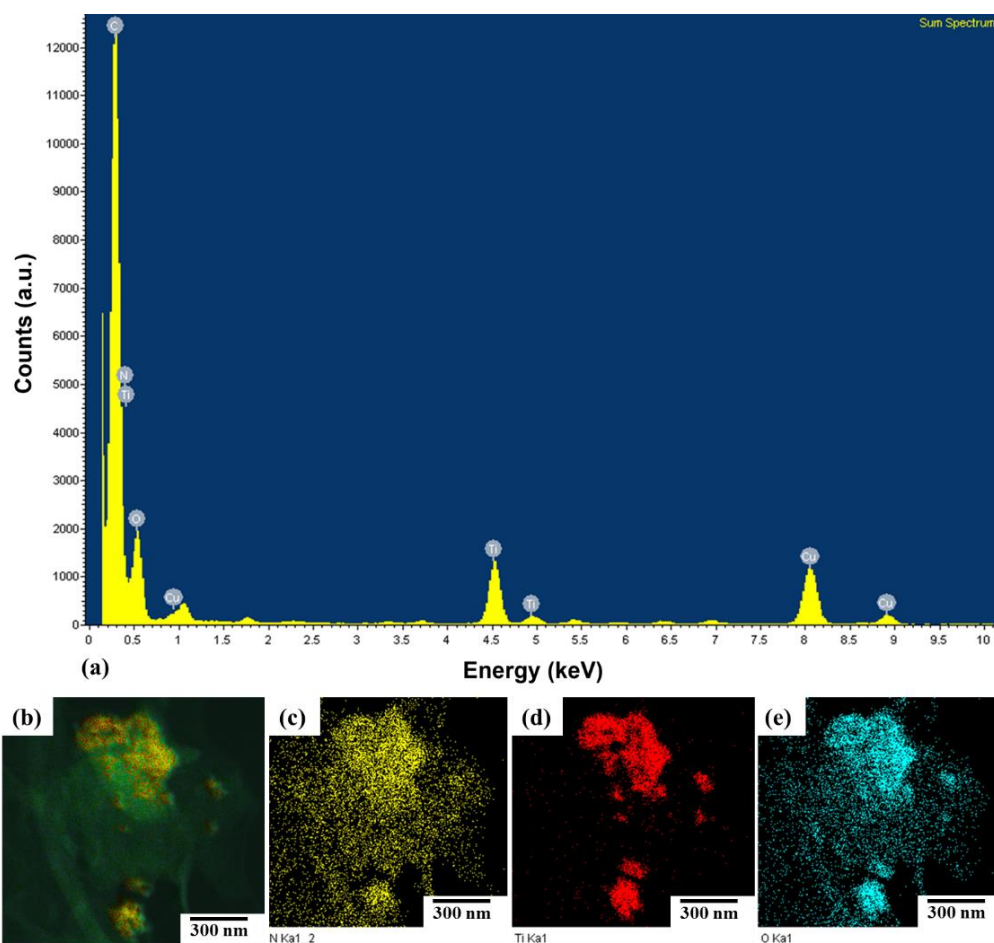
Figure S5.1: (a) EDX spectrum of a measurement conducted at the selected area of N-rGO/TiO₂, and elemental mapping of (b) N-rGO/TiO₂, (c) nitrogen, (d) titanium and (e) oxygen for N-rGO/TiO₂ nanocomposites.

Table S5.1: Elemental composition of the nanocomposites.

Sample	Elemental analysis				ICP-OES
	Carbon/%	Hydrogen/%	Oxygen/%	Nitrogen/%	Boron/%
rGO-TiO₂	60.94 ± 1	2.64 ± 1	1.36 ± 1	-	-
N-rGO-TiO₂	63.07 ± 1	2.32 ± 1	1.51 ± 1	3.08 ± 1	-
B-rGO-TiO₂	69.88 ± 1	4.65 ± 1	3.59 ± 1	-	1.46 ± 0.05

Table S5.2: Physicochemical properties of rGO and heteroatom-doped rGO.

Sample	Nitrogen/%	Boron/%	I_D/I_G	Surface area/m^2 g^{-1}
rGO	-	-	0.72	70.21
N-rGO	10.75	-	1.09	71.63
B-rGO	-	6.61	1.18	69.59
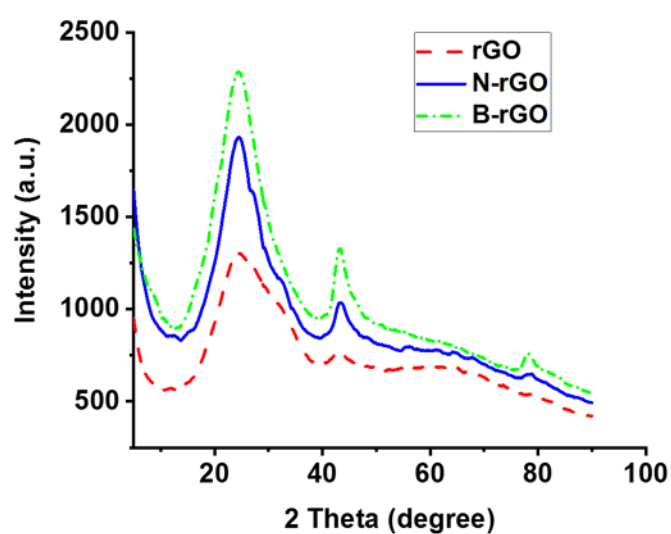
Figure S5.2: P-XRD diffractograms of rGO and heteroatom-doped rGO.
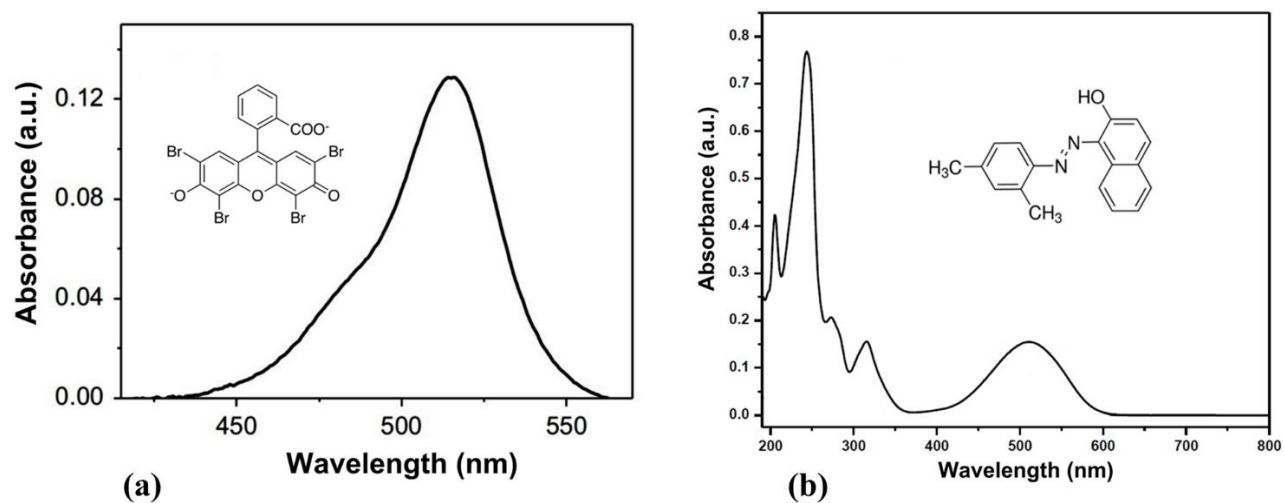
Figure S5.3: UV-Vis absorbance spectra of (a) eosin B and (b) Sudan II used in DSSCs.

Table S5.3: Photovoltaic parameters of DSSCs employing TiO$_2$-based nanocomposite photoanodes with various dye loading concentrations.

Eosin B dye concentration/mg L^{-1}	Photoanode	V$_{oc}$/V	J$_{sc}$/mA cm^{-2}	FF/%	PCE/%
10	rGO-TiO$_2$	0.21	4.36	27.8	0.31 ± 0.03
	N-rGO-TiO$_2$	0.33	5.46	30.4	0.59 ± 0.02
	B-rGO-TiO$_2$	0.48	4.51	31.2	0.43 ± 0.01
50	rGO-TiO$_2$	0.49	6.49	48.0	0.91 ± 0.02
	N-rGO-TiO$_2$	0.57	7.36	52.9	1.35 ± 0.01
	B-rGO-TiO$_2$	0.51	8.31	48.1	1.01 ± 0.01
100	rGO-TiO$_2$	0.70	11.67	48.6	1.78 ± 0.05
	N-rGO-TiO$_2$	0.78	13.82	60.3	3.94 ± 0.01
	B-rGO-TiO$_2$	0.78	12.50	55.1	2.55 ± 0.02
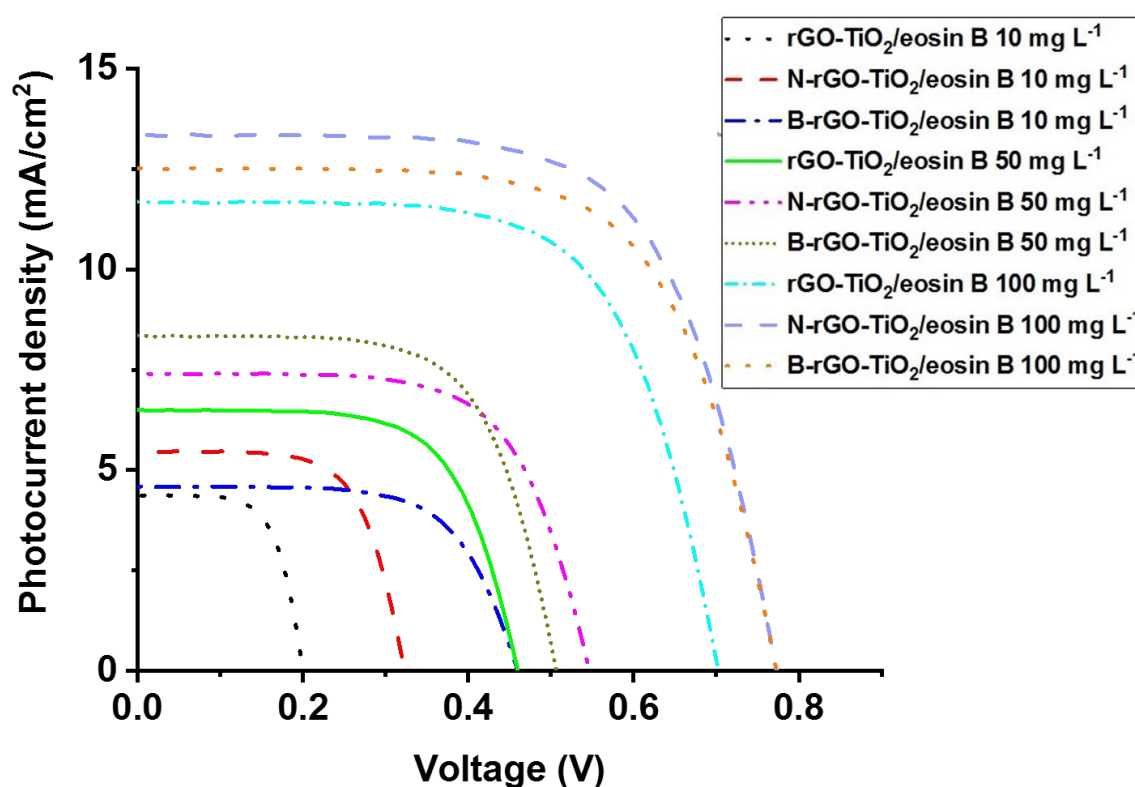
Figure S5.4: *J-V* characteristics of DSSCs employing TiO$_2$-based nanocomposite photoanodes with various dye loading concentrations.

Table S5.4: Photovoltaic parameters of DSSCs based on rGO and heteroatom-doped rGO with 100 mg L^{-1} of eosin B.

Photoanode	V_{oc}/V	J_{sc}/mA cm^{-2}	FF/%	PCE/%
rGO	0.52	6.00	16.7	0.41 ± 0.01
N-rGO	0.61	10.25	30.9	1.02 ± 0.01
B-rGO	0.56	9.13	28.5	0.98 ± 0.02
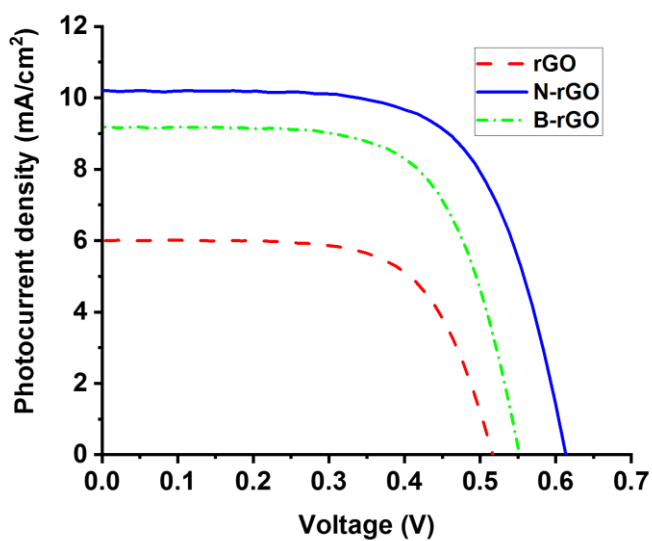
Figure S5.5: *J-V* characteristics of rGO- and heteroatom-doped rGO-based DSSCs using 100 mg L^{-1} of eosin B.

CHAPTER 6

Synthesis and characterisation of heteroatom-doped reduced graphene oxide/bismuth oxide nanocomposites and their application as photoanodes in DSSCs†

Nonjabulo P. D. Ngidi, [ID] Edigar Muchuweni [ID] ‡ and Vincent O. Nyamori [ID] *

Semiconductor materials have been recently employed in photovoltaic devices, particularly dye-sensitized solar cells (DSSCs), to solve numerous global issues, especially the current energy crisis emanating from the depletion and hazardous nature of conventional energy sources, such as fossil fuels and nuclear energy. However, progress for the past years has been mainly limited by poor electron injection and charge carrier recombination experienced by DSSCs at the photoanode. Thus, novel semiconductor materials such as bismuth oxide (Bi_2O_3) have been investigated as an alternative photoanode material. In this study, Bi_2O_3 was integrated with nitrogen- or boron-doped reduced graphene oxide (N-rGO or B-rGO, respectively) via a hydrothermal approach at a temperature of 200 °C. Various instrumental techniques were used to investigate the morphology, phase structure, thermal stability, and surface area of the resulting nanocomposites. The incorporation of N-rGO or B-rGO into Bi_2O_3 influenced the morphology and structure of the nanocomposite, thereby affecting the conductivity and electrochemical properties of the nanocomposite. B-rGO/Bi_2O_3 exhibited a relatively large surface area (65.5 m^2 g^{-1}), lower charge transfer resistance (108.4 Ω), higher charge carrier mobility (0.368 cm^2 V^{-1} s^{-1}), and higher electrical conductivity (6.31 S cm^{-1}) than N-rGO/Bi_2O_3. This led to the fabrication of B-rGO/Bi_2O_3 photoanode-based DSSCs with superior photovoltaic performance, as revealed by their relatively high power conversion efficiency (PCE) of 2.97%, which outperformed the devices based on N-rGO/Bi_2O_3, rGO/Bi_2O_3 and Bi_2O_3 photoanodes. Therefore, these results demonstrate the promising potential of heteroatom-doped rGO/Bi_2O_3-based nanocomposites as photoanode materials of choice for future DSSCs.

Synthesis and characterisation of heteroatom-doped reduced graphene oxide/bismuth oxide nanocomposites and their application as photoanodes in DSSCs

Nonjabulo P. D. Ngidi, Edigar Muchuweni and Vincent O. Nyamori

School of Chemistry and Physics, University of KwaZulu-Natal, Westville Campus, Private Bag X54001, Durban 4000, South Africa

Graphical abstract

Abstract

Semiconductor materials have been recently employed in photovoltaic devices, particularly dye-sensitized solar cells (DSSCs), to solve numerous global issues, especially the current energy crisis emanating from the depletion and hazardous nature of conventional energy sources, such as fossil fuels and nuclear energy. However, progress for the past years has been mainly limited by poor electron injection and charge carrier recombination experienced by DSSCs at the photoanode. Thus, novel semiconductor materials such as bismuth oxide (Bi_2O_3) have been investigated as an alternative photoanode material. In this study, Bi_2O_3 was integrated with nitrogen- or boron-doped reduced graphene oxide (N-rGO or B-rGO, respectively) via a hydrothermal approach at a temperature of 200 °C. Various instrumental techniques were used to investigate the morphology, phase structure, thermal stability, and surface area of the resulting nanocomposites. The incorporation of N-rGO or B-rGO into Bi_2O_3 influenced the morphology and structure of the nanocomposite, thereby affecting the conductivity and electrochemical properties of the nanocomposite. B-rGO/Bi_2O_3 exhibited a relatively large surface area (65.5 m^2 g^{-1}), lower charge transfer resistance (108.4 Ω), higher charge carrier mobility (0.368 cm^2 V^{-1} s^{-1}), and higher electrical conductivity (6.31 S cm^{-1}) than N-rGO/Bi_2O_3. This led to the fabrication of B-rGO/Bi_2O_3 photoanode-based DSSCs with superior photovoltaic performance, as revealed by their relatively high power conversion efficiency (PCE) of 2.97%, which outperformed the devices based on N-rGO/Bi_2O_3, rGO/Bi_2O_3, and Bi_2O_3 photoanodes. Therefore, these results demonstrate the promising potential of heteroatom-doped rGO/Bi_2O_3-based nanocomposites as photoanode materials of choice for future DSSCs.

Keywords

6.1   Introduction

Recent developments in technology have led to a tremendous demand for energy. Thus, renewable energy sources, especially solar energy, which can be converted to electrical energy by photovoltaic devices, particularly dye-sensitized solar cells (DSSCs), have been favoured by many researchers [1-5]. The main component of DSSCs is the photoanode, which is responsible for transferring photogenerated electrons from the excited dye molecules to the collecting electrode. Thus, a high electron-transport rate reduces the charge recombination rate and improves the power conversion efficiency (PCE). The development of DSSCs by means of tailoring the properties of semiconductor nanomaterials to suit photoanode applications has attracted a lot of attention in solar energy research. This is because semiconductor nanomaterials have unique physical, chemical, electronic and optical properties. Semiconductor photoanode nanomaterials with a high surface area can facilitate more dye absorption, effective photon harvesting, and fast charge transport, thereby improving the PCE of DSSCs. Various approaches, such as doping,[6] surface modification,[7] and the use of hybrid semiconducting nanomaterials [8-12], have been proposed to improve the properties of semiconductor materials. Semiconductor nanomaterials such as metal oxides, including titanium dioxide (TiO_2) [13], zinc oxide (ZnO) [14], zirconium dioxide (ZrO_2) [15], tungsten trioxide (WO_3) [16], and tin(IV) oxide (SnO_2) [17], have been extensively explored as photoanode materials in DSSCs.

To date, there are few studies based on the application of bismuth oxide (Bi_2O_3) as a photoanode in DSSCs, yet Bi_2O_3 has attracted great interest in photocatalysis [18] and supercapacitors [19] due to its unique crystal structure [20], non-toxicity [21], and wide bandgap, ranging from 2.47 to 3.55 eV [22]. Bi_2O_3 also exhibits a high dielectric permittivity, refractive index, photoconductivity, and oxygen ion conductivity. There are four polymorphs of Bi_2O_3, namely, body-centred cubic (ɤ), face-centred cubic (δ), tetragonal (β) and monoclinic (α).[23] Among these, α-Bi_2O_3 and δ-Bi_2O_3 are thermodynamically stable at ambient conditions, whereas β-Bi_2O_3 and ɤ-Bi_2O_3 are metastable, and are stabilised by the addition of impurities or by controlling the reaction conditions [24]. An investigation on the effect of β-Bi_2O_3 as a photoanode in DSSCs has been reported by Shaikh *et al.* [25] and resulted in a PCE of 0.078%. However, a slight improvement in the PCE to 1.5% was observed when β-Bi_2O_3 was incorporated with ZnO. Fatima *et al.* [26] reported a PCE of 0.05% for DSSCs with α-Bi_2O_3-based photoanodes. The low PCE was attributed to the presence of trapping states at the

interfaces within the photoanode. Thus, more research on Bi_2O_3 nanomaterials for photoanode applications in DSSCs is still required.

Recently, metal oxides have been integrated with an allotrope of carbon, especially graphene, and used as positive electrode material in energy storage devices [27,28]. Graphene has attracted significant interest due to its high charge carrier mobility, large specific surface area, high mechanical strength, high electrical conductivity, and chemical resilience. Also, graphene is reported to display predominant energy storage performance compared with other carbon nanostructures, such as carbon nanotubes and graphite [29,30]. Graphene oxide (GO) is defined as a cutting edge of graphene functionalised with carbonyl and carboxyl groups at the edges; and epoxy and hydroxyl groups in the basal plane [31]. The oxygen-based functional groups on the surface of GO are responsible for integrating GO with metal oxides, resulting in GO-based metal oxide nanocomposites.

The main focus in the reported studies of Bi_2O_3 was to integrate Bi_2O_3 with reduced graphene oxide (rGO) due to the distinctive mechanical, electrical, and electrochemical properties of rGO [32-34]. This is envisaged to help overcome the drawbacks of pristine rGO, such as its usual tendency to agglomerate or restack to form graphite due to π-π stacking and van der Waals forces when the rGO nanosheets are close to each other [35], resulting in poor electrochemical properties. Nitrogen-doped reduced graphene oxide (N-rGO) and boron-doped reduced graphene oxide (B-rGO) have been reported to have improved electrochemical properties than rGO [36]; thus, integrating Bi_2O_3 with N-rGO or B-rGO is expected to yield favourable device performance. However, to the best of our knowledge, no detailed studies have reported the electrochemical properties of heteroatom-doped rGO (N-rGO or B-rGO) integrated with Bi_2O_3 and their application as photoanodes in DSSCs. Hence, in this study, the effect of nitrogen or boron on the physicochemical and electrochemical properties of heteroatom-doped rGO/Bi_2O_3 nanocomposites was investigated for the first time by means of various instrumental techniques, so as to enhance the electrochemical properties of Bi_2O_3, reduce the aggregation of rGO, and subsequently improve the performance of DSSCs.

6.2   Experimental

6.2.1   Materials

Bismuth oxide (Bi_2O_3, 99.99%), 4-nitro-*o*-phenylenediamine (≥99%), boric anhydride (≥98%), boron standard solution (999.5 ± 20 mg L^{-1}), potassium hydroxide (KOH, ≥85%, pellets), bismuth standard for ICP traceCert® (1000 mg L^{-1} Bi in nitric acid), Nafion (≤100%), lithium

iodide (99.9%), 4-tert-butylpyridine (98%), guanidinium thiocyanate (99%), 1-methyl-3-propylimidazolium iodide (99.99%), acetonitrile ($\geq$99.9%), poly(vinyl acetate) (99.9%), absolute ethanol (99.5%), eosin B (97%) and indium tin oxide (ITO) coated glass slides (15 Ω, 30 x 30 x 0.7 mm) were purchased from Sigma-Aldrich, South Africa.

6.2.2 Synthesis of the nanocomposite

rGO was synthesised via thermal annealing of GO at a temperature of 600 °C under 10% H_2 in argon [37], while N-rGO or B-rGO was synthesised by thermal treatment of GO and a precursor of 4-nitro-o-phenylenediamine or boric anhydride, respectively, at a temperature of 600 °C [38,39]. Bi_2O_3 (0.2 g) and rGO, N-rGO, or B-rGO (0.5 g) were dispersed in absolute ethanol (60 mL) and sonicated for 2 h (Scheme 6.1). After sonication, the mixtures were transferred into a Teflon-lined stainless-steel autoclave and thermally treated at a temperature of 200 °C for 24 h. The nanocomposites were purified by washing them with double-distilled water, followed by drying the samples in an oven for 24 h at 60 °C before characterisation.
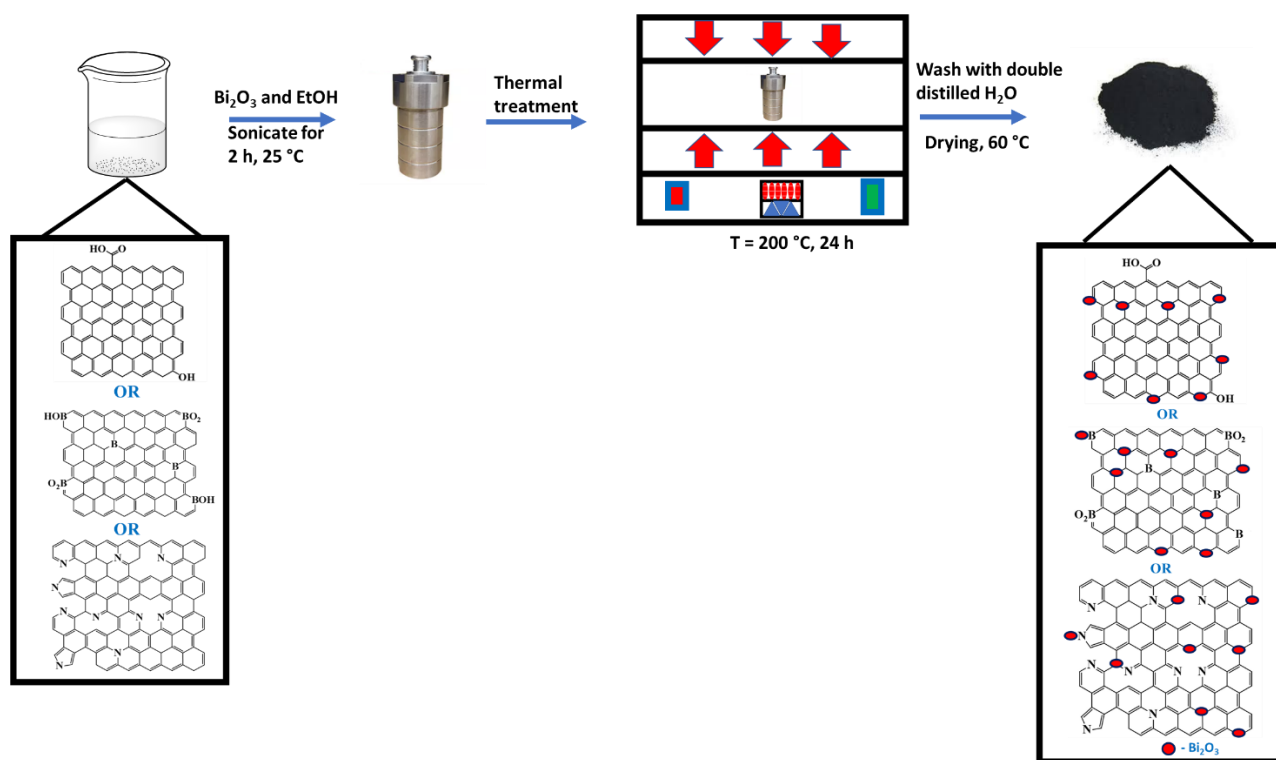
Scheme 6.1: Schematic diagram of the conversion of rGO, N-rGO and B-rGO to Bi_2O_3-based nanocomposites.

6.2.3 Device fabrication

The Bi_2O_3-based nanocomposite (100 mg) was dispersed in absolute ethanol (0.3 mL), sonicated, and deposited onto an ITO glass of the photoanode by using the Doctor Blade

method. The photoanode was then annealed at 300 °C for 30 min. After thermal annealing, 0.3 mM eosin B dye (150 μL) was loaded onto the photoanode. The iodide/triiodide gel state electrolyte was stained onto the dye-coated photoanode, followed by assembling the aluminium-coated cathode in a sandwich-like fashion. The iodide/triiodide gel state electrolyte was prepared by firstly synthesizing the liquid electrolyte. The liquid electrolyte was synthesised by mixing lithium iodide (0.3348 g), 4-tert-butylpyridine (1.6900 g), guanidinium thiocyanate (0.2954 g) and 1-methyl-3-propylimidazolium iodide (0.3173 g) and dissolved in acetonitrile (5 mL). The synthesised liquid electrolyte (1.2484) was mixed with poly(vinyl acetate) (0.6022 g) and stirred using a glass rod until a gel state electrolyte was formed, and further kept in a refrigerator at 0 °C.

6.2.4 Characterisation

Field emission-scanning electron microscopy (FE-SEM, Carl Zeiss Ultra Plus) was used to investigate the surface morphology of the nanocomposites. Transmission electron microscopy (TEM, JEOL JEM, 1010 model) was used to investigate the microstructure of the nanocomposites. The presence of various elements in the nanocomposites was investigated by elemental analysis (Elementar vario EL cube CHNSO elemental analyser), and Bi_2O_3 was quantified via inductively coupled plasma-optical emission spectrometry (ICP-OES, PerkinElmer Optima 5300 DV). The presence of various functional groups was determined by Fourier transform infrared spectroscopy (PerkinElmer Spectrum 100, FTIR spectrophotometer, with an attenuated total reflectance (ATR) accessory).

The phase compositions present in the nanocomposites were evaluated by means of powder X-ray diffraction (XRD, Bruker AXS, Cu K$_\alpha$ radiation source, $\lambda = 0.154$ nm). The graphitic nature of the nanocomposites was investigated by a Renishaw inVia Raman microscope at an excitation wavelength of 488 nm. The thermal stability was analysed with a TA Instruments Q series^{TM} thermal analyser DSC/TGA (Q600) instrument. The textural characteristics were determined using a Micromeritics Tristar II 3020 surface area and porosity analyser. The electrical conductivity of the nanocomposites was investigated by a four-point probe (Keithley 2400 source-meter). Hall effect measurements were carried out using an Ecopia Hall effect measurements system, model HMS 3000, equipped with HMS3000 VER 3.15.5 software.

Cyclic voltammetry (CV) and electrochemical impedance spectroscopy (EIS) were carried out on a VersaSTAT3F potentiostat/galvanostat electrochemical workstation, with ZSimpWin software utilised for EIS data analysis. A counter electrode (platinum wire (Pt)), a reference

electrode (Ag/AgCl), and a working electrode (mixture of nanocomposite) were used. A mixture of the nanocomposite and a binder (Nafion) were dispersed in absolute ethanol and cast onto the electrode. The potassium hydroxide redox couple was used as the electrolyte. CV was carried out at scan rates of 5, 25, 50, 75, and 100 mV s^{-1} in the potential range (-1.0 to 1.0 V). The photovoltaic measurements of the fabricated DSSCs with a photoanode active area of 0.96 cm^2 were performed with an Oriel Instruments LCS-100 solar simulator accompanied by a Keithley 2420 source meter under one sun illumination (AM 1.5 G, 100 mW cm^{-2}).

6.3   Results and discussion

The subsequent sections elucidate the physicochemical, electrical conductivity, electrochemical properties, and photovoltaic performance of the nanocomposites.

6.3.1   Elemental analysis

The incorporation of Bi_2O_3 into rGO or heteroatom-doped rGO is evident from the presence of bismuth peaks in the EDX spectrum (Figure 6.1). Supplementary Data - Figure S6.1 (a-f) also shows the EDX elemental mapping of the N-rGO/Bi_2O_3 nanocomposite, which confirms that all the constituent elements (carbon, oxygen, nitrogen, and bismuth) were distributed homogeneously in the N-rGO/Bi_2O_3 nanocomposite. This was also observed in rGO/Bi_2O_3 and B-rGO/Bi_2O_3 nanocomposites. The presence of carbon, nitrogen, oxygen, boron, and bismuth in nanocomposites was further confirmed by elemental analysis and ICP-OES (Supplementary Data − Table S6.1). The Bi_2O_3 content in rGO/Bi_2O_3, N-rGO/Bi_2O_3, and B-rGO/Bi_2O_3 was found to be 20.8, 28.5, and 25.0%, respectively. N-rGO/Bi_2O_3 had a nitrogen content of 3.76%, while B-rGO/Bi_2O_3 had a boron content of 2.56%. ATR-FTIR was further used to investigate the various functional groups present in the nanocomposites.
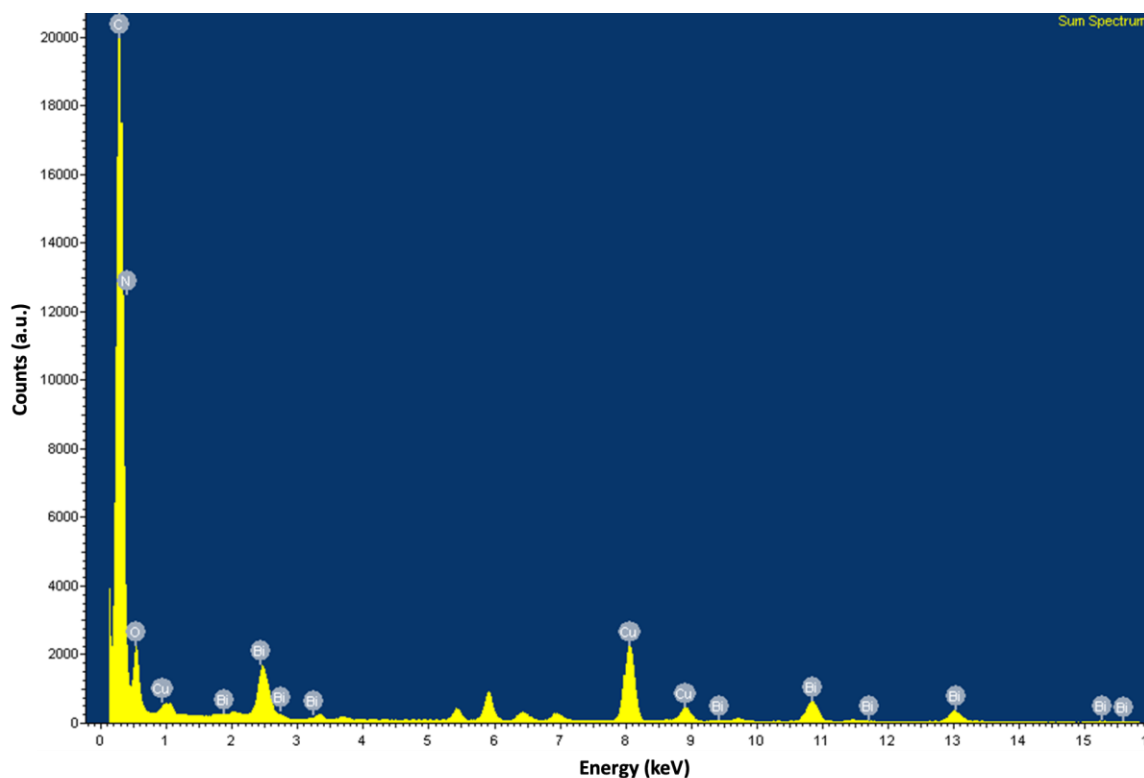
Figure 6.1: EDX spectrum of a measurement conducted at the selected area of N-rGO/Bi$_2$O$_3$.

6.3.2   Surface functional groups

The ATR-FTIR spectrum of Bi$_2$O$_3$ is shown in Figure 6.2 (a), where a peak at 850 cm^{-1} is attributed to the symmetrical stretching of Bi-O-Bi, while a peak at 1401 cm^{-1} is due to the presence of the metal-oxygen vibration (Bi-O) [40]. The heteroatom-doped rGO-Bi$_2$O$_3$-based nanocomposites exhibited peaks at around 800 - 850 cm^{-1} and 1402 cm^{-1}, associated with the Bi-O-Bi and Bi-O vibrations, respectively. The spectra exhibited a broader peak at around 3000 - 3400 cm^{-1} due to the Bi-OH bonds and hydrogen-bonded molecular water species. The weak peaks observed at 1665 cm^{-1} and 1250 cm^{-1} were assigned to N-H bending and C-N stretching in N-rGO/Bi$_2$O$_3$, respectively. The presence of boron in B-rGO/Bi$_2$O$_3$ was indicated by a peak at around 1180 cm^{-1}, which is due to the B-C stretching vibration. Quantitative analysis and ATR-FTIR spectroscopy confirmed the incorporation of Bi$_2$O$_3$ into heteroatom-doped rGO. Thus, to further study the structures of the nanocomposites, TEM and FE-SEM analyses were conducted.
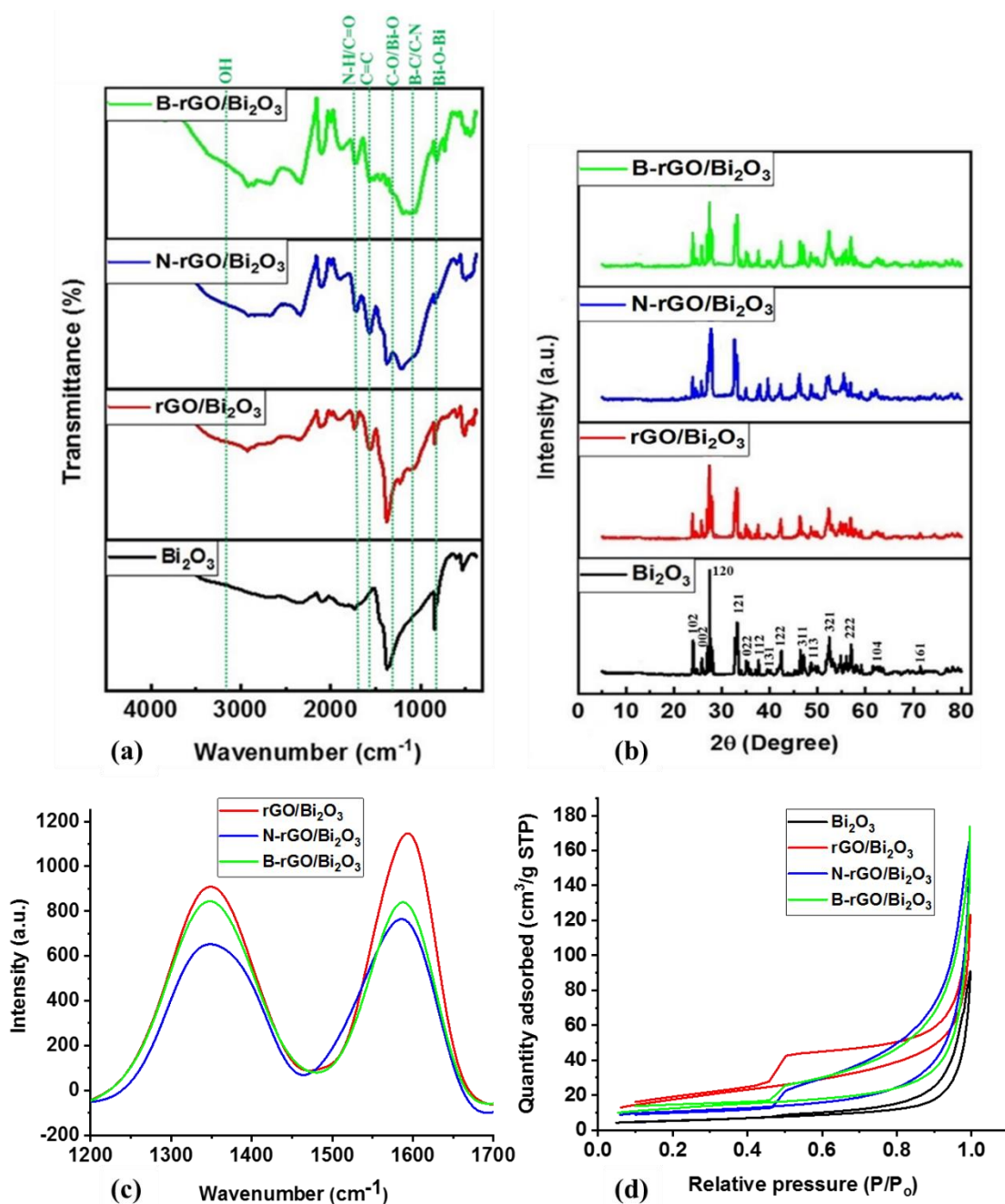
Figure 6.2: (a) ATR-FTIR spectra, (b) powder X-ray diffractograms, (c) Raman spectra and (d) N_2 adsorption-desorption isotherms of the Bi_2O_3-based nanocomposites.

6.3.3 Microstructure and surface morphology

The TEM images in Figures 6.3 (a) - (c) show wrinkled graphene sheets with Bi_2O_3 that is uniformly dispersed, indicating the existence of a strong interaction between rGO, N-rGO or B-rGO, and Bi_2O_3. Moreover, the interface between Bi_2O_3 and rGO, N-rGO, or B-rGO shows that the Bi_2O_3 was well anchored on the sheets. This confirms that Bi_2O_3 was successfully incorporated into heteroatom-doped rGO as indicated in the EDX spectrum (Figure 6.1).

Figures 6.3 (d) and (e) show SEM images, where agglomeration of Bi_2O_3 is observed in the graphene sheets. N-rGO/Bi_2O_3 exhibited a high degree of agglomeration due to the high Bi_2O_3 content.
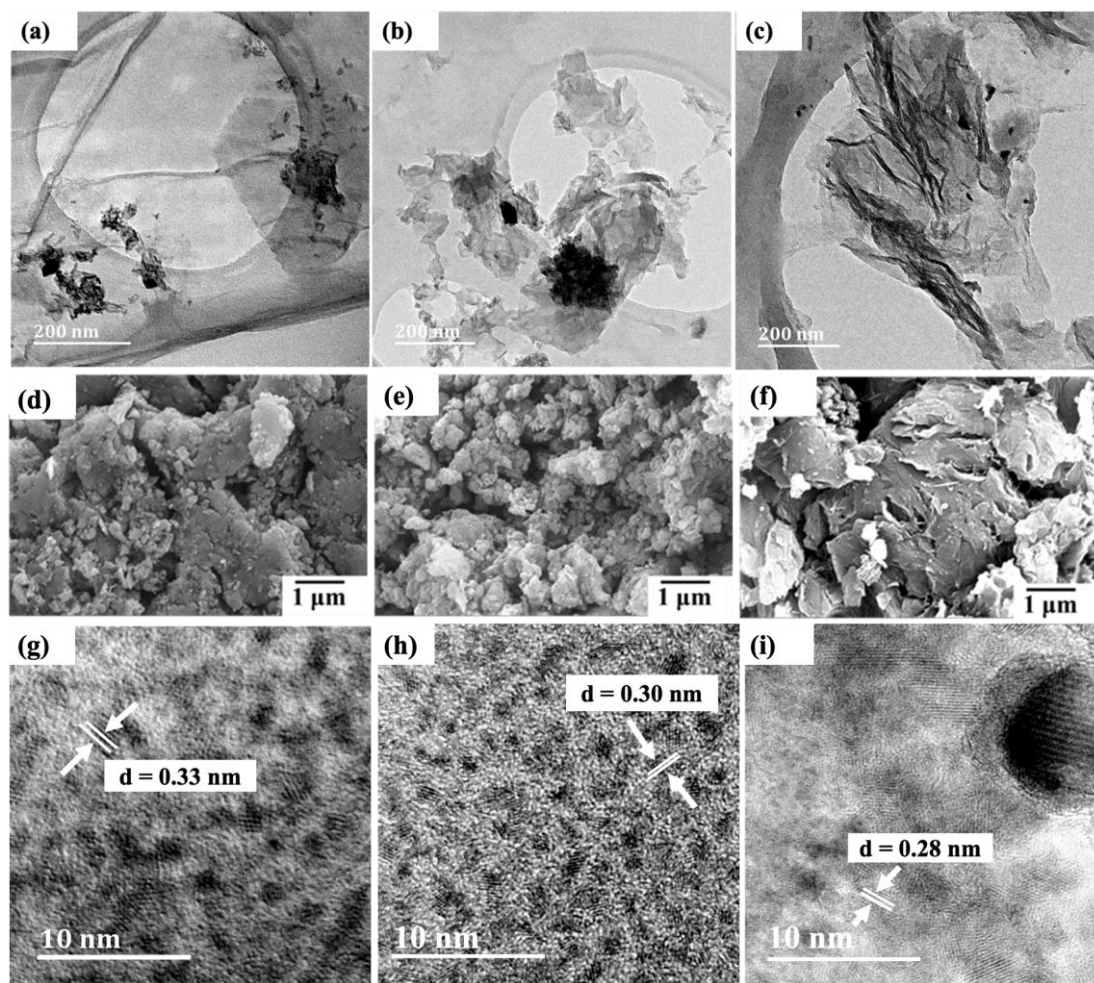
Figure 6.3: TEM images of (a) rGO/Bi_2O_3, (b) N-rGO/Bi_2O_3, and (c) B-rGO/Bi_2O_3. SEM images of (d) rGO/Bi_2O_3, (e) N-rGO/Bi_2O_3, and (f) B-rGO/Bi_2O_3. HR-TEM images of (g) rGO/Bi_2O_3, (h) N-rGO/Bi_2O_3, and (i) B-rGO/Bi_2O_3.

Consistent with SEM and TEM results, the HRTEM analysis also indicated the successful formation of Bi_2O_3-based nanocomposites. Figure 6.3 (g) to (i) revealed a decrease in interlayer spacing of the Bi_2O_3-based nanocomposites compared with rGO, N-rGO, or B-rGO (Supplementary Data – Figure S6.2) due to the distortion introduced by the inclusion of Bi_2O_3 and the reduction of oxygen functional groups, such as carboxyl, epoxy and hydroxyl groups.

6.3.4 Phase composition and defects on the graphitic structure

Figure 6.2 (b) shows the diffractograms of pure Bi_2O_3 and the Bi_2O_3-based nanocomposites. The P-XRD pattern of pure Bi_2O_3 shows five intense peaks at 2θ values of 24.7°, 26.8°, 33.5°,

42.0°, and 52.5°, which correspond to the (102), (120), (121), (122), and (321) planes, respectively, confirming the formation of an α phase. These characteristic peaks are confirmed by the reported standard JCPDS file number 76-1730, which is associated with the monoclinic phase with space group P2$_1$/c [41]. When comparing the diffractograms of Bi$_2$O$_3$ and heteroatom-doped rGO-Bi$_2$O$_3$-based nanocomposites, the diffraction peak representing the carbon species expected at 25° was not observed in all nanocomposites because the diffraction peak was obscured by the stronger diffraction peak of α-Bi$_2$O$_3$, and due to the low content of rGO, which was below the detection limit [34,42].

The sharp diffraction peak at 26.8° indicates that Bi$_2$O$_3$ is in a crystalline state, but this peak was reduced after integrating heteroatom-doped rGO with Bi$_2$O$_3$. Bi$_2$O$_3$ exhibited a relatively high 2θ peak intensity due to the presence of larger nanoparticles with few grain boundaries and low defect density. Theoretically, larger particles have sharp diffraction peaks, while the diffraction peak width increases as the particle sizes are reduced.[43] The most intense diffraction peak (120) was fitted with a Lorentzian distribution function to determine the full-width at half-maximum (FWHM) and the value obtained was employed to calculate the crystallite size of the nanocomposites with Scherrer's formula. The crystallite sizes of Bi$_2$O$_3$, rGO/Bi$_2$O$_3$, N-rGO/Bi$_2$O$_3$, and B-rGO/Bi$_2$O$_3$ were 29.2, 20.9, 19.5, and 16.8 nm, respectively. The boron content in B-rGO/Bi$_2$O$_3$ caused an increase in structural strain, thus leading to enhanced surface defects. An interlayer spacing of 0.33 nm was obtained for Bi$_2$O$_3$, which was comparable to previously reported values [44,45]. The decrease in interlayer spacing after integrating Bi$_2$O$_3$ with heteroatom-doped rGO was caused by lattice distortions, attributed to the incorporation of boron or nitrogen and the decrease in oxygen content during the reduction process.

The crystallite size and graphitic nature of the nanocomposites were further investigated by Raman spectroscopy. The crystallite size (L$_a$) was calculated using the equation reported by Mallet-Ladeira *et al.* [46]:

$$HWHM = 71 - 5.2\,L_a \qquad\qquad (1)$$

where HWHM is the half-width at a half maximum, which is the half of the full width at half maximum (FWHM) when the function is symmetric. The crystallite sizes of Bi$_2$O$_3$-based nanocomposites were smaller than that of Bi$_2$O$_3$, indicating that thermal treatment and the type of heteroatom-doping in rGO affected the crystallite size due to the formation of small crystals.

The crystallite sizes from Raman analysis are slightly larger than those from P-XRD analysis; however, they displayed a similar decreasing trend (Table 6.1).

Table 6.1: P-XRD parameters and crystallinity analysis of the nanocomposites.

Sample	P-XRD			Raman	
	2θ/degree	Crystallite size/nm	Interlayer spacing/nm	I_D/I_G	Crystallite size/nm
Bi_2O_3	26.8	29.2	0.33	-	34.4
rGO/Bi_2O_3	27.1	20.9	0.32	1.50	29.6
N-rGO/Bi_2O_3	27.9	19.5	0.30	1.79	28.1
B-rGO/Bi_2O_3	28.0	16.8	0.30	1.82	27.3

The graphitic nature of rGO, heteroatom-doped rGO, and Bi_2O_3-based nanocomposites was further investigated by Raman spectroscopy. The Raman spectrum of rGO (Supplementary Data – Figure S6.3 and Table S6.2) reveals a D-band at 1350 cm^{-1} and a G-band at 1594 cm^{-1}, whereby the peak area ratio (I_D/I_G) shows the disorder and the GO structure's graphitic symmetry, respectively. After nitrogen- or boron-doping, the G-bands revealed a minimal shift in the wavenumber. This shift indicated that incorporating nitrogen or boron atoms into the GO lattice prompted an increase in the disordered structure relative to rGO. According to Nanda *et al*. [47], the shift in the G-band of graphene represents the vibrational mode of sp^2-hybridized carbon atoms. Thus, the change in the G-band position suggests the change in the number of layers in graphene. The G-band shift towards a higher wavenumber indicates a decrease in the number of graphene layers.

Figure 6.2 (c) shows that the intensity of the G-band of rGO/Bi_2O_3 is highest, corresponding to the sp^2 structure of the graphite sheet [48]. The low intensities of the D- and G-band of N-rGO/Bi_2O_3 suggest a strong interaction between N-rGO and Bi_2O_3. This has also been evidenced by the presence of the highest Bi_2O_3 content in N-rGO/Bi_2O_3 (Supplementary Data – Table S6.1) compared with rGO/Bi_2O_3 and B-rGO/Bi_2O_3. Thus, Raman analysis demonstrated the chemical bonding between Bi_2O_3 and rGO, N-rGO, or B-rGO sheets, in agreement with elemental analysis.

The I_D/I_G ratio of rGO was lower (0.71 – Supplementary Data (Table S6.2)) due to the reduction of the oxygen functionalities and the recovery of sp^2-hybridized C-C bonds. However, the I_D/I_G ratios of N-rGO and B-rGO were higher than for rGO due to structural defects introduced

by nitrogen or boron atoms implanted at the radicalized graphene sites. B-rGO displayed an I_D/I_G ratio of 1.18, which was higher than that of N-rGO (1.09), revealing the presence of a higher degree of disorder in B-rGO than N-rGO. Bi_2O_3-based nanocomposites showed higher I_D/I_G ratios than rGO, N-rGO and B-rGO, demonstrating that these nanocomposites possess more defects with B-rGO/Bi_2O_3 exhibiting the highest I_D/I_G ratio (1.82).

6.3.5 Surface area and porosity

The specific surface area and pore size of the Bi_2O_3-based nanocomposites were investigated by the nitrogen adsorption/desorption method (Table 6.2). The B-rGO/Bi_2O_3 nanocomposite was found to have the largest specific surface area of 65.5 $m^2\ g^{-1}$. The relatively low surface area of 53.7 $m^2\ g^{-1}$ for rGO/Bi_2O_3 was attributed to the blockage of the rGO lattice by the Bi_2O_3 particles. The larger surface area of nanomaterials is beneficial for enhancing dye loading in the photoanode of DSSCs. Therefore, nanomaterials with a small surface area result in low dye loading, thereby reducing the short-circuit current density (J_{sc}) value and the PCE of DSSCs [49]. Thus, to enhance the PCE of DSSCs, the photoanode nanomaterials ought to have a larger surface area. All the nanocomposites exhibited pore sizes below 23 nm, which belong to mesoporous material. Such mesoporous materials with pore sizes between 2 and 50 nm have been widely reported to improve the infiltration of materials in electrolytes [50,51].

Table 6.2: Textural characterisation of the nanocomposites.

Sample	Surface area/$m^2\ g^{-1}$	Pore size/nm
Bi_2O_3	4.6	33.52
rGO/Bi_2O_3	53.7	20.37
N-rGO/Bi_2O_3	58.2	22.15
B-rGO/Bi_2O_3	65.5	17.80

Figure 6.2 (d) exhibited type IV adsorption-desorption isotherms with an H3 hysteresis loop in the range of 0.45-1.0 P/P$_0$. The H3 hysteresis loop indicates the presence of narrower pores, channel-like pores, and a pore network-linking effect [52]. This again suggests that the synthesised nanocomposites are mesoporous materials. The relative pressure tends to increase (P/P$_o$ > 0.85), and the shape of the adsorption isotherm rises, indicating an increase in the amount of N_2-adsorption and the presence of capillary condensation in the mesoporous material. This is attributed to the rGO nanomaterial having a larger pore size and being capable of adsorbing a large amount of N_2.

6.3.6   Thermal stability

The TGA analysis in Figure 6.4 (a) shows the thermal stability studies represented as TGA thermograms, and Supplementary Data (Table S6.3) shows the decomposition temperatures and residual content of the nanocomposites. All the nanocomposites exhibited few weight losses around the decomposition temperature of 100 °C, which was attributed to the removal of moisture adsorbed in the interlayers of the nanocomposites. Furthermore, the weight loss that occurred at 200 – 400 °C is due to the loss of amorphous carbon and other functional groups with the release of CO_x species. Such decrease in weight in the 200 – 400 °C range correlates with TEM and SEM analysis (Figure 6.3), inferring the presence of amorphous materials. The thermograms indicated that the order of the nanocomposites' tolerance to heat is B-rGO/Bi_2O_3 < N-rGO/Bi_2O_3 < rGO/Bi_2O_3, i.e., with decomposition temperatures of 437, 490, and 518 °C, respectively. The thermal stability trends agree with the graphitic nature (lower crystallinity) (Raman analysis - Table 6.1) of the nanocomposites. B-rGO/Bi_2O_3, with the highest fraction of layered graphene, exhibited the lowest thermal stability of 437 °C and the lowest residual content of Bi_2O_3 of 38%. The highest amount of residue (57%) for N-rGO/Bi_2O_3 could be attributed to some remnant Bi_2O_3 that remains entrapped in the nanocomposite. The elemental analysis also indicates a high Bi_2O_3 content in N-rGO/Bi_2O_3 (Supplementary Data – Table S6.1).
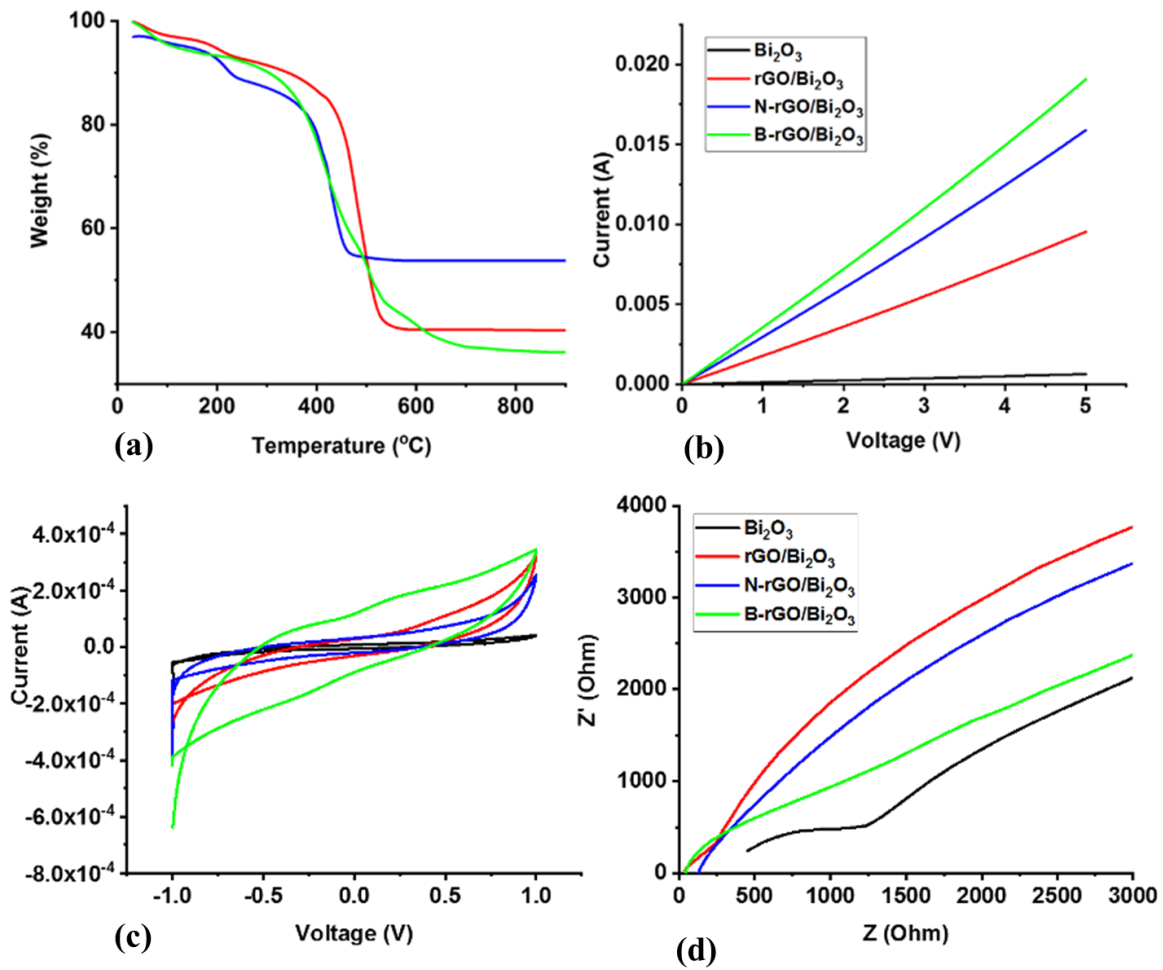
Figure 6.4: (a) Thermal stability studies represented as TGA thermograms, (b) current-voltage characteristics, (c) cyclic voltammograms and (d) Nyquist plots of the Bi_2O_3-based nanocomposites.

6.3.7 Electrical properties

Four-probe and Hall effect measurements were used to investigate the electrical conductivity and charge carrier mobility, respectively. Hall effect studies showed that Bi_2O_3, rGO/Bi_2O_3, and $N\text{-}rGO/Bi_2O_3$ have *n*-type charge carriers, while $B\text{-}rGO/Bi_2O_3$ has *p*-type charge carriers. Such *n*- and *p*-type charge carrier characteristics are due to the change in the electronic structure of the nanocomposite. This suggests that $N\text{-}rGO\text{-}Bi_2O_3$ is a good material for electron transport, while $B\text{-}rGO/Bi_2O_3$ is a good hole transporter. The *I-V* characteristics (Figure 6.4 (b) and Table 6.3) revealed that the maximum conductivity (6.31 S cm^{-1}) was obtained from $B\text{-}rGO/Bi_2O_3$ with an improved charge carrier mobility (0.368 cm^2 V^{-1} s^{-1}). The improvement in charge carrier mobility is attributed to the decrease in the scattering probability of the charge carriers. The size of boron ions is smaller than that of bismuth ions (the ionic radius of B^{3+} is

0.23 Å and Bi^{3+} is 1.17 Å). Thus, there is less scattering of electrons, thereby increasing the charge carrier mobility. $B-rGO/Bi_2O_3$ had significantly improved electrical conductivity, and this is attributed to its relatively large surface area and high charge carrier mobility.

Table 6.3: Electrical properties of the Bi_2O_3-based nanocomposites.

Sample	Conductivity/S cm^{-1}	Carrier mobility/cm^2 V^{-1} s^{-1}
Bi_2O_3	2.10×10^{-2}	0.080
rGO/Bi_2O_3	3.09	0.267
$N-rGO/Bi_2O_3$	3.84	0.295
$B-rGO/Bi_2O_3$	6.31	0.368

6.3.8   Electrochemical properties

6.3.8.1 Electrode potential characteristics

The cyclic voltammograms of the samples are shown in Figure 6.4 (c), where a comparison of Bi_2O_3 and the nanocomposites was obtained at a scanning rate of 100 mV s^{-1}. The variation of scan rate, i.e., 5, 25, 50, 75, and 100 mV s^{-1} in the -1.0 to 1.0 V potential range (Supplementary Data – Figure S6.4), showed that the cyclic voltammograms maintained certain curve stability [48,53], indicating that the nanocomposites were mainly electric double layer capacitive. Bi_2O_3 exhibited a small rectangular area, indicating a small capacitance, whereas the Bi_2O_3-based nanocomposites exhibited extensive background and peak currents.   This shows that the effective area of the electrodes was improved, and the electron exchange rate was accelerated by the conductive properties of the Bi_2O_3-based nanocomposites.

The presence of oxygen-functional groups in Bi_2O_3 decreases its electrical conductivity and it deteriorates in the aqueous electrolyte.   During the integration of Bi_2O_3 with rGO or heteroatom-doped rGO, the oxygen-functional groups were reduced during thermal treatment and the high-pressure environment of the hydrothermal system. Therefore, reducing oxygen-functional groups increased the degree of wetting between the electrode and the electrolyte, thus resulting in an enhanced electrical conductivity, consequently improving the capacitance. A similar observation has been reported by Yang *et al.* [54], who reported an increase in the capacitance of highly orientated Bi_2O_3/rGO nanocomposites. The electrochemical activity and electrochemical reversibility are also enhanced due to the introduction of defects and heteroatom-containing groups at the electrode surface, which accelerates the charge transfer rate across the electrode.   This also indicates that Bi_2O_3-based nanocomposites have ideal

capacitor characteristics. The reversible charge-discharge characteristics in Bi_2O_3-based nanocomposites can probably be attributed to the electrical conductivity of the randomly distributed β-Bi_2O_3 that is among the α- and δ-phases [55]. Thus, the nanocomposites were further investigated with EIS.

6.3.8.2 Interfacial charge transfer characteristics

For impedance measurements, the Bi_2O_3 and Bi_2O_3-based nanocomposite electrodes were characterised via Nyquist plots (Figure 6.4 (d). The Nyquist plots showed a semicircle corresponding to the Faradaic charge transfer resistance (R_{ct}) (Table 6.4) and a linear region, indicating a pure capacitive behaviour and a diffusion-limited process, respectively [56,57]. The Bi_2O_3 electrode exhibited a small semicircle in the high-frequency region due to lower resistance. A lower impedance, observed for rGO/Bi_2O_3 compared to Bi_2O_3, led to an improved electron transfer rate. All the heteroatom-doped rGO/Bi_2O_3-based nanocomposites exhibited no semicircle, indicating that the resistance is negligible, thus, suggesting a remarkable charge reversal with a change in voltage. This was attributed to the high electrical conductivity, large specific surface areas, and high nitrogen/boron-doping of the nanocomposites, which provided more sites for enhanced catalytic activity. For instance, in the case of B-rGO/Bi_2O_3, the lack of semicircle was attributed to the largest surface area of B-rGO and its sp^3 network, which behaves as an electron transport medium from the conduction band of Bi_2O_3 to B-rGO. Therefore, the presence of B-rGO in the nanocomposite decreases the charge recombination rate, thus resulting in an enhanced lifetime of the charge carriers.[58]

Table 6.4: Resistance values for the nanocomposites.

Sample	R_{ct}/Ω
Bi_2O_3	201.1
rGO/Bi_2O_3	169.8
N-rGO/Bi_2O_3	125.7
B-rGO/Bi_2O_3	108.4

The series resistance is different for different electrodes used in Figure 6.4 (d) due to the presence of various oxygen-functional groups in the Bi_2O_3-based nanocomposites. This could also be attributed to the constriction phenomenon of the thick porous film, which had a film thickness of 2 μm that might not be thick enough for electrodes to allow better current collection. Similar observations have been previously reported by Tezyk *et al.* [59].

The R_{ct} values (Table 6.4) were calculated from the EIS data. The R_{ct} values of the Bi_2O_3-based nanocomposites were lower than that of Bi_2O_3 due to the free charge transfer in the nanocomposites. The relatively small R_{ct} values for the nanocomposites indicate that the modification of Bi_2O_3 with heteroatom-doped rGO drastically reduces the electrode-electrolyte interfacial resistance. The introduction of heteroatom-doped rGO into Bi_2O_3 lowered the R_{ct} value, which indicates the efficient separation of photogenerated electron-hole pairs and faster interfacial charge transfer. Therefore, heteroatom-doped rGO acts as the conducting channels inside the Bi_2O_3 matrix. These results affirm that the effective incorporation of heteroatom-doped rGO sheets improves the electron transport and electrical conductivity of the nanocomposites, resulting in a significant enhancement in electrochemical performance.

6.3.9 Photovoltaic performance of the fabricated DSSCs

DSSCs were fabricated using pure Bi_2O_3, rGO/Bi_2O_3, N-rGO/Bi_2O_3, and B-rGO/Bi_2O_3 as photoanodes; and the open-circuit voltage (V_{oc}), J_{sc}, fill factor (FF) and PCE were determined. The photovoltaic properties of DSSCs are listed in Table 5, and the J-V curves are shown in Figure 6.5. Bi_2O_3-based DSSCs exhibited a higher V_{oc} than rGO/Bi_2O_3-based DSSCs due to back electron transfer (from Bi_2O_3 to the redox couple in the electrolyte), which is associated with electrons located in a shallow conduction band edge, thus resulting in a short lifetime. The low PCE in the Bi_2O_3-based DSSC is due to poor dye absorption and back recombination at the photoanode-electrolyte interface. A similar observation was reported by Fatima *et al.* [26], who obtained a PCE of 0.05% for the Bi_2O_3-based DSSC. Poor dye absorption causes a decrease in light absorption, which reduces the photogeneration of charge carriers, and hence, lowers the current density, resulting in poor device performance. Thus, optimisation by surface modification of Bi_2O_3 has been used to increase dye absorption and reduce back recombination, thereby improving the performance of DSSCs.

Table 6.5: Photovoltaic performance of DSSCs with Bi_2O_3-based nanocomposite photoanodes.

Photoanode	V_{oc}/V	J_{sc}/mA cm^{-2}	FF/%	PCE
Bi_2O_3	0.53	6.0	20.63	0.42 ± 0.04
rGO/Bi_2O_3	0.48	9.8	43.9	1.68 ± 0.01
N-rGO/Bi_2O_3	0.55	9.2	47.4	1.97 ± 0.02
B-rGO/Bi_2O_3	0.59	10.0	50.2	2.79 ± 0.01

When Bi_2O_3-based nanocomposites were used as a photoanode, the DSSCs exhibited a higher PCE than the Bi_2O_3-based DSSCs. From the EIS analysis and electrical properties of Bi_2O_3-based nanocomposites, it can be suggested that the improvement in PCE is attributed to the low charge transfer resistance and high electrical conductivity of these nanocomposites. When carbon atoms in the graphene lattice are substituted by nitrogen or boron atoms, the conductivity of N-rGO/Bi_2O_3 or B-rGO/Bi_2O_3 increases remarkably, and the excited electrons are transferred faster in the delocalized π structure of N-rGO/Bi_2O_3-based photoanodes or B-rGO/Bi_2O_3-based photoanodes than rGO/Bi_2O_3-based photoanodes.

B-rGO/Bi_2O_3-based DSSCs exhibited the highest PCE due to enhanced transportation and collection of photogenerated charge carriers. The high PCE is attributed to the hole (h^+) leaving the valence band of B-rGO and quickly moving to the valence band of Bi_2O_3, which facilitates electron and hole (e^-/h^+) separation. B-rGO has been reported to have a lower bandgap;[60] thus, the lower bandgap of B-rGO is responsible for providing a photovoltaic effect in Bi_2O_3 with a high bandgap [61], enhancing charge separation and extending the energy of photoexcitation in DSSCs. Moreover, the electron mobility rate in B-rGO/Bi_2O_3 is higher than in rGO/Bi_2O_3 and N-rGO/Bi_2O_3, enabling the efficient transportation of electrons and reducing charge recombination. Less charge recombination means more electron density and a shift of the Fermi level, resulting in an increased V_{oc}. This is consistent with EIS data, in which the B-rGO/Bi_2O_3 nanocomposite exhibited the lowest R_{ct} value. This results in fast electron collection and low charge carrier recombination, leading to the fabrication of a B-rGO/Bi_2O_3-based DSSC with the highest PCE of 2.79%.
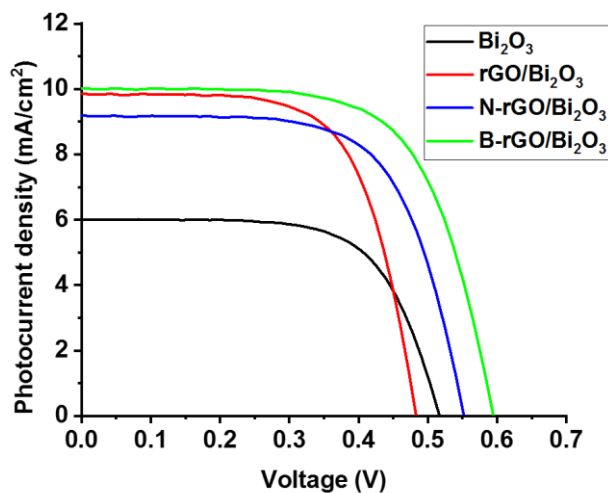
Figure 6.5: *J-V* characteristics of the Bi_2O_3-based nanocomposites.

The introduction of rGO or heteroatom-doped rGO into Bi_2O_3 did not only improve the PCE, but also enhanced the J_{sc} and V_{oc} values. In the case of the rGO/Bi_2O_3-based DSSC and N-rGO/Bi_2O_3-based DSSC, low V_{oc} values of 0.48 and 0.55 V, respectively (Table 6.5 and Figure 6.5), were attributed to faster dye regeneration, which reduces the lifetime of the oxidised dye molecule to suppress charge recombination, thus reducing the V_{oc}. The presence of a low Bi_2O_3 content in rGO/Bi_2O_3 increased the J_{sc} but lowered the V_{oc}, which substantially reduced the PCE of DSSCs. Although N-rGO/Bi_2O_3 showed a higher electrical conductivity and charge carrier mobility than rGO/Bi_2O_3, its performance in DSSCs as a photoanode resulted in a low J_{sc} due to charge recombination, which is attributed to various bonding configurations of nitrogen (pyrrolic-N, pyridinic-N, and graphitic-N) present on the GO surface.

The J_{sc} is simultaneously affected by electron transfer efficiency, light scattering, and dye absorption. Thus, the improvement of J_{sc} is due to the increase in the absorption of dye molecules in DSSCs. The large surface area of the nanocomposite is beneficial for enhancing dye loading in the photoanode of DSSCs. Therefore, the dye molecules are capable of harvesting more light energy for the effective photogeneration of charge carriers. B-rGO/Bi_2O_3 had the largest surface area for efficient dye-loading, which increased the J_{sc} and promoted a higher PCE in DSSCs.

6.4   Conclusion

In summary, heteroatom-doped rGO/Bi_2O_3-based nanocomposites were successfully synthesised and applied as photoanodes in DSSCs. P-XRD analysis showed that pristine Bi_2O_3 is in the monoclinic (α) form, and this polymorph was maintained even after introducing heteroatom-doped rGO. The heteroatom-doped rGO/Bi_2O_3-based nanocomposites exhibited better catalytic activity than pure Bi_2O_3. Favourable properties, such as large surface area, small pore size, low charge transfer resistance, high charge carrier mobility, and high electrical conductivity, were observed in the heteroatom-doped rGO/Bi_2O_3-based nanocomposites. This demonstrated the suitability of the prepared Bi_2O_3-based nanocomposites as potential photoanode materials for DSSCs. The highest PCE of 2.79% was achieved for the B-rGO/Bi_2O_3-based DSSC, which was attributed to the enhanced channels for electron transfer and electrolyte diffusion. Therefore, the synthesised heteroatom-doped rGO/Bi_2O_3-based nanocomposites are ideal materials for the photoanode in DSSCs.

References

1. G. Boschloo, *Front. Chem.*, **2019**, 7, 1-9.

2. Q. Huaulmé, V. M. Mwalukuku, D. Joly, J. Liotier, Y. Kervella, P. Maldivi, S. Narbey, F. Oswald, A. J. Riquelme, J. A. Anta and R. Demadrille, *Nat. Energy*, **2020**, 5, 468-477.

3. G. George, R. S. Yendaluru and A. Mary Ealias, *Energy Sources, Part A: Recovery, Utilization, and Environmental Effects*, **2020**, 1, 1-15.

4. J. Castro-Gutiérrez, A. Celzard and V. Fierro, *Front. Mater.*, **2020**, 7, 1-25.

5. Y. Ma, D. Chen, Z. Fang, Y. Zheng, W. Li, S. Xu, X. Lu, G. Shao, Q. Liu and W. Yang, *Proc. Natl. Acad. Sci.*, **2021**, 118, e2105610118-e2105610218.

6. R. Krishnapriya, C. Nizamudeen, B. Saini, M. S. Mozumder, R. K. Sharma and A. H. I. Mourad, *Sci. Rep.*, **2021**, 11, 16265-16277.

7. H. Ozawa, Y. Okuyama and H. Arakawa, *Dalton Trans.*, **2012**, 41, 5137-5139.

8. M. U. Rahman, M. Wei, F. Xie and M. Khan, *Catalysts*, **2019**, 9, 273-274.

9. P. M. Pataniya, D. Late and C. K. Sumesh, *ACS Appl. Energy Mater.*, **2021**, 4, 755-762.

10. P. M. Pataniya, V. Patel and C. K. Sumesh, *ACS Appl. Energy Mater.*, **2021**, 4, 7891-7899.

11. S. Yousaf, S. Zulfiqar, M. I. Din, P. O. Agboola, M. F. Aly Aboud, M. F. Warsi and I. Shakir, *J. Mater. Res. Technol.*, **2021**, 12, 999-1009.

12. M. Adeel, M. Saeed, I. Khan, M. Muneer and N. Akram, *ACS Omega*, **2021**, 6, 1426-1435.

13. T. Solaiyammal and P. Murugakoothan, *Materials Science for Energy Technologies*, **2019**, 2, 171-180.

14. R. Chauhan, A. Kumar, G. G. Umarji, U. P. Mulik and D. P. Amalnerkar, *J. Solid State Electrochem.*, **2015**, 19, 161-168.

15. M. Waghmare, N. Beedri, A. Ubale and H. Pathan, *Eng. Sci.*, **2019**, 6, 36-43.

16. X. Chen, J. Ye, S. Ouyang, T. Kako, Z. Li and Z. Zou, *ACS Nano*, **2011**, 5, 4310-4318.

17. A. Birkel, Y.-G. Lee, D. Koll, X. Van Meerbeek, S. Frank, M. J. Choi, Y. S. Kang, K. Char and W. Tremel, *Energy Environ. Sci.*, **2012**, 5, 5392-5400.

18. K. Yang, R. Li, C. Zhu and J. Pei, *J. Mater. Res.*, **2021**, 36, 2936-2949.

19. C. Li, P. He, F. Dong, H. Liu, L. Jia, D. Liu, L. Du, H. Liu, S. Wang and Y. Zhang, *Mater. Lett.*, **2019**, 245, 29-32.

20.   Y. Qiu, H. Fan, X. Chang, H. Dang, Q. Luo and Z. Cheng, *Appl. Surf. Sci.*, **2018**, 434, 16-20.

21.   J. M. Bothwell, S. W. Krabbe and R. S. Mohan, *Chem. Soc. Rev.*, **2011**, 40, 4649-4707.

22.   Y. Qiu, M. Yang, H. Fan, Y. Zuo, Y. Shao, Y. Xu, X. Yang and S. Yang, *CrystEngComm.*, **2011**, 13, 1843-1850.

23.   M. Ciszewski, A. Mianowski, P. Szatkowski, G. Nawrat and J. Adamek, *Ionics*, **2015**, 21, 557-563.

24.   M. Schlesinger, S. Schulze, M. Hietschold and M. Mehring, *Dalton Trans.*, **2013**, 42, 1047-1056.

25.   S. Shaikh, G. Rahman, R. S. Mane and O.-S. Joo, *Electrochim. Acta*, **2013**, 111, 593-600.

26.   M. J. Jabeen Fatima, C. V. Niveditha and S. Sindhu, *RSC Adv.*, **2015**, 5, 78299-78305.

27.   P. Fernández-Ibáñez, M. I. Polo-López, S. Malato, S. Wadhwa, J. W. J. Hamilton, P. S. M. Dunlop, R. D'Sa, E. Magee, K. O'Shea, D. D. Dionysiou and J. A. Byrne, *Chem. Eng. J.*, **2015**, 261, 36-44.

28.   E. Kusiak-Nejman, A. Wanag, Ł. Kowalczyk, J. Kapica-Kozar, C. Colbeau-Justin, M. G. Mendez Medrano and A. W. Morawski, *Catal. Today*, **2017**, 287, 189-195.

29.   J. P. Mensing, C. Poochai, S. Kerdpocha, C. Sriprachuabwong, A. Wisitsoraat and A. Tuantranont, *Adv. Nat. Sci.: Nanosci. Nanotechnol.*, **2017**, 8, 033001-033008.

30.   M. I. A. Abdel Maksoud, R. A. Fahim, A. E. Shalan, M. Abd Elkodous, S. O. Olojede, A. I. Osman, C. Farrell, A. H. Al-Muhtaseb, A. S. Awed, A. H. Ashour and D. W. Rooney, *Environ. Chem. Lett.*, **2021**, 19, 375-439.

31.   C. K. Chua and M. Pumera, *Chem. Soc. Rev.*, **2014**, 43, 291-312.

32.   Z. Bo, Z. Wen, H. Kim, G. Lu, K. Yu and J. Chen, *Carbon*, **2012**, 50, 4379-4387.

33.   F. M. Ascencio Aguirre and R. Herrera Becerra, *Appl. Phys. A*, **2015**, 119, 909-915.

34.   X. Liu, L. Pan, T. Lv, Z. Sun and C. Q. Sun, *J. Colloid Interface Sci.*, **2013**, 408, 145-150.

35.   T. Kuila, S. Bose, A. K. Mishra, P. Khanra, N. H. Kim and J. H. Lee, *Prog. Mater. Sci.*, **2012**, 57, 1061-1105.

36.   D.-Y. Yeom, W. Jeon, N. D. K. Tu, S. Y. Yeo, S.-S. Lee, B. J. Sung, H. Chang, J. A. Lim and H. Kim, *Sci. Rep.*, **2015**, 5, 9817-9836.

37.   S. Pei and H.-M. Cheng, *Carbon*, **2012**, 50, 3210-3228.

38.   N. P. D. Ngidi, M. A. Ollengo and V. O. Nyamori, *Materials*, **2019**, 12, 3376-3401.

39.   N. P. D. Ngidi, M. A. Ollengo and V. O. Nyamori, *New J. Chem.*, **2020**, 44, 16864-16876.

40.   Y. Astuti, B. M. Listyani, L. Suyati and A. Darmawan, *Indones. J. Chem.*, **2021**, 21, 108-117.

41.   M. Malligavathy and D. P. Padiyan, *Adv. Mat. Proc.*, **2017**, 2, 51-55.

42.   H. Zhang, X. Lv, Y. Li, Y. Wang and J. Li, *ACS Nano*, **2010**, 4, 380-386.

43.   Z. A. Zulkifli, K. A. Razak and W. N. W. A. Rahman, *AIP Conf. Proc.*, **2017**, 1901, 020011-020016.

44.   M. Jalalah, M. Faisal, H. Bouzid, J.-G. Park, S. A. Al-Sayari and A. A. Ismail, *J. Ind. Eng. Chem.*, **2015**, 30, 183-189.

45.   E. Pargoletti, S. Mostoni, G. Rassu, V. Pifferi, D. Meroni, L. Falciola, E. Davoli, M. Marelli and G. Cappelletti, *Environ. Sci. Pollut. Res.*, **2017**, 24, 8287-8296.

46.   P. Mallet-Ladeira, P. Puech, C. Toulouse, M. Cazayous, N. Ratel-Ramond, P. Weisbecker, G. L. Vignoles and M. Monthioux, *Carbon*, **2014**, 80, 629-639.

47.   S. S. Nanda, M. J. Kim, K. S. Yeom, S. S. A. An, H. Ju and D. K. Yi, *Trends Analyt. Chem.*, **2016**, 80, 125-131.

48.   W.-D. Yang and L. Yu-Jiang, *J. Electr. Eng.*, **2019**, 70, 101-106.

49.   K. Song, I. Jang, D. Song, Y. S. Kang and S.-G. Oh, *Solar Energy*, **2014**, 105, 218-224.

50.   G. Gryglewicz, J. Machnikowski, E. Lorenc-Grabowska, G. Lota and E. Frackowiak, *Electrochim. Acta*, **2005**, 50, 1197-1206.

51.   S. Liu, Y. Wang and Z. Ma, *Int. J. Electrochem. Sci.*, **2018**, 13, 12256-12265.

52.   K. S. Sing and R. T. Williams, *Adsorp. Sci. Technol.*, **2004**, 22, 773-782.

53.   H. Shen, Y. Zhang, X. Song, Y. Liu, H. Wang, H. Duan and X. Kong, *J. Alloys Compd.*, **2019**, 770, 926-933.

54.   W.-D. Yang and Y.-J. Lin, *Int. J. Electrochem. Sci.*, **2020**, 15, 1915-1929.

55.   X. Yang, X. Lian, S. Liu, G. Wang, C. Jiang, J. Tian, J. Chen and R. Wang, *J. Phys. D Appl. Phys.*, **2012**, 46, 035103-035110.

56.   T. Zhan, X. Wang, X. Li, Y. Song and W. Hou, *Sens. Actuators B Chem.*, **2016**, 228, 101-108.

57.   Z. Wei, Y. Wang and J. Zhang, *Sci. Rep.*, **2018**, 8, 6929-6937.

58.   X. Bai, X. Zhang, Z. Hua, W. Ma, Z. Dai, X. Huang and H. Gu, *J. Alloys Compd.*, **2014**, 599, 10-18.

59.   V. Tezyk, C. Rossignol, N. Sergent, E. Djurado, J. Laurencin and E. Siebert, *Electrochim. Acta*, **2019**, 304, 312-322.

60.   M. Junaid, M. H. M. Khir, G. Witjaksono, N. Tansu, M. S. M. Saheed, P. Kumar, Z. Ullah, A. Yar and F. Usman, *Molecules*, **2020**, 25, 3646-3665.

61.   J. Li, B. Z. Wu and Z. X. Zhou, *Micro Nano Lett.*, **2018**, 13, 1443-1446.

Appendix: Supporting information for Chapter 6
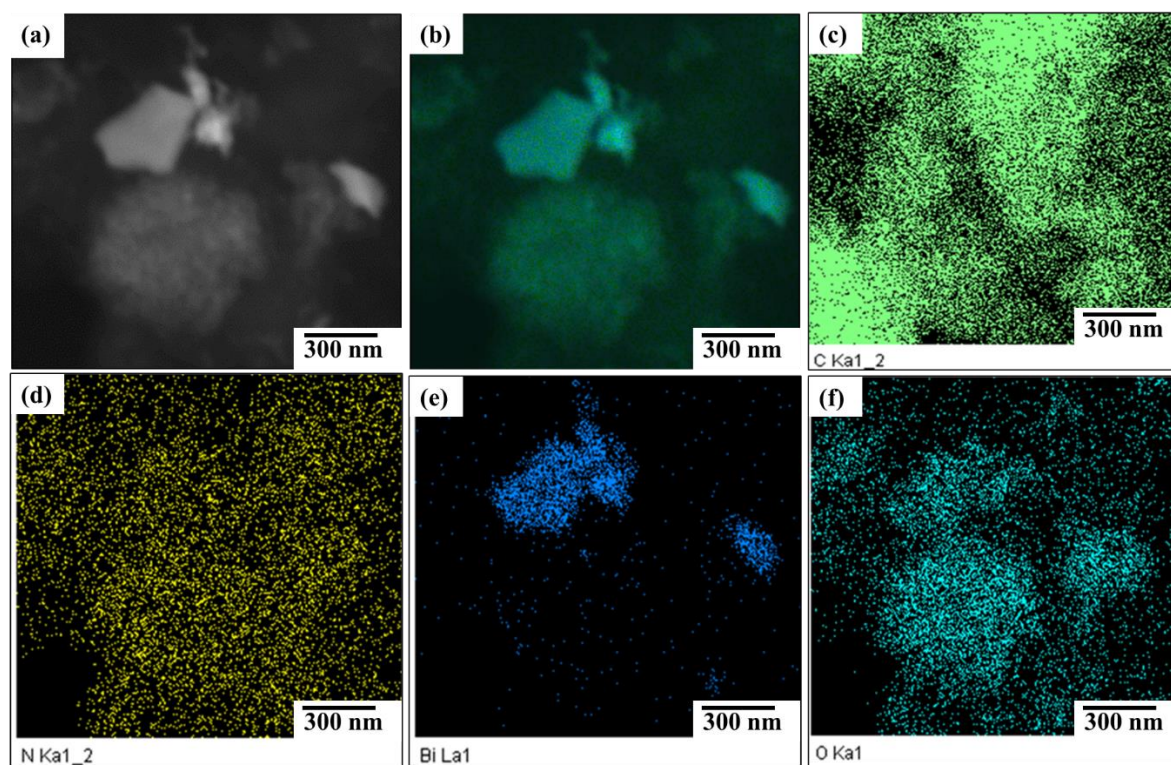
Figure S6.1: (a) TEM image of N-rGO/Bi_2O_3, and elemental mapping of (b) N-rGO/Bi_2O_3, (c) carbon, (d) nitrogen, (e) bismuth and (f) oxygen for N-rGO/Bi_2O_3 nanocomposites.

Table S6.1: Elemental composition of the nanocomposites.

Sample	Elemental analysis				ICP-OES	
	Carbon/%	Hydrogen/%	Oxygen/%	Nitrogen/%	Boron/%	Bi_2O_3/%
rGO/Bi_2O_3	67.61 ± 1	3.82 ± 1	3.57 ± 1	-	-	20.8 ± 0.01
N-rGO/Bi_2O_3	59.28 ± 1	5.43 ± 1	3.01 ± 1	3.76 ± 1	-	28.5 ± 0.02
B-rGO/Bi_2O_3	66.39 ± 1	3.69 ± 1	2.36 ± 1	-	2.56 ± 0.02	25.0 ± 0.01
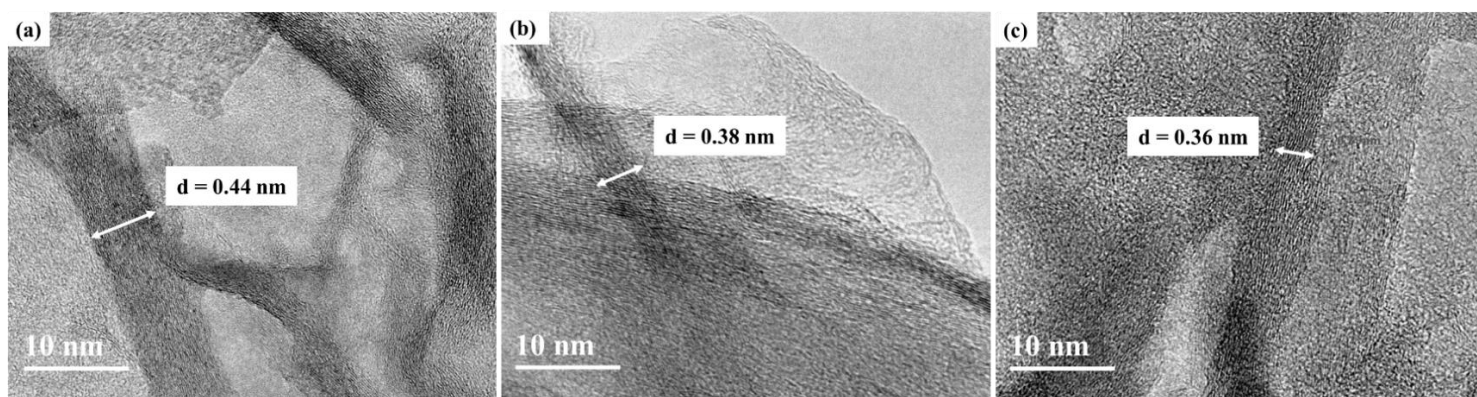
Figure S6.2: HRTEM image of (a) rGO, (b) N-rGO, and (c) B-rGO.
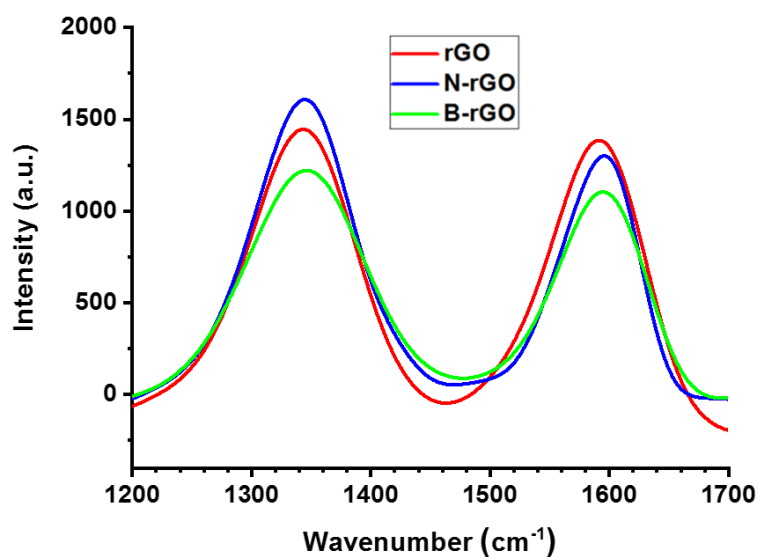
Figure S6.3: Raman spectra of rGO, N-rGO, and B-rGO.

Table S6.2: Physicochemical properties of rGO and heteroatom-doped rGO.

Sample	D-band/cm^{-1}	G-band/cm^{-1}	I_D/I_G
rGO	1350	1594	0.71
N-rGO	1350	1598	1.09
B-rGO	1350	1599	1.18

Table S6.3: Decomposition temperatures and residual content of the nanocomposites.

Sample	Decomposition temperature/°C	Residual content/%
rGO/Bi$_2$O$_3$	518	42
N-rGO/Bi$_2$O$_3$	490	57
B-rGO/Bi$_2$O$_3$	437	38
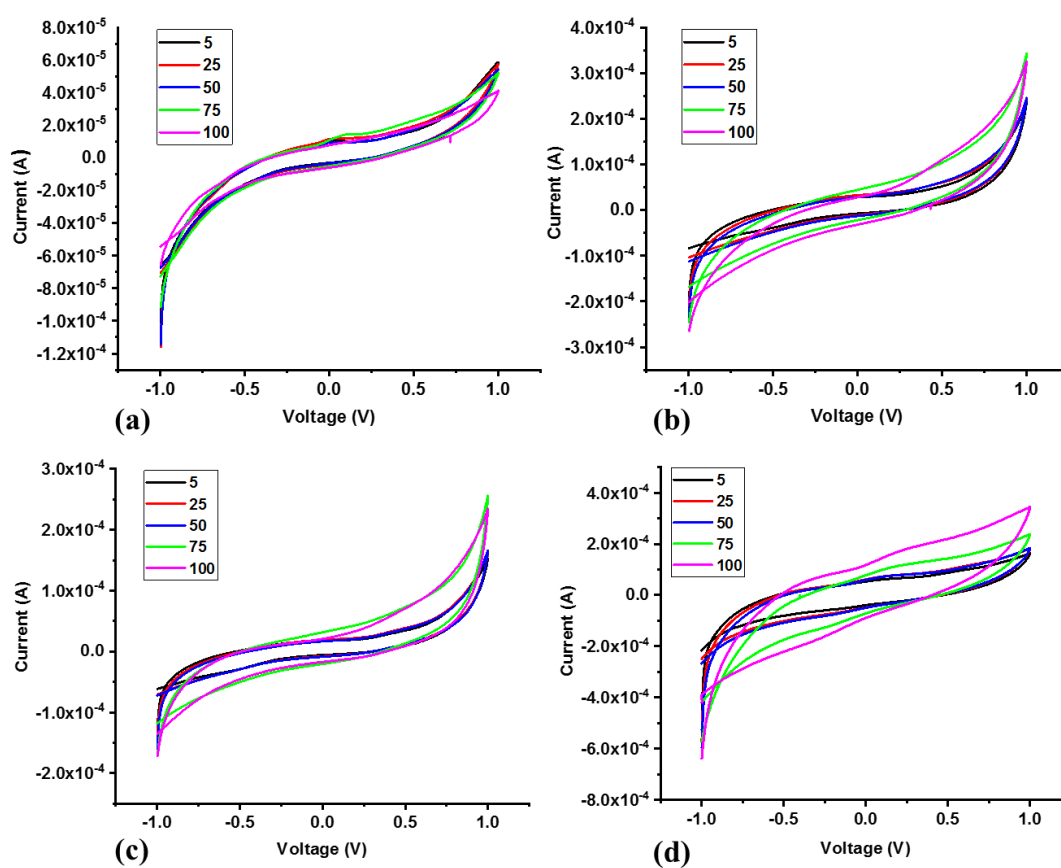
Figure S6.4: (a) Cyclic voltammograms of (a) Bi$_2$O$_3$, (b) rGO/Bi$_2$O$_3$, (c) N-rGO/Bi$_2$O$_3$ and B-rGO/Bi$_2$O$_3$ at scan rates of 5, 25, 50, 75, and 100 mV s^{-1}, in the potential range from -1.0 to 1.0 V.

CHAPTER 7

Dual heteroatom-doped reduced graphene oxide and its application in dye-sensitized solar cells

Nonjabulo P.D. Ngidi, Edigar Muchuweni, Vincent O. Nyamori [*]

School of Chemistry and Physics, University of KwaZulu-Natal, Westville Campus, Private Bag X54001, Durban, 4000, South Africa

ARTICLE INFO

ABSTRACT

The quick reduction and regeneration of the electrolyte (triiodide/iodide redox couple, I^{3-}/I^-) is one of the main issues in dye-sensitized solar cells (DSSCs). The well-known platinum counter electrodes (CEs) that facilitate electrolyte reduction and regeneration are very expensive; hence, low-cost and efficient CEs are in demand to substitute the platinum CEs. Herein, we report the hydrothermal synthesis of single (boron or nitrogen) and dual (boron/nitrogen mixture) heteroatom-doped reduced graphene oxide (rGO) and their comparison as CEs in DSSCs. The photovoltaic, electrochemical and conductivity properties were investigated. Dual heteroatom-doped rGO demonstrated a relatively large surface area and enhanced electrical conductivity (161.51 $m^2 g^{-1}$ and 22.07 $S cm^{-1}$, respectively) when compared to graphene oxide (GO), rGO and single heteroatom-doped rGO. The amount of boron- and nitrogen-doping, including their configuration, played a crucial role in the catalytic activity. The presence of pyridinic-N and pyrrolic-N in single and dual heteroatom-doped rGO promoted a triiodide reduction reaction, which shifted the redox potential, relative to GO and rGO. The BN-rGO-3 CE yielded a relatively higher PCE of 2.97%, further enhanced to 4.13% when the BN-rGO-3 CE was used in conjunction with polyaniline as a binder. Therefore, this showed that dual heteroatom-doped rGO CEs enhanced the PCE of the DSSCs due to the synergetic effect, doping configuration and higher doping levels. Thus, the present work provides a facile and productive strategy for configuring the dual heteroatom-doped graphene CE materials with high electrocatalytic activity for energy conversion devices.

Dual heteroatom-doped reduced graphene oxide and its application in dye-sensitized solar cells

Nonjabulo P.D. Ngidi, Edigar Muchuweni and Vincent O. Nyamori

School of Chemistry and Physics, University of KwaZulu-Natal, Westville Campus, Private Bag X54001, Durban 4000, South Africa
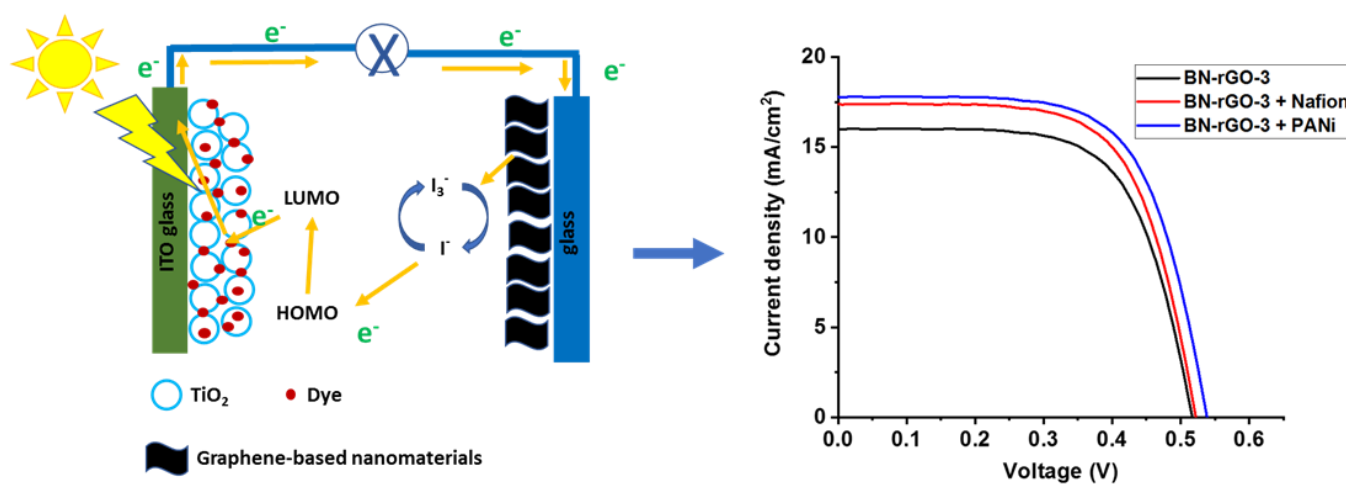
Graphical abstract

Abstract

The quick reduction and regeneration of the electrolyte (triiodide/iodide redox couple, I^{3-}/I^-) is one of the main issues in dye-sensitized solar cells (DSSCs). The well-known platinum counter electrodes (CEs) that facilitate electrolyte reduction and regeneration are very expensive; hence, low-cost and efficient CEs are in demand to substitute the platinum CEs. Herein, we report the hydrothermal synthesis of single (boron or nitrogen) and dual (boron/nitrogen mixture) heteroatom-doped reduced graphene oxide (rGO) and their comparison as CEs in DSSCs. The photovoltaic, electrochemical, and conductivity properties were investigated. Dual heteroatom-doped rGO demonstrated a relatively large surface area and enhanced electrical conductivity (161.51 m^2 g^{-1} and 22.07 S cm^{-1}, respectively) when compared to graphene oxide (GO), rGO, and single heteroatom-doped rGO. The amount of boron- and nitrogen-doping, including their configuration, played a crucial role in the catalytic activity. The presence of pyridinic-N and pyrrolic-N in single and dual heteroatom-doped rGO promoted a triiodide reduction reaction, which shifted the redox potential, relative to GO and rGO. The BN-rGO-3 CE yielded a relatively higher PCE of 2.97%, further enhanced to 4.13% when the BN-rGO-3 CE was used in conjunction with polyaniline as a binder. Therefore, this showed that dual heteroatom-doped rGO CEs enhanced the PCE of the DSSCs due to the synergetic effect, doping configuration, and higher doping levels. Thus, the present work provides a facile and productive strategy for configuring the dual heteroatom-doped graphene CE materials with high electrocatalytic activity for energy conversion devices.

Keywords

7.1   Introduction

Dye-sensitized solar cells (DSSCs) have attracted a lot of attention when compared to other third-generation photovoltaic cells due to their facile fabrication procedure, environmental friendliness, low-cost, and high power conversion efficiency (PCE) [1]. The structure of a DSSC consists of a photoanode, which is sensitized with a dye, a counter electrode (CE), and an electrolyte consisting of a redox couple. The working principle of DSSC involves three basic steps, namely, absorption of light, electron injection, and transportation of electrons. These basic steps are responsible for the conversion of photon energy into an electric current.

Among the DSSC components, the CE plays a crucial role as a reduction catalyst [2]. Therefore, to achieve good electron transport, the CE should have high electrical conductivity and good reduction activity. Platinum is the most commonly used CE in DSSCs [3-6] due to its ability to collect electrons from an external circuit and catalyze the reduction reaction of the electrolyte. Platinum transforms the oxidation state of the electrolyte into a reduction state. However, the scarcity and high cost of platinum limit its application in DSSCs, and hence there is enormous research interest in investigating advanced alternative CE materials.

Graphene, is a planar atomic sheet consisting of sp^2-hybridized carbon atoms in a hexagonal lattice structure, is one of the most promising CE materials for DSSC fabrication. Graphene has been extensively examined for electrocatalytic application as a replacement for noble metals [7] due to its large specific surface area, high crystallinity, and high electrical conductivity. As a CE in DSSCs, graphene enhances catalytic activity toward the reduction of triiodide (I_3^-) [8]. The high electrocatalytic activity in graphene is due to defects, exceptional surface area, and high electrical conductivity, thus enabling fast electron movement, resulting in high PCE [9]. However, the improvement of the electrical conductivity of graphene still remains a significant challenge.

The introduction of heteroatoms, such as oxygen, boron, nitrogen, phosphorus, or sulfur, into the graphene structure by the synthetic or physical approach has been reported to be a compelling method for tailoring the electronic properties of graphene by creating *n*- or *p*-type conductivity, thereby facilitating the use of graphene-based materials in energy devices [10]. Doping with a heteroatom assists by tuning the work function and carrier concentration of graphene [11]. Up until this point, even though the doping and application of single heteroatom-doped graphene have been widely reported [12,13], the exploration of doping with dual- or multi-heteroatoms has been relatively less studied.

In this respect, Wei *et al.* [14] reported nitrogen-doped reduced graphene (N-rGO)-based DSSCs with a PCE of 4.26%, which was higher than that of DSSCs based on reduced graphene oxide (rGO) fabricated under similar conditions, and less than 5.21% for the reference device with platinum CEs. Fang *et al.* [15] also demonstrated that boron-doped graphene as a CE resulted in DSSCs with a relatively higher PCE of 6.73%. In addition, boron and nitrogen co-doped reduced graphene oxide (BN-rGO), which was thermally treated at a higher temperature (1200 °C) and synthesized from ionic liquid-grafted GO, showed the best electrochemical performance as a CE, yielding a PCE of 8.08% [16]. However, to date, and as far as we know, 12.3% is still the highest PCE of DSSCs with platinum-based CEs [17]. Thus, a facile method of preparing a graphitic CE material with balanced electrocatalytic activity and electrical conductivity is still challenging.

Among the various heteroatoms reported, nitrogen and boron have been considered excellent choices for doping because they have the closest atomic radius to carbon and their distinctive electron richness and electron deficiency, respectively [18]. The nitrogen or boron atom provides more electrons or holes, respectively, to the valence band of graphene, thereby increasing the charge carrier concentration, hence increasing the electrical conductivity. Co-doping with nitrogen and boron atoms produces boron nitride due to carbon, nitrogen, and boron phase separation. It also results in a distinctive electronic structure with a synergistic coupling effect. Therefore, this effect can improve the electrocatalytic activity in the reduction reaction in DSSCs. However, the inquiry on how such doping effect controls the electrocatalytic activity is still unanswered. To additionally comprehend the co-doping synergistic impact and mechanism between the dopants, in this investigation, BN-rGO materials have been effectively synthesized through a facile and efficient hydrothermal reaction.

Herein, we report the effect of using different precursors, namely, boric anhydride (B_2O_3), 4-nitro-*o*-phenylenediamine ($C_6H_8ClN_3O_2$), borane ammonia (BH_6N), or borane-tert-butylamine ($C_4H_{14}BN$), in the synthesis of single and dual heteroatom-doped rGO. The use of individual 4-nitro-*o*-phenylenediamine or boric anhydride, as a nitrogen or boron precursor, in the synthesis of N-rGO or B-rGO, respectively, has been previously reported to produce higher doping content [19-22]. However, so far, the effect of combining the two precursors (4-nitro-*o*-phenylenediamine and boric anhydride) and using a single precursor that contains both nitrogen and boron (borane ammonia or borane-tert-butylamine) has not been reported and thus was investigated herein. The effect of boron and nitrogen atoms on the physicochemical,

optical, electrical conductivity, and electrochemical properties of single and dual heteroatom-doped rGO was also investigated. The effect of different concentrations of nitrogen and boron in heteroatom-doped rGO CEs on the efficiency of DSSCs was also studied. An evaluation of the DSSCs' performance when dual heteroatom-doped rGO CEs were used in conjunction with a binder (Nafion and polyaniline, PANi) will also be discussed.

7.2 Experimental

7.2.1 Materials and instrumentation

Graphite powder (99.99% - trace metal basis), sodium nitrate (99%), potassium permanganate (99%), hydrogen peroxide (100%), sulfuric acid (98%), boric anhydride (≥98%), 4-nitro-*o*-phenylenediamine (≥99%), borane ammonia (≥99%), borane-tert-butylamine (≥99%), ethanol absolute (≥99.8%), boron standard solution (9995 mg ± 20 mg L^{-1}), 1-methyl-3propylimidazolium iodine (99.99%), 4-tert-butylpyridine (98%), lithium iodide (99.9%), guanidinium thiocyanate (≥99%), acetonitrile (≥99.9%), poly (vinyl acetate), Nafion (≤100%), polyaniline (emeraldine) and eosin B (≥97%) were purchased from Sigma-Aldrich, South Africa. Double distilled water was obtained from a double distiller (Glass Chem water distiller model Ws4lcd) supplied by Shalom Laboratory Supplies, South Africa.

7.2.2 Synthesis of GO

A modified Hummers' method was used to synthesize GO [23]. Briefly, approximately 1 g of graphite powder and 1 g of sodium nitrate were mixed with 50 mL of concentrated sulfuric acid in a round-bottom flask placed in an ice-bath and stirred for 30 min. Afterward, 6 g of potassium permanganate was added slowly to the mixture with the temperature kept at 5 °C to prevent explosion and excessive heating. Thereafter, the mixture was stirred for 3 h at a temperature of 35 °C and then further treated with 200 mL of 3% hydrogen peroxide while stirring for 30 min. The resulting GO was washed with double distilled water until a pH of 6 was achieved. Subsequently, the GO was dialysed against double distilled water through a cellulose tube (pore size 45 nm, average diameter ≈27 mm), to reduce residual ions. After dialysis, the product was then filtered and dried in the oven for 24 h at a temperature of 80 °C.

7.2.3 Synthesis of heteroatom-doped rGO

GO was mechanically mixed with various nitrogen- or boron-containing precursors (boric anhydride, 4-nitro-*o*-phenylenediamine, borane ammonia, or borane-tert-butylamine). The mixture was dispersed in 15 mL of absolute ethanol (reducing agent) and sonicated for 1 h.

After sonication, the mixture was transferred into a 20 mL Teflon-lined stainless-steel autoclave and kept in an oven for the hydrothermal treatment (for 12 h) at various doping temperatures (150, 200, and 250 °C). The temperature of 250 °C was found to be the optimum doping temperature; therefore, this article focuses on nanomaterials synthesized at 250 °C. After 12 h, the product was washed with double distilled water to remove soluble residue and unreacted starting material and, thereafter, dried in an oven for 24 h at 60 °C.

7.2.4 Characterization

The microstructural characterization of the heteroatom-doped rGO samples was performed with a high resolution-transmission electron microscope (HR-TEM, JOEL JEM model 1010), and the surface morphology was investigated with a field-emission scanning electron microscope (FE-SEM, Carl Zeiss Ultra Plus). The graphitic nature of the heteroatom-doped rGO was analyzed with a Raman spectrophotometer (DeltaNu Advantage 532™) with an excitation source of Nd:YAG solid-state crystal class 3b diode laser. The phase composition of the heteroatom-doped rGO was determined with powder X-ray diffraction (XRD, Bruker AXS, Cu K_α radiation source, $\lambda = 0.154$ nm).

The presence of various functional groups in heteroatom-doped rGO was investigated with a Fourier transform infrared spectrophotometer (FTIR, PerkinElmer Spectrum 100) equipped with an attenuated total reflection (ATR) accessory. The elemental analyser (Elementar Analysensysteme GmbH) was used to investigate the chemical composition of carbon, hydrogen, oxygen, and nitrogen. In addition, the percentage of boron content was determined by inductively coupled plasma-optical emission spectrometry (ICP-OES, Perkin Elmer Optima 5300 DV). X-ray photoelectron spectroscopy (XPS, Thermo ESCAlab 250Xi with an X-ray source of monochromatic Al K_α (1486.7 eV)) was further used to investigate the chemical composition of boron, nitrogen, oxygen, and carbon present in heteroatom-doped rGO. The N_2 adsorption-desorption measurements of heteroatom-doped rGO were conducted on a Micromeritics TriStar II 3020 analyzer at 77 K. The surface area was determined by the Brunauer–Emmett–Teller (BET), and the pore size distribution was obtained from the Barrett-Joyner-Halenda (BJH) model. The thermal stability of heteroatom-doped rGO was investigated with the TA Instruments Q Series™ thermal analysis instrument (DSC/TGA (SDT-Q600)), where the heteroatom-doped rGO sample was heated from room temperature to 1000 °C at a rate of 10 °C min^{-1} under airflow.

The optical properties of heteroatom-doped rGO were investigated with an ultraviolet-visible spectrophotometer (Shimadzu, UV-1800). Four-point probe (Keithley 2400 source-meter) measurements were used to determine the electrical conductivity of heteroatom-doped rGO. Electrochemical properties were investigated with cyclic voltammetry (CV, Metrohm 797 VA Computrace electrochemical workstation). The counter, reference, and working electrodes used were a platinum wire (Pt), Ag/AgCl, and the heteroatom-doped rGO sample, respectively. The working electrode was prepared by dispersing a heteroatom-doped rGO sample (10 mg) in absolute ethanol (600 µL); the mixture was then sonicated for 10 min and drop-casted onto a carbon electrode. The 5 mM ferro/ferricyanide ($[Fe(CN)6]^{3-/4-}$) redox couple was used as an electrolyte. CV was performed at a scan rate of 100 mV s^{-1} over an applied potential range between -0.4 to 0.6 V.

7.2.5 Device fabrication and charactization

7.2.5.1 Synthesis of gel state electrolyte

The liquid electrolyte was synthesized by mixing lithium iodide (0.3348 g), 4-tert-butylpyridine (1.6900 g), guanidinium thiocyanate (0.2954 g) and 1-methyl-3-propylimidazolium iodide (0.3173 g). The mixture was dissolved in acetonitrile. The gel state electrolyte was formed by mixing the synthesized liquid electrolyte (1.2484 g) with poly(vinyl acetate) (0.6022 g). The gel state electrolyte was further stirred using a glass rod until the jelly polymer was formed. Thereafter, the electrolyte was kept in a fridge at 0 °C.

7.2.5.2 Counter electrode preparation

Single or dual heteroatom-doped rGO (30 mg), absolute ethanol (0.5 mL), and a binder (Nafion or PANi; 10 mg) were sonicated for 60 min to form a paste. The paste was then coated onto a microscope glass slide using the spin coating method and sintered in a tube furnace at 300 °C for 30 min under air and, thereafter, cooled down to room temperature.

7.2.5.3 Device fabrication

The photoanode was prepared by coating the ITO glass with TiO$_2$ paste (0.1000 g of TiO$_2$ was mixed with ethanol (0.3 mL) and sonicated for 60 min) using the doctor blade approach [24]. The Scotch tape was used to control the film thickness. The layer thickness (confirm active glass layer) was measured using the micrometre screw gauge. The coated electrode was further annealed at 300 °C for 30 min in the furnace. Eosin B dye was prepared by sonicating eosin B dye (0.3 mM) in ethanol absolute for 5 min. After preparation, the dye was stained on the

photoanode. This was followed by the gel state electrolyte addition and closed with a CE in a sandwich-like fashion.

7.2.5.4 Characterization of DSSCs

Photovoltaic measurements of DSSCs with an active area of 0.77 cm^2 were performed under one sun illumination (AM 1.5 G, 100 mW cm^{-2}) with a solar simulator and a Keithley 2420 source meter.

7.3 Results and discussion

A comparison of the chemical and physical characterization data of single and dual heteroatom-doped rGO is elucidated in the following sections. The nitrogen-doped reduced graphene oxide synthesized from 4-nitro-*o*-phenylenediamine is denoted by N-rGO, while B-rGO denotes boron-doped reduced graphene oxide synthesized from boric anhydride. Boron/nitrogen-doped reduced graphene oxide synthesized from a combination of 4-nitro-*o*-phenylenediamine, and boric anhydride is denoted as BN-rGO-1. The sample synthesized from borane ammonia is represented by BN-rGO-2, while BN-rGO-3 denotes the sample prepared from borane-tert-butylamine.

7.3.1 Elemental analysis

Table 7.1 shows that carbon, oxygen, and nitrogen elements were detected in the heteroatom-doped rGO samples. An increase in the composition of carbon was observed after heteroatom doping. This was attributed to the *sp*^{2} carbon hybridized structure carbon enhancement, i.e., increase in *sp*^{2} carbon lattices [25]. When comparing the calculated *wt.*% (Supplementary Data – Table S7.1) and experimental *wt.*% (Table 7.1) of nitrogen and boron in heteroatom-doped rGO samples, the nitrogen *wt.*% was observed to be higher than that of the boron atom. This serves as an indication that nitrogen-doping is easier than boron-doping. This is due to differences in the bond length, i.e., the B-C bond is about 0.5% longer than the C-C bond, whereas the N-C bond length is almost equal to that of the C-C bond. Thus, during nitrogen-doping, the replacement of carbon with nitrogen is relatively easier than with boron atoms during boron-doping [26].

The respective boron- and nitrogen-doping content in BN-rGO samples was lower than that in B-rGO and N-rGO, indicating the mutual proportion of nitrogen and boron doping in the dual-doping process. The use of two precursors (BN-rGO-1) during doping resulted in lower doping content of nitrogen (5.57%) and boron (2.89%) as compared to doping with a single precursor

(BN-rGO-2 and BN-rGO-3). Based on the theoretical calculations of the *wt.%* of N and B (Supplementary data – Table S7.1), BN-rGO-2 was expected to result in higher nitrogen and boron content; however, from the elemental analysis (Table 7.1), it was observed that BN-rGO-3 exhibited higher boron and nitrogen content. XPS measurements revealed a doping content of 6.89% for nitrogen and 3.71% for boron in BN-rGO-3, lower than the doping content obtained in the elementary analysis.

Table 7.1: Elemental composition of GO, rGO and heteroatom-doped rGO.

Sample	Elemental analysis				ICP-OES	XPS	
	Carbon/± 1%	Hydrogen/± 1%	Oxygen/± 1%	Nitrogen/± 1%	Boron/%	Nitrogen/%	Boron/%
GO	50.96	20.64	28.40	-	-	-	-
rGO	89.20	9.37	1.43	-	-	-	-
N-rGO	80.83	2.65	3.53	12.99	-	7.09	-
B-rGO	86.32	2.25	6.28	-	5.15 ± 0.05	-	4.56
BN-rGO-1	81.54	4.88	5.01	5.57	2.89 ± 0.3	-	-
BN-rGO-2	83.11	3.19	1.86	7.84	3.60 ± 0.1	-	-
BN-rGO-3	79.70	2.29	2.09	9.92	4.22 ± 0.4	6.89	3.71

The XPS peak deconvolution in Figure 7.1 and Supplementary Data (Figure S7.1 and Table S7.2) shows a detailed configuration of all the elements present in the single and dual heteroatom-doped rGO samples. Figure 7.1 presents the spectra showing the characteristic peaks of all the elements present in BN-rGO-3, such as C $1s$ (284.3 eV), O $1s$ (531.2 eV), N $1s$ (400.1 eV), and B $1s$ (192.2 eV). The intense peak in the C $1s$ spectra (Figure 7.1 (a)) corresponds to the C–C sp^2 bonded graphite carbon structure, which suggests that most carbon atoms are in a polyaromatic honeycomb structure. The N $1s$ peaks for N-rGO (Supplementary Data – Figure S7.1) and BN-rGO-3 (Figure 7.1 (c)) reveal the local chemical binding states and three prominent peaks for the nitrogen species, i.e., pyridinic-N, pyrrolic-N, and quaternary-N (graphitic-N). Pyridinic-N occurs on the edges of a six-member ring by donating one p-electron to the aromatic ring. In contrast, pyrrolic-N occurs in a five-member ring by donating two p-electrons to the π-conjugated ring, while quaternary-N is a substitution of a carbon atom in the GO basal plane linked with three carbon atoms in a hexagonal ring [27]. N-rGO has a mixture of quaternary-N (402.1 eV), pyridinic-N (398.9 eV) and pyrrolic-N (400.8 eV), while BN-rGO-3 mainly contains pyridinic-N (398.5 eV) and pyrrolic-N (400.2 eV). The content of pyrrolic-N was 37%, while pyridinic-N was 63% in the BN-rGO-3 sample. In the case of N-rGO, quaternary-N has the highest stability relative to pyrrolic-N and pyridinic-N. The percentage of pyridinic-N tends to depend on two factors. Firstly, it is enhanced by lowering the pyrrolic-N content and decreases when the quaternary-N content increases [28]. The interaction between these two factors is similar to the pyridinic-N in BN-rGO-3. It has been reported that the pyridinic-N and pyrrolic-N play critical roles in determining the limiting current density and conductivity [29].
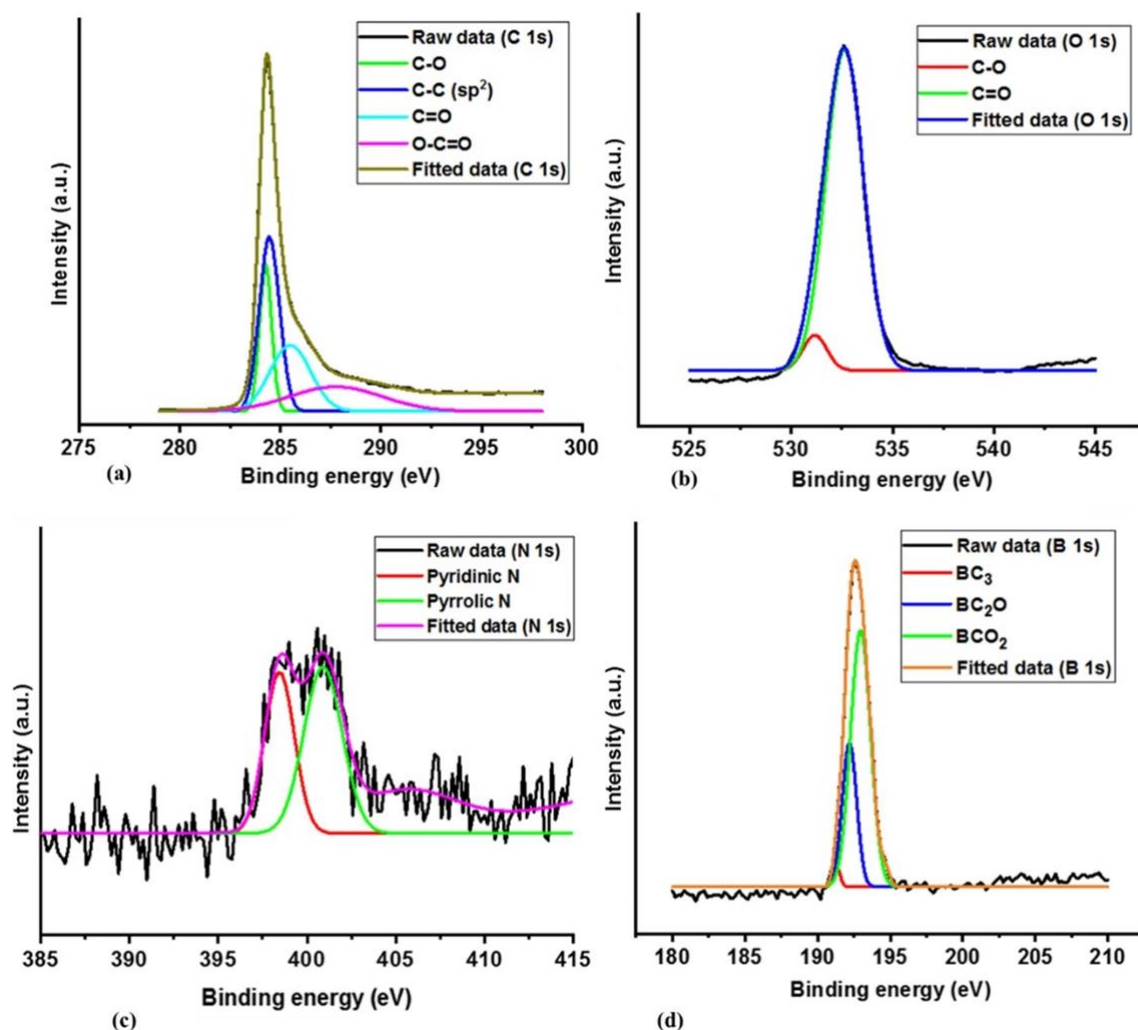
Figure 7.1: XPS spectra of (a) C 1*s* (b) O 1*s*, (c) N 1*s* and (d) B 1*s* of BN-rGO-3.

The B 1*s* of B-rGO (Supplementary Data – Figure S7.1 and Table S.2) and BN-rGO-3 (Figure 7.1 (d)) were deconvoluted into B–C–O (including BC_2O and BCO_2) and BC_3 moieties [30]. The peak for BC_3 appeared in BN-rGO-3 and B-rGO because of the replacement of the carbon atom by boron to give graphitic boron. The other two higher deconvoluted peaks (BC_2O and BCO_2) exhibited the bonding of boron with carbon and oxygen, indicating that no residual boron precursor is present, owing to its removal during thermal treatment and washing. Thus, to further confirm the presence of functional groups, FTIR was used.

7.3.2 Functional groups

The spectrum of GO (Figure 7.2) exhibited five peaks at 3300, 1736, 1620, 1232, and 1060 cm^{-1}, which were assigned to hydroxyl (–OH), carbonyl (C=O), aromatic (C=C), epoxy (C–O–C) and alkoxy (C–O) bonds, respectively [31]. The oxygen-containing functional groups were reduced after doping with either the single or dual heteroatom in the GO lattice. This is evident

in the spectra where the peaks associated with oxygen-containing functional groups disappeared or were weakened when compared with those from GO. The spectra of single heteroatom-doped rGO samples (N-rGO or B-rGO) exhibited peaks at 803, 1584, 659, and 1044 cm^{-1}, corresponding to C-N, C=N, B-O, and B-C, respectively. However, in the dual heteroatom-doped samples (BN-rGO-3), these peaks overlap because the hybridization between carbon and nitrogen, or boron, cannot occur to generate significant dipole moment changes. Similar observations after co-doping with nitrogen and boron were reported by Zhu *et al.* [32].
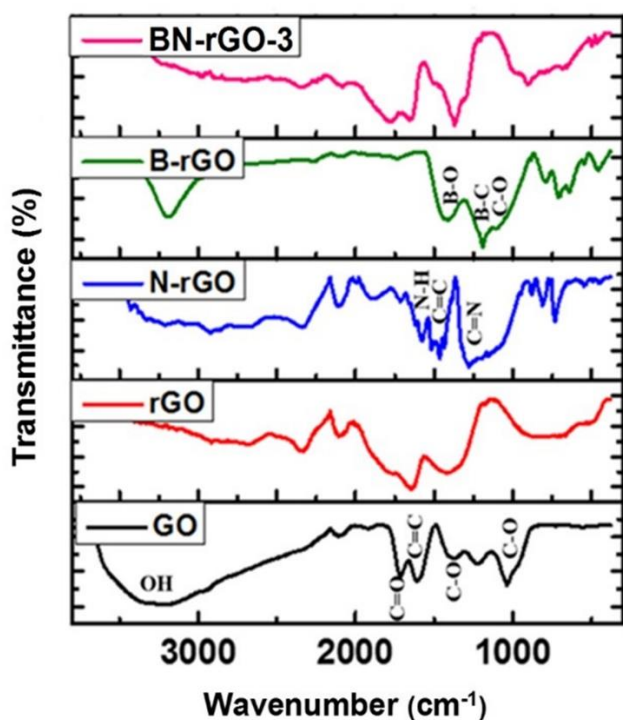
Figure 7.2: ATR-FTIR spectra of GO, rGO and heteroatom-doped rGO.

7.3.3 Morphology and microstructure

The surface morphologies of GO and BN-rGO-3 from FE-SEM analysis are shown in Figure 7.3 (a) and (b), respectively. The graphene layers of BN-rGO-3 are twisted and crumbled due to the shock experienced during the thermal treatment of GO, as well as the decomposition and sudden eruption of gaseous products, such as carbon monoxide or carbon dioxide. Figures 7.3 (c) and (d) show that the hydrothermal reaction of dual heteroatom-doped rGO resulted in a thin, layered transparent structure with few-layered GO. BN-rGO-3 showed a typical overlaid structure made of planar sheets with more wrinkles and corrugations. This indicated that the hydrothermal treatment effectively executed the exfoliation on GO layers. The few-layer

morphology of the BN-rGO sample is exceptionally significant for electron transport since it can provide an open pore structure for the electrolyte solution to access every individual sheet [33], consequently making it possible to combine the ultra-high power density and high energy density in the solar cells based on the BN-rGO-3 nanomaterials. Hence, this shows that the addition of the heteroatom could significantly influence the morphology of GO. The interlayer spacing, shown in Figures 7.3 (e) and (f), tends to vary with doping precursors, as illustrated in section 3.4 (Table 7.2).
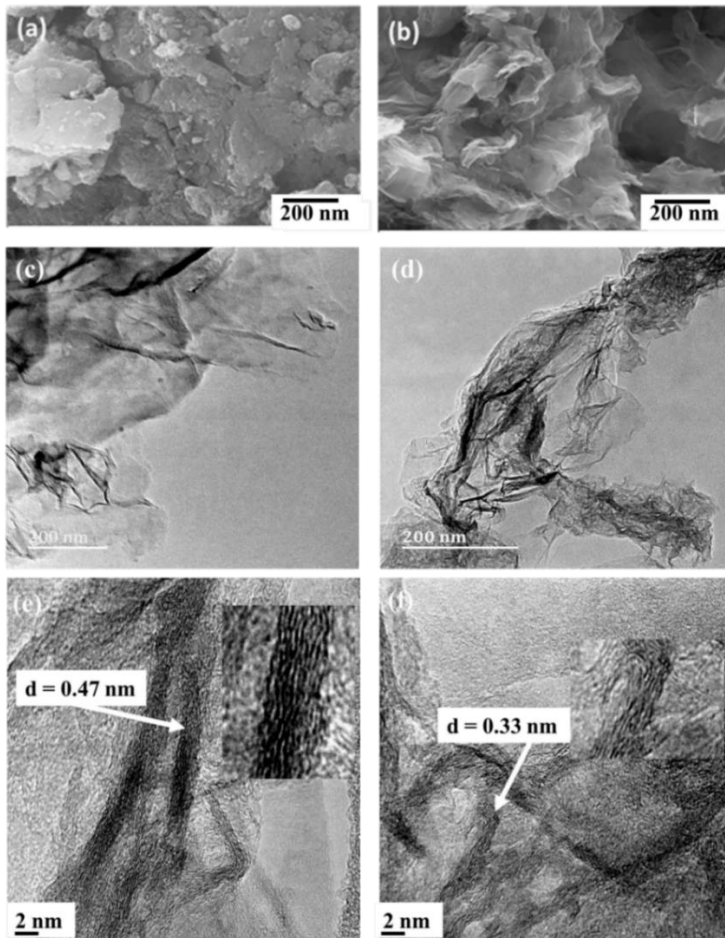
Figure 7.3: FE-SEM images of (a) GO and (b) BN-rGO-3; TEM images of (c) GO and (d) BN-rGO-3; and HR-TEM images of (e) GO and (f) BN-rGO-3.

7.3.4 Crystallinity

Figure 7.4 (a) shows the P-XRD patterns of GO, rGO and heteroatom-doped rGO. The characteristic diffraction peak of GO at 12° is attributed to the (001) crystalline plane [34-36], which disappeared after the reduction to rGO. rGO consists of nanocrystalline graphene stacks and random interlayer spaces [37]. Meanwhile, after single and dual-doping with boron and

nitrogen atoms, a broad (002) diffraction peak appeared at around 25.0 – 25.8°, indicating the recuperation of the π-conjugated system under thermal reaction [38]. The diffraction peak shift is attributed to the successful exfoliation [32], and it also indicated that few-layered graphene-based nanomaterials were synthesized [39]. The diffraction peak was also noted to be broader with weaker intensity, and this is due to the disorder along the stacking axis, where the oxygen-containing functional groups were reduced.
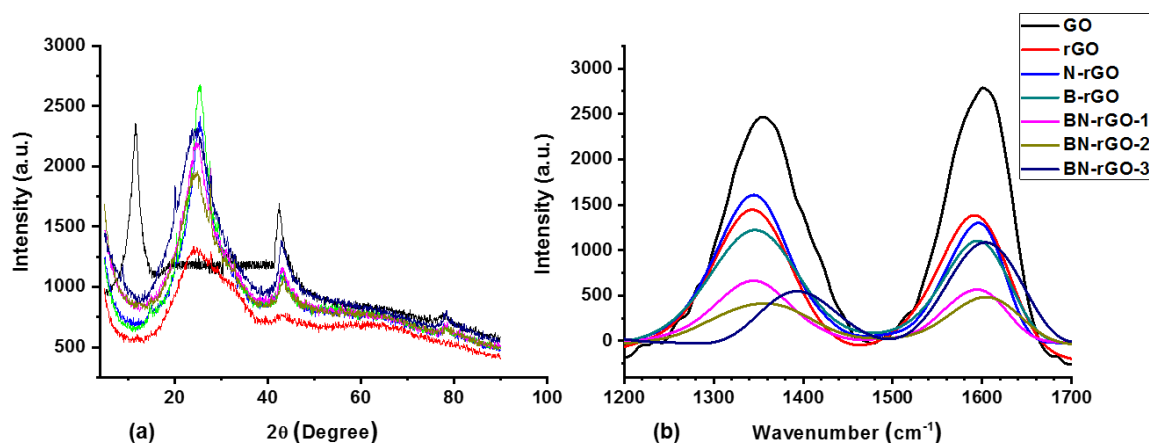
Figure 7.4: (a) Powder X-ray diffractograms and (b) Raman spectra of GO, rGO and heteroatom-doped rGO samples.

A massive decrease in the interlayer spacing from 0.76 to 0.34 nm (Table 7.2) after single and dual heteroatom-doping was caused by lattice distortions due to the incorporation of boron and nitrogen, as well as the decrease in oxygen content during the reduction process, which effectively restores the aromatic character in rGO. The reduction process tends to alter the chemical topography and strengthens the interlayer interactions of the resulting heteroatom-doped rGO, giving rise to more densely packed structures. The trend in interlayer spacings of the heteroatom-doped rGO samples obtained from P-XRD correlated well with those determined from HR-TEM analysis.

Table 7.2: P-XRD and HR-TEM parameters of GO, rGO and heteroatom-doped rGO.

Sample	2θ/degree	Interlayer spacing/nm	
		P-XRD	**HR-TEM**
GO	11.6	0.76 ± 0.05	0.47 ± 0.03
rGO	25.0	0.360 ± 0.004	0.392 ± 0.008
N-rGO	25.1	0.361 ± 0.003	0.361 ± 0.001
B-rGO	25.6	0.352 ± 0.001	0.353 ± 0.002
BN-rGO-1	25.7	0.350 ± 0.001	0.340 ± 0.001
BN-rGO-2	25.7	0.351 ± 0.001	0.342 ± 0.001
BN-rGO-3	25.8	0.343 ± 0.001	0.332 ± 0.002

The crystallinity of heteroatom-doped rGO was further studied by the use of Raman spectroscopy. The Raman spectrum of GO (Figure 7.4 (b)) shows a D-band at 1355 cm^{-1} and G-band at 1603 cm^{-1}, whereby the peak area ratio (I_D/I_G) reveals the disorder and the GO structure's graphitic symmetry [32,39]. After doping *via* hydrothermal treatment, the D-and G-bands showed a minimal shift in the wavenumber, demonstrating an insignificant effect on the GO structure. For example, the D-band peaks for the samples (rGO, N-rGO, B-rGO, BN-rGO-1, and BN-rGO-2) were almost similar to that of GO, apart from BN-rGO-3, with the D-band at 1401 cm^{-1} (Table 7.3). This shift was attributed to the change in the bond length and symmetry (C-C and C=C bonds) in the graphene lattice [40]. The shift to lower wavenumber in the G-band of rGO, N-rGO, B-rGO, and BN-rGO-1 is associated with an increase in the number of structured layers. A shift in the G-band position from 1603 to 1607 and 1610 cm^{-1} for BN-rGO-2 and BN-rGO-3, respectively, suggested incorporating boron and nitrogen atoms into the GO framework prompting an increment in the disordered structure relative to GO [41].

Table 7.3: Crystallinity analysis of GO, rGO and heteroatom-doped rGO.

Sample	D-band/cm^{-1}	G-band/cm^{-1}	I_D/I_G
GO	1355	1603	0.88
rGO	1350	1595	0.66
N-rGO	1350	1598	1.11
B-rGO	1350	1599	1.20
BN-rGO-1	1350	1601	1.23
BN-rGO-2	1358	1607	1.26
BN-rGO-3	1401	1610	1.30

The intensity ratio of D- and G-bands (I_D/I_G ratio) was calculated and presented in Table 7.3. The I_D/I_G ratio of rGO was lower than that of GO because of the removal of oxygen functionalities and the recovery of sp^2-hybridized C-C bonds [42,43]. However, the I_D/I_G ratio of the single and dual heteroatom-doped rGO samples was higher than that of GO, with BN-rGO-3 having the highest density of defects in the structure (I_D/I_G ratio = 1.30). This was attributed to the structural defects caused by both nitrogen and boron atoms implanted at the radicalized graphene sites in the dual heteroatom-doped rGO samples [39]. This suggests that the degree of disorder and defects are significantly increased after dual doping. Comparing the single and dual heteroatom-doped rGO shows that doping with two different atoms can further increase the I_D/I_G ratio, attributed to the variation of the bond distance between C-C and C-B or C-N. Such variation in bond distance tends to increase the asymmetry of the electron distribution [44] and increase the defective sites and smaller-sized graphitic nanosheets [42]. The results agree with some of the previous reports, which have shown that boron and nitrogen doping on the GO framework causes an increase in defects [16,45]. However, Zhu *et al.* [32] reported a decrease in the I_D/I_G ratio after co-doping with boron and nitrogen atoms in the GO framework. They reported that the low I_D/I_G ratio indicated that the defects decreased as the sp^2 domain was partially restored by the doping and reduction process. This was attributed to the introduction of boron and nitrogen atoms in the GO framework, which substituted the sp^3 carbon defect sites to quaternary-N, pyridinic-N, and BC_3 forms [46].

7.3.5 Thermal stability

Figure 7.5 shows the thermal analysis curves of single and dual heteroatom-doped rGO. The weight loss between 35 to 280 °C in the thermogram of GO (Figure 7.5 (a)) was due to the decomposition of oxygen groups and desorption of the adsorbed water in the interspace between graphene sheets [47]. The rGO sample had the highest thermal stability of 588.5 °C (Supplementary Data – Table S7.3), suggesting a relatively more well-ordered graphitic carbon framework [48]. Comparing the exothermic peak (Figure 7.5 (b)) of N-rGO and B-rGO suggests that single-atom doping decreases the thermal stability of GO. However, Duan *et al.* [49] reported an increase in thermal stability after doping with boron or nitrogen. They reported that doping with an atom, such as nitrogen or boron, tends to block the combustion site and depresses the generation of CO_x [49]. The doping (boron or nitrogen) content seems to prevail over the oxygen content and is liable for the observed diverse thermal oxidation stabilities. Thus, the higher thermal stability in N-rGO was attributed to the amount of nitrogen (7.09%) present and, importantly, the type of bonding configuration (quaternary-N). B-rGO was found

to have a much lower doping content of 4.56%, and also its thermal stability is lower than that of N-rGO. This is because the nitrogen atom can easily replace carbon when compared to boron during the doping process, and boron tends to provide more defects in the GO lattice.
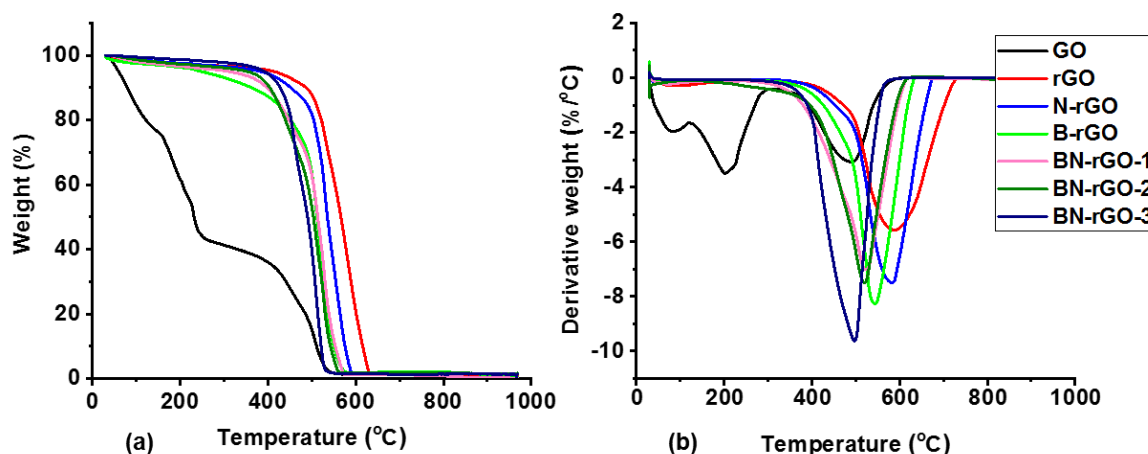
Figure 7.5: Thermal stability studies represented as (a) TGA thermograms and (b) derivative weight loss curves for GO, rGO and heteroatom-doped rGO samples.

The increase in doping content caused an increase in the density of structural defects in dual heteroatom-doped rGO, thus, reducing their thermal stability. The decrease in the thermal stabilities of the synthesized heteroatom-doped rGO correlates with its lower crystallinity observed in Raman analysis in Table 7.3. During the doping process, the use of a single precursor containing both nitrogen and boron tends to produce nanomaterials (BN-rGO-2 and BN-rGO-3) that are less thermally stable compared to the nanomaterials (BN-rGO-1) synthesized from a combination of precursors. Thermal stability is also affected by the bonding configuration of boron or nitrogen [50,51]. BN-rGO-3 consists of a higher percentage of pyridinic-N and pyrrolic-N, which lowers the thermal stability. In contrast, N-rGO consists of a low percentage of pyrrolic-N and a high percentage of quaternary-N, making it more graphitic and stable [51].

7.3.6 Surface properties

The BET surface area, pore size, and pore volumes are summarized in Table 7.4. The rGO sample had a larger surface area of 71.94 m^2 g^{-1} as compared to GO, which had a smaller surface area due to the strong hydrogen bond that causes agglomeration of sheets and reduces the contribution of spaces between sheets [52]. The large surface area of rGO is probably due to its fewer oxygen-containing functional groups. Also, the BET surface area of single atom

doped-rGO was found to be larger than that of GO and tended to be further increased after dual heteroatom-doping with both boron and nitrogen atoms. The difference in surface area of single and dual heteroatom-doped rGO is attributed to nitrogen and boron heteroatoms, which induce the restacking phenomenon, disorientation, and corrugation of graphitic basal planes [53]. This observation is similar to the study reported on nitrogen and sulfur-doped reduced graphene oxide (NSrGO) [54] and nitrogen-doped reduced graphene oxide (N-doped rGO) [55].

Table 7.4: Textural characteristics of GO, rGO and heteroatom-doped rGO.

Sample	Surface area/$m^2\ g^{-1}$	Pore volume/$cm^3\ g^{-1}$	Pore size/nm
GO	60.36	0.103	26.61
rGO	71.94	0.398	21.32
N-rGO	69.15	0.125	25.53
B-rGO	77.97	0.224	23.69
BN-rGO-1	80.34	0.311	20.35
BN-rGO-2	88.07	0.339	19.58
BN-rGO-3	161.51	0.646	15.37

The pore size of heteroatom-doped rGO was found to be in the range of 15.0 – 26.0 nm, which is associated with the presence of mesopores [56]. The mesopores are beneficial because they permit the insertion and de-insertion of ions during the charging-discharging process, which enhances the electrochemical properties [57]. The adsorption-desorption isotherms of BN-rGO-3 (Supplementary Data – Figure S7.2) exhibited type IV curves with a hysteresis loop in a relative pressure range of $P/P_o \sim 0.44 - 1.0$, which also serves as an indication that the sample is mesoporous [58]. The pore size distribution from Table 7.4 further affirms these results. The pore volume of heteroatom-doped rGO increased upon the increase in the content of boron and nitrogen atoms during doping. This was attributed to more defects being created, leading to the weakening of π-π interactions between the rGO sheets. The nitrogen- and boron-rich graphene-based nanomaterial (BN-rGO-3) attained the largest surface area because of its high mesoporosity, as observed from the hysteresis loop closed at P/P_o of 0.45. Mohamed *et al.* [59] reported a decrease in the surface area after nitrogen and boron doping onto the graphene lattice, and this was also due to the low mesoporosity recognized from the hysteresis loop closed at P/P_o of 0.1, which confirms the narrower pores.

7.3.7   Optical properties

Ultraviolet−visible (UV-Vis) absorption spectroscopy was used to investigate the optical properties and compare the energy bandgap (E_g) of single and dual heteroatom-doped rGO samples (Figure 7.6). All heteroatom-doped rGO samples exhibited an absorption peak in the region of 260 – 350 nm arising from $\pi \rightarrow \pi^*$ transitions. GO shows an absorption peak at a shorter wavenumber of 234 nm. A comparison of single and dual heteroatom-doped rGO shows that the absorbance of dual heteroatom-doped materials decreased slightly, which was due to the mixing effect of the two heteroatoms, which further introduced high defect levels [60]. This further demonstrates the heterogeneous distribution of boron and nitrogen atoms in the GO lattice. The Tauc's plots for GO (Figure 7.6 (b)) and heteroatom-doped rGO (Supplementary Data – Figure S7.3) provide the values of the direct energy bandgaps. These were obtained by extrapolating the UV-Vis absorption curves to the zero absorption on the x-axes. The associated energy bandgaps fell in the range of 1.3 – 3.4 eV by maximizing the sp^2 domains of heteroatom-doped rGO. The energy bandgaps of dual heteroatom-doped rGO samples are reduced due to the reduction in the number of oxygen-containing functional groups. The reduced energy bandgap was also attributed to the compensation of energy states related to incorporating boron and nitrogen atoms, which shift the direction of the valence and conduction band edges [61].
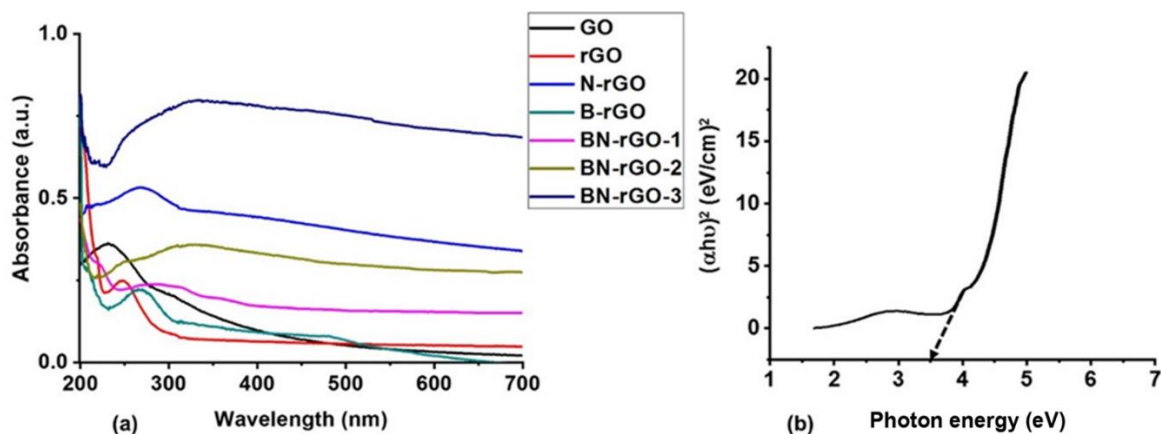

Figure 7.6: (a) UV-Vis absorption spectra for GO, rGO and heteroatom-doped rGO, and (b) Tauc's plot for GO.

7.3.8 Electrical properties

The electrical conductivities of GO, rGO, and heteroatom-doped rGO was investigated with a four-point probe and Hall effect measurement system. GO and rGO had electrical conductivities of 1.10×10^{-7} and 2.40×10^{-4} S cm^{-1}, respectively, while those of single and dual heteroatom-doped rGO were in the order of N-rGO (2.65 S cm^{-1}) < B-rGO (4.41 S cm^{-1}) < BN-rGO-1 (11.03 S cm^{-1}) < BN-rGO-2 (14.71 S cm^{-1}) < BN-rGO-3 (22.07 S cm^{-1}) as shown in Table 7.5. The poor electrical conductivity of GO comes from the oxidative disruption of the conjugated sp^2-hybridized carbon network. The reduction of oxygen in rGO has been reported to recoup the electrical conductivity by forming sp^2-bonded lateral domains [62]. Thus, in this case, an increase in the electrical conductivity of rGO was observed.

Table 7.5: Electrical properties of GO, rGO and heteroatom-doped rGO.

Sample	Sheet resistance/Ω sq^{-1}	Bulk resistivity/Ω cm	Electrical conductivity/S cm^{-1}
GO	1.00×10^{8}	9.09×10^{6}	1.10×10^{-7}
rGO	4.59×10^{6}	4.16×10^{3}	2.40×10^{-4}
N-rGO	8.30×10^{2}	3.76×10^{-1}	2.65
B-rGO	5.00	2.26×10^{-1}	4.41
BN-rGO-1	4.99	9.06×10^{-2}	11.03
BN-rGO-2	4.79	6.79×10^{-2}	14.71
BN-rGO-3	4.38	4.53×10^{-2}	22.07

The electrical conductivity of heteroatom-doped rGO depended on the surface area, and it was observed that the electrical conductivity increased with an increase in surface area (Table 7.4). GO synthesis resulted in an agglomerated material due to π-π interactions between the sheets, which caused a decrease in surface area. Thus, a lower electrical conductivity was observed for GO. The C/O ratio tends to increase during the hydrothermal approach, and rGO, N-rGO, and B-rGO restore their π-π conjugated structure, thereby enhancing their electrical conductivity. Also, doping with nitrogen substantially increased the electrical conductivity of N-rGO relative to that of GO and rGO. This is due to the insertion of non-bonding electrons responsible for enhancing electrical conductivity [63]. In the case of boron-doping, the electrical conductivity was found to be relatively higher than that of N-rGO. This is due to the greater distortion caused by the boron atom on the GO lattice and the change in the bonding configuration. Boron-doping causes a shift in the Fermi level away from the Dirac point,

resulting in a finite density of state at zero energy, which increases the quasi-particle weight in semiconductors [64]. Therefore, a substantial increase in the electrical conductivity of rGO is expected after boron doping. A similar observation was reported by Wu *et al.* [65], where boron-doped graphene resulted in higher electrical conductivity of 2.65×10^{-5} S cm^{-1} than for nitrogen-doped graphene (2.48×10^{-5} S cm^{-1}). On the contrary, Poh *et al.* [66] reported a relatively lower electrical conductivity for boron-doped graphene when compared with nitrogen-doped graphene. This was due to the generation of more holes in the valence band that act as traps for free electrons, thereby reducing the carrier mobility and electrical conductivity.

Higher electrical conductivities were observed in the dual heteroatom-doped rGO samples. However, among the dual heteroatom-doped rGO samples, BN-rGO-1 showed the least electrical conductivity because it contained the highest amount of oxygen in its structure (Table 7.1). Such a residual oxygen level has a negative impact on the electrical conductivity of the nanomaterials. Mohamed *et al.* [59] reported a decrease in the electrical conductivity after co-doping with boron and nitrogen and attributed this to the relatively higher boron content than nitrogen, which gave rise to fast recombination during the n → p transfer. However, in this case, all the synthesized dual heteroatom-doped rGO samples had a lower boron content than nitrogen. The presence of different nitrogen moieties also influences the electrical conductivity of heteroatom-doped rGO. BN-rGO-3 had the highest pyridinic-N and pyrrolic-N content, and this increase in particular nitrogen sites [29] subsequently made it have the best electrical conductivity.

7.3.9   Electrical transport mechanism

The electrical conductivity of heteroatom-doped rGO has been reported to be affected by two factors, which are charge carrier density (*n*) and mobility (μ). The values of *n* and μ were calculated using equations:

$$n = \frac{1}{R_H} \tag{1}$$

$$\mu = \frac{R_H}{\rho} \tag{2}$$

where R_H is the Hall coefficient and ρ is the resistivity [67,68]. Hall effect studies revealed that N-rGO (Table 7.6) and BN-rGO-1, BN-rGO-2, and BN-rGO-3, have a predominance of *n*-type charge carriers, whereas, in B-rGO, the *p*-type charge carriers were the most dominant.

The *n-* and *p*-type charge carrier characteristics are attributed to the change in the electronic structure of GO, caused by dopants. The conduction and valence band states of pristine graphene are reported to touch each other at the Fermi level, indicating that pristine graphene has zero-bandgap semiconducting characteristics [69]. N-rGO can be viewed as an electron donor, which tends to contribute electrons to the delocalized π-bond than the carbon atom. Therefore, the Dirac point shifts the valence band below the Fermi level and causes an increase in the intensity of the density of states (DOS) near the Fermi level and enhances the carrier density and mobility.

Table 7.6: Hall effect measurements for GO, rGO and heteroatom-doped rGO at a constant magnetic field of 1160 G.

Sample	Resistivity/ Ω cm	Hall coefficient/cm^3 C^{-1}	Carrier density/cm^{-3}	Carrier mobility/cm^2 V^{-1} s^{-1}
GO	-	-	-	-
rGO	1.83×10^{-1}	2.05×10^{-2}	48.7	0.112
N-rGO	2.61×10^{-1}	4.13×10^{-2}	24.2	0.158
B-rGO	6.66×10^{-2}	-1.37×10^{-2}	73.0	0.205
BN-rGO-1	2.42×10^{-3}	1.06×10^{-3}	943	0.436
BN-rGO-2	2.02×10^{-3}	9.43×10^{-4}	1060	0.467
BN-rGO-3	3.58×10^{-4}	1.76×10^{-4}	5681	0.493

In the case of B-rGO, the Dirac points move toward the conduction band, demonstrating the *p*-type semiconducting characteristics [70]. Such a shift of the Dirac point into unoccupied states in B-rGO causes an increase in the electrical conductivity. The *p*-type semiconducting characteristics are due to the creation of holes around the Fermi level, which arises from the *p*-orbitals of the boron, and carbon bonded to it. The conduction and valence bands of BN-rGO meet near the Fermi level; hence, the energy bandgap is smaller than that of a single heteroatom-doped rGO (as observed in this work). This tunes the work function and carrier concentration of BN-rGO, which broadens the range of optical and electronic applications of BN-rGO.

The calculated charge carrier density and mobility values show that the charge carrier density and mobility increase by increasing the heteroatom content on the GO lattice. The charge carrier density and mobility were affected by heteroatom-doping and the dopant concentration. In N-rGO, the number of transferred electrons increases with the content of doped nitrogen

atoms in the GO structure. This is because of the electron-donating nature of the nitrogen atom, thus boosting the electron density. Therefore, this serves as an indication that more active sites are created with high electron regions. The redistribution of charge density creates an active site in N-rGO and similarly occurs in B-rGO. However, when boron and nitrogen atoms are co-doped and separated by carbon atoms, they result in more electron transfer, indicating that a more active site is created around the doped atoms than in a single heteroatom-doped rGO. The carrier mobility of BN-rGO-3 was calculated to be 0.493 cm^2 V^{-1} s^{-1}. The higher carrier mobility indicates that BN-rGO-3 has a rich doping content, which is consistent with the XPS results. A relationship between the electrical and optical properties was observed for both single and dual heteroatom-doped rGO. The decrease in the bandgap of heteroatom-doped rGO caused an increase in electrical conductivity.

7.3.10 Electrode potential characteristics

The electrochemical properties of heteroatom-doped rGO samples were investigated using cyclic voltammograms. The GO exhibited a smaller quasi-rectangular curve (Figure 7.7), indicating a lower ion conductivity, which is attributed to the lower graphitization degree of GO. A similar observation was reported by Mohamed *et al.* [59]. The cyclic voltammograms showed the characteristics of an electrochemical double-layer capacitor (EDLC) and reversible Faradaic reactions for all the single and dual heteroatom-doped rGO samples. An ideal rectangular-like shape with an anodic and cathodic peak at ~ 0.2 and 0.3 V was observed in all heteroatom-doped rGO samples, which is attributed to the redox reaction of boron- and/or nitrogen-containing functional groups; hence, it provides a relative portion of a capacitance.
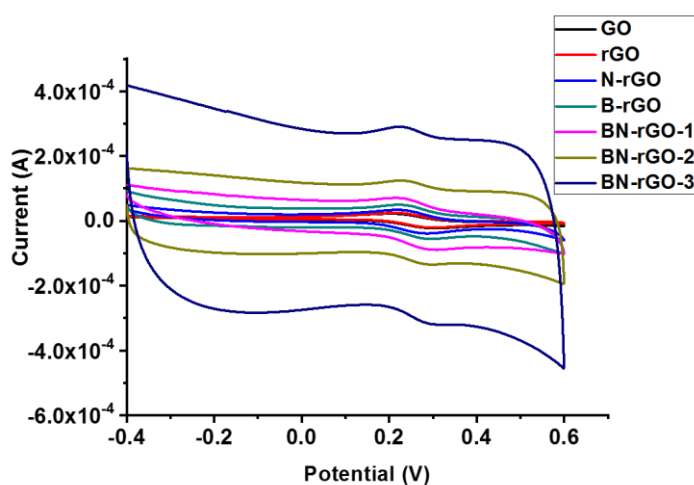

Figure 7.7: Cyclic voltammograms for GO, rGO and heteroatom-doped rGO.

Dual heteroatom-doped rGO tends to exhibit a higher double-layer capacitance than single heteroatom-doped rGO, indicating that the presence of two heteroatoms enhances the electrochemical activity of GO due to the strong synergistic effect of nitrogen and boron doping [71], which increases the charge transfer rate across an electrode (ferro/ferricyanide solution interface). This also suggests that BN-rGO-3 has the highest capacitance, exceeding in succession BN-rGO-2 > BN-rGO-1 > B-rGO > N-rGO > rGO > GO. The detailed mechanism of the Faradaic reaction in heteroatom-doped rGO is not fully understood, and the anodic and cathodic peaks observed manifest the reversible redox transition that involves the proton exchange taking place during sample polarization. The anodic and cathodic peaks are mainly affected by the surface area, graphitic crystallinity, and electrical conductivity. The great decrease in the electrical resistivity of the BN-rGO-3 electrode contributes to a significant increase in the electrical conductivity in the circuit.

The presence of nitrogen and boron atoms changes the electronic state of rGO for better facilitation of the adsorption of ions in the electrolyte and increases the specific capacitance [72]. The nitrogen- and boron-containing functional groups also show a contribution to the Faradaic redox capacitance. The capacitance in BN-rGO-3 is attributed to the higher content of pyridinic N and the BC_2O bonding configuration. This also correlates with the XPS results and previous reports, which state that the nitrogen bonding configuration of pyridinic-N and pyrrolic-N can give a higher capacitance [73,74]. Han *et al.* [75] also reported that the presence of boron-containing functional groups brings about an electrochemical redox reaction on the surface graphene. Thus, it can be deduced that a dual heteroatom-doped rGO electrode has improved electrochemical properties.

7.3.11 DSSC characterization

This section presents the discussion on the results of light-harvesting experiments carried out with GO, rGO, single and dual heteroatom-doped rGO. The effect of using single heteroatom-doped rGO or dual heteroatom-doped rGO CEs with a binder, such as Nafion or PANi in DSSCs, was investigated.

7.3.11.1 Photovoltaic performance

A comparison of the photovoltaic performance of DSSCs based on the various samples is shown in Table 7.7. The open-circuit voltage (V_{oc}) and short-circuit photocurrent density (J_{sc}) of DSSCs based on dual heteroatom-doped rGO CEs clearly showed that dual heteroatom-doped rGO CEs are superior to GO, rGO, and single heteroatom-doped rGO CEs. In addition,

they have a relatively excellent electrocatalytic activity to reduce the electrolyte (I_3^- to I^-). Intriguingly, the GO resulted in a smaller fill factor (*FF*) of 0.67% and a low PCE of 0.28%; whilst the J_{sc} and V_{oc} values of the GO CE-based devices were generally high. This suggests that GO as a CE has an insufficient electrocatalytic activity, which is ascribed to few defects and low conductivity on GO. The edge planes of GO have more defects, resulting in high electrocatalytic activity when compared to the basal planes on GO that are electrochemically inert sites. Despite that, electron transfer would be restrained because of these defects [16].

Table 7.7: Photovoltaic performance of DSSCs with GO, rGO and heteroatom-doped rGO CEs.

Counter electrode	V_{oc}/V	J_{sc}/mA cm^{-2}	FF/%	PCE/%
GO	0.65	10.35	0.67	0.28 ± 0.02
rGO	0.29	2.37	13.3	0.53 ± 0.03
N-rGO	0.50	9.11	42.0	1.01 ± 0.01
B-rGO	0.45	9.84	44.4	1.57 ± 0.01
BN-rGO-1	0.50	13.43	44.8	1.96 ± 0.02
BN-rGO-2	0.53	15.61	47.5	2.23 ± 0.01
BN-rGO-3	0.55	16.15	51.4	2.97 ± 0.03
BN-rGO-3 + Nafion	0.53	17.41	55.1	3.69 ± 0.01
BN-rGO-3 + PANi	0.56	17.84	60.3	4.13 ± 0.02

Incorporating a single or dual heteroatom into the GO framework consolidates the electrocatalytic activity and electrical conductivity into one material. It also alters the edge and basal planes of GO, thus, enhancing the electrochemical properties, consequently enriching the heteroatom-doped rGO with high activity. The dual heteroatom doped rGO devices exhibited a substantial improvement in photovoltaic performance as compared to the single heteroatom doped rGO devices. This is because of the relatively higher current density, inferring that the incorporation of dual heteroatoms results in the enhanced transportation and collection of photo-generated charge carriers. The increase in current density may also be attributed to the optical absorption at a higher wavelength (Figure 7.6 (a)), causing more photo-generated charge carriers.

CV (Figure 7.7) further shows that at a similar voltage, the current of dual heteroatom-doped rGO is essentially more than that of single heteroatom-doped rGO, demonstrative of good conductivity for dual heteroatom-doped rGO. Therefore, dual heteroatom-doped rGO can

effectively carry electrons from the outer circuit to the active electrochemical sites on its surface because of its high conductivity, and these defect sites act as catalytic sites for the reduction of triiodide, and two synergetic factors consolidate together, prompting a high energy conversion efficiency towards I_3^-/I^-. The outstanding electrocatalytic performance is ascribed to the doped nitrogen and boron atoms with diverse electronegativity, relative to carbon, making graphene sheets to be non-electroneutral and creating charged sites that are favourable for the electro-synthetic reaction.

For single heteroatom-doped rGO, the *FF* showed an increase with the variation of dopants (Table 7.7). The *FF* is associated with the series resistance (R_s) and shunt resistance (R_{sh}). A smaller R_s and higher R_{sh} result in a higher *FF*, thereby giving rise to a higher PCE. The lower PCEs achieved in DSSCs fabricated from GO, and rGO CEs were attributed to charge carrier recombination during the variation transfer along the DSSC's functional chain, such as from eosin B dye to the GO or rGO CE, and to the electrolyte, and back to the photoanode. The addition of heteroatoms to rGO tends to suppress recombination and enhance J_{sc}. This is because heteroatom-doped rGO has higher electron mobility than rGO, which facilitates the efficient transportation of electrons with minimum recombination; hence, improving the device performance.

A significant increase in the V_{oc} of dual heteroatom-doped rGO CE-based DSSCs was observed, which indicates that dual heteroatom-doped rGO CEs can accomplish more work than their single heteroatom-doped rGO counterparts. The improvement in V_{oc} is associated with a higher electron injection rate and lesser back electron transfer. This is a positive trait in heteroatom-doped rGO CEs since they are less expensive than platinum CEs. Thus, these results show that dual heteroatom-doped rGO is a potential candidate for CE fabrication and serves as a better replacement for platinum in DSSCs.

The effect of using BN-rGO-3 CEs with a binder (such as Nafion or PANi) was investigated. The binder played a crucial role in electron transportation. The binder was also able to reduce cracking in BN-rGO-3 CEs, thereby improving the contact in the DSSCs. The BN-rGO-3, as CE, showed an enhanced PCE of DSSC when used in conjunction with Nafion or PANi. The combination of a binder and graphene-based nanomaterials can assemble the electrocatalytic activity of the binder and the electron-conduction of graphene-based nanomaterials on their nanocomposite. When comparing the V_{oc} of BN-rGO-3 and BN-rGO-3+Nafion, BN-rGO-3+Nafion had a slightly lower V_{oc} (0.53) due to more I^- ions that can diffuse into the eosin B (dye molecule) for fast dye regeneration. However, fast dye regeneration tends to reduce the

lifetime of the oxidized dye molecules in order to prevent charge recombination, thus resulting in a decrease in the V_{oc} of the DSSC [76].

The best DSSC performance was observed when BN-rGO-3 and PANi (4.13%) were used as the CE. This indicated that PANi was successfully coated onto the surface of BN-rGO-3, which caused an increase in the electrical conductivity, thus, enhancing the electrocatalytic performance of the DSSC. The covalent bonds between BN-rGO-3 (−C=) and PANi (−NH−) are validated to significantly increase the charge transfer. The higher PCE from BN-rGO-3+PANi CE was attributed to fast charge transfer from BN-rGO-3 and PANi. It was also due to the high interfacial charge transfer at the counter electrode/electrolyte interface. Thus, the enhanced interfaces give reaction space for a good triiodide reduction. In Figure 7.8, the shape of the DSSC's photocurrent density-voltage (*J-V)* curves indicates the efficiency of the devices. The higher efficiency of DSSC fabricated from BN-rGO-3 with PANi corresponds with the large rectangle under the *J-V* curve, as shown in Figure 7.8.
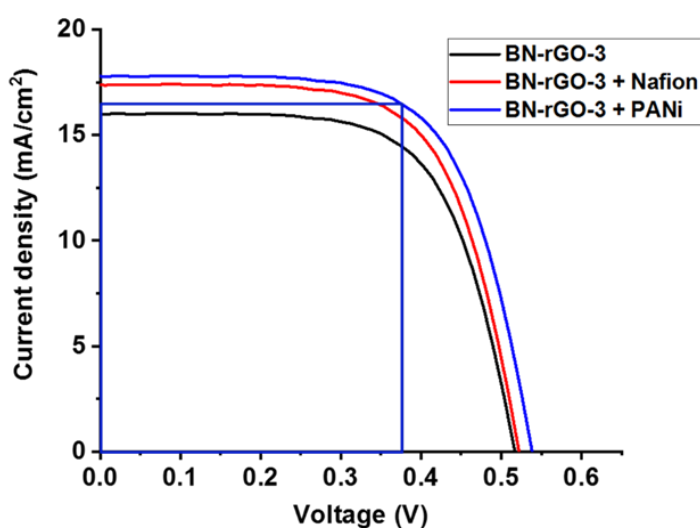
Figure 7.8: *J-V* curves for DSSCs fabricated from BN-rGO-3 with either Nafion or PANi and without the binder.

7.4   Conclusion

In conclusion, single and dual heteroatom-doped rGO have been effectively synthesized by hydrothermal treatment. Doping using the hydrothermal procedure was found to be suitable since it prevented the restacking of GO, resulting in high electrical conductivity. The physicochemical properties of single and dual heteroatom-doped rGO samples varied with the doping precursors. Single (N or B) heteroatom-doped rGO samples attained higher doping

levels when compared to dual heteroatom-doped rGO. However, when comparing the dual heteroatom-doped rGO samples, BN-rGO-3 resulted in the highest content of 3.71% for boron and 6.89% for nitrogen. The results obtained from BET, FE-SEM, and TEM prove that the dual heteroatom-doped rGO features a significant porous structure with interconnected mesopores, providing good electrochemical performance as an electrode material.

Incorporating the dual heteroatoms (B and N) tends to enhance the catalytic activity due to the synergistic effects. The active catalytic sites for the redox reduction reaction were pyridinic-N and pyrrolic-N due to reduced adsorbed energy and shift in redox potential. This was observed in BN-rGO-3, which had the highest pyridinic-N and pyrrolic-N content and showed the highest electrical conductivity and a PCE of 2.97%. Regardless of the high PCE in BN-rGO-3, there were some cracks on the CE during fabrication, which might have affected the PCE of the DSSCs. Thus, the effect of using a binder, such as Nafion or PANi, was investigated. The integration of BN-rGO-3 with PANi resulted in a relatively high PCE of 4.13%. Despite the various research approaches for the synthesis of dual heteroatom-doped graphene, there are still numerous issues that need to be tackled. For instance, controlling the doping position is still a critical issue in heteroatom-doped rGO, which is exceptionally needed in electrocatalysis for better performance of DSSCs. Nonetheless, the dual heteroatom-doped rGO materials exhibit great potential for solving energy issues because of their exceptional properties.

References

1. R. Kumar, V. Sahajwalla and P. Bhargava, *Nanoscale Adv.*, **2019**, 1, 3192–3199.

2. B.-K. Koo, D.-Y. Lee, H.-J. Kim, W.-J. Lee, J.-S. Song and H.-J. Kim, *J. Electroceramics*, **2006**, 17, 79-82.

3. A. Ghifari, D. X. Long, S. Kim, B. Ma and J. Hong, *Nanomaterials*, **2020**, 10, 501-510.

4. K. Shimada, T. Toyoda, M. Shahiduzzaman and T. Taima, *Jpn. J. Appl. Phys*, **2019**, 58, 124001-124004.

5. M. Wu and T. Ma, *ChemSusChem*, **2012**, 5, 1343-1357.

6. I. K. Popoola, M. A. Gondal, J. M. AlGhamdi and T. F. Qahtan, *Sci. Rep.*, **2018**, 8, 12864-12812.

7. S. Zhang, J. Jin, D. Li, Z. Fu, S. Gao, S. Cheng, X. Yu and Y. Xiong, *RSC Adv.*, **2019**, 9, 22092-22100.

8. O. Bayram, E. Igman, H. Guney, Z. Demir, M. T. Yurtcan, C. Cirak, U. C. Hasar and O. Simsek, *J. Mater. Sci.: Mater. Electron*, **2020**, 31, 10288-10297.

9.   X. Meng, C. Yu, X. Song, Y. Liu, S. Liang, Z. Liu, C. Hao and J. Qiu, *Adv. Energy Mater.*, **2015**, 5, 1500180-1500189.

10. H. Liu, Y. Liu and D. Zhu, *J Mater Chem*, **2011**, 21, 3335-3345.

11. B. Bhattacharya and U. Sarkar, *J. Phys. Chem. C*, **2016**, 120, 26793-26806.

12. S. Li, Z. Wang, H. Jiang, L. Zhang, J. Ren, M. Zheng, L. Dong and L. Sun, *ChemComm.*, **2016**, 52, 10988-10991.

13. Y. Wang, F. Yu, M. Zhu, C. Ma, D. Zhao, C. Wang, A. Zhou, B. Dai, J. Ji and X. Guo, *J. Mater. Chem. A*, **2018**, 6, 2011-2017.

14. L. Wei, P. Wang, Y. Yang, R. Luo, J. Li, X. Gu, Z. Zhan, Y. Dong, W. Song and R. Fan, *J. Nanoparticle Res.*, **2018**, 20, 110-112.

15. H. Fang, C. Yu, T. Ma and J. Qiu, *Chem. Comm.*, **2014**, 50, 3328-3330.

16. C. Yu, H. Fang, Z. Liu, H. Hu, X. Meng and J. Qiu, *Nano Energy*, **2016**, 25, 184-192.

17. A. Yella, H.-W. Lee, H. N. Tsao, C. Yi, A. K. Chandiran, M. K. Nazeeruddin, E. W.-G. Diau, C.-Y. Yeh, S. M. Zakeeruddin and M. Grätzel, *Science*, **2011**, 334, 629-634.

18. S. Umrao, T. K. Gupta, S. Kumar, V. K. Singh, M. K. Sultania, J. H. Jung, I.-K. Oh and A. Srivastava, *ACS Appl. mater. Interfaces*, **2015**, 7, 19831-19842.

19. N. P. D. Ngidi, M. A. Ollengo and V. O. Nyamori, *New J. Chem.*, **2020**, 44, 16864-16876.

20. N. P. D. Ngidi, M. A. Ollengo and V. O. Nyamori, *Materials*, **2019**, 12, 3376-3401.

21. W. D. Tennyson, M. Tian, A. B. Papandrew, C. M. Rouleau, A. A. Puretzky, B. T. Sneed, K. L. More, G. M. Veith, G. Duscher, T. A. Zawodzinski and D. B. Geohegan, *Carbon*, **2017**, 123, 605-615.

22. S.-Y. Yang, K.-H. Chang, Y.-L. Huang, Y.-F. Lee, H.-W. Tien, S.-M. Li, Y.-H. Lee, C.-H. Liu, C.-C. M. Ma and C.-C. Hu, *Electrochem. commun.*, **2012**, 14, 39-42.

23. L. Shahriary and A. A. Athawale, *Int. J. Renew. Energy Environ. Eng.*, **2014**, 2, 58-63.

24. I.-K. Ding, J. Melas-Kyriazi, N.-L. Cevey-Ha, K. G. Chittibabu, S. M. Zakeeruddin, M. Grätzel and M. D. McGehee, *Organic Electronics*, **2010**, 11, 1217-1222.

25. J. S. Roh, H. W. Yoon, L. Zhang, J.-Y. Kim, J. Guo and H. W. Kim, *ACS Appl. Nano Mater.*, **2021**, 4, 7897-7904.

26. S. Seenithurai, R. K. Pandyan, S. V. Kumar and M. Mahendran, *Nano Hybrids*, **2013**, 5, 65-83.

27. M. Vikkisk, I. Kruusenberg, U. Joost, E. Shulga, I. Kink and K. Tammeveski, *Appl. Catal. B*, **2014**, 147, 369-376.

28.   B. Zheng, J. Wang, F.-B. Wang and X.-H. Xia, *Electrochem. commun.*, **2013**, 28, 24-26.

29.   L. Lai, J. R. Potts, D. Zhan, L. Wang, C. K. Poh, C. Tang, H. Gong, Z. Shen, J. Lin and R. S. Ruoff, *Energy Environ. Sci.*, **2012**, 5, 7936-7942.

30.   Z.-R. Tang, Y. Zhang, N. Zhang and Y.-J. Xu, *Nanoscale*, **2015**, 7, 7030-7034.

31.   J. Song, X. Wang and C.-T. Chang, *J. Nanomater.*, **2014**, 2014, 1-6.

32.   X. Chen, X. Duan, W.-D. Oh, P.-H. Zhang, C.-T. Guan, Y.-A. Zhu and T.-T. Lim, *Appl Catal B-Environ*, **2019**, 253, 419-432.

33.   Y. Wang, Y. Wu, Y. Huang, F. Zhang, X. Yang, Y. Ma and Y. Chen, *J. Phys. Chem. C*, **2011**, 115, 23192-23197.

34.   M. Armand, F. Endres, D. R. MacFarlane, H. Ohno and B. Scrosati, *Nat. Mater.*, **2009**, 8, 621-629.

35.   X. Zhang, K. Li, H. Li, J. Lu, Q. Fu and Y. Chu, *Synth. Met.*, **2014**, 193, 132-138.

36.   N. I. Zaaba, K. L. Foo, U. Hashim, S. J. Tan, W.-W. Liu and C. H. Voon, *Procedia Eng.*, **2017**, 184, 469-477.

37.   S. Gadipelli and Z. X. Guo, *Prog. Mater. Sci.*, **2015**, 69, 1-60.

38.   Z. Lu, X. Xu, Y. Chen, X. Wang, L. Sun and K. Zhuo, *Green Energy & Environment*, **2020**, 5, 69-75.

39.   S. Elumalai, C.-Y. Su and M. Yoshimura, *Front. Mater.*, **2019**, 6, 211-216.

40.   B. J. Matsoso, K. Ranganathan, B. K. Mutuma, T. Lerotholi, G. Jones and N. J. Coville, *RSC Adv.*, **2016**, 6, 106914-106920.

41.   M. A. Mannan, Y. Hirano, A. T. Quitain, M. Koinuma and T. Kida, *Am. J. Mater. Sci.*, **2019**, 9, 22-28.

42.   S. Stankovich, D. A. Dikin, R. D. Piner, K. A. Kohlhaas, A. Kleinhammes, Y. Jia, Y. Wu, S. T. Nguyen and R. S. Ruoff, *Carbon*, **2007**, 45, 1558-1565.

43.   Z. González, C. Botas, P. Álvarez, S. Roldán, C. Blanco, R. Santamaría, M. Granda and R. Menéndez, *Carbon*, **2012**, 50, 828-834.

44.   Y. Zheng, Y. Jiao, L. Ge, M. Jaroniec and S. Z. Qiao, *Angew. Chem.*, **2013**, 52, 3110-3116.

45.   M. Sahoo, K. Sreena, B. Vinayan and S. Ramaprabhu, *Mater. Res. Bull.*, **2015**, 61, 383-390.

46.   A. Zehtab Yazdi, H. Fei, R. Ye, G. Wang, J. Tour and U. Sundararaj, *ACS Appl. Mater. Interfaces*, **2015**, 7, 7786-7794.

47. X.-k. Ma, N.-H. Lee, H.-J. Oh, S.-C. Jung, W.-J. Lee and S.-J. Kim, *J. Cryst. Growth*, **2011**, 316, 185-190.

48. S. M. Jung, E. K. Lee, M. Choi, D. Shin, I. Y. Jeon, J. M. Seo, H. Y. Jeong, N. Park, J. H. Oh and J. B. Baek, *Angew. Chem.*, **2014**, 53, 2398-2401.

49. X. Duan, S. Indrawirawan, H. Sun and S. Wang, *Catal. Today*, **2015**, 249, 184-191.

50. S. Sandoval, N. Kumar, A. Sundaresan, C. Rao, A. Fuertes and G. Tobias, *Chem. Eur. J.*, **2014**, 20, 11999-12003.

51. S. Sandoval and G. Tobias, *Nanomaterials*, **2020**, 10, 1451-1466.

52. T. Rath and P. P. Kundu, *RSC Adv.*, **2015**, 5, 26666-26674.

53. L. Qu, Y. Liu, J.-B. Baek and L. Dai, *ACS Nano*, **2010**, 4, 1321-1326.

54. M. Khandelwal, Y. Li, S. H. Hur and J. S. Chung, *New J. Chem.*, **2018**, 42, 1105-1114.

55. J. Yang, J. Shin, M. Park, G.-H. Lee, M. Amedzo-Adore and Y.-M. Kang, *J. Mater. Chem. A*, **2017**, 5, 12426-12434.

56. S. Chowdhury and R. Balasubramanian, *Sci. Rep.*, **2016**, 6, 21531-21541.

57. L. Liu, Y. Wang, Q. Meng and B. Cao, *J. Mater. Sci.*, **2017**, 52, 7969-7983.

58. J. Wang, B. Ding, Y. Xu, L. Shen, H. Dou and X. Zhang, *ACS Appl. Mater. Interfaces*, **2015**, 7, 22284-22291.

59. M. Mokhtar Mohamed, M. A. Mousa, M. Khairy and A. A. Amer, *ACS Omega*, **2018**, 3, 1801-1814.

60. F. Wei, H. Wang, W. Ran, T. Liu and X. Liu, *RSC Adv.*, **2019**, 9, 6152-6162.

61. R. Marschall and L. Wang, *Catal. Today*, **2014**, 225, 111-135.

62. C. Vallés, J. D. Núñez, A. M. Benito and W. K. Maser, *Carbon*, **2012**, 50, 835-844.

63. H. Xu, L. Ma and Z. Jin, *J. Energy Chem.*, **2018**, 27, 146-160.

64. A. Chen, Q. Shao, L. Wang and F. Deng, *Sci. China : Phys. Mech. Astron.*, **2011**, 54, 1438-1442.

65. Z.-S. Wu, W. Ren, L. Xu, F. Li and H.-M. Cheng, *ACS Nano*, **2011**, 5, 5463-5471.

66. H. L. Poh, P. Šimek, Z. Sofer, I. Tomandl and M. Pumera, *J. Mater. Chem. A*, **2013**, 1, 13146-13153.

67. M. Rein, N. Richter, K. Parvez, X. Feng, H. Sachdev, M. Kläui and K. Müllen, *ACS Nano*, **2015**, 9, 1360-1366.

68. A. Haque, M. Abdullah-Al Mamun, M. Taufique, P. Karnati and K. Ghosh, *IEEE Trans. Semicond. Manuf.*, **2018**, 31, 535-544.

69. N. E. Benti, G. A. Tiruye and Y. S. Mekonnen, *RSC Adv.*, **2020**, 10, 21387-21398.

70. H. R. Jiang, T. S. Zhao, L. Shi, P. Tan and L. An, *J. Phys. Chem. C*, **2016**, 120, 6612-6618.

71. Z. S. Wu, A. Winter, L. Chen, Y. Sun, A. Turchanin, X. Feng and K. Müllen, *Adv. Mater.*, **2012**, 24, 5130-5135.

72. R. Nankya, J. Lee, D. O. Opar and H. Jung, *Appl. Surf. Sci.*, **2019**, 489, 552-559.

73. D. W. Wang, F. Li, L. C. Yin, X. Lu, Z. G. Chen, I. R. Gentle, G. Q. M. Lu and H. M. Cheng, *Chem. Eur. J.*, **2012**, 18, 5345-5351.

74. H. M. Jeong, J. W. Lee, W. H. Shin, Y. J. Choi, H. J. Shin, J. K. Kang and J. W. Choi, *Nano Lett.*, **2011**, 11, 2472-2477.

75. J. Han, L. L. Zhang, S. Lee, J. Oh, K.-S. Lee, J. R. Potts, J. Ji, X. Zhao, R. S. Ruoff and S. Park, *ACS Nano*, **2013**, 7, 19-26.

76. V. Paranthaman, K. Sundaramoorthy, B. Chandra, S. P. Muthu, P. Alagarsamy and R. Perumalsamy, *Phys. Status Solidi A*, **2018**, 215, 1800298-1800307.

Appendix: Supporting information for Chapter 7

Table S7.1: Calculated weight percentage (wt.%) of N and B in heteroatom-doped rGO.

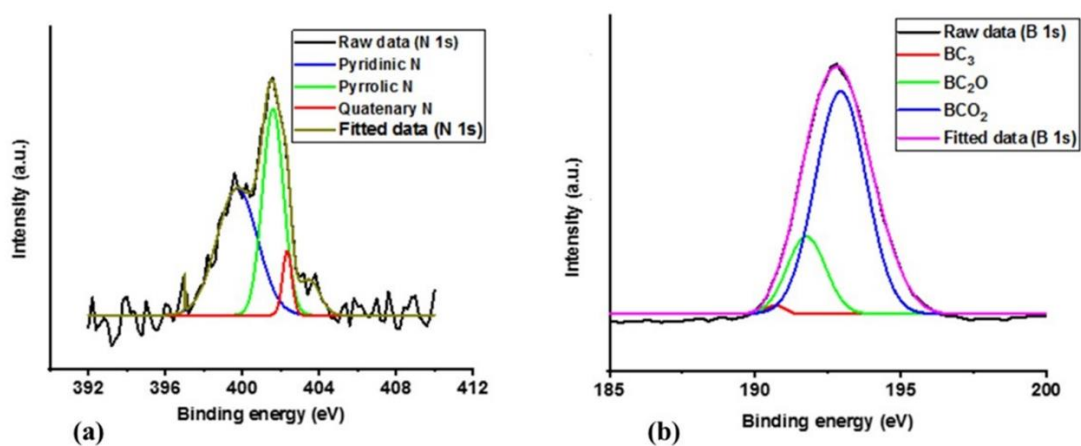| Sample	Nitrogen/wt.%	Boron/wt.%
GO	-	-
rGO	-	-
N-rGO	13.64	-
B-rGO	-	15.47
BN-rGO-1	6.98	7.91
BN-rGO-2	22.68	17.50
BN-rGO-3	8.33	6.43

Figure S7.1: XPS spectra of (a) N 1s of N-rGO and (b) B 1s of B-rGO.

Table S7.2: Atomic percentage (%) of N 1*s*, B 1*s*, O 1*s* and C 1*s* peak binding energy (eV).

Sample	Element	Atomic %	Peak binding energy (eV)	Functional group
N-rGO	C	88.10	284.5	C-C
			284.6	C-O
			285.8	C-N
			287.7	C=O
			289.3	O-C=O
	O	1.81	532.6	C=O
	N	7.09	398.9	pyridinic-N
			400.8	pyrrolic-N
			402.1	quaternary-N
B-rGO	C	93.31	284.3	C-C
			284.5	C-O
			289.1	O-C=O
	O	2.34	532.0	C-O
			532.8	C=O
	B	4.56	190.0	BC_3
			191.2	BC_2O
			192.3	BCO_2
BN-rGO-3	C	86.82	284.7	C-C (*sp^2*)
			284.8	C-O
			287.5	C=O
			288.9	O-C=O
	O	1.08	531.9	C-O
			532.7	C=O
	B	3.71	190.9	BC_3
			191.8	BC_2O
			192.7	BCO_2
	N	6.89	398.5	pyridinic-N
			400.2	pyrrolic-N

Table S7.3: Decomposition temperatures of GO, rGO and heteroatom-doped rGO.

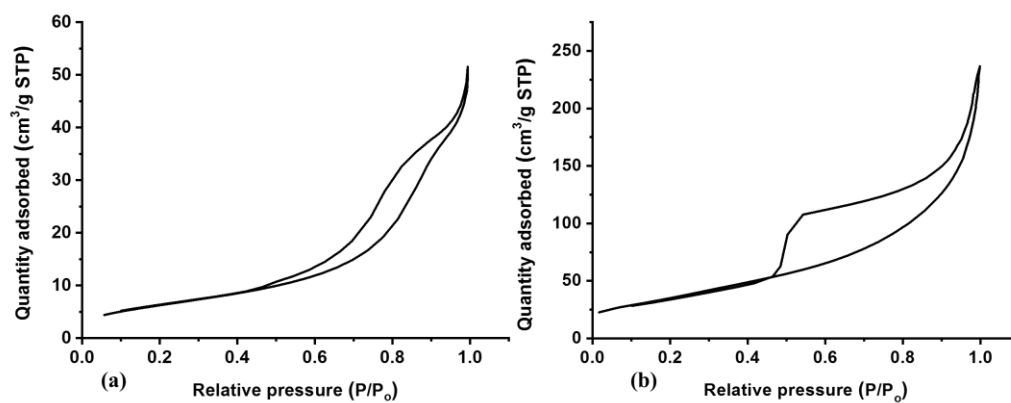| Sample	Decomposition temperature/°C
GO	491.9
rGO	588.5
N-rGO	582.4
B-rGO	533.6
BN-rGO-1	521.8
BN-rGO-2	520.5
BN-rGO-3	498.9

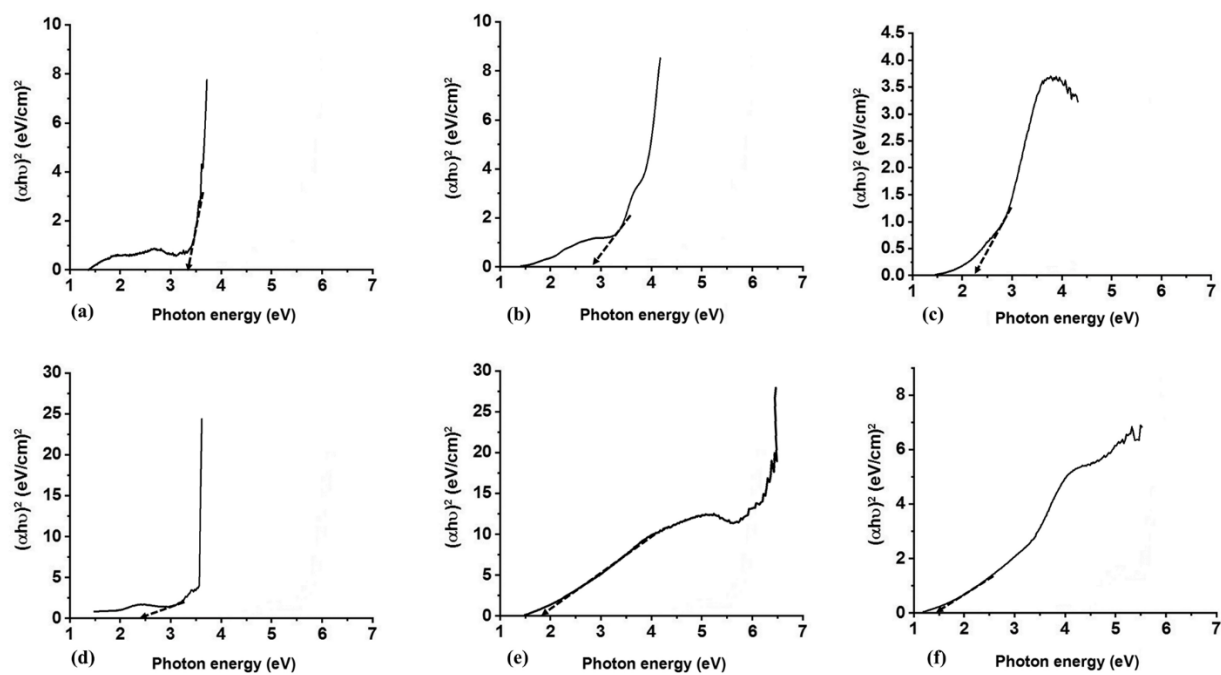**Figure S7.2:** N_2 adsorption-desorption isotherms of (a) GO and (b) BN-rGO-3.

Figure S7.3: Tauc's plot for (a) rGO, (b) N-rGO, (c) B-rGO, (d) BN-rGO-1, (e) BN-rGO-2 and (f) BN-rGO-3.

CHAPTER 8

Conclusions and future work

8.1   Conclusions

DSSCs still require focused studies to improve their stability and PCE. One of the important ways to accomplish this is to advance potential photoanode and CE materials with graphene-based nanomaterials, especially by introducing heteroatom-doped rGO or heteroatom-doped rGO-metal oxide-based nanocomposites. Heteroatom-doped rGO nanomaterials were effectively synthesized from graphite, doped with different heteroatoms (nitrogen and boron), and thermally treated by means of the CVD and hydrothermal methods. The doping temperature is among the most crucial parameters, which needs to be optimized to tune the graphitic nature and doping content in heteroatom-doped rGO. The variation of precursors and their ratio is also beneficial in controlling the bonding configuration in the rGO lattice. In this thesis, the synthesis, characterization, and application of graphene-based nanomaterials, viz, GO, rGO, N-rGO, B-rGO, N-rGO, BN-rGO, and heteroatom-doped rGO-metal oxide-based nanocomposites, such as N-rGO-TiO_2, N-rGO-Bi_2O_3, B-rGO-TiO_2, B-rGO-Bi_2O_3, in DSSCs were examined.

A study to investigate the influence of various doping temperatures (600, 700 and 800 °C), and different nitrogen precursors (4-aminophenol, 4-nitroaniline, and 4-nitro-o-phenylenediamine) on the electrical conductivity and physicochemical properties, such as surface morphology, structural properties, phase composition, thermal stability, surface chemistry (surface area and porosity) and nitrogen content of N-rGO, was done. Herein, one of the main key objectives was to determine the best doping temperature and nitrogen precursor that can be used with the rest of the heteroatom-doped rGO nanomaterials. By lowering the doping temperature (600 °C), a higher nitrogen content was incorporated into the rGO lattice. It also resulted in a less thermally stable N-rGO, yet with higher porosity, while the highest doping temperature (800 °C) produced the opposite results. An increase in the surface area and degree of disorder in N-rGO was ascribed to the reduction of oxygen-containing functional groups. N-rGO showed a lower thermal stability as the nitrogen content increased because of more deformities and distortions experienced in the N-rGO structure. The nitrogen content was affected by the various nitrogen precursors used. The nitrogen-rich precursor, 4-nitro-o-phenylenediamine, provided N-rGO with favourable physicochemical properties (larger surface area of 154.02 m^2 g^{-1}) and an enhanced electrical conductivity (0.133 S cm^{-1}). The choice of nitrogen precursors

significantly impacted the atomic percentage of nitrogen in N-rGO; thus, two major components of pyridinic-N and pyrrolic-N were observed, which assisted in improving the electrical conductivity of N-rGO and making it more valuable in DSSCs. Therefore, this study showed that by merely adjusting the doping temperatures and nitrogen precursors, one could tailor the various properties of N-rGO.

Doping depends on the tuning of Fermi levels by adding electron-withdrawing (p-type) or electron-donating (n-type) species that cause changes in the electron density and enhance the electrochemical properties. Thus, attaching a boron-containing moiety (electron-withdrawing) on the GO lattice showed to be a fruitful approach in tailoring the properties and positively tuning-up the PCE of DSSCs. All the synthesized B-rGO samples exhibited a p-type conductivity behaviour, which was due to an increase in the density of states near the Fermi level. A significant difference in the electronic properties of B-rGO samples demonstrated the highest level of boron doping and higher electrical conductivity. Increasing the boron-containing moieties on the graphitic sheets of rGO tends to amplify their defect density and was associated with a decrease in thermal stability. The boron content in B-rGO increased with boric anhydride concentration and reached its highest doping level of 7.12%, which imposed a significant change in the various properties. B-rGO with the highest boron content (B-rGO-70) and largest surface area showed an enhanced capacitance. B-rGO-70 also exhibited a typical semiconductor characteristic, with a sheet resistance of 1.863×10^1 Ω sq^{-1}. It also showed the lowest R_{ct} of 20.23 Ω, which is an indicator of good electron transport through the electrode-electrolyte interface, which is also a good and promising feature for the design and fabrication of electronic nanodevices.

The study of heteroatom-doped rGO-metal oxide-based nanocomposites showed that the textural characteristics are dependent on the metal oxide (TiO_2 and Bi_2O_3) content. rGO-TiO_2 with higher titania content yielded a smaller surface area, whereas N-rGO-TiO_2 with lower titania content resulted in a larger surface area. All the heteroatom-doped rGO-TiO_2-based nanocomposites showed an improvement in optical properties by decreasing the energy bandgap. A series of DSSCs consisting of various TiO_2-based nanocomposites as photoanodes and dyes (eosin B and Sudan II) were investigated. A higher light-harvesting efficiency was obtained from eosin B, indicating the presence of more dye molecules anchored to the TiO_2 photoanode. The presence of nitrogen and boron in the TiO_2-based nanocomposite led to a significant improvement in the photovoltaic performance of the DSSCs. In the case of Bi_2O_3-based nanocomposites, they showed an enhanced capacitance which could be credited to lower

charge transfer resistance, enhanced surface area, and better electrical conductivity properties than their counterpart Bi_2O_3.

The study of single and dual heteroatom-doping has shown a large influence on the physicochemical, optical, electrical conductivity, and electrochemical properties of rGO. Dual heteroatom-doping was the most effective approach when compared with single heteroatom-doping since it produced doped nanomaterials with the largest surface area but with lowered thermal stability. Single heteroatom-doped rGO attained the higher doping of nitrogen or boron atom than dual heteroatom-doped rGO. Yet, when comparing all the dual heteroatom-doped rGO samples synthesized, BN-rGO-3 from the boron and nitrogen-rich precursor resulted in the highest content of 3.71% for boron and 6.89% for nitrogen. The highest heteroatom content in dual heteroatom-doped rGO improved the catalytic activity and increased the photovoltaic performance, and this is due to increased synergetic effects. The bonding configuration and doping content significantly influenced the catalytic activity. The active catalytic sites for the redox reduction reaction were pyridinic-N and pyrrolic-N due to reduced adsorbed energy and a shift in the redox potential.

An improvement in the photovoltaic performance was observed for both single and dual heteroatom-doped rGO than GO and rGO. When heteroatom-doped rGO is used as a CE, it helps in selective electron blocking and hole injection at the interface; hence, it disables charge recombination, resulting in better J_{sc} and PCE. In general, this study has shown that high J_{sc} can be achieved in DSSCs by incorporating dual heteroatoms into rGO. Thus, incorporating dual heteroatoms into rGO created charge percolation pathways because of the high electrical conductivity properties. This was observed in BN-rGO-3, which had the highest pyridinic-N and pyrrolic-N content, and showed the highest electrical conductivity, and a PCE of 2.97%. Regardless of the high PCE in BN-rGO-3, there were some cracks on the CE during the fabrication, which might have affected the PCE of the DSSCs. Thus, the effect of using BN-rGO-3 with a binder, such as Nafion or PANI, was investigated. When PANi was incorporated with BN-rGO-3, it produced an enhanced PCE of 4.13%, FF of 60.3%, J_{sc} of 17.84 mA cm$^{-2,}$ and V_{oc} of 0.56 V. Therefore, for a higher PCE to be achieved in DSSCs, a high FF, J_{sc} and V_{oc} are required. This study has provided a strategy to simultaneously improve the PCE, J_{sc}, and FF of DSSCs, albeit with no effect on the V_{oc}.

This thesis presents the evaluation of the allied CE and photoanode characteristics, which exhibited an increase in PCE with an increase in pyrrolic-N and pyridinic-N content in heteroatom-doped rGO. The hydrothermal approach was suitable for producing heteroatom-

doped rGO-TiO$_2$- or Bi$_2$O$_3$-based nanocomposites with larger surface area, low defect intensity, and higher PCE. In summary, the methods used to synthesize the heteroatoms-rGO and nanocomposites are feasible strategies to tune the physicochemical, optical, electrical conductivity, and electrochemical properties. The boron or nitrogen precursors, doping temperatures, and various ratios of heteroatom-rGO and their nanocomposites were effectively exploited to control the various properties mentioned.

8.2   Future work

Despite the various research approaches for the synthesis of single and dual heteroatom-doped rGO and their nanocomposites, there are yet numerous issues to be tackled, for instance:

- Although the effect of pyridinic-N and pyrrolic-N composition on the electrical conductivity and performance of DSSCs was studied in this current work, controlling the nitrogen bonding configuration is still a critical issue in N-rGO, which is exceptionally needed in electrocatalysis for better performance of DSSCs.

- The synthesized single and dual heteroatom-doped rGO and their nanocomposites can be applied in capacitors.

- The effect of the size of the heteroatom-doped rGO-metal oxide-based nanocomposites on the optical properties should be investigated for optoelectronic applications, such as light-emitting diodes and photodetectors.

- The successful syntheses of N-rGO and B-rGO-metal oxide-based nanocomposites opens avenues for the use of different heteroatom-doped rGO (e.g., S-rGO or P-rGO) to be coated with different metal oxides, such as TiO$_2$, Bi$_2$O$_3$, ZnO, etc., and further investigate their effect on DSSCs or organic solar cells.

- An investigation of the magnetic and surface energy properties of the synthesized heteroatom-doped rGO-metal oxide-based nanocomposites and their potential in magnetic-based technological applications, for example, spintronics ought to be performed.

- Another interesting study would be on the use of different electrolytes (sulfate (lithium sulfate, sodium sulfate, and potassium sulfate), ionic liquid, or sulfuric acid) and optimization of its concentration during the analysis of electrochemical properties (CV and EIS), which can be investigated with heteroatom-doped rGO or heteroatom-doped rGO-metal oxide-based nanocomposites.

- Lastly, a theoretical investigation *via* computational studies can be used to investigate further the influence of single and dual heteroatom-rGO and the heteroatom-doped rGO-metal oxide-based nanocomposites on DSSCs.

In short, this research has identified a wide scope of fascinating endeavours that one could investigate further.